AD_____

FIELD MEASUREMENT AND MODEL EVALUATION PROGRAM FOR ASSESSMENT OF THE ENVIRONMENTAL EFFECTS OF MILITARY SMOKES

THE ATTERBURY-87 FIELD STUDY OF SMOKE DISPERSION AND A NEW STOCHASTIC DISPERSION MODEL FINAL REPORT

prepared by

J.C. Liljegren, W. E. Dunn, and G. E. DeVault
Department of Mechanical and Industrial Engineering
University of Illinois at Urbana-Champaign
Urbana, IL 61801
217-333-3832

and

A. J. Policastro
Energy and Environmental Systems Division
Argonne National Laboratory
9700 South Cass Avenue
Argonne, IL 60439
312-972-3235

FEBRUARY 1, 1989

Supported by
U. S. ARMY MEDICAL RESEARCH AND DEVELOPMENT COMMAND
Fort Detrick, Frederick, MD 21701

Contract No. 84PP4822

Contracting Officer's Representatives: Major John Young, Major David L. Parmer
Health Effects Research Division
U. S. ARMY BIOMEDICAL RESEARCH AND DEVELOPMENT LABORATORY
Fort Detrick, Frederick, MD 21701

NOTICE

Disclaimer

The findings in this report are not to be construed as an official Department of the Army position unless so designated by other authorized documents.

Disposition

Destroy this report when it is no longer needed. Do not return it to the originator.

SECURITY CLASSIFICATION OF THIS PAGE

REPORT DOCUMENTATION PAGE

1a. REPORT SECURITY CLASSIFICATION Unclassified	1b. RESTRICTIVE MARKINGS
2a. SECURITY CLASSIFICATION AUTHORITY	3 DISTRIBUTION / AVAILABILITY OF REPORT Approved for public release; distribution unlimited
2b. DECLASSIFICATION / DOWNGRADING SCHEDULE	
4. PERFORMING ORGANIZATION REPORT NUMBER(S)	5. MONITORING ORGANIZATION REPORT NUMBER(S)
6a. NAME OF PERFORMING ORGANIZATION Argonne National Laboratory 6b. OFFICE SYMBOL (If applicable)	7a. NAME OF MONITORING ORGANIZATION
6c. ADDRESS (City, State, and ZIP Code) Argonne, Illinois 60439	7b. ADDRESS (City, State, and ZIP Code)
8a. NAME OF FUNDING/SPONSORING ORGANIZATION U.S. Army Medical Research & Development Command 8b. OFFICE SYMBOL (If applicable)	9. PROCUREMENT INSTRUMENT IDENTIFICATION NUMBER 84PP4822
8c. ADDRESS (City, State, and ZIP Code) Fort Detrick Frederick, Maryland 21701-5012	10. SOURCE OF FUNDING NUMBERS PROGRAM ELEMENT NO. 62720A; PROJECT NO. 3E1-62720A835; TASK NO. AA; WORK UNIT ACCESSION NO 012

11. TITLE (Include Security Classification)
(U) Field Measurement and Model Evaluation Program for Assessment of the Environmental Effects of Military Smokes: The Atterbury-87 Field Study of Smoke Dispersion Compared with a New Stochastic Dispersion Model

12. PERSONAL AUTHOR(S)
J. C. Liljegren, W. E. Dunn, G. E. DeVaull, and A. J. Policastro

13a. TYPE OF REPORT	13b. TIME COVERED	14. DATE OF REPORT (Year, Month, Day)	15. PAGE COUNT
Final	FROM 1987 TO 1988	1989 February 1	311

16. SUPPLEMENTARY NOTATION

17. COSATI CODES		
FIELD	GROUP	SUB-GROUP
04	01	
07	03	

18. SUBJECT TERMS (Continue on reverse if necessary and identify by block number)
RA 3, smoke, screening smoke, obscuring smoke, atmospheric boundary layer, atmospheric dispersion, meteorological measurements, aerosol sampling, and particle size.

19. ABSTRACT (Continue on reverse if necessary and identify by block number)

The atmospheric dispersion of the military obscurant smokes produced by the M3A4 fog oil smoke generator and 30-lb M5 HC smoke pots has been studied in a program of field trials carried out in a grassy meadow in south-central Indiana. The investigation focused on four areas. Measurements of the mass rate of release and exit temperature were performed to define the smoke sources. The smoke aerosol was characterized in terms of the particle size distribution. A description of the prevailing meteorology was obtained from measurements of the wind speed, wind direction, temperature and relative humidity at four levels on a 10-m instrument tower located on the test site. Measurements of the average smoke concentration over the period of release were carried out at 50 locations on 5 transects located 50, 100, 250, 450 and 675 m from the release point. At each location concentration measurements were performed at 1, 2, 4 and 8 m above ground level except on the fifth transect where they were performed at 2 and 8 m. (continued on back)

20. DISTRIBUTION / AVAILABILITY OF ABSTRACT ☐ UNCLASSIFIED/UNLIMITED ☒ SAME AS RPT. ☐ DTIC USERS	21. ABSTRACT SECURITY CLASSIFICATION Unclassified
22a. NAME OF RESPONSIBLE INDIVIDUAL Mary Frances Bostian	22b. TELEPHONE (Include Area Code) 301-663-7325 22c. OFFICE SYMBOL SGRD-RMI-S

DD FORM 1473, 84 MAR 83 APR edition may be used until exhausted. All other editions are obsolete.

SECURITY CLASSIFICATION OF THIS PAGE

BLOCK 19 (continued)

The particle size distribution for fog oil smoke was determined to be lognormal with a mass median diameter of 0.9 μm and a geometric standard deviation of 1.5. The particle size distribution of the HC smoke particles was also observed to be lognormal. Assuming a density of 2 g/cm^3, the mass median diameter of the HC smoke particles was determined to be 0.8 μm with a geometric standard deviation of 2.2.

The average smoke concentrations were observed to decline with distance whereas the width of the smoke plume increased. No discernable vertical gradients in the smoke concentration were observed in the data. Comparisons of the crosswind-integrated concentration and plume spread computed from the test data with the results of previous field studies of atmospheric dispersion indicated strong agreement. These comparisons revealed that the centerline of the smoke plume rose as the plume moved downwind due to the effects of thermal convection.

Comparison of the concentration data with the predictions of a new stochastic model, described herein, also showed good agreement and confirmed that the centerline of the smoke plume lifted off the ground. This was in sharp contrast to the calculations of a generic Gaussian plume model which did not predict the rising centerline and substantially over-predicted the ground level concentrations.

FORWARD

Opinions, interpretations, conclusions and recommendations are those of the author and are not necessarily endorsed by the U.S. Army.

WED Where copyrighted material is quoted, permission has been obtained to use such material.

_____Where material from documents designated for limited distribution is quoted, permission has been obtained to use the material.

WED Citations of commercial organizations and trade names in this report do not constitute an official Department of the Army endorsement or approval of the products or services of these organizations.

_____In conducting research using animals, the investigator(s) adhered to the "Guide for the Care and Use of Laboratory Animals," prepared by the Committee on Care and Use of Laboratory Animals of the Institute of Laboratory Animal Resources, National Research Council (NIH Publication No. 86-23, Revised 1985).

_____For the protection of human subjects, the investigator(s) have adhered to policies of applicable Federal Law 45CFR46.

W. E. Dunn 9/5/89

PI Signature Date

EXECUTIVE SUMMARY

This report summarizes the development and testing of a new stochastic model for predicting the dispersion of smoke in the convective boundary layer. The report also describes the methods and procedures employed and the results obtained from the Atterbury-87 field study of fog oil smoke and hexachloroethane (HC) smoke.

The stochastic model represents a substantial improvement over previous modelling approaches in that it provides a more realistic treatment of the atmospheric turbulence, especially for the large-scale convective motions occurring in the daytime planetary boundary layer which are largely responsible for the dispersion process. Using the Langevin equation to model the Lagrangian velocities, the dispersion of a large number of passive tracer particles is computationally simulated. The highly inhomogeneous turbulent vertical velocities are modelled as a skewed random process having the correct first, second, third and fourth moments. The shape of the resulting probability density function closely matches observations. The behavior of the autocorrelation of the modelled Lagrangian velocities also matches the non-exponential form computed from balloon-borne measurements by using the local integral time scale of the turbulence.

The model was verified against the results of dispersion measurements published in the literature. The comparisons include data from laboratory simulations of the boundary layer carried out in water tanks and wind tunnels as well as from actual field measurements. The predictions of the stochastic model were in agreement with both the trends and magnitudes observed in the data, including the lift-off of the plume centerline from the ground due to the influence of the rising thermal updrafts.

The Atterbury-87 field study was conducted in a grassy meadow at the Atterbury Reserve Forces Training Center (ARFTC) in south-central Indiana during October and November, 1987. The study involved four releases of fog-oil smoke and five releases of HC smoke. The fog-oil smoke was produced from SGF-2 fog oil using a single M3A4 military smoke generator. The HC smoke was produced using approximately twenty 30-lb M5 HC smoke pots per test. Time-dependent measurements of the exit temperature and mass rate of release of the smoke material were carried out in order to define the source conditions. The wind speed, wind direction, temperature and humidity were also measured at a near-source location.

To define atmospheric conditions, meteorological measurements were carried out at heights of 2, 4, 6 and 10 m on an instrument tower located roughly in the middle

of the test site. These measurements included wind speed, wind direction (both horizontally and vertically), temperature and relative humidity. From these data, parameters were computed which characterize the local meteorological conditions. The meteorological measurements were generally in good agreement with published results of extensive atmospheric turbulence research although some terrain effects were observed. The data analysis indicated that the tests were conducted during atmospheric conditions ranging from nearly neutral to moderately unstable (convective).

Measurements of the smoke particle size distribution indicated that 98% of the fog-oil droplets by mass are between 0.3 and 3.0 μm, and that the mass median (50%) diameter of the fog-oil droplets is 0.9 μm. These results agree with our previous field measurements as well as with other laboratory studies of fog-oil smoke. For the HC smoke, 98% of the particles by mass were found to lie between 0.25 and 4.0 μm; the mass median diameter was found to be 0.8 μm.

Measurements of average smoke concentration were carried out at 50 locations on five linear transects at distances of 50, 100, 250, 450 and 675 m from the release point. On each of the first four transects concentrations were measured at heights of 1, 2, 4 and 8 m above the ground; on the fifth transect concentrations were measured at heights of 2 and 8 m.

In all cases the trajectory of the smoke plume was defined by the measurements, and the width of the plume was almost always completely resolved. The results are in agreement with the findings of previous laboratory and field studies. The data provide a consistent and useful picture of the smoke dispersion and demonstrate the significant effects of convection on the dispersion, even for cases where the insolation was relatively small.

The field data were compared with the predictions of the stochastic model and a generic Gaussian plume model. The qualitative and quantitative agreement between the data and the stochastic model is encouraging. The effect of the convection, which is manifested in the lift-off of the plume centerline and the corresponding decrease in ground-level concentration observed in the field data, was correctly predicted by the stochastic model whereas the Gaussian plume model failed to predict either the correct magnitudes or trends observed in the field data.

ACKNOWLEDGEMENT

The authors with to thank the staff of the Atterbury Reserve Forces Training Center for their assistance in executing this field study. Especially noteworthy were Colonel (ret.) Robert Abel and Major John Robertson who deftly coordinated our use of the test range and other facilities. However, numerous other members of the staff participated to varying degrees in the project, and their valuable efforts are gratefully acknowledged.

We also wish to thank our former USAMBRDL Contracting Officer's Representative, Major David Parmer, and our present Contracting Officer's Representative, Major John Young for their important role in shaping this project. Their many helpful suggestions and insightful comments added enormously to the success of the effort. The direct contribution of Major Young to the field effort, during his visit to the test site, was particularly valuable.

TABLE OF CONTENTS

Page

LIST OF FIGURES

LIST OF TABLES

NOMENCLATURE

English Symbols

c	Concentration
c_p	Specific heat at constant pressure
C	Mean concentration
C_∞	Free stream concentration
C_c	Cunningham slip correction factor
C^y	Crosswind-integrated mean concentration
C^y_{WD}	Crosswind-integrated mean concentration neglecting diffusion in the x-direction
C_n	Carbon number; the number of carbon atoms in a molecule
$\bar{d}$	Mass mean diameter
d_{av}	Number mean diameter
d_f	Fiber diameter
d_g	Geometric mass mean diameter
d_p	Particle diameter
D	Turbulent diffusivity transfer function, Eq. (2.15)
D_{EXIT}	Smoke source exit diameter
D_j	Jet diameter
$\mathcal{D}$	Coefficient of molecular diffusion
e	Charge on an electron
E	Overall filter efficiency
E_Σ	Total single-fiber collection efficiency
E_T	Strength of the terrestrial electric field
E_G	Single-fiber capture efficiency due to gravitational settling
E_I	Single-fiber capture efficiency due to inertial impaction

E_R	Single-fiber capture efficiency due to interception
f	Coriolis force
f_S	Frequency of oscillation of QCM cascade impactor measurement crystal
f_R	Frequency of oscillation of QCM cascade impactor reference crystal
f_{OUT}	Output frequency ($f_S - f_R$)
Fr	Densimetric Froude number $\left(\sqrt{\frac{\rho_\infty V_{EXIT}^2}{\Delta\rho \; g \; D_{EXIT}}} \right)$
g	Gravitational acceleration
G	Spatial filter function used in Large Eddy Simulation, Eq. (2.23); also the ratio of terminal settling velocity to free stream velocity, Eq. (5.27)
h	Boundary layer height
I	Turbulence intensity (σ_u / U)
k	Boltzmann's constant
κ	Wavenumber ($2\pi/\lambda$)
k_T	Thermal conductivity
K	Eddy diffusivity
Ku	Kuwabara hydrodynamic factor
K_y, K_z	Eddy diffusion coefficients in the y- and z-directions, respectively
K_1	Value of K_z at the reference height z_1
L	Monin-Obukov length
L_E	Eulerian integral length scale
m	Mass
n	Frequency
n_{max}	Frequency at which the frequency-weighted power spectrum has a maximum
q	Surface heat flux

Q	Source strength
Q_o	Kinematic heat flux at the surface ($q / \rho c_p = \overline{T'w'}$)
p	Probability density function
P	Probability distribution function $\left(\int p(x)dx\right)$
Pe	Peclet number
$\mathbf{r}$	Position vector (x, y, z)
$\mathbf{r}_0$	Initial position vector (x_0, y_0, z_0)
R	Turbulent exchange rate, Eq. (2.18)
Re	Reynolds number
R_L	Lagrangian correlation coefficient, Eq. (2.31)
s	Horizontal wind speed ($\sqrt{u^2+v^2}$)
S	Source distribution function
S_E	Eulerian power spectrum
S_L	Lagrangian power spectrum
Sk	Skewness ($\langle w'^3 \rangle / \langle w'^2 \rangle^{3/2}$)
Stk	Stokes number
Stk_{50}	Value of Stk for which 50% (by mass) of particles are collected on a given impactor stage
S_y, S_z	Dimensionless functions in Eq. (2.39) describing the evolution of σ_y and σ_z, respectively.
t	Time
t_{TEST}	Test duration
Δt	Time increment
T	Potential or absolute temperature
T_c	Characteristic time scale
T_E	Eulerian integral time scale
T_K	Kolmogorov time scale
T_L	Lagrangian integral time scale

T_R	Relaxation time
T_0	Extrapolated temperature at z = 0
T_*	Temperature scale ($-\overline{T'w'} / u_*$)
u	Velocity vector (u, v, w)
u, v, w	Components of the air (wind) velocity in the x-, y- and z-directions, respectively
u', v', w'	Turbulent velocity fluctuations in the x-, y- and z-directions, respectively
u_*	Friction velocity
U, V, W	Mean velocity components in the x-, y- and z-directions, respectively
U_0	Value of U at $\mathbf{r}_0$, the initial position of the particles
U_1	Value of U at the reference height z_1
U_G	Component of the geostrophic wind parallel to the isobars
V_j	Jet velocity
V_s	Terminal settling velocity
V_E	Terminal electrostatic velocity
V_{EXIT}	Source exit velocity
V_G	Component of the geostrophic wind perpendicular to the isobars
$\dot{V}$	Volumetric flow rate
w_*	Convective velocity scale
$\mathcal{W}(t)$	Weiner process
x, y, z	Spatial coordinates (x in the direction of the mean wind, y in the horizontal crosswind direction, z in the vertical direction)
X, Y, Z	Time-dependent spatial position of a particle
z_i	Inversion height
z_1	Reference height

Greek Symbols

β	Ratio of the Lagrangian to Eulerian integral scales (T_L / T_E)
δ	Dirac delta function
Δ	Grid spacing in Large Eddy Simulation
Δ_a	Averaging volume in Large Eddy Simulation
Γ	Adiabatic lapse rate (g/c_p)
ε	Rate of viscous dissipation of turbulent energy
$\eta(t)$	White noise process
η	Fluid viscosity
θ	Wind direction (azimuth, horizontal angle)
ϕ	Wind inclination (vertical angle)
ϕ_h, ϕ_m	Dimensionless vertical fluxes of heat and momentum, respectively
κ	von Kármán's constant
λ	Wavelength
λ_m	Wavelength at which the frequency-weighted power spectrum has a maximum
λ_{mfp}	Mean free path length
ψ	Universal function in Lagrangian similarity theory, Eq. (2.45)
ρ	Density
ρ_{EXIT}	Source exit density
$\Delta\rho$	Density difference ($\rho_\infty - \rho_{EXIT}$)
ρ_∞	Ambient fluid density
ρ_p	Particle density
τ	Surface shear stress
$\mu(t)$	A discrete random process
μ_x, μ_y, μ_z	Components of the discrete random process in the x-, y- and z-directions, respectively

ν	Kinematic fluid viscosity (η/ρ)
σ_g	Geometric standard deviation
$(\sigma_g)_{H\text{-}C}$	Geometric standard deviation computed using the Hatch-Choate relations for a lognormal distribution
$\sigma_x, \sigma_y, \sigma_z$	Standard deviations of particle distribution in the x-, y- and z-directions, respectively
$\sigma_u, \sigma_v, \sigma_w$	Standard deviations of the fluctuations in the wind velocity in the x-, y- and z-directions, respectively
$\sigma_\theta, \sigma_\phi$	Standard deviations of the fluctuations in the wind direction (horizontal angle) and wind inclination (vertical angle)
$\sigma_{Nx}, \sigma_{Ny}, \sigma_{Nz}$	Resolution bandwidth of the kernal estimator in the x-, y- and z-directions, respectively
ξ	Time lag
χ	Spatial lag
X	Dimensionless travel time $\left(\frac{x/U}{h/w_*}\right)$
ζ	Stability parameter (h/-L)

Miscellaneous Symbols

' (prime)	Indicates fluctuating quantity (velocity, temperature or concentration) or dummy variable of integration (position or time)
$\overline{\quad}$ (overbar)	Indicates time average
$\langle\,\rangle$	Indicates ensemble average
$\{\,\}$	Indicates volume average
~	Indicates Fourier transform
^	Indicates moment generating function

1. INTRODUCTION

1.1 Motivation

One of the most important features of turbulence in the planetary boundary layer is its capability to quickly disperse concentrated airborne pollutants. This has significant ramifications for man's relationship with his environment. Turbulent atmospheric dispersion has long been studied in order to assess the effects of chronic, long-term exposures to continuously released airborne pollutants such as emissions from automobile exhausts and industrial, municipal and utility smokestacks. Current analytical and experimental efforts deal almost exclusively with this problem of describing the evolution of mean concentrations over large distances and long times.

Of a more critical nature, however, is the assessment of brief, acute exposures over distances up to a few kilometers. Such exposures may result from instantaneous or short-term releases of toxic agents due, for example, to vehicular mishaps or industrial accidents. In this scenario, models which predict short-term concentrations near the point of release are required. Such models must describe the evolution of the mean concentration field. This presents a much more difficult task which has received correspondingly little attention. The present investigation addresses this task for aerosols comprised of sufficiently small particles that they behave as a passive scalar contaminant or tracer. Since most materials for which acute exposures are of interest exist as fine aerosols or gases that do behave as passive tracers, this is a reasonable assumption.

In addition, the effects of the solar heating of the earth's surface on the behavior of the turbulence and the resulting dispersion have traditionally been neglected. Over the last two decades, extensive studies of the planetary boundary layer have demonstrated the important role of the surface heat flux in determining the dispersion at distances less than two kilometers. The present investigation is thus concerned with quantifying this role and incorporating it into a model of short range dispersion.

1.2 Background

Atmospheric phenomena may be conveniently divided into three categories according to their spatial and time scales. *Macroscale* phenomena such as the "jet stream" are those which extend over horizontal distances in excess of 2000 km or

have time scales on the order of a week or more. Macroscale phenomena are global processes which arise due to the global temperature gradient between the tropics and the polar regions. This temperature gradient is induced by the difference in the absorption of incident solar radiation (insolation) and creates large horizontal pressure gradients between the low and high latitudes. The force exerted on the atmosphere by these pressure gradients is balanced by the Coriolis force due to the rotation of the earth. The atmospheric motion resulting from this force balance, the *geostrophic wind*, is parallel to the isobars (lines of constant pressure) $U_G = -\frac{1}{\rho f}\frac{\partial p}{\partial n}$ where U_G is the component along the isobars, ρ is the air density, f is the Coriolis parameter and $\partial p/\partial n$ is the pressure gradient normal to the isobars. The geostrophic wind attains a maximum at an elevation of about 1 km, just above the boundary layer where friction affects the flow.

The only surface features which are sufficiently large to influence macroscale motions are the oceans and the continents. Convection in the oceans enables them to quickly distribute heat and destroy temperature gradients near the surface. As a result, the surface temperature of the oceans responds very slowly to diurnal and seasonal variations in insolation. Obviously, convective heat transfer is not possible in the continental land masses. The fact that only a relatively thin layer of land becomes heated, coupled with relatively low heat capacity, causes surface temperatures over land to vary strongly with diurnal and seasonal variations in insolation.

Smaller scale, regional phenomena such as thunderstorms are referred to as *mesoscale* events. These are defined as phenomena with horizontal dimensions between 2 and 2000 km. Mesoscale processes receive their energy primarily from the latent heat released in the condensation of water vapor during cloud formation and from their interaction with regional surface features. The variations in surface heating between large bodies of water and coastal regions, mountain ranges and valleys as well as large cities and rural areas can also produce substantial regional temperature gradients which are capable of generating mesoscale motions.

Microscale phenomena have horizontal scales less than 2 km and time scales in the range of minutes or seconds. Because they are confined vertically to the boundary layer, microscale motions are strongly affected by the local terrain and vegetation as well as local temperature gradients. Although this investigation will deal exclusively with microscale phenomena, the effect of the larger scales on our analysis of the microscale motions must be considered.

The turbulent planetary boundary layer is idealized in Figure 1.1. Momentum transfer between the geostrophic wind above the boundary layer and the ground,

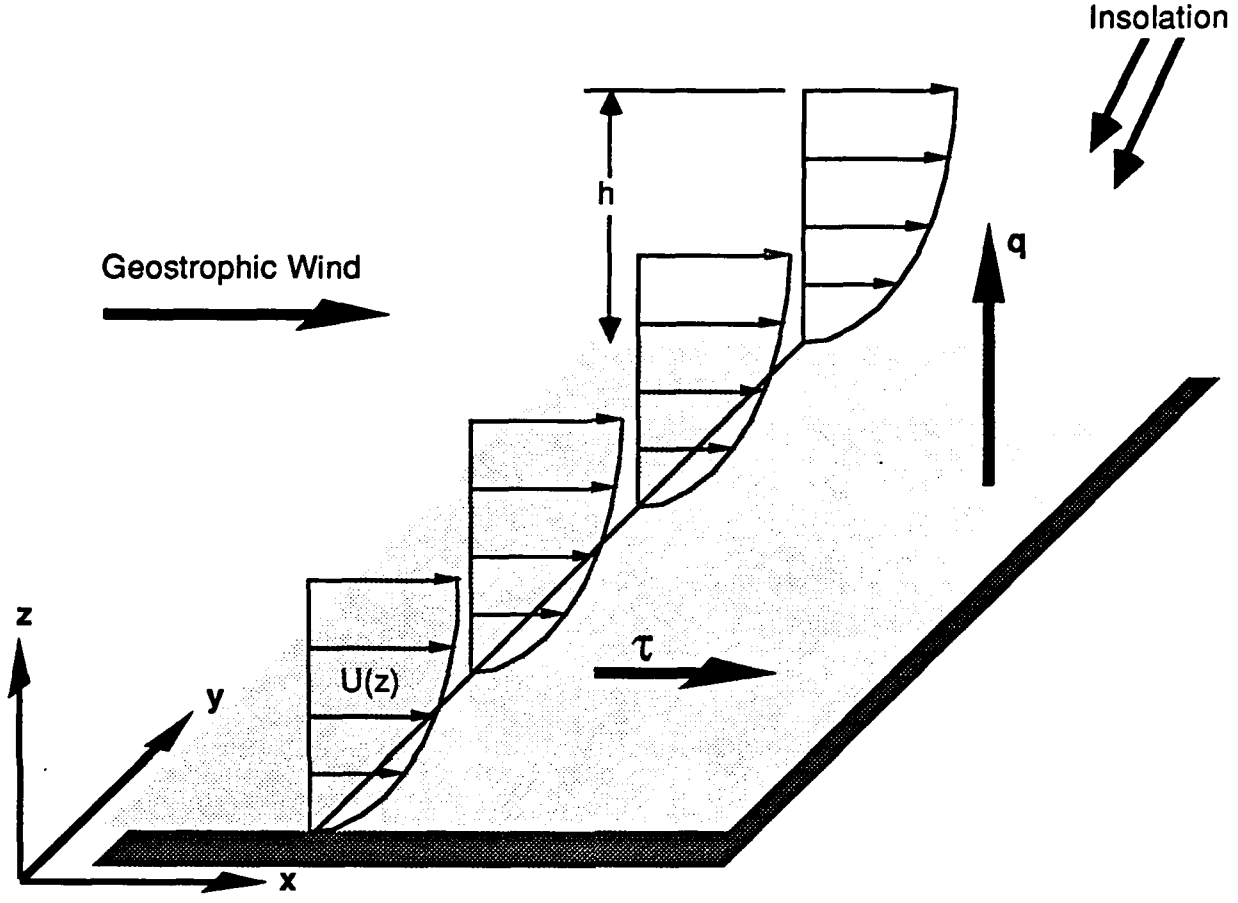

Figure 1.1 The idealized planetary boundary layer.

characterized by a roughness length z_0, give rise to a shear stress τ at the surface. The shear flow creates turbulence which transfers momentum to the surface. This momentum flux is characterized by the friction velocity $u_*^2 = \tau/\rho = -\overline{u'w'}$ where the primes denote the fluctuating components of the velocity. The logarithmic form of the mean wind profile in the boundary layer results from this interaction. The coordinate axes are aligned such that the streamwise axis (x-axis) is in the direction of this stress. The x-y plane is taken to be parallel to the ground and the z-axis is directed vertically upward. The result of this choice of coordinate orientation is that the mean wind velocity is given by $\overline{(u,v,w)} = (U,0,0)$.

In these respects the planetary boundary layer has much in common with boundary layers observed in other engineering flows. However, certain additional features of the planetary boundary layer make its description uniquely challenging.

Unlike most engineering flows in which the scales of motion are bounded by the physical size of the apparatus, we have seen that the range of time and spatial scales in the atmosphere is very great. One result of this large range of scales is that observed statistics of the microscale are not time-invariant. That is, they generally increase with increasing observation time. Long observation times are not generally possible because of the non-stationary nature of the atmosphere due to the variations in the macro- and mesoscale motions.

At the microscale, this non-stationarity is complicated by the diurnal cycle of solar heating which creates a time-varying surface heat flux and causes the temperature gradient in the boundary layer to also vary diurnally. In the absence of a surface heat flux, such as a heavily overcast day with high winds, the temperature of the atmosphere would still decrease with height because of the decreasing hydrostatic pressure. If a parcel of air at the surface was lifted to a higher altitude sufficiently quickly that it did not lose any heat to its surroundings, it would still have a lower temperature given by $T = T_0 + \Gamma\Delta z$ where $\Gamma = g/c_p = -0.0098$ °C/m is the *adiabatic lapse rate*. The temperature defined by this relation is known as the *potential temperature*. If the actual temperature gradient is close to the adiabatic lapse rate, then the potential temperature gradient would be zero and a parcel of air which is displaced vertically will remain at its new elevation. This is referred to as *neutral* atmospheric stability. If the true temperature decreases more rapidly with height than the adiabatic lapse rate, possibly due to a large surface heat flux typical of a sunny day, then the potential temperature gradient would be negative and an upwardly displaced parcel of air would still be warmer than its surroundings and would continue to rise vertically. These are known as *unstable* conditions. If, on the other hand, the temperature increases with height, perhaps due to nighttime radiative cooling of the surface, then the potential temperature gradient will be positive; an upwardly displaced parcel will be cooler than its surroundings and will sink down to its original position. These are referred to as *stable* conditions.

The relative magnitudes of the turbulence energy produced by the shear flow and that produced by the heating of the ground determine the structure of the planetary boundary layer. This balance between mechanical turbulence and convective turbulence is characterized by the Monin-Obukhov length $L = \frac{-u_*^3}{[\kappa(g/T)Q_o]}$ (Monin and Obukhov, 1954) where κ is von Karman's constant (≈ 0.4); the kinematic heat flux $Q_o = q/(\rho c_p) = \overline{T'w'}$ and q is the heat flux at the surface. The Monin-Obukhov length

indicates the approximate upper limit of the *surface layer*, where shear dominates the flow. Thus in the shear layer the Monin-Obukhov length is the appropriate length scale. On very windy, heavily overcast days as well as in the transition between the stable nighttime boundary layer and the convective daytime boundary layer (near sunrise and sunset) the heat flux is essentially zero and the boundary layer is said to be neutrally stratified. In this case $L \rightarrow \infty$ which indicates that shear dominates over the entire height of the boundary layer. On such occasions the height of the boundary layer h is determined by the balance of the shear and the Coriolis force arising from the earth's rotation: $h = cf/u_*$ where c is a constant of order unity and f is the Coriolis parameter.

At night, radiative cooling of the earth's surface results in a positive potential temperature gradient and a negative surface heat flux. In this case $L > 0$. On clear, sunny days, solar heating of the ground leads to a negative potential temperature gradient and unstable thermal stratification of the boundary layer, indicated by negative values for L. As the surface heat flux increases, L becomes smaller. This leads to the formation of the convective structures illustrated in Figure 1.2.

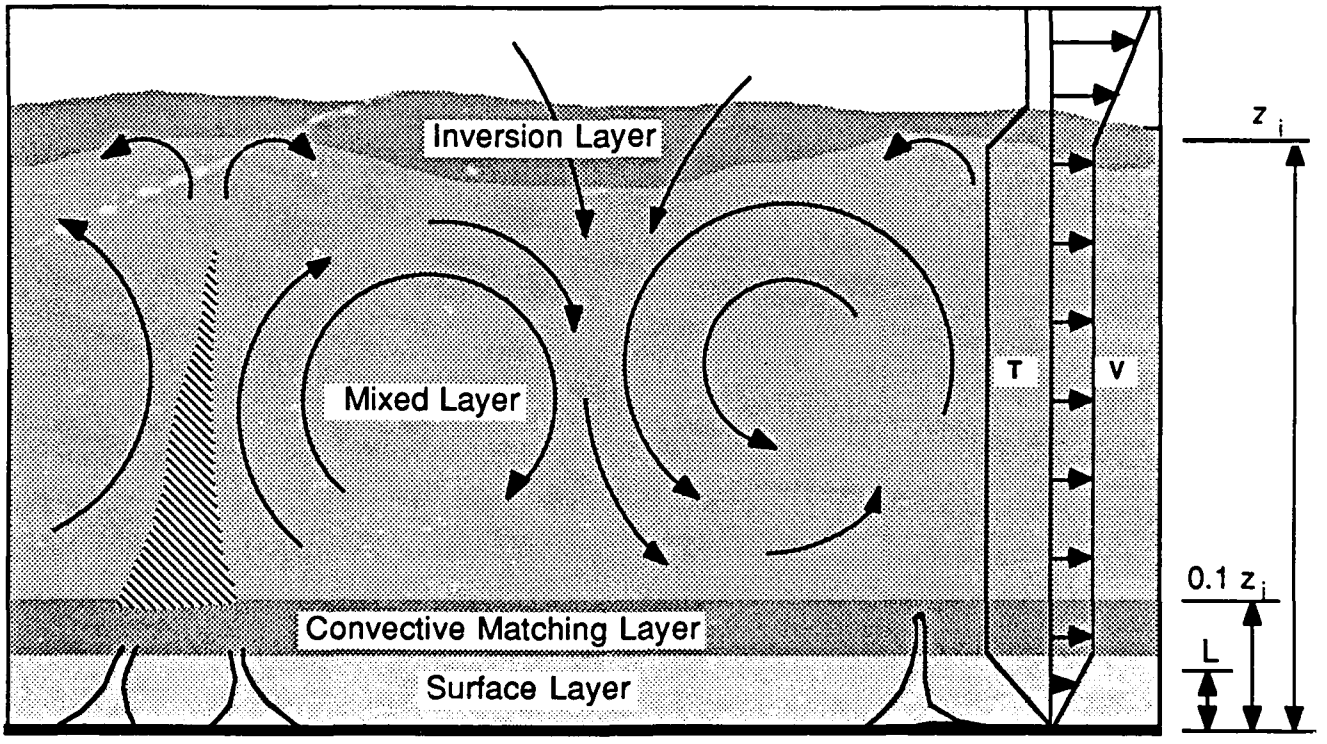

Figure 1.2 Illustration of the instantaneous behavior of the convective planetary boundary layer (after Wyngaard, 1985).

In the convective boundary layer the shear-dominated surface layer is confined to a shallow region near the ground. The updrafts of warmer air from the surface ("thermals") and downdrafts of cooler air from the temperature inversion ("subsidence") give rise to large scale vertical motions. Deardorff (1970) has shown that the relevant velocity scale in the mixed layer is the convective velocity scale $w_*^3 = z_i \frac{g}{T} Q_0 = -u_*^3 \frac{z_i}{\kappa L}$

where T is the average absolute potential temperature of the layer and z_i is the "mixing depth" indicated by the height of the temperature inversion. These motions tend to eliminate vertical gradients and give the mixed layer its name. The top of the convective boundary layer ($h \equiv z_i$) is marked by a strong thermal inversion of varying thickness. It can be penetrated from below by the most energetic thermals and from above by powerful motions of the macroscopic weather system, providing a challenging boundary condition. A more thorough discussion of the planetary boundary layer is given by Wyngaard (1985).

The adiabatic conditions which characterize the neutral boundary layer represent a rarely observed limiting case of a continuously variable diabatic ("non-adiabatic") process which is strongly affected by the surface heat flux; the convective boundary layer is the rule rather than the exception. Figure 1.3 schematically illustrates the various regions of the planetary boundary layer along with the parameters relevant to their description and the values of the dimensionless quantities z/h and z/L which characterize them. On windy, overcast days for which the surface heat flux is small, |L| is very large, $|h/L| < 1$ and Figure 1.3 shows that the boundary layer is neutrally stable throughout its depth as previously explained. However, Figure 1.3 also shows that a relatively small heat flux can lead to a large, well-developed convectively-mixed boundary layer. For example, with a typical friction velocity of 0.4 m/s, a value of L = −100 is produced by a surface heat flux of just 50 W/m^2. To put this value in perspective, of the 1400 W/m^2 insolation at the top of the atmosphere, approximately 26% or 350 W/m^2 reaches the surface directly when the sun is exactly overhead. Neglecting scattered insolation, even if only 15% of the possible direct insolation reaches the surface in a 1000 m thick boundary layer such that h/L = -10, a well developed mixed layer occupies the upper 90% of the planetary boundary layer. Tennekes (1984, page 59) presents scaling arguments to show that h/L = -3 is sufficient to produce a boundary layer dominated by convection. Therefore, attempts to measure or model the turbulent planetary boundary layer must account for this infinitely variable heating and the convection which results.

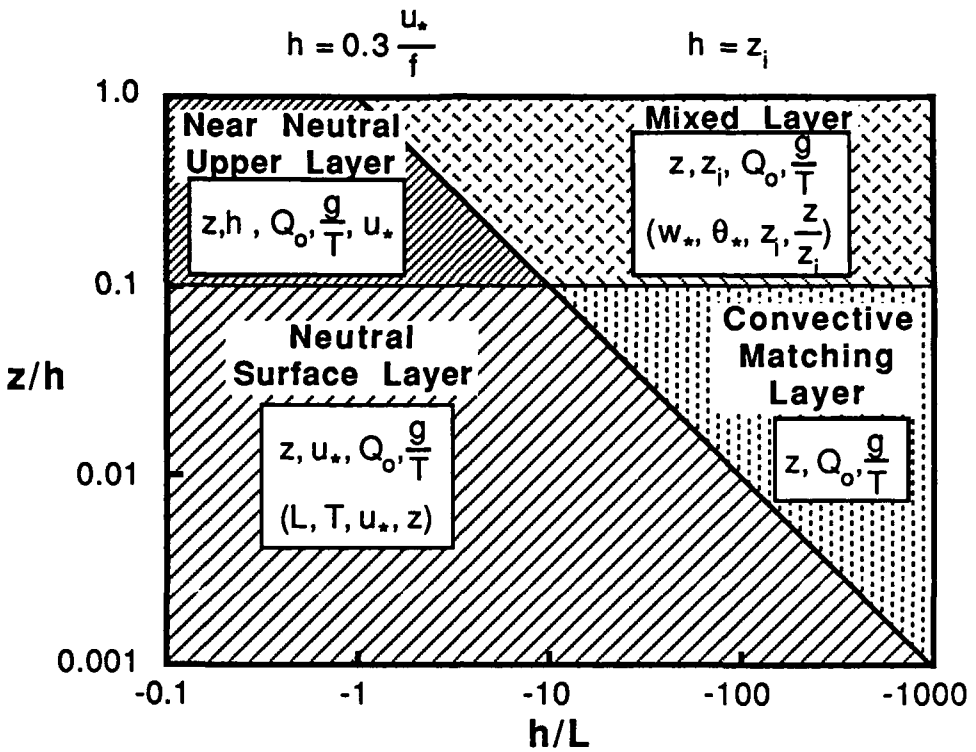

Figure 1.3 Schematic diagram showing the various scaling regions of the planetary boundary layer which exist for different ranges of the dimensionless ratios z/h and h/L. The diagonal line indicates z=-L. Adapted from Oleson, Larson and Højstrup (1984).

1.3 Overview

The objective of the proposed investigation is to model the turbulent dispersion of an aerosol in terms of the mean concentration field with a new, stochastic approach which emphasizes the proper modelling of atmospheric turbulence under arbitrarily convective conditions. Model development and evaluation are primarily based on data gathered as part of a larger project concerned with the environmental effects of military smokes and obscurants used in training exercises.

The following sections describe the present investigation of atmospheric dispersion. In Chapter 2 the current state-of-the-art in atmospheric dispersion modelling is presented and the necessary background for the present approach is developed. In Chapter 3 we present our model which represents a new, stochastic approach to the problem of atmospheric dispersion. Chapter 4 provides a comparison of our model calculations with theory, laboratory experiments, and data from several field studies of dispersion in the actual planetary boundary layer. In Chapter 5 we describe our Atterbury-87 field study of atmospheric dispersion. The methods and

procedures employed to acquire and analyze the data are described first, followed by a discussion of the results. These field data are then compared with the predictions of our stochastic model. A summary of the major findings of our work are subsequently presented in Chapter 6 along with conclusions drawn from our results.

2. REVIEW OF CURRENT MODELLING APPROACHES

The objectives of this review are two-fold: to present an overview of the current state-of-the-art in dispersion modelling with an emphasis on the treatment of atmospheric turbulence, and to demonstrate the relationships between the various modelling approaches. Models describing the turbulent transport and dispersion of material in the planetary boundary layer may be conveniently divided into two broad categories: the Eulerian approach in which the transport and dispersion processes are described relative to a fixed coordinate system and the Lagrangian approach in which the concentration field is determined by following the motion of the fluid elements.

2.1 Eulerian Methods

2.1.1 The Ensemble-Averaged Mass Conservation Equation

We begin the discussion of Eulerian models with the mass conservation equation for a passive scalar contaminant. Here "passive" means that the material does not influence the fluid flow; the material follows the fluid motion exactly. For an incompressible fluid this equation is

$$\frac{\partial c}{\partial t} + \frac{\partial}{\partial x_i} u_i c = \mathcal{D}\frac{\partial^2 c}{\partial x_i^2} + S, \tag{2.1}$$

where c is the instantaneous concentration of material, u_i is the i^{th} component of the fluid velocity, $\mathcal{D}$ is the molecular diffusivity of the material, and S is a function that represents the sources or sinks of material. The extreme complexity of turbulent flow precludes the specification of the instantaneous fluid velocity and renders impossible the analytical solution of Eq. (2.1), although direct computational simulations of the Navier-Stokes equation are now within the realm of possibility for low Reynolds number situations due to recent advances in computer technology. However, the results of these simulations are difficult to interpret in other than statistical terms. The statistical characteristics (e.g., means, variances, etc.) of the turbulence remain the description of practical interest. It is therefore assumed that the fluid motions can be separated into a slowly varying mean flow and a rapidly varying turbulent component. In order to determine mean values, an ensemble average is performed, that is, an average is taken over a large number of realizations. Because ensemble averages

are frequently difficult or impossible to obtain, the flow is usually assumed to be statistically stationary, which means that the ensemble averages are invariant with time and may be replaced by time averages at a point in the fluid. In the present analysis, the ensemble average will be denoted by angle brackets $\langle\ \rangle$, and the time average will be denoted by an overbar $\overline{\ }$. Thus the concentration and velocity may be written as

$$c = \langle c \rangle + c',$$

and

$$u_i = \langle u_i \rangle + u_i'. \tag{2.2}$$

Substituting these back into (2.1) gives

$$\frac{\partial}{\partial t}\left(\langle c \rangle + c'\right) + \left(\langle u_i \rangle + u_i'\right)\frac{\partial}{\partial x_i}\left(\langle c \rangle + c'\right) = \mathcal{D}\frac{\partial^2}{\partial x_i^2}\left(\langle c \rangle + c'\right) + S. \tag{2.3}$$

Taking the ensemble average of this equation leads to

$$\frac{\partial \langle c \rangle}{\partial t} + \frac{\partial}{\partial x_i}\left(\langle u_i \rangle \langle c \rangle + \langle u_i'\, c' \rangle\right) = \mathcal{D}\frac{\partial^2 \langle c \rangle}{\partial x_i^2} + S. \tag{2.4}$$

Some simplification of this equation is possible if the coordinate system is aligned with the direction of the mean wind as shown in Figure 1.1 such that 1) $\langle u_i \rangle = (U,0,0)$; 2) molecular diffusion is negligible compared with turbulent diffusion so that $\mathcal{D} \rightarrow 0$; and 3) turbulent diffusion in the mean wind direction is negligible. With these assumptions, Eq. (2.4) reduces to

$$\frac{\partial C}{\partial t} + U\frac{\partial C}{\partial x} = -\frac{\partial}{\partial y}\langle v'c' \rangle - \frac{\partial}{\partial z}\langle w'c' \rangle + S. \tag{2.5}$$

where $C \equiv \langle c \rangle$ for brevity. This equation cannot be solved for C because of the additional unknown quantities $\langle v'c' \rangle$ and $\langle w'c' \rangle$. In order to proceed, a relationship must be found between these unknown quantities and the mean concentration C. This problem of more unknowns than equations, referred to as the "closure problem", is universal in the study of turbulence and turbulent diffusion. All of the approaches that we will discuss in this review vary essentially in their treatment of closure.

Local Closures

The simplest closure scheme, the gradient transfer approach, assumes that turbulent diffusion behaves in a manner analogous to molecular diffusion: a net movement of material down the gradient of material concentration occurs at a rate which is proportional to the local magnitude of the gradient. To illustrate this process consider an eddy that leaves the level z_0+z where the mean concentration is $C(z_0+z)$ and reaches the level z_0 without a change in its concentration. This causes a fluctuation in the concentration at z_0 of magnitude

$$c'(z_o) = C(z_o+\Delta z) - C(z_o) \tag{2.6}$$

and a corresponding velocity fluctuation w'. Expanding $C(z_0+\Delta z)$ in a Taylor series about z_0, substituting it back into Eq. (2.6), multiplying both sides of the resulting equation by w' and averaging yields

$$\langle w'\, c'\rangle = -\langle w'\, \Delta z\rangle \frac{\partial C}{\partial z} + \langle w'\, \Delta z^2\rangle \frac{\partial^2 C}{\partial z^2} + \cdots \tag{2.7}$$

which leads to the gradient transfer hypothesis

$$\langle w'\, c'\rangle = -K_z \frac{\partial C}{\partial z} \tag{2.8a}$$

and

$$\langle v'\, c'\rangle = -K_y \frac{\partial C}{\partial y}, \tag{2.8b}$$

where K_z and K_y are the eddy diffusivities in the vertical and transverse directions respectively. A comparison of Eqs. (2.7) and (2.8) reveals two important points. First, the eddy diffusivity is equal to the mean of the product of the velocity of an eddy and the distance over which it transports material. Second, in order for the gradient transfer (or "K-theory") approach to be valid, the scale of the spatial variations in C must be much larger than the characteristic mixing length scale Δz of the eddies. In other words, gradient diffusion theory considers that only the *local* properties of the turbulence contribute to the turbulent diffusion. If this condition is not met then the additional terms in Eq. (2.7) involving the second and higher order derivatives of C cannot be neglected. Substituting the gradient transport relations Eq. (2.8) into Eq. (2.5) yields

$$\frac{\partial C}{\partial t} + U\frac{\partial C}{\partial x} = -\frac{\partial}{\partial y}\left(K_y \frac{\partial C}{\partial y}\right) - \frac{\partial}{\partial z}\left(K_z \frac{\partial C}{\partial z}\right) + S \tag{2.9}$$

which is referred to as the advection-diffusion equation. It is the basic equation of the gradient transfer approach.

It should be apparent from the above discussion that eddy diffusivity is a property of the flow. As such it cannot be specified *a priori* without some knowledge of the features of the flow. Usually, a sufficiently detailed description of the flow is unavailable prior to performing the calculations. As a result, three methods of specifying K have arisen: 1) choose constant K values; 2) prescribe functional forms for K which depend on position and time; or 3) develop differential equations for K.

Employing a constant value of K assumes that the turbulence is stationary and homogeneous; that is, the eddies in a given direction are assumed to have the same characteristic size for all time. With this assumption the advection-diffusion equation is analogous to the equation of Fickian (Brownian) diffusion or heat conduction. Roberts (1923) solved the steady-state ($\partial C/\partial t=0$) advection-diffusion equation assuming K to be uniform in space and time for the instantaneous and continuous ground level point source and the continuous ground–level infinite line source configurations. It is not surprising that Roberts' solutions failed to adequately describe turbulent diffusion from ground level since the assumption of constant K does not account for correlated velocity fluctuations. In addition, the presence of a boundary causes the turbulence to be inhomogeneous in the direction perpendicular to the boundary; the characteristic size of the eddies increases with distance from the boundary.

Specifying K as a function of height allows inhomogeneous flows, such as those arising from the presence of a boundary, to be more nearly accommodated. An early analytical solution of the advection-diffusion equation was given by Roberts (unpublished, see Sutton, 1953). Roberts solved the 2-dimensional advection-diffusion equation for the continuous infinite line source using power law forms of the wind and eddy diffusivity profiles which approximate the logarithmic form

$$K_z(z) = K_1\left(\frac{z}{z_1}\right)^n, \quad U(z) = U_1\left(\frac{z}{z_1}\right)^m \tag{2.10}$$

where K_1 and U_1 are the values of K_z and U at a fixed reference height z_1. With the boundary conditions

$$C \to 0 \text{ as } x, z \to \infty, \tag{2.11a}$$

$$C \to \infty \text{ at } x = z = 0 \tag{2.11b}$$

and $$K_z \frac{\partial C}{\partial z} \to 0 \text{ as } z \to 0, x > 0, \tag{2.11c}$$

the solution is given by

$$C(x,z) = \frac{Q\ r}{U_1\ \Gamma(s)} \left(\frac{U_1}{r^2\ K_1\ x}\right)^s \exp\left(\frac{U_1\ z^r}{r^2\ K_1\ x}\right) \tag{2.12}$$

where Q is the rate of emission per unit crosswind length, r=m-n+2, s=(m+1)/r and Γ is the Gamma function. For n=m=0 Eq. (2.12) reduces to the Fickian form

$$C(x,z) = \frac{Q}{\sqrt{2\pi}\ \sigma} \exp\left(-\frac{1}{2}\frac{z^2}{\sigma^2}\right) \tag{2.13}$$

where $\sigma = (2Kx/U_1)^{1/2}$, which has a Gaussian, or normal, distribution.

Since Roberts' time, many investigators have attempted to define the eddy diffusivity in such a way that the solution of the advection-diffusion equation matches some macroscopic feature of the concentration field, most notably the decay of the maximum mean concentration with distance from the release point. Pasquill (1974) presents a detailed review of some of these. Owing to the scale dependent nature of the turbulent mixing process, the diffusivity not only depends on spatial position but also on the size of the dispersing cloud. This scale dependence is most often handled by making K a function of travel time since release or, alternatively, downwind distance (x = Ut). Taylor (1959) has pointed out the theoretical shortcomings of such an approach.

Numerical solution of the advection-diffusion equation is necessary except when K assumes one of several special forms. A vast amount of literature has thus evolved dealing with the numerical solution of the advection-diffusion equation for a variety of postulated diffusivity forms. Questions concerning numerical algorithms, boundary conditions, and computational stability have dominated the discussion, however. The result, as Hanna (1984) points out, is that much of the literature on numerical solutions deals with numerical methods and input/output routines rather than the physics of turbulent dispersion.

The gradient transfer closure produces acceptable results only in situations where its underlying assumptions are valid: when the spatial scale of the diffusing material is much larger than the scale of the turbulence. For example, since the horizontal scales of atmospheric turbulence are quite large, the gradient transfer

approach is unsuitable for predicting horizontal dispersion from point sources except at distances which are much greater than the integral scale of the turbulence. It is also inappropriate for calculating vertical dispersion from ground level sources during convective conditions which are dominated by large-scale buoyant motions. In stable conditions however, the effect of the thermal stratification is to make the flow more nearly homogeneous by reducing the effect of the boundary. In such situations, gradient transport models have been somewhat successful (van Ulden, 1978; Gryning et al., 1983). However, any particular choice for K is limited to a narrow range of applicability. The gradient transfer approach is inappropriate for calculating vertical dispersion from elevated sources under any conditions since the scale of the turbulence, which is proportional to the distance from the boundary, is much larger than the spatial scale of the dispersing material at least until the material reaches the ground.

Non-local Closures

In the convective boundary layer, solar heating of the ground results in much non-local turbulent activity. Large, coherent parcels of warm air (referred to as thermal plumes or "thermals") rise quickly to the height of the capping inversion (1-2 km) transferring momentum, heat and mass as they rise. This process is referred to as "bottom-up diffusion". Upon reaching the inversion layer these thermals give way to larger, slower downdrafts of cool air (referred to as "subsidence") necessitated by conservation of mass. Depending on the strength and thickness of the inversion layer, warmer air from above the inversion may be entrained by the subsidence in a process referred to as "top-down diffusion." These large-scale motions represent extremely non-local turbulence effects which are virtually impossible to accurately model with local closures such as gradient transfer. As the physics underlying these processes have been more and more clearly delineated by experiments, non-local models of turbulent dispersion have been developed to incorporate them.

One recent method of extending gradient transfer theory to include non-local effects is the spectral diffusivity approach proposed by Berkowicz and Prahm (1979a). The one-dimensional advection-diffusion equation for vertical dispersion, with $K_z = K$, is Fourier transformed into

$$\frac{\partial \tilde{C}(k,t)}{\partial t} = - k^2 K \tilde{C}(k,t). \qquad (2.14)$$

The tilde indicates the transformed concentration and $\kappa = 2\pi/\lambda$ is the wavenumber. In order to account for the varying size of the eddies responsible for the diffusion, the spectral turbulent diffusivity coefficient $K(\kappa)$ is substituted for K in (2.14). Converting this equation back to real space results in the integro-differential equation

$$\frac{\partial C(z,t)}{\partial t} = \frac{\partial}{\partial z} \int_{-\infty}^{\infty} D(z,z') \frac{\partial C(z',t)}{\partial z'} \, dz' \tag{2.15}$$

where the turbulent diffusivity transfer function is given by

$$D(z,z') = \frac{1}{2\pi} \int_{-\infty}^{\infty} K(\kappa) \exp\left(i\kappa(z-z')\right) \, d\kappa \tag{2.16}$$

Thus the closure problem becomes one of specifying the spectral turbulent diffusivity function $K(\kappa)$. Note that $K(\kappa) = K \Rightarrow D(z,z') = K\,\delta(z-z')$ and Eq. (2.15) reduces to the one-dimensional advection-diffusion equation. For the non-homogeneous case, the turbulent diffusivity transfer function becomes a function of vertical position also. Berkowicz and Prahm subsequently attempted to incorporate this spectral diffusivity model into a model of homogeneous turbulent plume dispersion (1979b) and to establish $K(\kappa)$ for homogeneous turbulence (1980). Unfortunately, transforming the closure problem into wavenumber space offers no apparent advantages in determining K from theory or data.

Fiedler (1984) began with Eq. (2.15) and, in an analogy to models of radiative transfer in the atmosphere, proposed the expression

$$\frac{\partial C(z,t)}{\partial t} = \int R(z,z') \left(C(z',t) - C(z,t)\right) dz', \tag{2.17}$$

where

$$R(z,z') = \frac{\partial^2 D(z,z')}{\partial z \, \partial z'} \tag{2.18}$$

and R(z,z') is proportional to the rate at which layers at z and z' exchange turbulent energy. Here the closure problem is to specify the turbulent exchange rate R(z,z'). Owing to a lack of high quality atmospheric data from which to determine the

exchange function, Fiedler can only suggest qualitative forms for R(z,z') which reproduce certain gross behavior of the convective boundary layer.

An alternative to these methods is to develop differential equations which describe the evolution of the turbulent fluxes $\langle u_i'c' \rangle$. Multiplying Eq. (2.3) by u_j and averaging the result gives

$$\frac{\partial \langle u_i'c' \rangle}{\partial t} = -\frac{\partial}{\partial x_j}\left(U_j \langle u_i'c' \rangle + C\langle u_i'u_j' \rangle + \langle u_i'u_j'c' \rangle \right), \tag{2.19}$$

where molecular diffusivity has again been neglected. Assuming as before that a sufficiently detailed description of the fluid flow is available such that the product $\langle u_i'u_j' \rangle$ is known, the coupled Eqs. (2.4) and (2.19) still cannot be closed because of the unknown quantity $\langle u_i'u_j'c' \rangle$. This quantity is usually modeled in a manner analogous to the gradient transfer closure for $\langle u_i'c' \rangle$. For example, Lewellen (1977) uses

$$\langle w'\, w'\, c' \rangle = -K\frac{\partial \langle w'c' \rangle}{\partial z} \tag{2.20}$$

where K is the diffusivity which must be empirically determined for a given configuration (e.g., convective boundary layer). More detailed reviews of closure methods are given by Reynolds and Cebeci (1978) for turbulence modeling and by Launder (1978) for turbulent diffusion modeling.

2.1.2 The Volume-Averaged Mass Conservation Equation

Large Eddy Simulation

The second Eulerian approach is fundamentally different from that just described in that it deals with volume averages rather than ensemble or time averages. In this method, known as large eddy simulation, each flow variable is decomposed into resolvable and subgrid scale components. Because the large eddies extract their energy directly from the mean flow, they are most sensitive to the flow geometry and thermal stratification. With this method these large eddies, which are principally responsible for the momentum, heat and mass transfer, are treated explicitly. On the other hand, the averaging volume is chosen small enough that the eddies contained entirely within it (i.e., the unresolved eddies) are in the inertial subrange and smaller. These inertial subrange, subgrid scale eddies are rendered nearly isotropic by the vortex-stretching "energy-cascade" process and are affected very little by environmental details. As a result, they may be modeled in a very simple manner without significantly affecting the solution. This is an important advantage over the

closure methods of the ensemble averaged models which must treat the entire spectrum of eddy scales including the largest scales. Such a broad treatment can substantially affect the solution.

In the large eddy simulation approach, each flow variable is decomposed into resolvable and subgrid scale components. Thus the flow variable $f(x_i,t)$ would be written

$$f(x_i,t) = \{ f(x_i,t) \} + f'(x_i,t) \tag{2.21}$$

where the braces denote the result of volume averaging by the use of a spatial filter or weighting function. This filtering operation removes the subgrid scale fluctuations (small eddies) from the flow field. It is defined by Leonard (1974) as

$$\{ f(x_i,t) \} = \int G(x_i - s)\, f(s,t)\, ds \tag{2.22}$$

where G is the filter function; the integral is over the entire flow domain. The simplest form for the filter function is the "top hat" function: $G = 1/\Delta^3$ within a grid volume Δ^3 and zero outside. This form was employed by Deardorff (1973). Large eddy simulation models developed by researchers at Stanford, which use pseudospectral methods rather than finite differences to evaluate derivatives (Mansour et al., 1977), prefer to use the Gaussian function

$$G(x_i - s) = \left(\sqrt{\frac{6}{\pi}}\,\frac{1}{\Delta_a}\right)^3 \exp\left[-\frac{6(x_i - s)^2}{\Delta_a^2}\right], \tag{2.23}$$

where Δ_a is the averaging scale, since the Fourier transform of a Gaussian function is another Gaussian function. Another possibility is to use an ideal low pass filter – a step function applied in wave space – which corresponds to a truncated Fourier expansion.

When this filter is applied to the mass conservation Eq. (2.1) and molecular diffusion is neglected the result is given by

$$\frac{\partial\{C\}}{\partial t} + \frac{\partial}{\partial x_i}\left\{\{U_i\}\{C\}\right\} = -\frac{\partial}{\partial x_i} R_i \tag{2.24}$$

where $R_i=\{u_i'\{C\}\}+\{\{U_i\}c'\}+\{u_i'c'\}$ represents the subgrid scale interaction terms. Here the closure problem lies in the specification of the subgrid scale terms.

At first, modelling the subgrid scale terms appears somewhat difficult since they have received comparatively meager theoretical and experimental attention. However, it turns out that even very simple subgrid models may be adequate. Recalling that the effects of the small, subgrid motions on the large, resolved scales is being modeled, it is clear that in the limit $\Delta/L_E \rightarrow \infty$, where L_E is the Eulerian integral length scale of the resolved scales, gradient transport theory should be effective. Even in convective flows, which are problematic for ensemble-averaged gradient transport closures due to the large-scale buoyant motions present, the gradient transport subgrid scale closure would still work since shear effects still dominate as $\Delta/L_E \rightarrow \infty$. Moreover, because of the tendency of such small scales toward isotropy, it seems reasonable that their models may exhibit some universal properties independent of the large-scale motions.

Deardorff (1970, 1972) pioneered the use of large eddy simulation to study the convective atmospheric boundary layer. As previously discussed, the convective boundary layer is dominated by the large-scale motion of thermals, which makes it an ideal candidate for large eddy simulation. Deardorff found that in convective boundary layers where the ratio of the boundary layer height to the Monin-Obukhov length $h/-L > 10$, the statistical properties of the turbulence above $z \approx 0.1h$ assumed universal forms when scaled by h and w_*, a convective velocity scale proposed by Deardorff, rather than the surface layer scales u_* and L. Further numerical studies (Deardorff, 1973, 1974) and laboratory experiments (Willis and Deardorff, 1974; Deardorff and Willis, 1975) confirmed this result and also showed that beginning at a travel time of about $0.5h/w_*$ the centerline of a ground-level plume begins to rise rapidly until by a travel time on the order of h/w_* it has reached an elevation of 0.75h.

More recently, Moeng (1984) constructed a state-of-the-art large eddy model for studying the planetary boundary layer. It incorporates the pseudospectral method of evaluating derivatives in the assumed homogeneous horizontal directions and centered finite differences in the vertical and uses a simple gradient transport closure for the subgrid scale turbulent fluxes. It has been utilized to study "top-down" and "bottom-up" diffusion in the convective boundary layer by Moeng and Wyngaard (1984) and to generally examine the convective and near-neutral planetary boundary layer by Cederwall, Ohmstede and Meyers (1985).

Although large eddy models are acknowledged to be one of the best available methods for calculating the three-dimensional, time-dependent structure of high Reynolds number flows, they are very expensive to run. Moeng (1984) reported that with a 32 x 32 x 40 mesh and a time step of 3 s, one hour of simulation time required

one hour of computer time on the NCAR CRAY-1. As a result, most large eddy simulation runs are performed to acquire "data" for studying atmospheric physics: the detailed computations are analogous to placing tens of thousands of probes in the atmosphere (one at each point of the grid for primitive quantities such as velocity or temperature as well as for more sophisticated quantities such as turbulent fluxes.) These "data" can then be utilized to improve existing models and to develop more successful closures. Fiedler and Moeng (1985) use data from Wyngaard and Moeng (1984) to model top-down and bottom-up diffusion with Fiedler's (1984) non-local closure method.

Another problem with large eddy models of the planetary boundary layer is that near the surface a much greater proportion of the energy is subgrid due to the presence of the boundary. Meyers et al. (1985) noted that Moeng (1984) overly suppressed the subgrid energy at the lowest level by specifying too great a value for the "dissipation coefficient". By numerical experimentation, they found that a much lower value was more appropriate. In his review of subgrid scale turbulence modeling, Herring (1977) mentions more sophisticated approaches such as Deardorff's (1973) second order scheme and the relation of subgrid eddy viscosity to the magnitude of vorticity by Mansour et al. (1977). Deardorff's work was motivated by the overdamping problem pointed out by Meyers et al. Mansour et al. report only a slight improvement for isotropic turbulence. Love and Leslie (1977) show that the simple gradient transfer closure works well if the gradient is averaged over several grid volumes to include more non-local effects. Clearly, subgrid modelling is an area of major concern and controversy in large eddy simulation.

2.2 Lagrangian Methods

2.2.1 Statistical Considerations

Due to the complexity of the Lagrangian form of the governing equations, Taylor's (1921) statistical description of particle motion forms the basis of all Lagrangian models. It is therefore appropriate to begin this discussion with a review of the statistical description of dispersion.

Consider a marked "fluid particle" moving in a field of stationary and homogeneous turbulence. Let $\mathbf{r}_0 = (x_0,y_0,z_0)$ be the initial position of this fluid particle at time t_0, and let $\mathbf{r} = (x,y,z)$ be the position at some later time t. The probability that a particle will move from $\mathbf{r}_0$ at t_0 to $\mathbf{r}$ at time t is given by $P(\mathbf{r}, t \mid \mathbf{r}_0, t_0)$; this is known as the

transition probability. The probability of finding a particle at **r** at time t, denoted as p(**r**, t), is thus determined by integrating the product of the probability of the initial location and the transition probability over all possible initial locations:

$$p(\mathbf{r}, t) = \int_{-\infty}^{\infty} p(\mathbf{r}_0, t_0)\, P(\mathbf{r}, t \mid \mathbf{r}_0, t_0)\, d\mathbf{r}_0. \tag{2.25}$$

(In stationary, homogeneous turbulence, $P(\mathbf{r}, t \mid \mathbf{r}_0, t_0) = P(\mathbf{r} - \mathbf{r}_0, \xi)$ where $\xi = t - t_0$.) Equation (2.25) is equal to the mean concentration of marked fluid particles at time t normalized by the release rate Q. Thus the ensemble average concentration of marked fluid may be expressed as

$$C(\mathbf{r}, t) = Q\, p(\mathbf{r}, t). \tag{2.26}$$

The condition that marked fluid be conserved requires that the integration of (2.25) over all space equal unity, i.e.:

$$\int_{-\infty}^{\infty} p(\mathbf{r}, t)\, d\mathbf{r} = \int_{-\infty}^{\infty} p(\mathbf{r}_0, t_0)\, d\mathbf{r}_0 = 1. \tag{2.27}$$

From the above discussion it is apparent that a knowledge of the transition probability density function implies knowledge of the mean concentration distribution. To completely determine the transition probability requires a knowledge of all of its moments; this is a difficult task. For purposes of describing the turbulent transport and dispersion of a "cloud" of marked fluid particles, a knowledge of the movement of the center of mass of the cloud and the evolution of the size of the cloud are often sufficient. These are given, respectively, by the first and second moments of the particle displacement ($Z(\xi) \equiv z(\xi) - z_0$):

$$\mu_Z = \int_{-\infty}^{\infty} Z(\xi)\, P_z(Z(\xi))\, dZ \tag{2.28}$$

and

$$\sigma_z^2(\xi) = \int_{-\infty}^{\infty} Z^2(\xi)\, P_z(Z(\xi))\, dZ\ , \tag{2.29}$$

where $P_z(Z(\xi)) = \int\int P(\mathbf{r} - \mathbf{r}_0, \xi)\, dX\, dY$ is the marginal density for Z. The marginal densities are assumed independent: $P(\mathbf{r} - \mathbf{r}_0, \xi) = P_x(X(\xi)) \cdot P_Y(Y(\xi)) P_Z \cdot (Z(\xi))$. Similar equations may be written for the x- and y-directions. Taylor (1921) showed that for marked fluid particles in stationary homogeneous turbulence, the variance is given by

$$\sigma_z^2(t) = 2\,\overline{w'^2} \int_0^t \left[\int_0^\eta R_{L,w}(\xi)\, d\xi \right] d\eta, \tag{2.30}$$

where $R_{L,w}$ is the Lagrangian correlation coefficient of the vertical velocity fluctuations defined by

$$R_{L,w}(\xi) = \frac{\overline{w'(t)\, w'(t+\xi)}}{\overline{w'^2}} \tag{2.31}$$

Note that, by the ergodic hypothesis, time averages have been substituted for ensemble averages. Also note that expressions for the variances σ_x^2 and σ_y^2 may be obtained by substituting the appropriate fluctuating quantity and its Lagrangian correlation coefficient. Thus for stationary homogeneous turbulence the Lagrangian correlation coefficient is a function of the time interval ξ only. Taylor also showed that for ξ very small, $R_{L,w}(\xi) \approx 1$ and so

$$\sigma_z^2(t) \approx \overline{w'^2}\, t^2, \quad (t \to 0) \tag{2.32}$$

and that as ξ became very large, $R_{L,w}(\xi) \approx 0$, and its integral converges to

$$\lim_{\eta \to \infty} \int_0^\eta R_{L,w}(\xi)\, d\xi = T_L, \tag{2.33}$$

where T_L is the Lagrangian integral time, and thus the variance is given by

$$\sigma_z^2(t) = 2\,\overline{w'^2}\, T_L\, t, \quad (t \to \infty) \tag{2.34}$$

which is just the gradient transfer result $\sigma_z^2(t) = 2\,K\,t$ with $K = \sigma_w^2 T_L$. This supports the earlier statement that the advection-diffusion equation is valid in the limit $t/T_L \to \infty$.

2.2.2 The Gaussian Assumption

In order to utilize Taylor's result, Sutton (1932, 1934, 1947a) proposed a form for the Lagrangian correlation function for the turbulent motion in a diabatic ("non-

adiabatic") boundary layer. He argued that the correlation must depend on $\langle w'^2 \rangle$, on the molecular viscosity ν and on the separation time ξ. In order to satisfy the conditions that $R_{L,w}(0) = 1$ and $R_{L,w}(\infty) = 0$, Sutton suggested

$$R_{L,w}(\xi) = \left(\frac{\nu}{\langle w'^2 \rangle \xi + \nu} \right)^n \qquad 0 \le n \le 1 \tag{2.35}$$

where n was empirically determined to vary according to the potential temperature gradient in the atmosphere:

Conditions	n
Stable ($\partial T/\partial z > 0$)	0.20
Neutral ($\partial T/\partial z = 0$)	0.25
Moderately Unstable ($\partial T/\partial z < 0$)	0.33
Strongly Unstable ($\partial T/\partial z << 0$)	0.50

Substituting Eq. (2.35) into Eq. (2.30) and carrying out the integration for $\nu \ll \langle w'^2 \rangle \xi$, Sutton obtained

$$\sigma_z^2(t) = \frac{1}{2} D_w^2 (Ut)^{2-n}, \tag{2.36}$$

where D_w^2 is a "virtual diffusion coefficient" given by

$$D_w^2 = \frac{4\nu^n}{(1-n)(2-n)U^2} \left(\frac{\langle w'^2 \rangle}{U^2} \right)^{1-n}. \tag{2.37}$$

Sutton obtained similar forms for D_u^2 and D_v^2.

Based on experimental evidence and Roberts' solution of the advection-diffusion equation, Sutton postulated that the transition probability, and hence the mean concentration distribution, was Gaussian in form. This proved to be a very convenient choice because the Gaussian distribution is completely specified by its first two moments; mean concentration distributions could thus be obtained from only a few parameters. Theoretical justification of the Gaussian assumption is usually made by an appeal to the Central Limit Theorem. This theorem states that the probability density function of the sum of a sequence of independent random variables tends toward a Gaussian as their number tends to infinity. In other words, even if the

instantaneous concentration distribution is not Gaussian, an average concentration computed over a long period of time in comparison to the Lagrangian integral time T_L will have a Gaussian concentration distribution.

Steady Mean Wind

Sutton (1947b) gives the form for the case of an elevated plume (continuous point source) in a uniform mean wind without settling or deposition:

$$C(x,y,z) = \frac{Q}{2\pi U \sigma_y \sigma_z} \exp\left(-\frac{y^2}{2\sigma_y^2}\right)\left[\exp\left(-\frac{(z-h)^2}{2\sigma_z^2}\right) + \exp\left(-\frac{(z+h)^2}{2\sigma_z^2}\right)\right], \quad (2.38)$$

where dispersion in the streamwise direction has been assumed negligible. The second term in brackets refers to an image source located at z=–h to account for reflection of the plume at z=0. Sutton's work has been extended to include reflective or absorptive boundaries, settling and deposition, and various source configurations both at ground level and elevated above ground level.

Thus the only parameters required are the standard deviations of the dispersion $\sigma_y(x)$ and $\sigma_z(x)$. However, these so-called Gaussian plume parameters embody the description of the turbulence and thus constitute the treatment of the closure problem. They are usually considered to be empirical functions of travel time or downwind distance and are either computed from measurements of the turbulence or estimated by an empirical technique. An example of the former method is given by (Doran et al., 1978)

$$\sigma_y = \sigma_\theta \times S_y\left(\frac{x}{UT_{Lv}}\right) \quad \text{and} \quad \sigma_z = \sigma_\phi \times S_z\left(\frac{x}{UT_{Lw}}\right) \quad (2.39)$$

where σ_θ and σ_ϕ are the standard deviations of horizontal and vertical wind angle, respectively and S_y and S_z are dimensionless functions. An example of the latter method is the Pasquill - Gifford - Turner curves which graphically relate σ_y and σ_z to downwind distance. The graphs contains six curves, one for each of the six categories of atmospheric stability ranging from A (extremely unstable) to D (neutral) to F(stable). Several such stability classification schemes and many formulas for σ_y and σ_z have been developed and equally many reviews of them written. An updated set of formulas credited to Briggs are presented in equation form by Hanna (1984). A detailed review of the subject is provided by Irwin (1983).

Unsteady Mean Wind

For low wind speed situations where the neglect of streamwise dispersion is incorrect and where the wind direction may vary considerably with time, or for situations where there are multiple sources, the plume can be modelled as a series of non-interacting differential elements or "puffs" (instantaneous point sources emitted at time intervals dt_0). The instantaneous point source solution of the advection-diffusion equation is given by Rote (1980, page 214)

$$P(\mathbf{r}, t \mid \mathbf{r}_0, t_0) = \frac{1}{(2\pi)^{3/2}\,\sigma_x\sigma_y\sigma_z} \exp\left[-\frac{1}{2}\left(\frac{x-x_0-U(t-t_0)}{\sigma_x}\right)^2 - \frac{1}{2}\left(\frac{y-y_0-V(t-t_0)}{\sigma_y}\right)^2\right]$$

$$\times\left\{\exp\left[-\frac{1}{2}\left(\frac{z-z_0}{\sigma_z}\right)^2\right] + \exp\left[-\frac{1}{2}\left(\frac{z+z_0}{\sigma_z}\right)^2\right]\right\}, \qquad (2.40)$$

where $\mathbf{r}_0 = (x_0,y_0,z_0)$ is the initial location of the puff emitted at t_0 and $\mathbf{r} = (x,y,z)$ is the location at which the concentration is to be estimated. Note that the dispersion coefficients σ_x, σ_y and σ_z are all functions of the travel time $t-t_0$. For an instantaneous point source

$$p(\mathbf{r}, t) = \delta(\mathbf{r} - \mathbf{r}_0)\,\delta(t - t_0). \qquad (2.41)$$

With Eq. (2.41) the contribution to the mean concentration at $\mathbf{r}$ at time t due to a puff of strength Qdt_0 released from $\mathbf{r}_0$ at time t_0 can be expressed as

$$C(\mathbf{r}, t \mid \mathbf{r}_0, t_0) = Q\,dt_0\,\delta(\mathbf{r}' - \mathbf{r}_0)\,\delta(t' - t_0)\,P(\mathbf{r}, t \mid \mathbf{r}', t') \qquad (2.42)$$

where δ is the Dirac delta function and the primes indicate a variable of integration. The superposition of the mean concentration due to a series of non-interacting puffs can be expressed as

$$C(\mathbf{r}, t) = \int_{-\infty}^{\infty}\int_{t_1}^{t} C(\mathbf{r}, t \mid \mathbf{r}_0, t_0)\,dt_0\,d\mathbf{r}_0$$

$$= \int_{-\infty}^{\infty}\delta(\mathbf{r}'-\mathbf{r}_0)\left[\int_{t_1}^{t} Q\,\delta(t'-t_0)\,P(\mathbf{r}, t \mid \mathbf{r}', t')\,dt_0\right]d\mathbf{r}_0$$

$$= \int_{t_1}^{t} Q\, P(\mathbf{r}, t \mid \mathbf{r}_0, t_0)\, dt_0, \qquad (2.43)$$

where t_1 is the time at which the source at $\mathbf{r}_0$ began to emit material. Lamb (1980, page 202) shows that for a single continuous steady point source in a uniform and steady mean wind, Eq. (2.43) reduces to Eq. (2.38) in the limit $t \to \infty$ (i.e., steady state conditions).

2.2.3 Similarity and Scaling

Near a boundary surface, where the velocity shear of the mean flow is strong, turbulence is no longer vertically homogeneous so that the statistical theory of dispersion presented above is no longer applicable. The Lagrangian similarity theory of dispersion overcomes this restriction of vertical homogeneity to describe the dispersion from a source near the surface in a boundary layer.

The Surface Layer

In an analysis of the rate of dispersion from a smoke plume in the surface layer, Monin (1959) proposed a Lagrangian similarity theory relating the movement of the plume to the vertical flux of momentum and sensible heat for adiabatic (neutral) conditions. The theory has since been extended to diabatic conditions.

According to Lagrangian similarity theory, the behavior of horizontally homogeneous turbulence is fully described by the same two parameters as earlier proposed for Eulerian similarity (Monin and Obukhov, 1954). These parameters are the friction velocity, $u_* = -\overline{u'w'}^{1/2} = (\tau/\rho)^{1/2}$ which characterizes the vertical momentum flux and the Monin-Obukhov length

$$L = -\frac{u_*^3}{\kappa \frac{g}{T} \frac{q}{c_p \rho}} \qquad (2.44)$$

which expresses the balance between the vertical fluxes of momentum and sensible heat; the latter is related to the turbulence by $\overline{w'T'} = q/c_p\rho$. τ is the turbulent shear stress due to friction, ρ and c_p are, respectively, the density and specific heat of the air, κ is von Karman's constant, g is the acceleration of gravity, T is the average surface layer temperature and q is the vertical heat flux. Thus for stable conditions, $q < 0 \rightarrow L > 0$; for unstable conditions, $q > 0 \rightarrow L < 0$. L becomes infinite for neutral conditions (q

= 0). The rate of increase of the ensemble averaged particle elevation depends on the friction velocity, heat flux and mean particle elevation

$$\frac{\partial\langle Z(t)\rangle}{\partial t} = A\, u_* \psi\left(\frac{\langle Z\rangle}{L}\right) \tag{2.45}$$

Here $\langle Z(t)\rangle$ is the mean vertical displacement after a travel time t, A is a universal constant and ψ is a universal function; for neutral conditions, ψ=1. Additionally, the rate of increase of the mean horizontal displacement $\langle X(t)\rangle$ after a travel time t is given by the mean wind speed at a level related to $\langle Z\rangle$

$$\frac{\partial\langle X(t)\rangle}{\partial t} = B\, U\langle Z\rangle \tag{2.46}$$

where U is the mean wind speed and B is another universal constant. These two expressions, for which A is usually taken equal to von Karman's constant κ and B is usually taken equal to unity, form the basis of the Lagrangian similarity theory. In order to solve these equations for the dispersion from a ground-level source, forms for the mean wind profile and for the function ψ are required. However, even without these, a functional form of the probability density and hence the concentration distribution downwind of a point source may be obtained as follows.

The position of any particle at time t after release will have coordinates (X(t), Y(t), Z(t)). These are random functions having means $\langle X(t)\rangle$, 0, and $\langle Z(t)\rangle$ respectively. The theory predicts that the statistical departures of X, Y, and Z from their mean values depends only on u_* and t or on $\langle Z\rangle$. Thus the probability p(x,y,z,t) of finding a particle at (x,y,z) after a travel time t should have a universal shape when scaled by u_*t or $\langle Z\rangle$

$$p(x, y, z, t) = \frac{1}{\langle Z\rangle^3}\, g_1\left(\frac{x-\langle X\rangle}{\langle Z\rangle}, \frac{y}{\langle Z\rangle}, \frac{z-\langle Z\rangle}{\langle Z\rangle}\right) \tag{2.47}$$

where g_1 is a universal function. For a continuous source, the average relative concentration at a point C(x,y,z) is equivalent to finding a particle at (x,y,z) at any time. This will have contributions from all travel times and thus is proportional to the integral of Eq. (2.45). Using Eq. (2.45) to change the variable of integration to $\langle Z\rangle$ gives

$$C(x, y, z, t) = \frac{Q}{Au_*} \int_0^\infty g_2\left(\frac{x-\langle X\rangle}{\langle Z\rangle}, \frac{y}{\langle Z\rangle}, \frac{z-\langle Z\rangle}{\langle Z\rangle}\right) \frac{d\langle Z\rangle}{\langle Z\rangle^3 \psi(\langle Z\rangle/L)} , \tag{2.48}$$

where g_2 is another universal function.

In order to obtain estimates of the crosswind integrated surface concentrations $C^y(\langle X\rangle,0)$, forms for U(z), ψ, g_1 and g_2 must first be obtained from experimental data. These forms are given or may be derived from the flux-profile relations determined by Businger (1971), Dyer and Hicks (1970) or Hansen (1980).

Alternatively, Horst (1979) used expressions for the vertical distribution of C^y in the surface layer determined from continuous ground level releases:

$$\frac{C^y(\langle X\rangle,z)}{C^y(\langle X\rangle,0)} = \exp\left(-\left(\frac{z}{b\langle Z\rangle}\right)^s\right), \tag{2.49}$$

where $b = \Gamma(1/s)\Gamma(2/s)$, Γ is the Gamma function and s varies with stability, together with the mass conservation equation

$$\int_0^\infty U(z)\, C^y(\langle X\rangle,z)\, dz = Q \tag{2.50}$$

which he solved numerically to yield predictions of $C^y(\langle X\rangle,0)$. These predictions were shown to agree with data from the Project Prairie Grass (Barad, 1956) dispersion experiments. The value of s was found to vary with stability: for stable conditions the Gaussian value s=2 was obtained; for neutral conditions s=1.5; and for unstable conditions s<1.5. These findings reflect our earlier remark that stable conditions tend to make the turbulence more homogeneous whereas unstable conditions increase the inhomogeneous character of the turbulence.

The Mixed Layer

The parameters u_* and L are only valid in the surface layer, z<L. For unstable conditions, L/h « 1, a mixed layer occurs for z > 0.1h where Deardorff (1970) has shown that convective scaling is appropriate. In the mixed layer, similarity depends on the convective velocity scale $w_* = [h(g/T)(q/\rho c_p)]^{1/3}$ and h, where h is the height of the boundary layer. Nieuwstadt (1980) employed mixed layer similarity to show that the similarity law

$$\frac{C^y(\langle X\rangle,0)\ Uh}{Q} = a\left(\frac{w_* x}{Uh}\right)^{3/2} \tag{2.51}$$

with a=0.9 fits the most unstable Prairie Grass data well.

The main limitation of the similarity approach is the necessity for experimental data to empirically determine the forms of the universal functions. However, this has provided a fruitful area for research and many forms of these functions are available in the open literature (Panofsky and Dutton, 1984; Wyngaard, 1984). Most current models incorporate similarity scaling in their non-dimensionalization. For example, if g_2 were assumed to have a Gaussian form, then Eq. (2.48) would lead to a Gaussian plume model which obeys surface layer similarity. As a result, one model can accommodate a broader range of atmospheric conditions than might otherwise be possible.

Current work includes the development of similarity variables for dispersion from buoyant plumes (Willis and Deardorff, 1983; Deardorff, 1985) and for stable atmospheric conditions (Hunt, 1984a; Hunt et al., 1985).

2.2.4 The Hyperbolic Diffusion Equation

Monin and Yaglom (1971, page 676), drawing on earlier work of Monin, indicate that the parabolic nature of the advection-diffusion equation requires that marked fluid introduced into a flow at a given time spreads instantly throughout the entire space. As a result small amounts are immediately present at arbitrarily large distances from the source. This implies that the instantaneous velocities of the fluid particles are infinite; clearly, this is impossible. Following Chandrasekhar (1943; see Wax, 1954), they consider the displacement and velocity to be <u>jointly</u> Markovian. Thus, the probability p(z,t) of finding a particle at location z at time t is given by

$$p(z,t) = \sum_i p_i(z,w_i,t), \tag{2.52}$$

where p_i is the probability of finding a particle at z at time t with the velocity $w_i = i\ \Delta w$ (the velocity has been divided into n intervals) and is given by

$$\frac{\partial p_i}{\partial t} = \sum_i a_{ji} p_j - \frac{\partial \sigma_{wi} p_i}{\partial z}. \tag{2.53}$$

Here a_{ji} is the probability that the velocity jumps from $j\ \Delta w$ to $i\ \Delta w$ at time t and σ_w is a characteristic velocity of the turbulence. If the characteristic velocity can only take on

two distinct values, $w_1=-w_2$, and $a_{ji}=a_{12}=a_{21}=-a_{11}=-a_{22}=a$ is the frequency of a change in the direction of motion, then Eq. (2.53) becomes

$$\frac{\partial p_1}{\partial t} + \frac{\partial (w p_1)}{\partial z} = a\,(p_2 - p_1), \qquad (2.54)$$

and

$$\frac{\partial p_2}{\partial t} + \frac{\partial (w p_2)}{\partial z} = a\,(p_1 - p_2).$$

Monin and Yaglom then show that the Eulerian diffusion equation corresponding to a limited propagation velocity must be hyperbolic

$$\frac{\partial^2 C}{\partial t^2} + 2a\frac{\partial C}{\partial t} = \sigma_w \frac{\partial}{\partial z}\left(\sigma_w \frac{\partial C}{\partial z}\right), \qquad (2.55)$$

where a is a characteristic frequency of the turbulence which can be determined from similarity theory

$$a = \frac{u_*}{z}\,\psi\left(\frac{z}{L}\right) \qquad (2.56)$$

and ψ is a universal function. For stationary homogeneous turbulence where a and σ_w are constants, Eq. (2.55) reduces to

$$T_c \frac{\partial^2 C}{\partial t^2} + \frac{\partial C}{\partial t} = \sigma_w^2 T_c \frac{\partial^2 C}{\partial z^2}, \qquad (2.57)$$

where the result has been multiplied by the characteristic turbulent time scale $T_c = 1/2a$. If $\sigma_w^2 \to \infty$ and $T_c \to 0$ such that $\sigma_w^2 T_c = K$ (a constant), then Eq. (2.57) reduces to the parabolic advection-diffusion equation.

Meyers et al. (1985) use exactly this approach to model top-down and bottom-up diffusion in the convective boundary layer. They formulate their equations as in the example above, relaxing the restrictions on w and a such that the ratio $w_1/(w_1+w_2)$ is a similarity ratio (i.e., is a function of z/z_i where z_i is the height of the lowest inversion) and the values of a are inversely proportional to the characteristic times of the updrafts and downdrafts. They use the results of their large eddy simulations (Cederwall et al., 1985) to determine various parameters required by their hyperbolic diffusion model.

Van Stijn and Nieuwstadt (1986) extend Monin and Yaglom's work to the case where three discrete particle velocities are possible and show that the resulting Lagrangian model is equivalent to an Eulerian model with a third order closure. They

generalize this result to show that a Lagrangian model where the particles may take on n distinct velocities is equivalent to an n^{th} order Eulerian closure.

2.2.5 The Stochastic Approach

The Monte Carlo approach is based on the Lagrangian statistical analysis of Taylor (1921), discussed previously. It was shown that the statistics of the concentration field are derived from the displacement statistics of marked fluid particles and that the ensemble mean concentration at a location in the fluid is given by (Tennekes and Lumley, 1972; page 236)

$$C(\mathbf{r}, t) = \int_{-\infty}^{t} \int_{-\infty}^{\infty} S(\mathbf{r}_0, t_0)\, P(\mathbf{r}, t | \mathbf{r}_0, t_0)\, d\mathbf{r}_0\, dt_0. \qquad (2.58)$$

Here $\mathbf{r}$ is the position vector, $S(\mathbf{r}_0, t_0) = Q\, p(\mathbf{r}_0, t_0)$ is the source distribution function, Q is the mass rate of release and $P(\mathbf{r}, t \mid \mathbf{r}_0, t_0)$ is the conditional or transition probability that a particle observed at $\mathbf{r}'$ at time t' will arrive at $\mathbf{r}$ at time t. In the Monte Carlo approach, the unknown transition probability $P(\mathbf{r}, t \mid \mathbf{r}_0, t_0)$ is determined by direct simulation of particle trajectories from the initial location $(\mathbf{r}_0, t_0)$ to the receptor location $(\mathbf{r}, t)$ as shown in Figure 2.1.

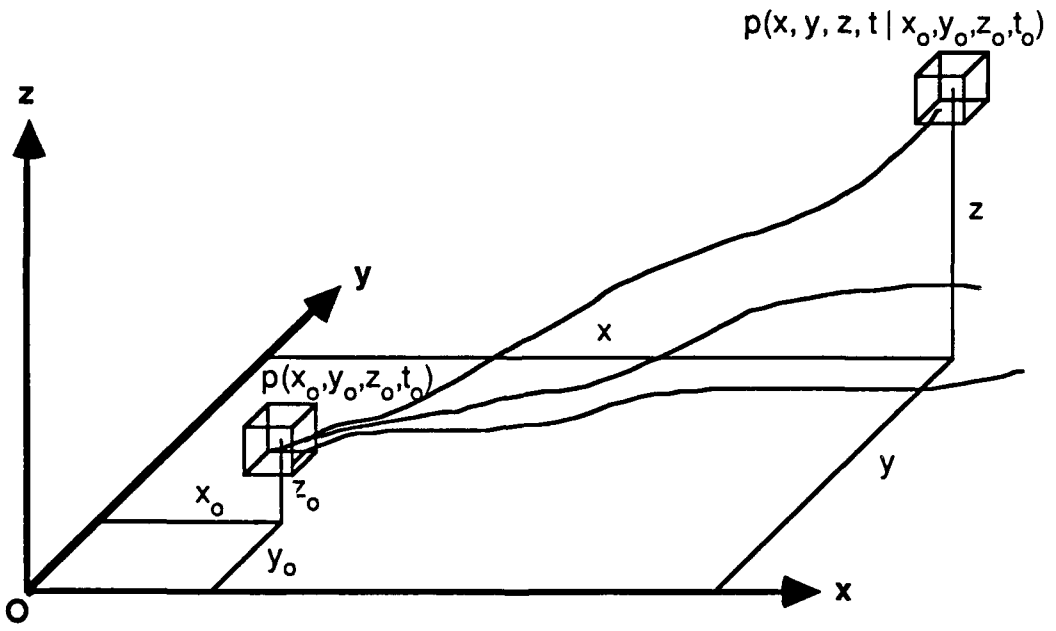

Figure 2.1 Schematic drawing illustrating the Monte Carlo simulation process.

Equation (2.58) may then be solved separately for an arbitrary source configuration. Note that for a continuous point source $S(\mathbf{r}, t) = Q\,\delta(\mathbf{r}-\mathbf{r}_0)$, Eq. (2.58) becomes

$$C(\mathbf{r}, t) = \int_{-\infty}^{t}\int_{-\infty}^{\infty} Q\,\delta(\mathbf{r}'-\mathbf{r}_0)\,P(\mathbf{r}, t \mid \mathbf{r}', t_0)\,d\mathbf{r}_0\,dt_0$$

$$= \int_{-\infty}^{t} Q\,P(\mathbf{r}, t \mid \mathbf{r}_0, t_0)\,dt_0\,, \qquad (2.59)$$

where the primes indicate a variable of integration and Q could be a function of time.

Markovian Displacements

The simulation of the particle trajectories is based on a Markovian analysis, in which case it describes the (one-dimensional, in this case) position of a particle as a random function of time by the stochastic differential equation

$$\frac{dZ(t)}{dt} = a\,\eta(t) \qquad (2.60)$$

where the random velocity $\eta(t)$ is a stationary, Gaussian random process (white noise) with mean zero and autocorrelation given by

$$\langle \eta(t_1)\eta(t_2) \rangle = \delta(t_2 - t_1),\ t_2 > t_1. \qquad (2.61)$$

Although white noise is discontinuous, its integral

$$\mathcal{W}(t) = \int_{0}^{t} \eta(t_1)\,dt_1, \qquad (2.62)$$

is continuous but nowhere differentiable. Equation (2.62) defines the Wiener process (Papoulis, 1984; page 344) which is a nonstationary, Gaussian process with independent increments $\xi = t_2 - t_1$:

$$\langle d\mathcal{W}(t+\xi)\,d\mathcal{W}(t) \rangle = \begin{cases} 0, & \xi \neq 0; \\ dt, & \xi = 0. \end{cases} \qquad (2.63)$$

As a result, future values $\mathcal{W}(t+\xi)$ only depend on the present value:

$$\mathcal{W}(t+\xi) = \mathcal{W}(t) + \int_{t}^{t+\xi} d\mathcal{W}(t), \tag{2.64}$$

because the integral is independent of the past; this is the definition of a Markov process. This means that the Brownian diffusion described by (2.60) is also a Markov process. Since $d\mathcal{W}(t)$ is not a function of position, the diffusion takes place in a homogeneous fluid. For convenience, we will rewrite Eq. (2.60) in terms of $\mathcal{W}(t)$ rather than $\eta(t)$

$$dZ(t) = a\big(Z(t)\big)\, d\mathcal{W}(t), \tag{2.65}$$

where a is now some function of position in order to accommodate non-homogeneous situations. It is important to note that the function $a(Z(t))$ depends neither on future values of $\mathcal{W}(t)$ nor on the increment $d\mathcal{W}(t)$ because the increments are independent. For example, this gives a mean of zero for Eq. (2.65):

$$\langle dZ(t)\rangle = \langle a(Z(t))\, d\mathcal{W}(t)\rangle = \langle a(Z(t))\rangle \times \langle d\mathcal{W}(t)\rangle = 0 \tag{2.66}$$

Particles in non-homogeneous turbulence can, in general, have a nonzero mean velocity. In this case Eq. (2.65) becomes

$$dZ = b(Z)\, dt + a(Z)\, d\mathcal{W}(t), \tag{2.67}$$

which has the mean velocity

$$\frac{\langle dZ\rangle}{dt} = \langle b(Z)\rangle. \tag{2.68}$$

Following Chandrasekhar (1943, see Wax, 1954) the Fokker-Planck equation describing the probability density p(z,t) corresponding to Eq. (2.67) is given by

$$\frac{\partial p}{\partial t} + \frac{\partial}{\partial z}\big(b(z)\, p(z,t)\big) = \frac{1}{2}\frac{\partial^2}{\partial z^2}\big(a^2(z)\, p(z,t)\big). \tag{2.69}$$

Clearly this has the same form as the advection-diffusion equation; in fact, Eq. (2.69) is also known as the forward diffusion equation (Papoulis, 1984; page 401). If an eddy diffusivity is defined as $K(z) = a^2(z)/2$, then (2.69) becomes

$$\frac{\partial p}{\partial t} + \frac{\partial}{\partial z}\left[\left(b - \frac{\partial K}{\partial z}\right) p\right] = \frac{\partial}{\partial z}\left(K\frac{\partial p}{\partial z}\right) \tag{2.70}$$

When the quantity $(b - \partial K/\partial z)$, which here acts as an Eulerian mean advection velocity, is zero, $b = \partial K/\partial z$ and Eq. (2.70) becomes

$$\frac{\partial p}{\partial t} = \frac{\partial}{\partial z}\left(K\frac{\partial p}{\partial z}\right) \tag{2.71}$$

Boughton et al. (1987) account for a time-dependent settling velocity $-w_s(t)$ in their Monte Carlo model by choosing $b - \partial K/\partial z = -w_s(t)$. Recalling that the mean concentration $C(z,t) = Qp(z,t)$, Eq. (2.71) may be recognized as the z-component of the advection-diffusion equation, Eq. (2.9). Thus the advection-diffusion equation is seen to represent Brownian or molecular diffusion in the limit $t/T_L \gg 1$ where the particle velocity fluctuations are not correlated. With $b = \partial K/\partial z$, (2.67) becomes

$$dZ = \frac{\partial K(z)}{\partial z} dt + \sqrt{2K(z)}\, d\mathcal{W}(t). \tag{2.72}$$

If this is ensemble-averaged over a large number of trajectories, the mean velocity is given by

$$\frac{d\langle Z\rangle}{dt} = \frac{dK(z)}{dz}. \tag{2.73}$$

This result demonstrates a very important feature of inhomogeneous turbulence: the Lagrangian mean velocity of fluid particles may be nonzero even if the Eulerian mean velocity is zero.

Markovian Velocities

In an effort to account for the correlation of velocity fluctuations when $t/T_L \sim 1$, some Monte Carlo models treat the particle velocity rather than the displacement as a Markov process. These models employ the Langevin equation

$$dw(t) = -\frac{w(t)}{T_L} dt + \sigma_w \left(\frac{2}{T_L}\right)^{1/2} d\mathcal{W}, \tag{2.74}$$

where w(t) is an instantaneous component of the Lagrangian velocity, T_L is the velocity correlation time and $d\mathcal{W}$ is an increment of the Wiener process discussed earlier. This equation was used by Uhlenbeck and Ornstein to describe the effects of inertia on the

Brownian motion (Uhlenbeck and Ornstein, 1930; in Wax, 1954). The force on a fluid particle is thus modeled as the sum of a constant retarding force due to inertia and a random, impulsive force due to turbulent accelerations. The actual correlation time of the turbulent accelerations is given by the Kolmogorov time scale $T_K \sim T_L\, Re^{-1/2}$. Thus Eq. (2.74) is valid only for Reynolds numbers sufficiently large that $T_K \to 0$; in the atmosphere this is usually the case.

If Eq. (2.74) is multiplied by $w(t+\xi)$ and the result ensemble-averaged, then the autocorrelation $R_L(\xi)$ is given by

$$dR_L(\xi) = \frac{\langle dw(t+\xi)w(t)\rangle}{\sigma_w^2} = -\frac{\langle w(t+\xi)w(t)\rangle}{T_L\sigma_w^2}\,dt + \left(\frac{2}{T_L\sigma_w^2}\right)^{1/2}\langle w(t+\xi)\,\mathcal{W}(t)\rangle$$

$$= R_L(\xi)\,\frac{dt}{T_L}, \tag{2.75}$$

which has the solution

$$R_L(\xi) = e^{-\xi/T_L} \tag{2.76}$$

and T_L is seen to equal the Lagrangian integral scale

$$\int_0^\infty R_L(\xi)\,d\xi = \int_0^\infty e^{-\xi/T_L}\,d\xi = T_L. \tag{2.77}$$

The resulting exponential form of the Lagrangian autocorrelation, which is implicit in the Langevin equation, is not completely correct since its derivative at zero lag time is infinite. However, an investigation by Neumann (1978) showed that the horizontal crosswind spreads of material computed using the exponential form agreed well with those based on the Pasquill-Gifford curves. An analysis by Tennekes (1979) demonstrated that the exponential form yields results which are consistent with turbulence in the inertial subrange.

Integrating Eq. (2.74) gives the correlated instantaneous velocity; the particle trajectory is given by integrating

$$dZ(t) = w(t)\,dt. \tag{2.78}$$

Because the velocities are now correlated, the trajectories are no longer Markovian; that is, future displacements no longer depend only on the present displacement but

on the entire history of the motion. However, Wang and Uhlenbeck (1945; in Wax, 1954) show that the trajectories and velocities are jointly Markovian. They derive the Fokker-Planck equation for the probability density p(z,w,t). It is this jointly Markovian nature which Monin and Yaglom (1971, page 676) exploit to develop the hyperbolic diffusion equation discussed earlier.

If $\xi/T_L \to \infty$ then $R_L \to 0$ and the Markovian behavior of the trajectories is recovered. Note that $\xi/T_L \to \infty$ can mean $\xi \to \infty$ or $T_L \to 0$. This reveals an important relationship between Markovian velocities and Markovian displacements. If the dispersion process is to be studied for travel times ξ which are much larger than the Lagrangian integral time scale T_L then the velocity correlations are not significant; the Markovian displacement analysis is appropriate. However, if the time of interest is of the order of T_L then the velocity correlations must be included. The same reasoning applies to the turbulent accelerations: if the time period under study is much larger than the Kolmogorov time scale T_K then treating the accelerations as uncorrelated random processes is sufficient. Figure 2.2 illustrates this situation for "typical" values of T_L in the planetary boundary layer.

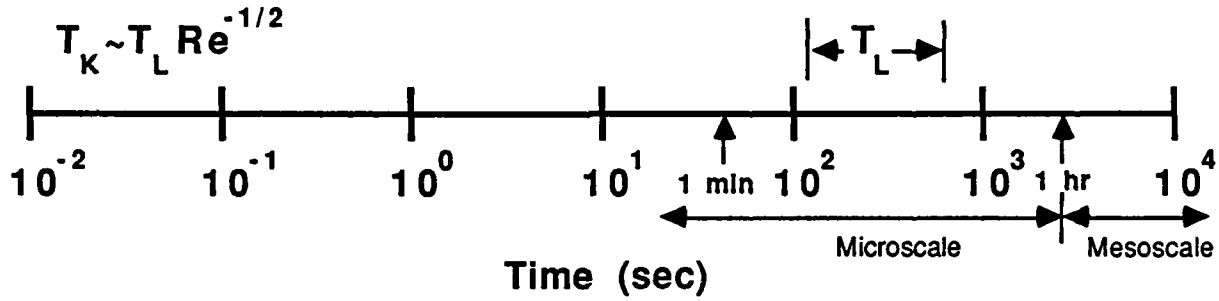

Figure 2.2 The relationship between turbulence scales and atmospheric scales.

Homogeneous Flow

The only properties of the turbulence required as input by the Monte Carlo model are σ_w and T_L. In stationary and homogeneous turbulence both are constant; furthermore, the Eulerian and Lagrangian velocity variances are equivalent while the Lagrangian time scale is considered to be proportional to the Eulerian length scale L_E of the turbulence

$$\frac{T_L \sigma_w}{L_E} = \beta \qquad (2.79)$$

with $\beta \approx 0.35\text{-}0.8$ (Pasquill and Smith, 1983). Boughton (1983) found good agreement between the results of his Monte Carlo simulations for Markovian displacements, which included settling and deposition, for ground-level sources in a uniform mean wind and Ermak's (1977) analytical solutions of the advection-diffusion equation which also accounted for settling and deposition. Boughton (1983) also found agreement between the results of his Markovian velocity simulation for homogeneous turbulence (σ_w and T_L both constant) and Sutton's Gaussian plume model for a ground-level source, both in a uniform wind.

Adiabatic Inhomogeneous Flow

Turbulence in the atmospheric surface layer is inhomogeneous due to the presence of the boundary at the ground. This causes the length and time scales to increase linearly with height above the boundary. In the absence of a temperature gradient (neutral conditions) the velocity scale σ_w remains essentially constant. The Langevin equation has been extended to this situation (Durbin, 1980; Wilson et al., 1981a; Ley, 1982; Legg, 1983) through the use of the forms

$$\sigma_w = b_1 u_*$$

and

$$T_L = b_2 \frac{z(t)}{\sigma_w}, \tag{2.80}$$

where u_* is the friction velocity and b_1 and b_2 are constants. Boughton et al. (1987) use K(z) and U(z) in this situation to reproduce the results of an analytical solution of the advection-diffusion equation given by Rounds (1955). From Eq. (2.80) it is apparent that T_L is treated as a local property of the turbulence. Durbin (1983) points out that for inhomogeneous turbulence, T_L cannot be regarded as an integral time scale, but rather should be considered the local decorrelation time scale,

$$T_L = \left(\left| \frac{1}{R_L(\xi)} \frac{dR_L(\xi)}{d\xi} \right|^{-1} \right)_{\xi=0}. \tag{2.81}$$

With these forms for σ_w and T_L, the Langevin model satisfies surface layer similarity, Eq. (2.45), which requires the mean Lagrangian vertical velocity under neutral stratification to be

$$\frac{\partial \langle Z(t) \rangle}{\partial t} = Au_* \tag{2.82}$$

even though the mean Eulerian vertical velocity is zero. This confirms the previous result, Eq. (2.73), which indicates that there is a constant mean drift of particles up the gradient of T_L. This drift arises because the particles moving in the direction of increasing T_L (i.e., upward) maintain their direction of motion longer on average than particles moving in the direction of decreasing T_L (downward).

Diabatic Inhomogeneous Flow

In the convective (unstable) surface layer, σ_w varies with height (Kaimal et al., 1976) due to the heat flux at the ground. A height dependence is also found in crop and forest canopies (Raupach and Thom, 1981). Extending the Langevin equation to address these situations has proven to be more difficult. In weakly inhomogeneous turbulence, Eqs. (2.34) and (2.73) may be combined to produce an expression for the mean Lagrangian vertical velocity

$$\frac{\partial \langle Z \rangle}{\partial t} = \frac{\partial}{\partial z}\left(\sigma_w^2 T_L\right) = \sigma_w^2 \frac{\partial T_L}{\partial z} + T_L \frac{\partial \sigma_w^2}{\partial z}. \tag{2.83}$$

In the non-neutral surface layer, the gradient in σ_w is nonzero and should contribute to the drift. However, numerical experiments by Wilson et al. (1981b) and Legg and Raupach (1982) show that simply using the local value of $\sigma_w(z)$ in Eq. (2.74) does not produce this effect and that as a result particles slowly settle and become trapped in regions where σ_w is small. This behavior is due to the assumed Gaussian nature of the velocity fluctuations which dictates that the (downward) motion of a particle from a region of relatively large σ_w to one of low σ_w and the (upward) motion in the direction of increasing σ_w are equally probable. Since the average number of particles moving in either direction is the same but downward moving particles have a greater average velocity, a net downward flux arises. In order to overcome this problem a term is added to the Langevin equation which explicitly produces this mean drift velocity

$$dw = -\frac{w}{T_L(z)}dt + \sigma_w(z)\left(\frac{2}{T_L(z)}\right)^{1/2} d\mathcal{W} + a_d\, dt. \tag{2.84}$$

Several forms for a_d have been suggested. Legg and Raupach (1982) and Ley and Thomson (1983) appeal to the vertical component of the Navier-Stokes equation and

argue that the Reynolds stress term $\partial(\rho\sigma_w^2)/\partial z$ (where $\sigma_w^2 \equiv \langle w'w' \rangle$) which balances the pressure gradient and gravitational force there must be accounted for in the Langevin equation. They contend that when there is a gradient in the vertical velocity variance, the equation of motion for a fluid particle must include a mean force due to the action of the mean pressure gradient on the particle. They propose

$$a_d = \frac{\partial \sigma_w^2}{\partial z}. \tag{2.85}$$

Wilson et al. (1981b) apply a more heuristic argument based on the continuity equation to a modified form of the Langevin equation

$$d\left(\frac{w}{\sigma_w}\right) = -\left(\frac{w}{\sigma_w T_L}\right) dt + \left(\frac{2}{T_L}\right)^{1/2} d\mathcal{W} + \left(\frac{b_d}{\sigma_w}\right) dt \tag{2.86}$$

to show

$$b_d = \frac{1}{2} \frac{\partial \sigma_w^2}{\partial z}. \tag{2.87}$$

Durbin (1983) proposes an alternative modification to provide the correct mean drift

$$d\left(\frac{w}{\sigma_w^2}\right) = -\left(\frac{w}{\sigma_w^2 T_L}\right) dt + \left(\frac{2}{\sigma_w^2 T_L}\right)^{1/2} d\mathcal{W}. \tag{2.88}$$

Using the chain rule, (2.86) and (2.88) can be put in the form of (2.84) which leads to the following expressions for a_d:

$$a_d = \frac{1}{2}\left(1 + \frac{w^2}{\sigma_w^2}\right) \frac{\partial \sigma_w^2}{\partial z} \tag{2.89}$$

and

$$a_d = \left(\frac{w^2}{\sigma_w^2}\right) \frac{\partial \sigma_w^2}{\partial z}. \tag{2.90}$$

A comparison of these corrections (Eqs. (2.85), (2.89) and (2.90)) reveals that they only differ in terms involving w^2/σ_w^2. Noting that $\langle w^2 \rangle = \langle w \rangle^2 + \sigma_w^2$, all three forms should be equivalent in the weakly inhomogeneous limit when $\langle w \rangle \rightarrow 0$. For strongly inhomogeneous turbulence these terms will not be equivalent; in that case, (2.90) provides the greatest correction while (2.85) provides the least.

By requiring that the steady state Lagrangian particle velocity momen's equal the steady state Eulerian fluid velocity moments, Thomson (1984) rigorously derives the moments of the random velocity forcing function. He demonstrates that the mean drift velocity provided by Eq. (2.89) is essential if the steady state probability density of the particles is to equal the probability density of the fluid; that is, if material released into the inhomogeneous turbulent flow is to eventually become uniformly distributed. Thomson further demonstrates that the skewness of the vertical velocity must also be included in simulations of strongly inhomogeneous turbulence. DeBaas et al. (1986) utilize Thomson's results to build a one-dimensional Monte Carlo model which incorporates the correct skewness of the vertical velocity. Although their finite-difference form for the Langevin equation violates the independent increment property of the Wiener process discussed earlier, their results are in reasonable agreement with the water tank experiments of Willis and Deardorff (1978). In order to achieve this agreement, however, they found that they had to substantially increase the Lagrangian vertical time scale over reported values.

Lamb (1978) avoided this problem by using the turbulence field computed by Deardorff's (1974) large eddy simulation of the convective boundary layer as input to a Monte Carlo model. His dispersion predictions (discussed in greater detail in Lamb, 1984) were in agreement with Deardorff's numerical work (1973, 1974) and laboratory experiments (Willis and Deardorff, 1974; Deardorff and Willis, 1975). As a side note, Lamb (1981) has proposed a Monte Carlo scheme for simulating the subgrid scale, bandwidth-limited turbulence encountered in large eddy models. Thus a symbiotic relationship between Monte Carlo and large eddy models seems to be developing.

Bærentsen and Berkowicz (1984) developed a Monte Carlo simulation of the convective boundary layer which uses two Langevin equations: one to represent ascending particles carried by thermals, and one to represent descending particles in the subsidence. Their model depends on four time scales: one for each Langevin equation and one for each of the exponentially distributed probabilities of an ascending (descending) particle changing direction. These in turn depend on a "Lagrangian dissipation rate" which they treat as a free parameter. They are able to

choose these parameters such that their results agree rather well with Willis and Deardorff's water tank experiments.

Van Dop et al. (1985) begin with the extended Langevin equation

$$dw = -\frac{w}{T_L}dt + d\mathcal{W}(z,t), \tag{2.91}$$

where

$$d\mathcal{W}(z,t) \equiv a_1(z,t)\,dt + \sqrt{a_2(z,t)}\,d\mathcal{W}(t) \tag{2.92}$$

and, in general

$$\langle d\mathcal{W}^n(z,t)\rangle = a_n(z,t)\,dt \quad (n = 1,2,3,\ldots). \tag{2.93}$$

They proceed to derive the Fokker-Planck equation for the probability density p(z,w,t), for which the displacements and velocities are jointly Markovian:

$$\frac{\partial p}{\partial t} + w\frac{\partial p}{\partial z} = \frac{\partial}{\partial w}\left[\left(\frac{w}{T_L} - a_1\right)\,p\right] + \frac{1}{2}a_2\frac{\partial^2 p}{\partial w^2}, \tag{2.94}$$

where

$$C(z,t) = Q\,p(z,t) = Q\int_{-\infty}^{\infty} p(z,w,t)\,dw \tag{2.95}$$

and

$$\langle w^n(z,t)\rangle = \frac{\int_{-\infty}^{\infty} w^n\,p(z,w,t)\,dw}{p(z,t)}. \tag{2.96}$$

By multiplying Eq. (2.94) by w^n and integrating over w, they generate an infinite series of equations for the moments of p. By requiring these moments match their Eulerian counterparts, van Dop et al. derive expressions for the first few $a_n(z,t)$ for *unsteady*, inhomogeneous conditions. For the steady case, their results agree with Thomson (1984) confirming his results but more importantly, rigorously demonstrating the link between the Eulerian conservation equations and the Langevin-based Lagrangian stochastic models of atmospheric dispersion.

The derivation of the Fokker-Planck equation assumes a Gaussian forcing which is known to be incorrect for the convective boundary layer. Sawford (1986) extends the work of van Dop et al. for non-Gaussian forcing by using the Kramers-Moyal expansion:

$$\frac{\partial p}{\partial t} + \frac{\partial (wp)}{\partial z} = \frac{\partial}{\partial w}\left(\frac{w}{T_L}\, p\right) + \sum_{i=1}^{\infty} (-1)^i \frac{a_i}{i!} \frac{\partial^i p}{\partial w^i}. \qquad (2.97)$$

Truncating the series at i = 2 returns the Fokker-Planck equation corresponding to a Gaussian $d\mathcal{W}(z,t)$. Sawford uses Eq. (2.97) to derive a hierarchy of Eulerian conservation equations. By requiring that an initially uniform distribution remain uniform, which he claims is necessary to satisfy the second law of thermodynamics, Sawford derives an expression for a_n, the moments of $d\mathcal{W}(z,t)$:

$$a_n = \frac{d\langle w^n \rangle}{dt} + \frac{n \langle w^n \rangle}{T_L} - \sum_{i=1}^{n-1} \binom{n}{i} a_i \langle w^{n-i} \rangle. \qquad (2.98)$$

Pope (1987) points out that Sawford's "thermodynamic constraint" (the requirement that an initially uniform distribution remain uniform) is completely satisfied if the mean velocity field satisfies the continuity equation. Pope demonstrates that only the correct mean drift term (n = 1 in Eq. (2.98)) is necessary to ensure compliance with continuity and that the correct mean drift is that which balances the mean pressure gradient arising in the Navier-Stokes equations as discussed earlier by Legg and Raupach (1982) and Ley and Thomson (1983). Pope also points out that the additional constraints imposed by Sawford in order to determine Eq. (2.98) are not required to satisfy the thermodynamic constraint but rather are consistency conditions which are necessary to ensure that the computed probability density of the particles matches the probability density of the fluid. Viewed from this perspective, Sawford's work is seen to closely parallel Thomson's earlier effort (1984). More recently, Thomson (1987) has united these different approaches and shown that all of them are essentially equivalent.

The most interesting aspect of Sawford's (1986) work is his observation that the theorem of Marcinkiewicz (Rajagopal and Sudarshan, 1974) shows that either all but the first two cumulants of $d\mathcal{W}(z,t)$ vanish, or else there are an infinite number of nonvanishing cumulants. He points out that this theorem ensures that Eq. (2.97) is either truncated at i = 2 or not at all and therefore that p correctly represents a

probability density, even though in practice it may only approximate the correct density. Thus, unless the turbulence is Gaussian, a random process which incorporates an infinite number of moments of $d\mathcal{W}(z,t)$ must be constructed for the exact p to be obtained. Thomson (1984) demonstrated computationally that a Gaussian $d\mathcal{W}(z,t)$ yields a uniform steady state distribution only for weakly inhomogeneous turbulence. (Note that for a Gaussian $d\mathcal{W}(z,t)$, a_3 is nonzero despite $\langle w^3 \rangle = 0$ since a_3 also depends on a_2 and a_1, according to Eq. (2.98).) For increasing inhomogeneity, Thomson obtained a uniform steady state distribution by adding a nonzero $\langle w^3 \rangle$ to a_3. However, as the inhomogeneity was further increased, a uniform steady state distribution was not obtainable; more terms in Eq. (2.98) have to be included. This is the closure problem.

2.3 Summary

In this review we have shown that the problem of atmospheric dispersion has been approached from both Eulerian and Lagrangian perspectives. The Eulerian methods approach the problem by finding solutions of the mass conservation equation whereas the Lagrangian methods seek to determine the conditional or transition probability density function which describes the evolution of marked fluid from some known initial location. All of these methods must deal with the unavoidable problem of closure.

If the mass conservation equation is ensemble averaged the closure problem is to specify a relationship for the turbulent fluxes which arise in the averaging process. If a local closure such as gradient transfer is utilized to relate the turbulent fluxes to the local gradient of the mean concentration via an "eddy diffusivity" (K-theory), the advection-diffusion equation results. Through the Fokker-Planck equation we have shown that this corresponds to the Markovian displacement approach. The parabolic advection-diffusion equation can thus describe the dispersion of atmospheric pollutants at times or distances from the source of pollutant emission which are large in comparison with the Lagrangian integral time scale. Although it is possible to force eddy diffusivity closures to correctly model the mean concentration close to a source, this requires a time-dependent diffusivity which is thus no longer a property of the flow. Non-local schemes for closing the advection-diffusion equation have the potential to be valuable for describing dispersion under convective conditions when the spatial scale of the turbulence is large compared to the dispersing cloud of material. Despite this potential, they have achieved little success to date, largely due to the lack of high

quality data necessary to determine the correct numerical formulations for their complicated closures. Higher order closure schemes which utilize a set of differential equations to describe the moments of the turbulent fluxes are generally restricted to academic use in studying the physics of turbulent dispersion as well as for developing more successful closures for gradient transfer models.

The main difficulty with closures of the ensemble averaged mass conservation equation is that they must treat all scales of motion, including the largest scales which are responsible for most of the heat, mass and momentum transfer. The large eddy simulation method overcomes this problem by solving the volume-averaged mass continuity equation. In this manner the large, energy-containing eddies are treated explicitly while the subgrid scale eddies which are essentially isotropic may be modelled very simply without adversely affecting the results. This approach can achieve impressive results and is a valuable research tool for studying the planetary boundary layer. However, its prodigious computational requirements necessitate the use of a fairly coarse spatial mesh. In the vicinity of the boundary this results in insufficient resolution and anomalous behavior because most of the energy containing eddies near the boundary are at subgrid scales.

The Gaussian plume approach is largely empirical; it is based on an empirically derived Gaussian transition probability and empirically determined plume parameters. Nevertheless it enjoys tremendous popularity and has achieved sanction by U. S. Government regulatory agencies. This popularity is due in no small measure to its predictive success in situations where its underlying assumptions are valid combined with its relative ease of application. It is this same combination of predictive success and ease of use which lead to abuse and misapplication of the approach, however. The statistical theory from which it was derived assumes that the field of turbulence is stationary and homogeneous; the assumption of a Gaussian transition probability implies Markovian displacements. The Gaussian plume approach is strictly valid only when these conditions are met. Thus, horizontal dispersion and, for a limited distance from elevated sources, vertical dispersion can be considered to be homogeneous for near-neutral atmospheric conditions. For travel times much larger than the Lagrangian integral time scale, predictive success is reasonably good for appropriately chosen plume parameters. For inhomogeneous cases, such as vertical dispersion from a ground level source, or under diabatic conditions – especially strongly convective situations – the Gaussian assumption is not correct. For such cases, model predictions generally do not agree with experimental results.

Lagrangian similarity methods are extremely valuable for extending Taylor's statistical theory of turbulent dispersion to the inhomogeneous planetary boundary layer and suggesting forms for modelling it. The difficulty here lies in determining from existing data the values of the universal constants and expressions for the universal functions deduced with the theory. Probably the most useful aspect of the similarity methods is within the context of other modelling approaches where appropriately scaled results may be applicable for a wide range of atmospheric conditions.

The infinite propagation velocity of marked fluid implied by the parabolic form of the advection-diffusion equation emphasizes its theoretical limitation to large distances and times from the release point. In order to correctly model short range dispersion, the propagation velocities must be constrained to remain finite; that is, the velocities and displacements must be jointly Markovian. If the propagation velocity is further restricted to two values, $\pm w$, and the turbulence is assumed to be stationary and homogeneous, then the problem reduces to the so-called telegraph equation which has a hyperbolic form. It has also been shown that a system wherein the propagation velocity may take on n distinct values corresponds to an n^{th} order Eulerian closure. As with other approaches, the major obstacle to applying these models lies in determining certain necessary parameters, "characteristic" time and velocity scales, from existing data.

We have chosen to implement the Monte Carlo approach because it offers the best potential for modelling the microscale dispersion process in the convective planetary boundary layer. Although there is no direct theoretical link between the Langevin equation and the Navier-Stokes equations, the demonstrated equivalence of the Markovian trajectory analysis and the parabolic advection-diffusion equation, the equivalence of jointly Markovian velocities and displacements and higher order Eulerian closures, as well as the phenomenological agreement presented by many workers have led to a general acceptance of the Monte Carlo approach to dispersion modelling. Figure 2.3 indicates the relationship between the various modelling approaches we have discussed.

Monte Carlo models are becoming increasingly popular for studying atmospheric transport and dispersion because they are simpler and physically more transparent than high-order Eulerian models based on the advection-diffusion equation. Their popularity is enhanced by their potential to be more computationally efficient than Eulerian models since they only involve that portion of the flow (the marked fluid) which is of interest. Also, they are free from numerical problems such as stability and pseudo-diffusion. Moreover, Eulerian analyses require closures based on

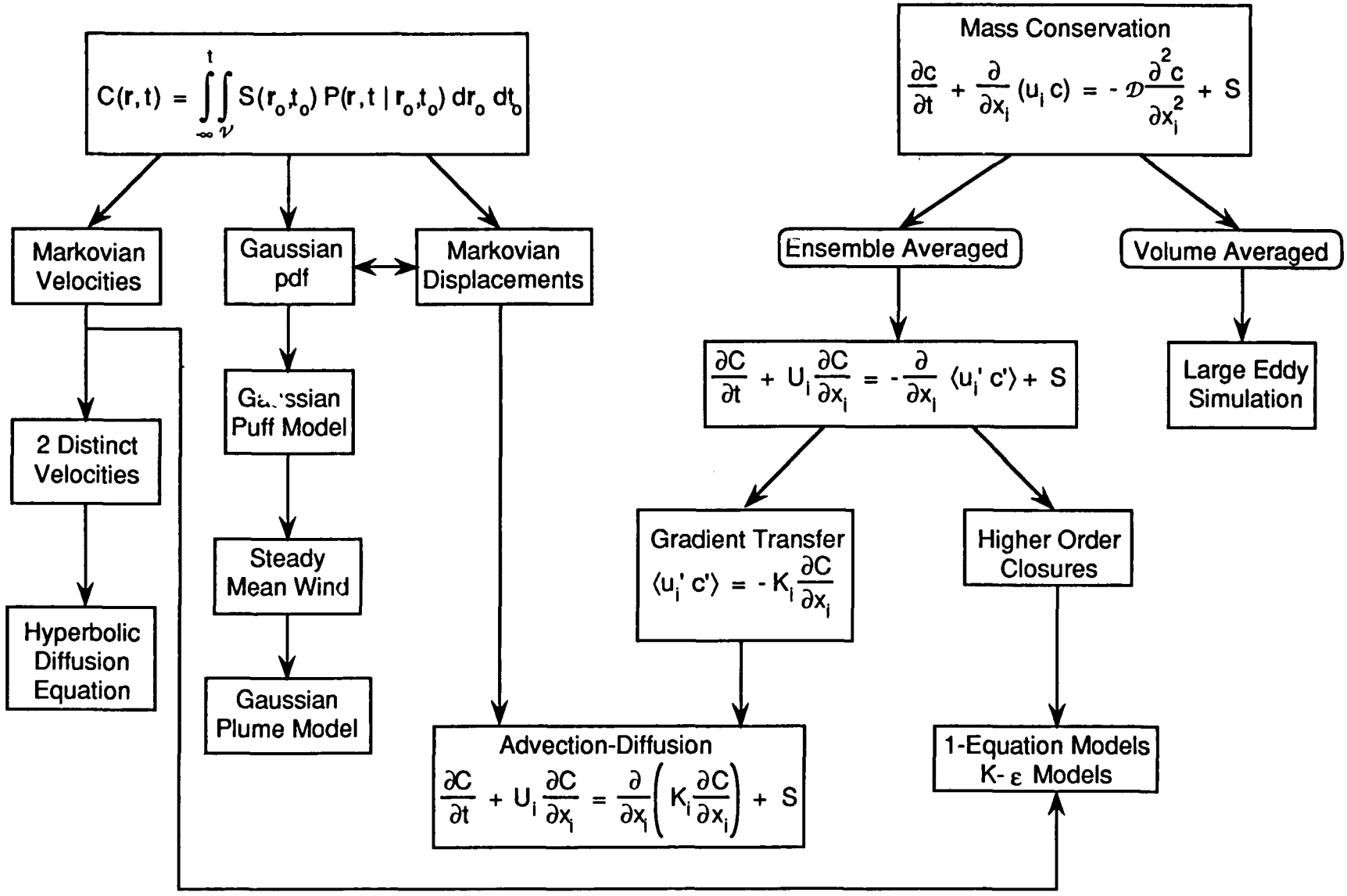

Figure 2.3 The relationship between the various approaches to modelling atmospheric dispersion.

approximate relations among certain joint moments of the velocity and concentration fields. Since these approximations depend on the concentration itself, they are not uniformly valid, as has been discussed above. In contrast, the probability density functions computed by the Monte Carlo approach are determined solely by modelling the velocity field. Although this also requires approximations (the closure problem is unavoidable), they do not involve the concentration and so are uniformly valid.

3. THE STOCHASTIC MODEL

The purpose of this section is to present our stochastic model for the simulation of turbulent particle dispersion. As was discussed in §2.2.5, the ensemble average concentration at time t for some point **r** in space is given by

$$C(\mathbf{r}, t) = \int_{-\infty}^{t} \int_{-\infty}^{\infty} S(\mathbf{r}_0, t_0)\, P(\mathbf{r}, t \mid \mathbf{r}_0, t_0)\, d\mathbf{r}_0\, dt_0. \tag{3.1}$$

The stochastic approach to this problem is to determine the transition probability $P(\mathbf{r}, t \mid \mathbf{r}_0, t_0)$ by simulating the motion of many particles. In order to accurately treat the dispersion process for times comparable to the Lagrangian integral time scale of the velocity, during which the velocities are autocorrelated, we employ a form of the Langevin equation to simulate the particle velocities. From these velocities, the particle trajectories are determined.

Our method is based on the Langevin equation which has been extended to include a non-Gaussian forcing function for three dimensions. The simulation incorporates the current state-of-the-art understanding of the physics of the planetary boundary layer and utilizes recent measurement of atmospheric turbulence.

3.1 The Stochastic Equations

In its simplest form, the discrete, one-dimensional form of the Langevin equation is given by

$$u(t+\Delta t) = R(\Delta t)\, u(t) + \mu(t), \tag{3.2}$$

where $R(\Delta t)$ is the autocorrelation coefficient at time lag Δt. The last term $\mu(t)$ is a random component of the turbulence and is assumed to be independent of $u(t)$. As was shown earlier, an exponential form for the autocorrelation is implicit in the Langevin equation: $R(\Delta t) = \exp(-\Delta t/T_L)$. In order to test the validity of Eq. (3.2) and its implicit exponential autocorrelation, Hanna (1979) analyzed both Eulerian data from towers and tethered balloons and Lagrangian data from free-floating balloons in the convective daytime boundary layer. Hanna found a strong linear relationship between the conditional average velocity $(\langle u(t+\Delta t)\rangle \mid u(t))$ and the instantaneous velocity $u(t)$. The Lagrangian data maintained this linearity even at extreme values of $u(t)$ although the Eulerian data did not. Hanna also found that the Eulerian data were well represented by an exponential autocorrelation. Of the autocorrelations computed from

the Lagrangian data by Hanna and presented in Fig. 3.1, only the transverse velocity component v could be considered to be exponential in form. Both of the vertical velocity autocorrelations become negative. In order to construct a simulation which would provide this negative tail for the autocorrelation, Lamb (1981) suggested replacing Eq. (3.2) with the Markov-2 chain

$$u(t+\Delta t) = au(t-\Delta t) + bu(t) + \mu(t). \tag{3.3}$$

In this expression a and b are constants chosen such that the correlation has a suitable appearance (i.e., a negative tail.) Because of the subjectivity involved in determining these constants, this method has not achieved much popularity and we shall not use it here. Although Hanna (1979) does not discuss it, the fact that the autocorrelations of the vertical Lagrangian velocity have negative tails, whereas the autocorrelations computed from the Eulerian data and the autocorrelation of the transverse Lagrangian velocity do not, has a straightforward explanation. The turbulence in the transverse direction is essentially homogeneous and therefore the transverse integral time $T_{L,v}$ is constant. Because of this, an exponential form for the autocorrelation $R_L(\Delta t)$ would yield a velocity record whose autocorrelation is also exponential. In the vertical direction however, the turbulence is highly inhomogeneous due to the combined effects of the ground and the convection. Because of this the vertical integral time is not constant; rather, it increases with distance from the ground $T_{L,w} = T_{L,w}(z)$. Although the autocorrelation function in Eq. (3.2) has an implicit exponential form, a spatially varying integral time would result in a Lagrangian autocorrelation which is not necessarily exponential. Because the Eulerian data are collected at a fixed elevation, they experience a constant integral time and so display an exponential autocorrelation. Thus the exponential form for the autocorrelation which is implicit in Eq. (3.2) will yield a Lagrangian velocity record having an autocorrelation with a negative tail if only the local, spatially varying value of the integral time scale is used. This has been verified computationally for our model and the results presented in Fig. 3.2 in terms of the dimensionless time t^+. (We will define this dimensionless time scale later.) In this figure the vertical and transverse velocity autocorrelations averaged over an ensemble of particles are indicated for three release heights ranging from very close to the surface ($z_0/h = 0.0025$) to almost the midpoint of the boundary layer ($z_0/h = 0.49$). All three autocorrelations for the vertical velocity become negative whereas the autocorrelation for the transverse velocity demonstrates approximately exponential behavior.

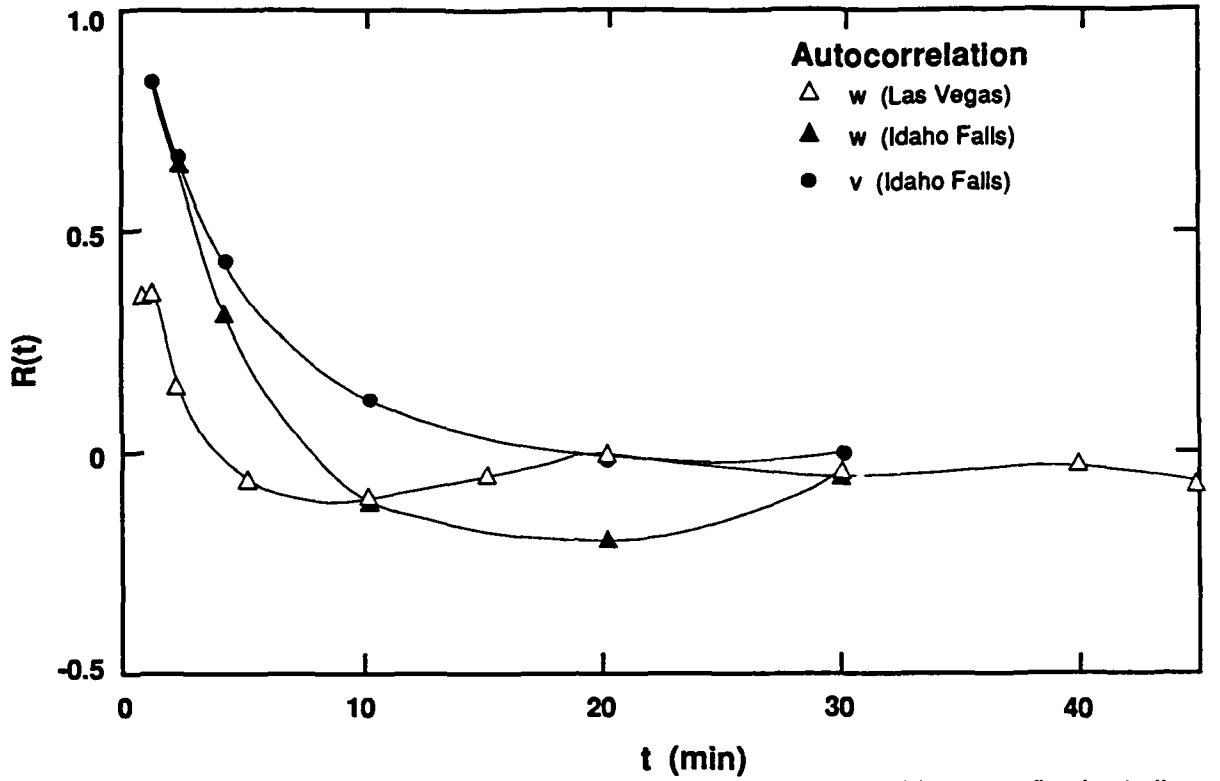

Figure 3.1 Autocorrelations of Lagrangian velocity fluctuations computed from free-floating balloons (Hanna, 1979).

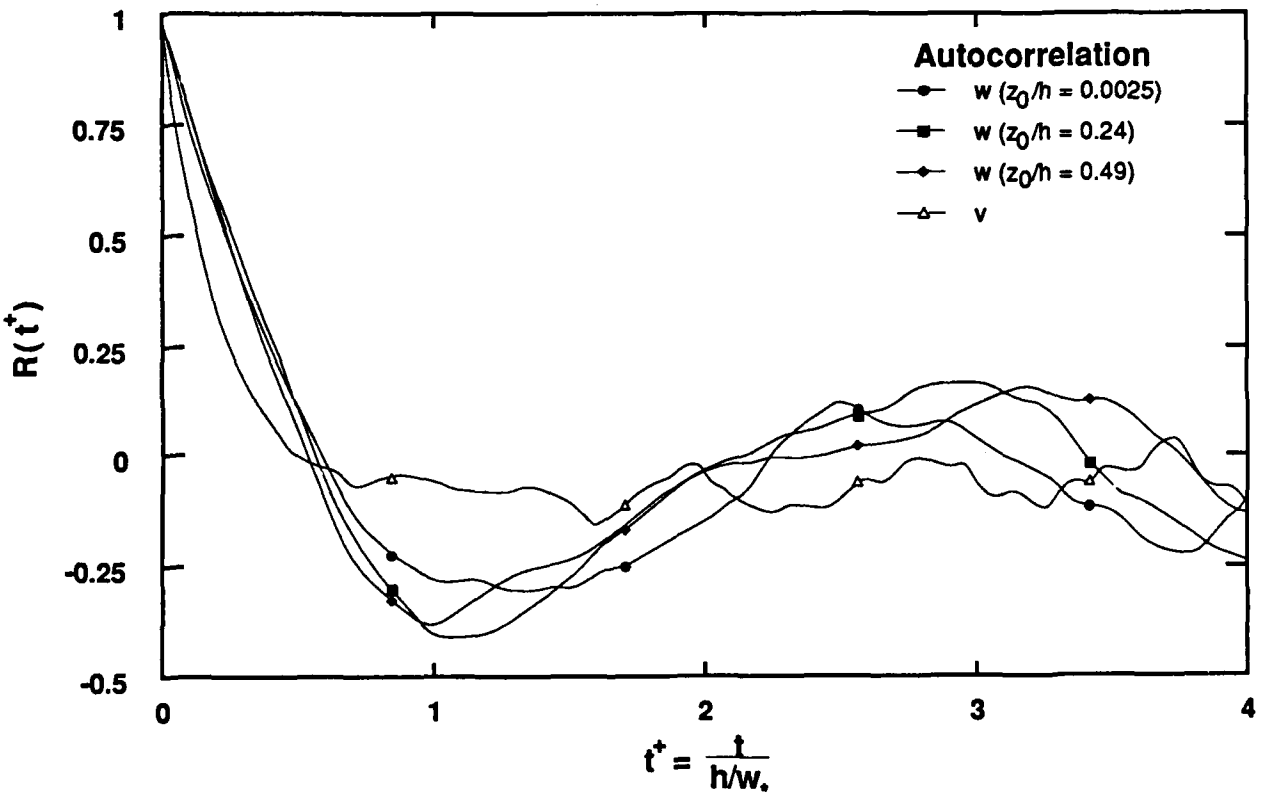

Figure 3.2 Autocorrelations of Lagrangian velocity fluctuations computed by the stochastic model.

3.1.1 The Discrete Extended 3-D Langevin Equation

The Langevin equation extended to the case of an arbitrary forcing function, Eq. (2.91), is given in three dimensions by

$$du_i(t) = -T_{ij}(X_i(t))\, u_j(t)\, dt + d\mathcal{W}_i(t), \tag{3.4}$$

where T_{ij} is a rank two tensor of the form $T_{ij} = 1/T_{Lij}$. Note that $T_{L11} = T_{Lu}$, $T_{L22} = T_{Lv}$, and $T_{L33} = T_{Lw}$. For $i \neq j$, T_{Lij} is the "local decorrelation time scale" (discussed in §2.2.5) for the cross-covariances. Thus

$$T_{ij} = 1/T_{Lij} = \begin{pmatrix} 1/T_{L,u} & 1/T_{L,uv} & 1/T_{L,uw} \\ 1/T_{L,uv} & 1/T_{L,v} & 1/T_{L,vw} \\ 1/T_{L,uw} & 1/T_{L,vw} & 1/T_{L,w} \end{pmatrix} \tag{3.5}$$

and the Einstein convention of summation over repeated indices is indicated. In discrete form Eq. (3.4) becomes

$$u_i(t+\Delta t) = \left[\delta_{ij} - T_{ij}(X_i(t+\Delta t))\Delta t\right] u_j(t) + \mu_i(t+\Delta t), \tag{3.6}$$

where μ_i is the discrete random process corresponding to $d\mathcal{W}_i$. (The discrete random process is discussed in §3.2.) The trajectories of the marked fluid particles are computed by integrating

$$dX_i(t) = u_i(t)\, dt, \tag{3.7}$$

which yields the following discrete form for $X_i(t+\Delta t)$

$$X_i(t+\Delta t) = X_i(t) + u_i(t)\, \Delta t. \tag{3.8}$$

The simulation proceeds by using the velocity u_i and position X_i of the particle at t to compute the new position at $t+\Delta t$ with Eq. (3.8). The reciprocal of the integral time scale T_{ij} and the value of the random process μ_i computed at the new position at $t+\Delta t$, along with the velocity at the old position, are combined according to Eq. (3.6) to determine the new velocity at $t+\Delta t$.

For the one-dimensional case, Eq. (3.6) reduces to

$$u_i(t+\Delta t) = \left(1 - \frac{\Delta t}{T_{Li}}\right) u_j(t) + \mu_i(t+\Delta t). \tag{3.9}$$

For $\Delta t/T_{L,i} \ll 1$, $R_{L,i}(\Delta t) \equiv \dfrac{\langle u_i(t+\Delta t)u_i(t)\rangle}{\langle u_i(t)u_i(t)\rangle} = \exp(-\Delta t/T_{L,i}) = 1 - \Delta t/T_{L,i} + O(\Delta t/T_{L,i})^2$. Squaring both sides and taking the average leads to

$$\langle u_i^2(t+\Delta t)\rangle = R_{L,i}^2(\Delta t)\,\langle u_i^2(t)\rangle + \langle \mu_i^2(t+\Delta t)\rangle + 2\,R_{L,i}(\Delta t)\,\langle u_j(t)\mu_i(t+\Delta t)\rangle \qquad (3.10)$$

The last term in Eq. (3.10) is zero because the increments of the Wiener process are independent. For neutral (adiabatic) atmospheric conditions the velocity variance must be constant; thus, $\langle u_i^2(t+\Delta t)\rangle = \langle u_i^2(t)\rangle = \sigma_i^2$. Substituting this back into Eq. (3.10) and solving for $\langle \mu_i^2(t+\Delta t)\rangle$ gives

$$\langle \mu_i^2(t+\Delta t)\rangle = \sigma_i^2\left(1 - R_{L,i}^2(\Delta t)\right)$$

$$= \sigma_i^2\left[1 - \left(1 - \frac{\Delta t}{T_{L,i}}\right)^2\right] = 2\sigma_i^2\frac{\Delta t}{T_{L,i}} + O(\Delta t^2). \qquad (3.11)$$

Then to $O(\Delta t)$ Eq. (3.9) becomes

$$u_i(t+\Delta t) = \left(1 - \frac{\Delta t}{T_{L,i}}\right)u_j(t) + \sigma_i\sqrt{\frac{2\Delta t}{T_{L,i}}}\,r$$

$$= R_{L,i}(\Delta t)\,u_i(t) + \left(1 - R_{L,i}^2\right)\sigma_i\,r;\quad R_{L,i}(\Delta t) = \exp(-\Delta t/T_{L,i}), \qquad (3.12)$$

where r is a (computer generated) normal random variable with $\langle r\rangle = 0$ and $\langle r^2\rangle = 1$. Equation (3.12) is the discrete form of the Langevin equation which is employed in one-dimensional Monte Carlo simulations where the velocity correlations are included. Thus our formulation is seen to be a generalization of the one-dimensional case. In a similar fashion Eq. (3.6) may be rewritten as

$$u(t+\Delta t) = R_{L,u}(\Delta t)\,u(t) - [1 - R_{L,uv}(\Delta t)]\,v(t) - [1 - R_{L,uw}(\Delta t)]\,w(t) + \mu_u(t+\Delta t),$$

$$v(t+\Delta t) = R_{L,v}(\Delta t)\,v(t) - [1 - R_{L,uv}(\Delta t)]\,u(t) - [1 - R_{L,vw}(\Delta t)]\,w(t) + \mu_v(t+\Delta t)$$

and $$w(t+\Delta t) = R_{L,w}(\Delta t)\,w(t) - [1 - R_{L,uw}(\Delta t)]\,u(t) - [1 - R_{L,vw}(\Delta t)]\,v(t) + \mu_w(t+\Delta t), \qquad (3.13)$$

where, for example

$$R_{L,uw} = \exp(-\Delta t/T_{L,uw}) = \exp(-T_{13}\Delta t) = 1 - T_{13}\Delta t + \mathcal{O}(\Delta t^2). \qquad (3.14)$$

3.1.2 Scaling and Non-Dimensionalization

In order to allow our model to accommodate the broadest possible range of atmospheric conditions, we must choose appropriate length, time and velocity scales with which to non-dimensionalize the equations. Because we are primarily interested in concentrations at the ground-level which arise from release point near the ground, it would at first seem that the surface layer scaling of Monin and Obukhov (1954) would be most appropriate. However, for very convective conditions, the surface layer may only be a few meters thick. Additionally we have shown in Chapter 1 that a well developed mixed layer can range over most of the the planetary boundary layer for relatively weak insolation. For these reasons, we have chosen to formulate our model in terms of the mixed layer scales suggested by Deardorff. As was discussed in §2.2.3, the appropriate scaling length in the mixed layer is the boundary layer height h. The velocity scale was shown to be the convective velocity $w_* = [h\,(g/T)\,(q/\rho c_p)]^{1/3}$. From these a convective time scale can be formed, $t_* = h/w_*$. If we let $x_i^+ = x_i/h$, $u_i^+ = u_i/w_*$, $\mu_i^+ = \mu_i/w_*$, $t^+ = t/t_*$ and $T_{ij}^+ = T_{ij}t_*$ then Eq. (3.6) becomes

$$u_i^+(t^+\!+\!\Delta t^+) = \left[\delta_{ij} - T_{ij}^+(t^+\!+\!\Delta t^+)\,\Delta t^+\right] u_i^+(t^+) + \mu_i^+(t^+\!+\!\Delta t^+), \qquad (3.15)$$

which is identical in form to Eq. (3.6). From this point on we will drop the superscripts and always refer to Eq. (3.15) rather than Eq. (3.6).

3.1.3 Boundary and Initial Conditions

The boundary condition at the ground must be highly idealized due to the complexity of the physical processes involved. In his monograph on stochastic differential equations and turbulent diffusion, Durbin (1983) discusses three types of boundary conditions at the ground: reflective, absorptive and nonattainable. Reflection is appropriate for most passive tracers such as nonreacting gases for which the ground is simply a barrier; absorption may be appropriate for reactive gases or particles which stick to the ground or vegetation. Nonattainable boundaries arise due to the effect of the boundary on the turbulence rather than on the tracer. According to Durbin, if the eddy diffusivity $K(z) = \sigma_w^2 T_L \to 0$ as $z \to 0$ then the boundary at the ground will be statistically unattainable. In our model both σ_w^2 and $T_L \to 0$ as $z \to 0$; however, this leads

to computational difficulties since $\Delta t/T_L \rightarrow \infty$ near the ground. To avoid this problem we follow DeBaas et al. (1985) and require that both σ_w^2 and T_L remain finite (and constant) in a shallow layer (≤ 0.0025 z/h). In this layer $\Delta t/T_L$ is large enough that the displacements may be considered Markovian. Under these conditions the boundary is indeed attainable and we model it as reflective since our particles are passive tracers. Specifically, if a particle descends a distance Δz below the roughness height z_0 it is placed at $z_0 + \Delta z$ and the sign of its velocity is reversed. The upper boundary is certainly attainable since both σ_w^2 and T_L remain finite. Since we consider the upper boundary to be impenetrable, we model it as reflective also.

The initial condition is modelled as a "finite size" point source. That is, the particles are normally distributed in space with a small but finite deviation about the initial location $(0,0,z_0)$. Their initial velocity distribution is that of the fluid at their initial location. Thus the horizontal distributions are Gaussian and the vertical velocity distribution is skewed according the the fluid moments rather than the moments of the random process μ_i.

3.2 The Discrete Random Processes

3.2.1 The Moment-Generating Function

Thomson (1984) determined the moments of the random forcing function μ by deriving an expression for the moment generating function of the marked fluid (the "particles") in terms of the moment generating function of the unmarked fluid, requiring that the steady-state density function of the marked fluid in $(\mathbf{u}, \mathbf{r})$ space match the density function of the unmarked fluid. He finds that the moment generating function for the marked fluid $\hat{f}(\vartheta_j)$ is given by

$$\hat{f}(\vartheta_j) = 1 + \Delta t\left(\frac{\vartheta_i T_{ij}}{\hat{g}}\right)\left(\frac{\partial \hat{g}}{\partial \vartheta_j}\right) + \left(\frac{\Delta t}{\hat{g}}\right)\left(\frac{\partial^2 \hat{g}}{\partial \vartheta_i \partial x_i}\right) + \mathcal{O}(\Delta t^2), \tag{3.16}$$

where the ^ indicates the moment generating functions defined by

$$\hat{f}(\vartheta_j) = \int \exp(\mu_i \vartheta_i) f(\mu_j)\, d\mu_1\, d\mu_2\, d\mu_3 \tag{3.17}$$

and

$$\hat{g}(\vartheta_j, \mathbf{r}) = \int \exp(u_i \vartheta_i) g(u_j, \mathbf{r})\, du_1\, du_2\, du_3, \tag{3.18}$$

and $f(\mu_i)$ and $g(u_i, \mathbf{r})$ are the probability density functions of the marked and unmarked fluid, respectively. Differentiating Eq. (3.16) with respect to ϑ and evaluating at $\vartheta = 0$ yields to $O(\Delta t)$

$$\langle \mu_j \rangle = \left(\langle u_i \rangle T_{ij} + \frac{\partial \langle u_i u_j \rangle}{\partial x_i} \right), \tag{3.19}$$

where the incompressible continuity equation $\partial u_i / \partial x_i = 0$ has been used to simplify the expression. Assuming horizontal homogeneity $\partial/\partial x_x = \partial/\partial x_y = 0$ and that $\langle u_i \rangle = (U,0,0)$ Eq. (3.19) further reduces to

$$\langle \mu_u \rangle = \left(U T_{11} + \frac{\partial \langle uw \rangle}{\partial z} \right) \Delta t,$$

$$\langle \mu_v \rangle = \left(U T_{12} + \frac{\partial \langle vw \rangle}{\partial z} \right) \Delta t$$

and

$$\langle \mu_w \rangle = \left(U T_{13} + \frac{\partial \langle w^2 \rangle}{\partial z} \right) \Delta t. \tag{3.20}$$

For convenience, these expressions may be split into two parts and the first term containing the mean advection velocity substituted back into Eq. (3.6). The Langevin equations for each component of the particle velocity are thus given by

$$u(t+\Delta t) = u(t)\left(1 - T_{11}\Delta t\right) - v(t)\, T_{12}\Delta t - w(t)\, T_{13}\Delta t + U T_{11}\Delta t,$$

$$v(t+\Delta t) = v(t)\left(1 - T_{22}\Delta t\right) - u(t)\, T_{12}\Delta t - w(t)\, T_{23}\Delta t + U T_{12}\Delta t$$

and

$$w(t+\Delta t) = w(t)\left(1 - T_{33}\Delta t\right) - u(t)\, T_{13}\Delta t - v(t)\, T_{23}\Delta t + U T_{13}\Delta t. \tag{3.21}$$

Upon rearranging these simplify to

$$u(t+\Delta t) = \left(u(t)-U\right)\left(1 - T_{11}\Delta t\right) - v(t)\, T_{12}\Delta t - w(t)\, T_{13}\Delta t + U,$$

$$v(t+\Delta t) = v(t)\left(1 - T_{22}\Delta t\right) - \left(u(t)-U\right) T_{12}\Delta t - w(t)\, T_{23}\Delta t$$

and $$w(t+\Delta t) = w(t)\left(1 - T_{33}\Delta t\right) - \left(u(t)-U\right) T_{13}\Delta t - v(t)\, T_{23}\Delta t. \tag{3.22}$$

These may also be expressed in terms of the exponential correlation as in Eq. (3.13):

$$u(t+\Delta t) = \left(u(t)-U\right) \exp\left(-T_{11}\Delta t\right) - v(t) \exp\left(-T_{12}\Delta t\right) - w(t) \exp\left(-T_{13}\Delta t\right) + U,$$

$$v(t+\Delta t) = v(t) \exp\left(-T_{22}\Delta t\right) - \left(u(t)-U\right) \exp\left(-T_{12}\Delta t\right) - w(t) \exp\left(-T_{23}\Delta t\right)$$

and $$w(t+\Delta t) = w(t) \exp\left(-T_{33}\Delta t\right) - \left(u(t)-U\right) \exp\left(-T_{13}\Delta t\right) - v(t) \exp\left(-T_{23}\Delta t\right), \tag{3.23}$$

where again $U = U(z)$ and $T_{ij} = T_{ij}(z)$. These are the forms used in our simulation. The means of the random process are thus given by

$$\langle \mu_u \rangle = \frac{\partial \langle uw \rangle}{\partial z} \Delta t,$$

$$\langle \mu_v \rangle = \frac{\partial \langle vw \rangle}{\partial z} \Delta t$$

and $$\langle \mu_w \rangle = \frac{\partial \langle w^2 \rangle}{\partial z} \Delta t. \tag{3.24}$$

Taking a second derivative of Eq. (3.16) and evaluating at $\eta = 0$ yields the following expression for the second moment of the random processes:

$$\langle \mu_i \mu_j \rangle = \Big[T_{ik}(\langle u_j u_k \rangle - \langle u_j \rangle \langle u_k \rangle) + T_{jk}(\langle u_i u_k \rangle - \langle u_i \rangle \langle u_k \rangle) + \frac{\partial \langle u_i u_j u_k \rangle}{\partial x_k}$$

$$- \langle u_i \rangle \frac{\partial \langle u_j u_k \rangle}{\partial x_k} - \langle u_j \rangle \frac{\partial \langle u_i u_k \rangle}{\partial x_k} \Big] \Delta t. \tag{3.25}$$

Applying the assumptions regarding horizontal homogeneity and the mean wind to Eq. (3.25) yields

$$\langle \mu_u^2 \rangle = \left(2T_{11}\langle u^2 \rangle + 2T_{12}\langle uv \rangle + 2T_{13}\langle uw \rangle + 2\langle uw \rangle \frac{\partial U}{\partial z} + \frac{\partial \langle u^2 w \rangle}{\partial z} \right) \Delta t,$$

$$\langle \mu_v^2 \rangle = \left(2T_{22}\langle v^2 \rangle + 2T_{12}\langle uv \rangle + 2T_{23}\langle vw \rangle + \frac{\partial \langle v^2 w \rangle}{\partial z} \right) \Delta t,$$

$$\langle \mu_w^2 \rangle = \left(2T_{33}\langle w^2 \rangle + 2T_{13}\langle uw \rangle + 2T_{23}\langle vw \rangle + \frac{\partial \langle w^3 \rangle}{\partial z} \right) \Delta t,$$

$$\langle \mu_u \mu_v \rangle = \left(T_{12}(\langle u^2 \rangle + \langle v^2 \rangle) + (T_{11}+T_{22})\langle uv \rangle + T_{13}\langle vw \rangle + T_{23}\langle uw \rangle + \langle vw \rangle \frac{\partial U}{\partial z} + \frac{\partial \langle uvw \rangle}{\partial z} \right) \Delta t,$$

$$\langle \mu_u \mu_w \rangle = \left(T_{13}(\langle u^2 \rangle + \langle w^2 \rangle) + (T_{11}+T_{33})\langle uw \rangle + T_{12}\langle vw \rangle + T_{23}\langle uv \rangle + \langle w^2 \rangle \frac{\partial U}{\partial z} + \frac{\partial \langle uw^2 \rangle}{\partial z} \right) \Delta t,$$

$$\langle \mu_v \mu_w \rangle = \left(T_{13}(\langle v^2 \rangle + \langle w^2 \rangle) + (T_{22}+T_{33})\langle vw \rangle + T_{12}\langle uw \rangle + T_{13}\langle uv \rangle + \frac{\partial \langle vw^2 \rangle}{\partial z} \right) \Delta t, \qquad (3.26)$$

and here we have used lower case to indicate the fluctuating Eulerian quantities. It is interesting to note that even if the three components of the fluid velocity were *uncorrelated* (i.e., $\langle u_i u_j \rangle = 0$), the marked fluid would still be correlated. For example, assuming homogeneous turbulence

$$\frac{\langle \mu_u \mu_w \rangle}{\left[\langle \mu_u^2 \rangle \langle \mu_w^2 \rangle \right]^{1/2}} = \frac{T_{13}(\sigma_u^2 + \sigma_w^2)}{2\sigma_u \sigma_w \sqrt{T_{11} T_{33}}}. \qquad (3.27)$$

If we extend Thomson's work and differentiate Eq. (3.16) one more time, we obtain the third moments

$$\langle \mu_u^3 \rangle = \left(3T_{11}\langle u^3 \rangle + 3T_{12}\langle u^2 v \rangle + 3T_{13}\langle u^2 w \rangle + 3\langle u^2 w \rangle \frac{\partial U}{\partial z} + \frac{\partial \langle u^3 w \rangle}{\partial z} - 3\langle u^2 \rangle \frac{\partial \langle uw \rangle}{dz} \right) \Delta t,$$

$$\langle \mu_v^3 \rangle = \left(3T_{22}\langle v^3 \rangle + 3T_{12}\langle v^2 u \rangle + 3T_{23}\langle v^2 w \rangle + \frac{\partial \langle v^3 w \rangle}{\partial z} - 3\langle v^2 \rangle \frac{\partial \langle vw \rangle}{dz} \right) \Delta t$$

$$\text{and} \qquad \langle \mu_w^3 \rangle = \left(3T_{33}\langle w^3 \rangle + 3T_{13}\langle uw^2 \rangle + 3T_{23}\langle vw^2 \rangle + \frac{\partial \langle w^4 \rangle}{\partial z} - 3\langle w^2 \rangle \frac{\partial \langle w^2 \rangle}{dz} \right) \Delta t. \qquad (3.28)$$

Thus we have obtained expressions which relate the moments of the random process describing the particles to the Eulerian moments of the turbulent fluid. We could continue this process and obtain expressions for the fourth and higher moments of the random process. However, this is impractical for two reasons. First, it would require information regarding the higher order Eulerian moments of the turbulence. For the planetary boundary layer such data is not available; indeed, we shall have to simplify the expressions for the first three moments of μ_i for lack of a description of some of the second- and third-order Eulerian moments. Even if we had such data available, the construction of a random variable with arbitrary moments is extremely difficult from a computational standpoint. This problem of closure has an analogue in the Eulerian equation of motion: although in principle one can derive an infinite number of differential equations describing the higher turbulent moments, in practice one is forced to "close" the set of equations by postulating a relationship between the higher and lower order moments. The consequences of matching only the first three moments of the random process (and implicitly assuming that higher order moments equal zero) are, according to the theorem of Marcinkiewicz (discussed in §2.2.5), that the resulting probability density function for the particle motion is not everywhere positive-definite; it is at best an approximation to the true density function. That it is a good approximation will be demonstrated. Orszag (1970) discusses the exact counterpart of this problem for Eulerian turbulence closures.

Because of the difficulty, and therefore expense, of collecting data regarding turbulence in the planetary boundary layer, the available information is largely limited to the first three central moments. For this reason, third and fourth order moments of the fluid turbulence will be neglected. Specifically $\langle u_i^2 u_j \rangle = 0$ and $\langle u_i^3 u_j \rangle = 0$. Additionally we will assume the kurtosis $Ku_w \equiv \langle w^4 \rangle / (\langle w^2 \rangle)^2 = 3$, which is supported by the laboratory measurements of Adrian, Ferriera and Boberg (1986). Figure 3.3 presents their data for $\langle w^4 \rangle / w_*^4$ and $3\sigma_w^4$. That there is no discernable difference justifies our assumption. We shall also use $\langle uv \rangle = \langle vw \rangle = 0$, which is generally the case for the bounded, barotropic planetary boundary layer, and $\langle u^3 \rangle = \langle v^3 \rangle = 0$ which is a consequence of horizontal homogeneity. Substituting these back into the above expressions for the moments of the random process yields

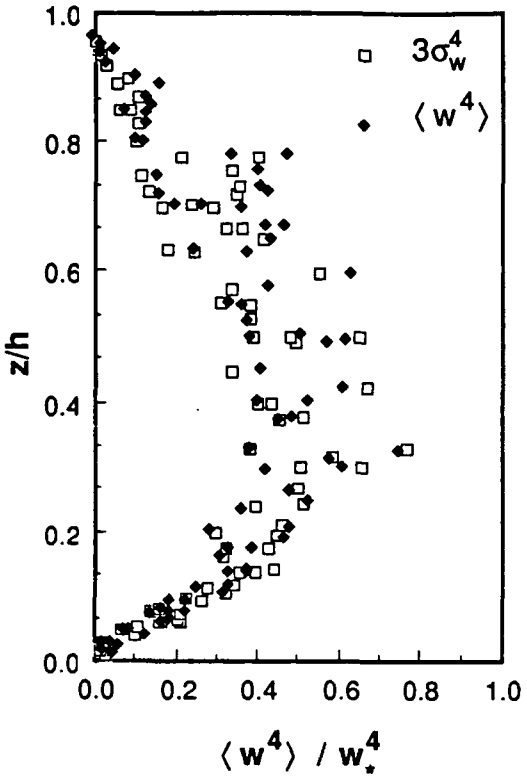

Figure 3.3 A comparison of $\langle w^4 \rangle / w_*^4$ with $3\sigma_w^4 / w_*^4$ from the data of Adrian et al. (1986) to justify the use of $Ku_w = 3$.

$$\langle \mu_u \rangle = \frac{\partial \langle uw \rangle}{\partial z} \Delta t,$$

$$\langle \mu_v \rangle = 0$$

$$\langle \mu_w \rangle = \frac{\partial \langle w^2 \rangle}{\partial z} \Delta t; \qquad (3.29)$$

$$\langle \mu_u^2 \rangle = \left(2T_{11} \langle u^2 \rangle + 2T_{13} \langle uw \rangle + 2 \langle uw \rangle \frac{\partial U}{\partial z} \right) \Delta t,$$

$$\langle \mu_v^2 \rangle = \left(2T_{22} \langle v^2 \rangle \right) \Delta t$$

$$\langle \mu_w^2 \rangle = \left(2T_{33} \langle w^2 \rangle + 2T_{13} \langle uw \rangle + \frac{\partial \langle w^3 \rangle}{\partial z} \right) \Delta t,$$

$$\langle \mu_u \mu_v \rangle = \left(T_{12} (\langle u^2 \rangle + \langle v^2 \rangle) + T_{23} \langle uw \rangle \right) \Delta t,$$

$$\langle \mu_u \mu_w \rangle = \left(T_{13} (\langle u^2 \rangle + \langle w^2 \rangle) + (T_{11} + T_{33}) \langle uw \rangle + \langle w^2 \rangle \frac{\partial U}{\partial z} \right) \Delta t$$

and

$$\langle \mu_v \mu_w \rangle = \left(T_{13} \langle v^2 \rangle + \langle w^2 \rangle \right) + T_{12} \langle uw \rangle) \Delta t; \qquad (3.30)$$

$$\langle \mu_u^3 \rangle = -3 \langle u^2 \rangle \frac{\partial \langle uw \rangle}{\partial z} \Delta t,$$

$$\langle \mu_v^3 \rangle = 0$$

and

$$\langle \mu_w^3 \rangle = \left(3T_{33} \langle w^3 \rangle + 3 \langle w^2 \rangle \frac{\partial \langle w^2 \rangle}{\partial z} \right) \Delta t. \qquad (3.31)$$

Equations (3.29), (3.30) and (3.31) are the forms for the moments of the random process employed in our simulations.

3.2.2 Construction of the Discrete Random Process

We must now use the expressions for the moments $\langle \mu_i^n \rangle$ to construct individual realizations of the discrete random vector μ_i by scaling and shifting (computer generated) random numbers r(t):

$$\mu_i(t) = \langle \mu_i \rangle + \left(\langle \mu_i^2 \rangle \right)^{1/2} r_i(t), \tag{3.32}$$

where $\langle r_i(t)\, r_i(t+\Delta t) \rangle = 0$. Thus

$$\langle \mu_i \rangle = \langle \mu_i \rangle + \left(\langle \mu_i^2 \rangle \right)^{1/2} \langle r_i \rangle \rightarrow \langle r_i \rangle = 0 \tag{3.33}$$

$$\langle \mu_i^2 \rangle = \left(\langle \mu_i \rangle \right)^2 + 2 \langle \mu_i \rangle \left(\langle \mu_i^2 \rangle \right)^{1/2} \langle r_i \rangle + \left(\langle \mu_i^2 \rangle \right) \langle r_i^2 \rangle \rightarrow \langle r_i^2 \rangle = 1, \tag{3.34}$$

(note that $\left(\langle \mu_i \rangle \right)^2 \sim \mathcal{O}(\Delta t^2)$ but we are only including terms to $\mathcal{O}(\Delta t)$ since $\langle dw^2 \rangle = \Delta t$),

and $$\langle \mu_i^3 \rangle = \left(\langle \mu_i \rangle \right)^3 + 3 \left(\langle \mu_i \rangle \right)^2 \left(\langle \mu_i^2 \rangle \right)^{1/2} \langle r_i \rangle + 3 \langle \mu_i \rangle \left(\langle \mu_i^2 \rangle \right) \langle r_i^2 \rangle + \left(\langle \mu_i^2 \rangle \right)^{3/2} \langle r_i^3 \rangle$$

$$\rightarrow \langle r_i^3 \rangle = Sk_i = \langle \mu_i^3 \rangle / \left(\langle \mu_i^2 \rangle \right)^{3/2} \tag{3.35}$$

to $\mathcal{O}(\Delta t^{3/2})$. In order to produce a truly three dimensional simulation however, we must also incorporate the cross-covariance terms $\langle \mu_i \mu_j \rangle$, $(i \neq j)$. To do this we must relate the random numbers $r_i = (r_u, r_v, r_w)$ in the following manner

$$r_u = \alpha_u r_v + \beta_u r_1, \tag{3.36}$$

and

$$r_w = \alpha_w r_u + \beta_w r_v + \gamma_w r_2, \tag{3.37}$$

where r_v is a random number satisfying Eqs. (3.33) - (3.35) for the transverse (y) direction; that is, it has zero mean and skewness and unit variance. The random numbers r_1 and r_2 also have zero mean and unit variance but their skewness must be determined such that Eq. (3.35) is satisfied for r_u and r_w. Because the random numbers are

independent, $\langle r_v\, r_1\rangle = \langle r_v\, r_2\rangle = \langle r_u\, r_2\rangle = 0$. We must now determine α and β. To determine β_u, square and average Eq. (3.36) and recall that the random numbers have unit variance and are independent:

$$\langle r_u^2\rangle = 1 = \alpha_u^2\langle r_v^2\rangle + \beta_u^2\langle r_1^2\rangle + 2\alpha_u^2\beta_u^2\langle r_v\, r_1\rangle \rightarrow \beta_u^2 = 1 - \alpha_u^2. \tag{3.38}$$

Multiplying both sides of Eq. (3.36) by r_v and averaging yields an expression for α_u in terms of $\langle r_u\, r_v\rangle$

$$\langle r_u\, r_v\rangle = \alpha_u\langle r_v^2\rangle + \beta_u\langle r_1\, r_v\rangle \rightarrow \alpha_u = \langle r_u\, r_v\rangle. \tag{3.39}$$

To determine $\langle r_u\, r_v\rangle$ we must substitute Eq. (3.36) into Eq. (3.32) and determine $\langle \mu_u\, \mu_v\rangle$

$$\langle \mu_u\, \mu_v\rangle = \langle \mu_u\rangle\langle \mu_v\rangle + \langle \mu_v\rangle\left(\langle \mu_u^2\rangle\right)^{1/2}\langle r_u\rangle + \langle \mu_u\rangle\left(\langle \mu_v^2\rangle\right)^{1/2}\langle r_v\rangle + \left(\langle \mu_u^2\rangle\right)^{1/2}\left(\langle \mu_v^2\rangle\right)^{1/2}\langle r_u\, r_v\rangle$$

$$= \left(\langle \mu_u^2\rangle\right)^{1/2}\left(\langle \mu_v^2\rangle\right)^{1/2}\langle r_u\, r_v\rangle + O(\Delta t^2). \tag{3.40}$$

We can now solve for $\langle r_u\, r_v\rangle$:

$$\langle r_u\, r_v\rangle = \alpha_u = \frac{\langle \mu_u\mu_v\rangle}{\left(\langle \mu_u^2\rangle\right)^{1/2}\left(\langle \mu_v^2\rangle\right)^{1/2}}. \tag{3.41}$$

Similarly,

$$\langle r_u\, r_w\rangle = \frac{\langle \mu_u\mu_w\rangle}{\left(\langle \mu_u^2\rangle\right)^{1/2}\left(\langle \mu_w^2\rangle\right)^{1/2}} \tag{3.42}$$

and

$$\langle r_v\, r_w\rangle = \frac{\langle \mu_v\mu_w\rangle}{\left(\langle \mu_v^2\rangle\right)^{1/2}\left(\langle \mu_w^2\rangle\right)^{1/2}}. \tag{3.43}$$

To determine $\langle r_1^3\rangle$ we proceed by cubing and averaging Eq. (3.36)

$$\langle r_u^3\rangle = \alpha_u^3\langle r_v^3\rangle + 3\alpha_u^2\beta_u\langle r_v^2 r_1\rangle + 3\alpha_u\beta_u^2\langle r_v r_1^2\rangle + \beta_u^3\langle r_1^3\rangle, \tag{3.44}$$

and because $\langle r_v^2 r_1 \rangle = \langle r_v r_1^2 \rangle = 0$,

$$\langle r_u^3 \rangle = \alpha_u^3 \langle r_v^3 \rangle + \beta_u^3 \langle r_1^3 \rangle; \tag{3.45}$$

thus

$$\langle r_1^3 \rangle = \frac{1}{\beta_u^3}\left[\langle r_u^3 \rangle - \alpha_u^3 \langle r_v^3 \rangle\right] = \frac{1}{\beta_u^3}\left(Sk_u - \alpha_u^3 Sk_v\right). \tag{3.46}$$

If we repeat this procedure with Eq. (3.37) we obtain

$$\alpha_w = \frac{\langle r_u r_w \rangle - \langle r_u r_v \rangle \langle r_v r_w \rangle}{1 - \left(\langle r_u r_v \rangle\right)^2}, \tag{3.47}$$

$$\beta_w = \langle r_v r_w \rangle - \alpha_w \langle r_u r_v \rangle, \tag{3.48}$$

$$\gamma_w^2 = 1 - \alpha_w^2 - \beta_w^2 - 2\alpha_w \beta_w \langle r_u r_v \rangle \tag{3.49}$$

and

$$\langle r_2^3 \rangle = \frac{1}{\gamma_w^3}\left(1 - \alpha_w^3 Sk_u - \beta_w^3 Sk_v\right), \tag{3.50}$$

where we have assumed $\langle r_u^2 r_v \rangle = \langle r_u r_v^2 \rangle$.

To construct the discrete random process we now proceed as follows: 1) generate a random number with first three moments given by Eqs. (3.33-3.35) for the y direction; 2) use Eqs. (3.36), (3.38) and (3.41) to generate a random number for the x direction correlated with the y direction; 3) use Eqs. (3.37) and (3.47-3.50) to generate a random number for the z direction correlated with those for x and y; 4) use these correlated random triples and Eq. (3.32) to generate the components of the random process μ_i. All that now remains is to construct random numbers with zero mean, unit variance and specified skewness.

3.2.3 Generating Skewed Random Variables

We will construct a skewed random variable r by summing two normal random variables $N_1(m_1,\sigma_1)$ and $N_2(m_2,\sigma_2)$ having probability of occurrence p_1 and p_2, means m_1 and m_2 and variances σ_1 and σ_2. The normal random variables are generated from

uniformly distributed random variables† using the method of Box and Muller (DeLaurentis and Boughton, 1988). These normal random variables must satisfy the constraints

$$\int_{-\infty}^{\infty} p(r)\, dr = p_1 + p_2 = 1, \tag{3.51}$$

$$\int_{-\infty}^{\infty} r\, p(r)\, dr = p_1 m_1 + p_2 m_2 = 0, \tag{3.52}$$

$$\int_{-\infty}^{\infty} r^2\, p(r)\, dr = p_1 (m_1^2 + \sigma_1^2) + p_2 (m_2^2 + \sigma_2^2) = 1 \tag{3.53}$$

and

$$\int_{-\infty}^{\infty} r^3\, p(r)\, dr = p_1 (m_1^3 + 3\sigma_1^3) + p_2 (m_2^3 + 3\sigma_2^3) = Sk. \tag{3.54}$$

However, these only provide four equations and we have six unknowns. At this point, van Dop et al. (1986), who sum two non-overlapping uniform distributions, chose the width of each distribution equal to its mean. Thomson (1984) sums two normal distributions and requires $\sigma_1 = \sigma_2$; he also chooses $m_1 = Sk + 1$. Neither of these methods produce a particularly smooth skewed distribution. Therefore we choose $m_1^2 = \sigma_1^2$ and $m_2^2 = \sigma_2^2$, which reduces the number of unknowns to four. Equations (3.51-3.54) then lead to

$$p_2 = 1 - p_1, \tag{3.55}$$

$$p\, m_1 + (1 - p)\, m_2 = 0, \tag{3.56}$$

$$p\, (2m_1^2) + (1 - p)\, (2m_2^2) = 1 \tag{3.57}$$

---

† Actually, these computer-generated numbers are "pseudo-random" because 1) they have a period of 2^{48} and 2) given the same initial "seed" or starting value, they will repeat the exact same sequence. Although this has no practical consequence for our simulation since we will use far fewer than 2^{48} random numbers, it is interesting to note that chaoticians believe turbulence itself may be pseudo-random (Feigenbaum, 1987).

and $$p\,(4m_1^3) + (1-p)\,(4m_2^3) = Sk. \tag{3.58}$$

These are solved to yield

$$p_2 = 1 - p_1 = 1 - p, \tag{3.59}$$

$$p = \frac{m_2}{m_2 - m_1} \tag{3.60}$$

and $$m_{1,2} = \frac{Sk \pm \sqrt{Sk^2+8}}{4}, \tag{3.61}$$

where m_1 is taken to be the sum and m_2 is the difference of the terms in Eq. (3.61).

To construct a random variable with the required statistics, two normal random variables $N_1(m_1,\sigma_1)$ and $N_2(m_2,\sigma_2)$ are generated. If the value of an independent, uniformly distributed random variable is less than p then $N_1(m_1,\sigma_1)$ is selected, otherwise $N_2(m_2,\sigma_2)$ is chosen. Figure 3.4 shows the resulting distribution for Sk = 0, 1/2, 1 and 2 for 10^4 trials.

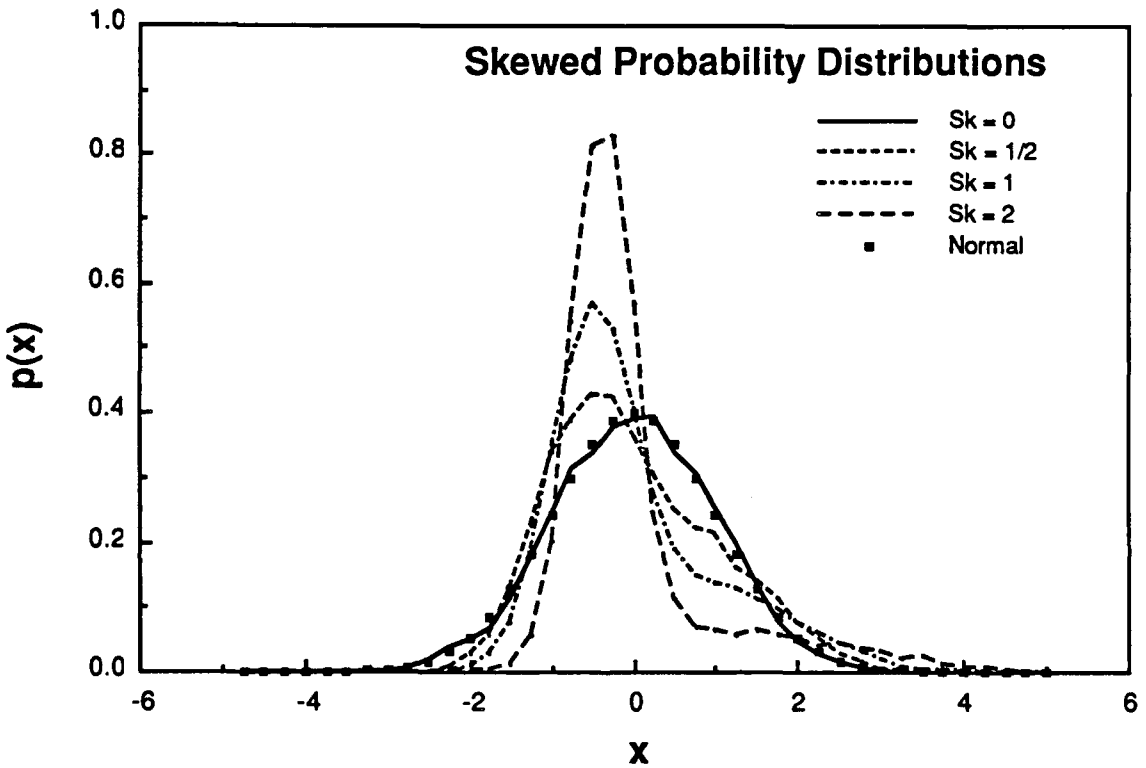

Figure 3.4 Skewed distributions computed from 10^4 trials for different values of Sk. A normal distribution constructed using the Box-Muller algorithm is indicated by Sk = 0. An exact normal distribution is indicated by dots (•).

3.3 Turbulence Description

In order to determine the moments of the stochastic process describing the motion of the particles, we require a formulation for the velocity moments of the atmospheric turbulence. Specifically, we need formulations for $\langle u_i u_j \rangle$ and $\langle u_i^3 \rangle$. Estimates of the time scales, Eq. (3.5), are required by the three-dimensional Langevin equation. Fortunately, a significant body of literature (and data) has been accumulated over the past two decades which deals with the structure of the convective boundary layer.

Much of the data describing the convective planetary boundary layer was gathered during two major field studies known as the Kansas and Minnesota experiments. The Kansas study (Kaimal et al., 1972) was designed to investigate turbulence in the surface layer. All measurements were made from a 32-meter tower. Based on the results of this test, the Minnesota study (Kaimal et al., 1976) was designed to provide measurements covering the entire depth of the boundary layer.

In addition to these experiments, many smaller studies of the convective boundary layer have been conducted using aircraft. The work of Warner and Telford (1963, 1964, 1967) and Lenschow (1970), Lenschow, Wyngaard and Pennell (1980) and Lenschow and Stephens (1980) are important for their focus on the role and description of thermals. The laboratory measurements of Willis and Deardorff (1974), Ferreira (1978) and Adrian, Ferreira and Boberg (1986) provide extremely thorough and detailed data regarding non-penetrative thermal convection which would have been difficult and expensive to attain in the atmosphere.

Many other researchers have analyzed these data to determine formulations for means, variances and occasionally higher moments as well as spectra of velocity, heat and humidity.

3.3.1 Velocity Moments

In neutral (adiabatic) atmospheric conditions, the second central moment or variance of the relatively short wavelength vertical velocity fluctuations can be treated as constant with height. In the convective boundary layer however, the presence of a heat flux at the ground due to solar heating gives rise to thermals. With increasing distance from the ground the damping effect of the boundary declines, allowing longer wavelength disturbances to contribute to the turbulent energy. As a result, the vertical variance increases with height in the convective boundary layer.

Nearly all of the studies described above include measurements of $\sigma_w^2 \equiv \langle w^2 \rangle$. Table 3.1 presents some of the formulations developed in terms of mixed layer scaling (σ_w^2 / w_*^2):

Table 3.1 Formulations for the variance of the vertical velocity fluctuations (σ_w^2 / w_*^2) in a convective boundary layer.

Data Source	Reported by	Formulation
Minnesota	Smith & Blackall (1979)	$0.56\left(1+0.255\left(\frac{z}{h}\right)^{-2/3}\right)^{-1}$
Minnesota, Aircraft & Water Tank	Bærentsen & Berkowicz (1984)	$1.54\left(\frac{z}{h}\right)^{2/3}\exp\left(-2\frac{z}{h}\right)$
Aircraft	Lenschow & Stephens (1980)	$1.8\left(\frac{z}{h}\right)^{2/3}\left(1-0.8\frac{z}{h}\right)^{2}$

In addition to these direct formulations for the vertical variance, Højstrup (1982) developed a spectral model based on the Minnesota data which, when (numerically) integrated over all frequencies, provides an estimate of the variance. These four formulations for the vertical variance are presented graphically in Fig. 3.5 along with relevant data.

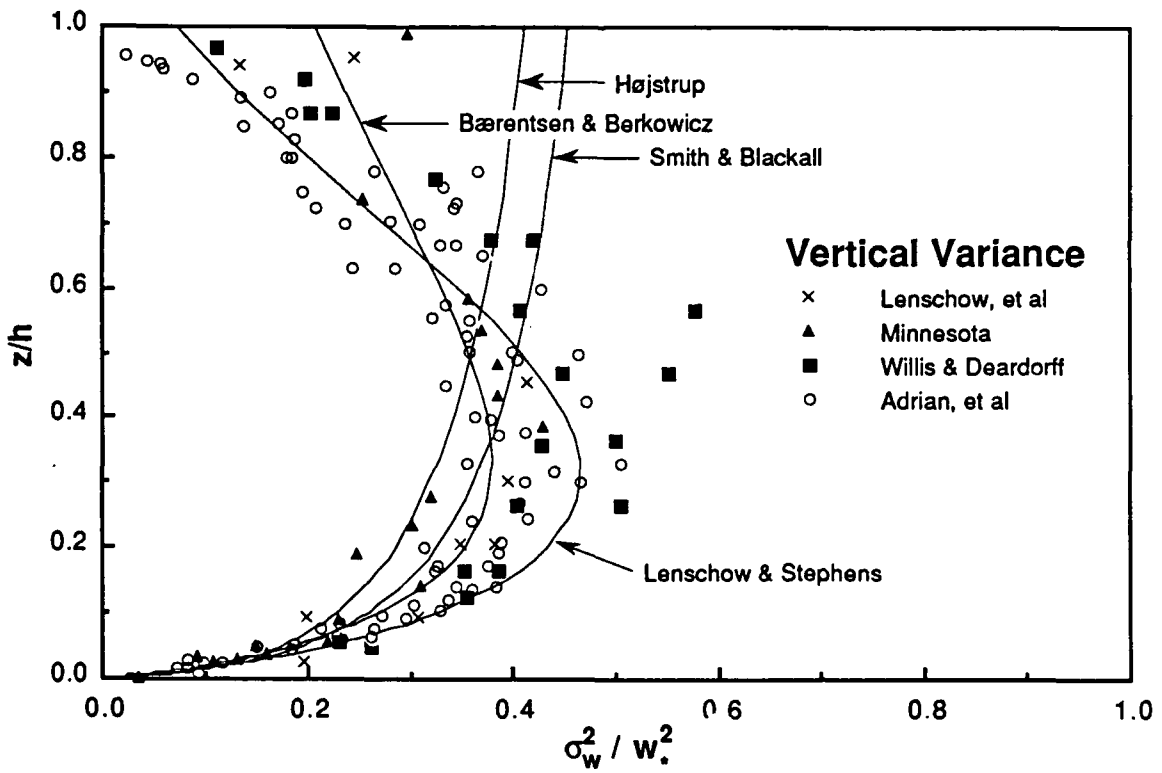

Figure 3.5 Comparison of several formulations for the vertical velocity variance with data.

As the figure clearly shows, the formulations based solely on the Minnesota data are substantially different from those incorporating data from studies which examined the region at the top of the boundary layer in detail. The formulations which provide for a decrease in variance near the top of the boundary layer are supported by data collected in the Ashchurch experiment, reported by Cauhey and Palmer (1979), in which the interfacial layer was specifically investigated. The formulation of Lenschow et al. (1980) demonstrates remarkable agreement with the measurements of Adrian et al. (1986), for unsteady, non-penetrative turbulent thermal convection, and yet over-predicts the atmospheric data. For this reason we will use the formulation due to Bærentsen and Berkowicz (1984).

In addition, the effects of penetration and entrainment through the interfacial layer at the top of the mixed layer can significantly affect the turbulence in the planetary boundary layer (Deardorff, 1973, 1974). The importance of the interfacial region is confirmed and thoroughly investigated by Kumar (1983) and Kumar and Adrian (1986) in their water tank studies. The present investigation, however, is restricted to non-penetrative situations.

The action of the thermals rising relatively quickly to the top of the boundary layer combined with the slow downward subsidence required by continuity cause the vertical velocity fluctuations to be positively skewed. Although there are far fewer measurements of the third moment of the vertical fluctuations available in the open literature, we will employ the following formulation, due to Bærentsen and Berkowicz (1984), based on data obtained by Lenschow et al. (1980), and Willis and Deardorff (1974)

$$\frac{\langle w^3 \rangle}{w_*^3} = 0.8 \frac{(z/h)\,(1 - z/h)}{1 + 0.667\, z/h}, \tag{3.62}$$

which is plotted in Fig. 3.6(a). This may be combined with the formulations for the vertical variance to produce the skewness, $Sk = \langle w^3 \rangle / \sigma_w^3$ shown in Fig. 3.6(b). The third moment formulation compares favorably with the water tank measurements of Adrian, Ferreira and Boberg (1986), although the formulation appears to over-predict slightly above z/h = 0.3. Both have maximum values of about 0.15; the atmospheric data reach this maximum at about z/h = 0.45 and then decline whereas the water tank values are approximately constant over the range $0.25 \leq z/h \leq 0.75$.

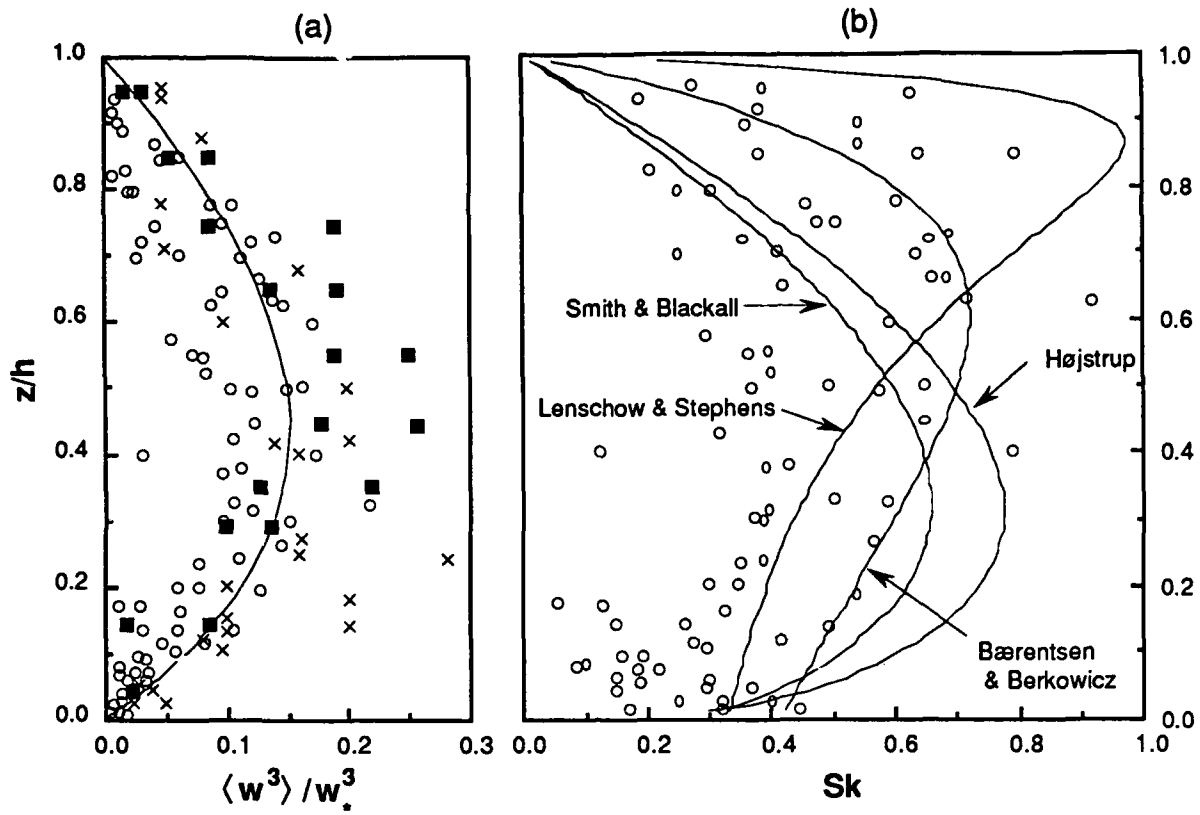

Figure 3.6 (a) The 3rd moment of the vertical velocity; the solid line indicates the formulation given by Bærentsen and Berkowicz (1984); circles (Adrian et al., 1986), squares (Willis & Deardorff, 1974), crosses (Lenschow et al, 1980); (b) the skewness computed using (a) and the formulations for the variance given in Fig. 3.5.

The skewness, however, is a different matter altogether. The variance of Bærentsen and Berkowicz (1984) produces a maximum skewness of 0.7 at z/h = 0.6. However, the measurements of Cauhey, Kitchen and Leighton (1983) made in the convective boundary layer over Cardington, England indicate that the skewness reaches a maximum much lower, at about z/h = 0.42; the probability density functions computed by Lamb (1981) showed similar behavior. Aircraft measurements by Lenschow (1970) also showed that the skewness was greater at z/h = 0.08 than at z/h = 0.8. These results support the skewness formed by using the variance formulations of Smith and Blackall or Højstrup. The measurements of Adrian et al. (1986) show considerable scatter; some of the data appear to support Bærentsen and Berkowicz while some are qualitatively more similar to Smith and Blackall. Perhaps if the third moment formulation declined more quickly above z/h = 0.3, the skewness computed from Lenschow's variance formulation would produce the best agreement with the water tank data.

The skewness formed using Lenschow's expression for the variance reaches a maximum near the top of the mixed layer. The resolvable-scale velocity fluctuations computed with a large eddy simulation of the boundary layer by Deardorff (1974) exhibited similar behavior although the magnitude of the maximum model skewness was about 50% greater. The model skewness also became negative near the ground. Deardorff points out that this behavior reflects the fact that the subgrid contributions to the skewness are not included. He shows that near the top and bottom of the boundary layer, these subgrid contributions are significant and that this would certainly affect the trend and magnitude of the model skewness.

The issue of whether or not the horizontal velocity variances are constant with height has not been fully resolved. Many experiments, including the Minnesota study, show that both σ_u^2 and σ_v^2 are invariant with height. Figure 3.7 presents data from atmospheric and water tank experiments which supports both conclusions.

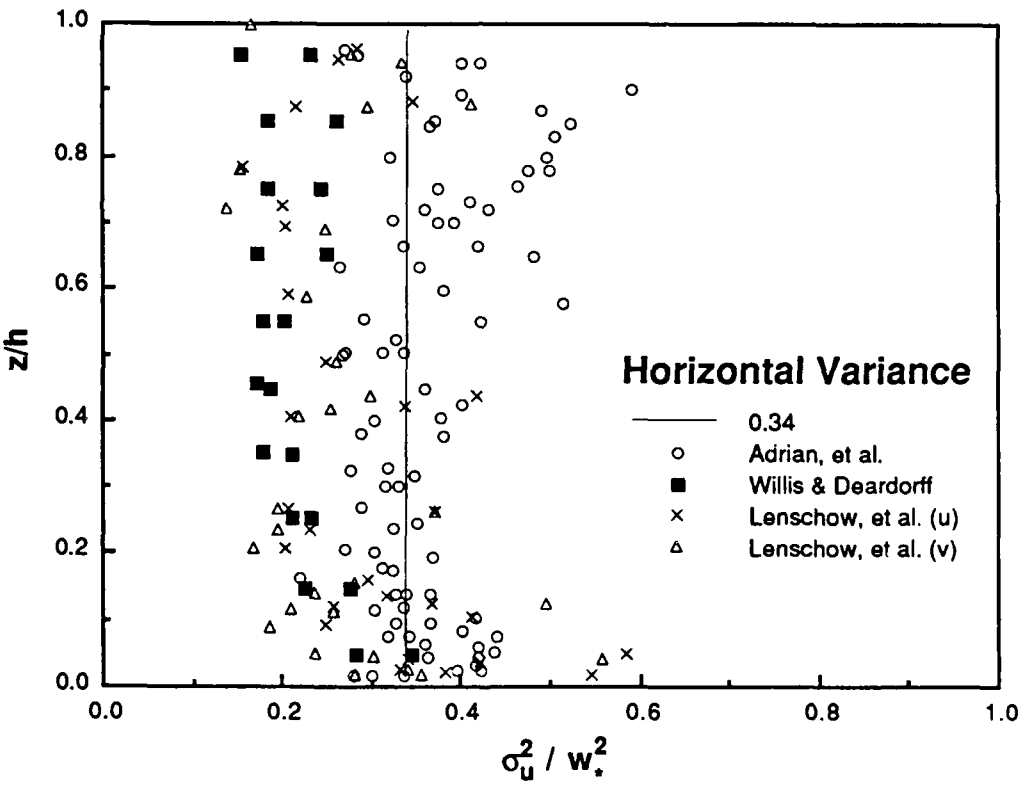

Figure 3.7 Comparison of horizontal variance data from atmospheric and laboratory experiments with the free convection limit of Panofsky's (1977) formulation.

Based on data from the Minnesota experiment and from aircraft measurements, Panofsky et al. (1977) recommend

$$\sigma_{u,v}^2/w_*^2 = \kappa^{2/3}\left(12/\zeta - 0.5\right)^{2/3} \tag{3.63}$$

which yields, for $\kappa = 0.4$ and $\zeta = h/-L \rightarrow \infty$, $\sigma_{u,v}^2/w_*^2 = 0.34$. Integrating Højstuρ's u- and v-spectra leads to $\sigma_u^2/w_*^2 = 0.34$ and $\sigma_v^2/w_*^2 = 0.39$. The water tank data of Willis and Deardorff and Adrian et al. clearly show an increase in the variance near the lower boundary. Lenschow's aircraft data are in good agreement with Adrian *et al.* in the lower half of the boundary layer, whereas Wills and Deardorff's data are about 25% less in magnitude. We will side with simplicity and use Panofsky's formulation; for a near-ground source, this should be sufficient.

Cross-covariances and higher order velocity moments are rarely presented in the literature. Even then, the Minnesota data indicate anomalously large Reynolds stress terms (Kaimal,*et al.*, 1976). Deardorff (1973, 1974) explains similar occurrences in other data and in the predictions of his large eddy simulation of the convective boundary layer in terms of entrainment across the interfacial layer at the top of the boundary layer. We have chosen a simpler approach; given our neglect of entrainment and penetration, and our alignment of the streamwise direction (x-axis) with the direction of the shear stress at the surface such that $\langle u_i \rangle = (U,0,0)$, we model the Reynolds stresses as follows

$$\frac{\langle uw \rangle}{w_*^2} = -\left(1 - \frac{z}{h}\right)\frac{u_*^2}{w_*^2} = -\kappa^{2/3}\left(1 - \frac{z}{h}\right)\left(\frac{h}{-L}\right)^{-2/3} \tag{3.64}$$

and

$$\frac{\langle vw \rangle}{w_*^2} = 0, \tag{3.65}$$

where κ is von Karman's constant. This is similar to the form used by Ley and Thomson (1983) and Brusasca et al. (1987) in their Monte Carlo models of the boundary layer.

3.3.2 Lagrangian Time Scales

The motions of smoke puffs in the atmosphere usually appear to persist longer than the corresponding records of wind behavior gathered from fixed points on a tower indicate. Taylor's "frozen eddy" hypothesis, i.e. the assumption that the spatial pattern of turbulence is virtually unchanged as it is swept along by the mean advection veloc-

ity U, gives the (Eulerian) integral time scale T_E of the fluctuations evident at a fixed point to be L_E/U where L_E is the integral length scale. Based on this hypothesis, particles may be considered to move through the fixed eddy pattern at a speed which may be statistically represented by σ_u the root-mean-square (rms) of the advection velocity fluctuations. As a result, the (Lagrangian) integral time scale of the particle motion should be proportional to L_E/σ_u, and the ratio of the two scales T_L/T_E ($\equiv\beta$) is given by U/σ_u which is the reciprocal of the turbulence intensity I_u.

This argument was first put forward by Gifford (1955) who conducted simultaneous measurements of wind statistics from neutrally buoyant pilot balloons, tethered balloons and aircraft in an effort to investigate the relationship. Gifford found that the Lagrangian and Eulerian spectra were similar in shape but that the Lagrangian spectra were shifted toward lower frequencies as shown in Fig. 3.8. His data also revealed a decrease in β with increasing turbulent intensity. Based on their experiments involving the dispersion of particles released at a height of 150 m, Hay and Pasquill (1957) concluded that the particle motions were indeed correlated for much longer periods than indicated by the Eulerian wind data. In a subsequent paper Hay and Pasquill (1959) proposed that the Lagrangian and Eulerian autocorrelations were related by $R_L(\beta t) = R_E(t)$ which they also showed to be equivalent to the spectral relationship $nS_L(n) = \beta nS_E(\beta n)$ where n is the frequency. Their experiments gave an average value of β=4. Subsequent measurements by Angell (1964), Angell et al., (1970) and Hanna (1981) have led to the widely quoted relation $\beta = 0.68/I$.

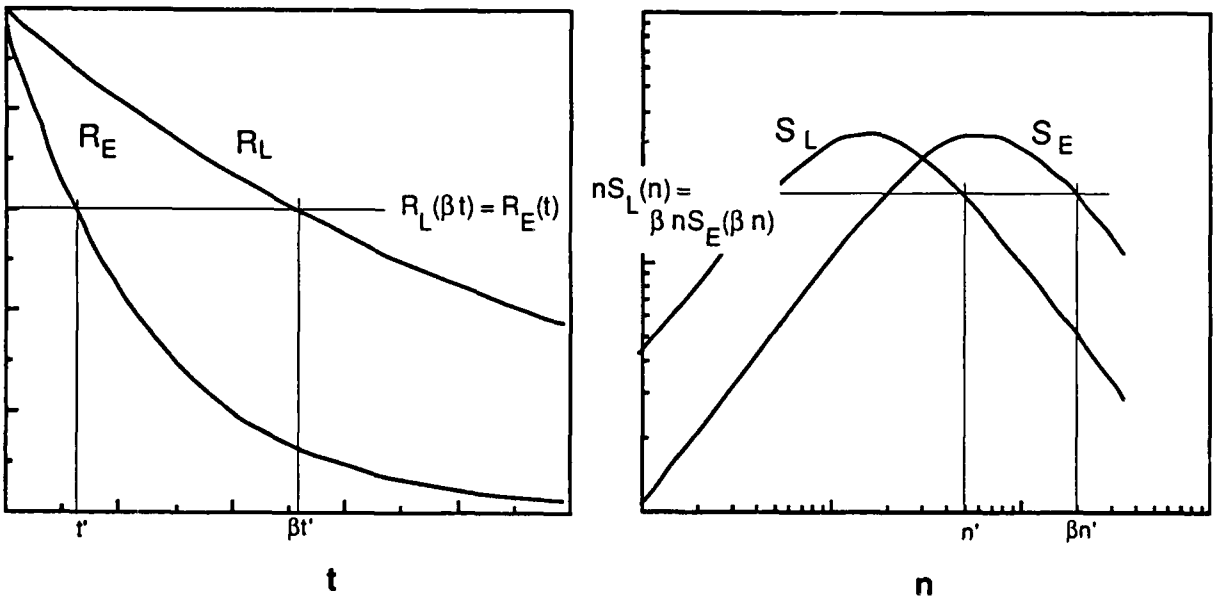

Figure 3.8 Hypothetical relation between Eulerian and Lagrangian correlograms and spectra (Hay and Pasquill, 1959).

Reid (1979) developed an expression for T_L based on similarity arguments. He proposed

$$K = \frac{\kappa u_* z}{\phi_h(0)} = \sigma_w^2 T_L \tag{3.66}$$

where K is the eddy diffusivity of heat, $\phi_h(0)$ is the dimensionless vertical heat flux at the ground and u_* is the friction velocity. Solving this equation with κ=0.41, $\phi_h(0)$ =1 (adiabatic conditions) and σ_w^2 =1.56 u_*^2 gives T_L = 0.26 z/u_*. Hunt and Weber (1979) argue similarly and achieve the same result. This result has been used in Monte Carlo dispersion simulations by Ley (1982), Legg and Raupach (1982), Ley and Thomson (1983) and Legg (1983).

Several other workers have attempted to derive a relation for β by comparing the analytical forms of the Lagrangian and Eulerian spectra. Corrsin (1963) assumed that the spectra could be represented entirely by their inertial subrange forms:

$$S_E(n) = \begin{cases} A u^{2/3} \varepsilon^{2/3} n^{-5/3} & n \geq n_E \\ 0 & n < n_E \end{cases} \tag{3.67}$$

$$S_L(n) = \begin{cases} B \varepsilon n^{-2} & n \geq n_L \\ 0 & n < n_L. \end{cases} \tag{3.68}$$

Integration of these two expressions yields σ_E and σ_L, which are assumed equal. Eliminating ε gives

$$\frac{n_E}{n_L} = \left(\frac{3}{2}\right)^{3/2} \frac{A^{3/2}}{B} \frac{1}{I}, \tag{3.69}$$

where $n_E \propto 1/T_E$ and $n_L \propto 1/T_L$. Pasquill used more realistic spectral forms and derived

$$\frac{T_L}{T_E} = 2.76 \frac{A^{3/2}}{B} \frac{1}{I} = \frac{C}{I}. \tag{3.70}$$

Using Angell's (1964) data, Pasquill and Smith (1983) compute values of 0.4 and 0.6 for C in Eqs. (3.69) and (3.70). Reid (1979) attempted to compute T_L using an empiri-

cal representation of the neutral spectrum determined by Kaimal (1976). He used the relation

$$T_L = \beta T_E = \beta \int_0^\infty R_E(t)\, dt = \frac{\beta \int_0^\infty \int_0^\infty S_E(n)\, e^{2\pi n t}\, dn\, dt}{\int_0^\infty S_E(n)\, dn} \tag{3.71}$$

and computed $T_L = 2.15\ \beta\ z/U$. This result is in error by a factor of 2π which Reid failed to account for in transforming from frequency to wavenumber space. When this factor is included the result is $T_L = 0.34\ \beta\ z/U$.

Alternatively, if one assumes an exponential autocorrelation, then $T_E = 1/(2\pi n_E)$ where n_E is the frequency at which the logarithmic spectrum $nS_E(n)$ is maximum. Differentiating Kaimal's expression for the neutral w-spectrum (which is the same form as Højstrup (1982) for neutral conditions) to find the maximum gives $n_E = 2.13\ z/U$ or $T_L = 0.34\ \beta\ z/U$ which agrees with Reid's corrected results. Using $\beta = 0.68/I$ and noting that $\sigma_w^2 = \int S_E\ (n)\ dn = 1.46\ u_*^2$ leads to $T_L = 0.19\ z/u_*$, which is close to the similarity-based result.

Yet another approach was initiated by Corrsin (1959) who suggested that in the limit of large travel times

$$\sigma_w^2\, R_L(\xi) = \langle w(z,t)\, w(z+\Delta z, t+\xi)\rangle = \int_{-\infty}^{\infty} R_E(\chi,\xi)\, p(\chi)\, d\chi, \tag{3.72}$$

where

$$R_E(\chi,\xi) = \langle w(z,t)\, w(z+\chi, t+\xi)\rangle \tag{3.73}$$

and $p(\chi)$ is the probability that $\Delta z = \chi$ Given forms for $p(\chi)$ and $R_E(\chi,\xi)$, β could be determined. Saffman (1963) and Philip (1967) assume $p(\chi)$ is normally distributed and derive $\beta = 0.8/I$ and $\beta = 0.35/I$ for their respective forms of $R_E(\chi,\xi)$. Lee and Stone (1983) use this idea to define an Eulerian autocorrelation R_C for a reference frame moving with the mean advection velocity U. For the lateral component

$$R_L(\Delta t) = \frac{\langle v^2\, R_C(\Delta y = v\Delta t, \Delta t)\rangle}{\langle v^2\rangle}. \tag{3.74}$$

Assuming the displacements are normally distributed and further assuming $R_C = (e^{-\Delta y/L_E})(e^{-\Delta t/T_E})$ yields

$$\beta = \left[1 - \left(\frac{U\,T_E}{L_E}\right)\left(1 - \sqrt{\frac{8}{\pi}\,I}\right)\right]^{-1}. \tag{3.75}$$

Letting $L_E = UT_E$ gives $\beta = 0.63/I$. Lee and Stone further point out that $L_E/(UT_E) = 1 + I/\alpha$, where $\alpha \equiv \sigma_v T_E/L_E \approx 1$, implies that the frozen field approximation $L_E \approx UT_E$ is only valid for $I \ll 1$.

The Lagrangian integral time scale may also be estimated from diffusion data. Hay and Pasquill (1959) first attempted this by using a spectral interpretation of Taylor's (1921) theory

$$\sigma_y^2 = \sigma_v^2 t^2 \int_0^\infty F_L(n) \left(\frac{\sin(\pi nt)}{\pi nt}\right)^2 dn, \tag{3.76}$$

where $F_L(n) = S_L(n)/\sigma^2$. Hay and Pasquill substituted the Eulerian spectrum, obtaining

$$\sigma_y^2 = \sigma_v^2 t^2 \int_0^\infty \beta F_E(\beta n) \left(\frac{\sin(\pi nt)}{\pi nt}\right)^2 dn \tag{3.77}$$

or

$$\sigma_y^2 = \sigma_v^2 t^2 \int_0^\infty F_E(n) \left(\frac{\sin(\pi nt/\beta)}{\pi nt/\beta}\right)^2 dn, \tag{3.78}$$

which is valid for travel times t that are greater then the period of release. Pasquill and Smith (1983) point out that assuming similar shapes for the Eulerian and Lagrangian spectra, even when they are not similar, does not introduce significant error; of greater importance is the integral scale T_L. Pasquill and Smith argue that using a value of β' when the true value is β introduces an error in σ_y proportional to $(\beta'/\beta)^n$ where n varies from zero for travel times $t \ll T_L$ to 0.5 for $t \gg T_L$. Hay and Pasquill reported an average value of $\beta = 4$ which has been widely quoted. In his analysis of dispersion data from Project Prairie Grass, Haugen (1959, 1966) reported values of β in the range 3-5. Smith (1968) suggested a method for determining T_L based on conditioned particle motion. Considering only particles with a given initial cross-stream velocity v(0), Smith showed that

$$\sigma_y^2 = 2\,\sigma_v^2 \frac{t^3}{3} T_L \tag{3.79}$$

providing a more direct method of determining T_L if conditioned particle release could be effected.

We will combine the relationship $T_E = 1/(2\pi n_{max})$ with the definition of wavelength $\lambda = U/n$ to give

$$T_L = \beta \frac{\lambda_m}{2\pi U} \tag{3.80}$$

or, with $\beta = 0.68/I$

$$T_L = \frac{0.68\,\lambda_m}{2\pi\,\sigma}, \tag{3.81}$$

where λ_m is the peak wavelength corresponding to the peak frequency n_{max}. We can now take advantage of extensive measurements of λ_m in the convective boundary layer. Kaimal et al. (1976) present the data collected from the Minnesota boundary layer experiment. They find that λ_m is well represented by

$$\lambda_{m,u} = \lambda_{m,v} \approx 1.5\ h, \tag{3.82}$$

$$\lambda_{m,w} = \begin{cases} z/(0.55 - 0.38\ z/|L|) & 0 \le z \le |L| \\ 5.9z & |L| \le z \le 0.1h \\ 1.5h[1 - \exp(-5z/h)] & 0.1h \le z \le h. \end{cases} \tag{3.83}$$

Cauhey and Palmer (1979) supplement the Minnesota data with measurements taken near the top of convective boundary layer during the Ashchurch study. These data indicate that $\lambda_{m,w}$ declines near the inversion height. Cauhey and Palmer offer the following representation of the data

$$\lambda_{m,u} = \lambda_{m,v} = 1.3\ h, \tag{3.84}$$

$$\lambda_{m,w} = \begin{cases} 6z/(3 - 2\ z/|L|) & 0 \le z \le |L| \\ 5.9z & |L| \le z \le 0.1h \\ 1.8h[1 - \exp(-4z/h) - 0.0003\exp(8z/h)] & 0.1h \le z \le h. \end{cases} \tag{3.85}$$

If exponential velocity autocorrelations are assumed, then we may determine λ_m from Højstrup's spectral model for the convective boundary layer. For the horizontal components this produces $\lambda_{m,u} = 1.26$ h and $\lambda_{m,v} = 1.33$ h, in agreement with Cauhey and Palmer.

A comparison of $T_{L,w}/(h/w_*)$ computed using Eq. (3.81) with either Kaimal's expression for $\lambda_{m,w}$ Eq. (3.83) or Cauhey and Palmer's expression Eq. (3.85) and the variance given by the formulations listed in Table 3.1 is presented in Fig. 3.9. The value of T_L for the horizontal components is also given for $\lambda_{m,u} = 1.3$ h and $\lambda_{m,u} = 1.5$ h.

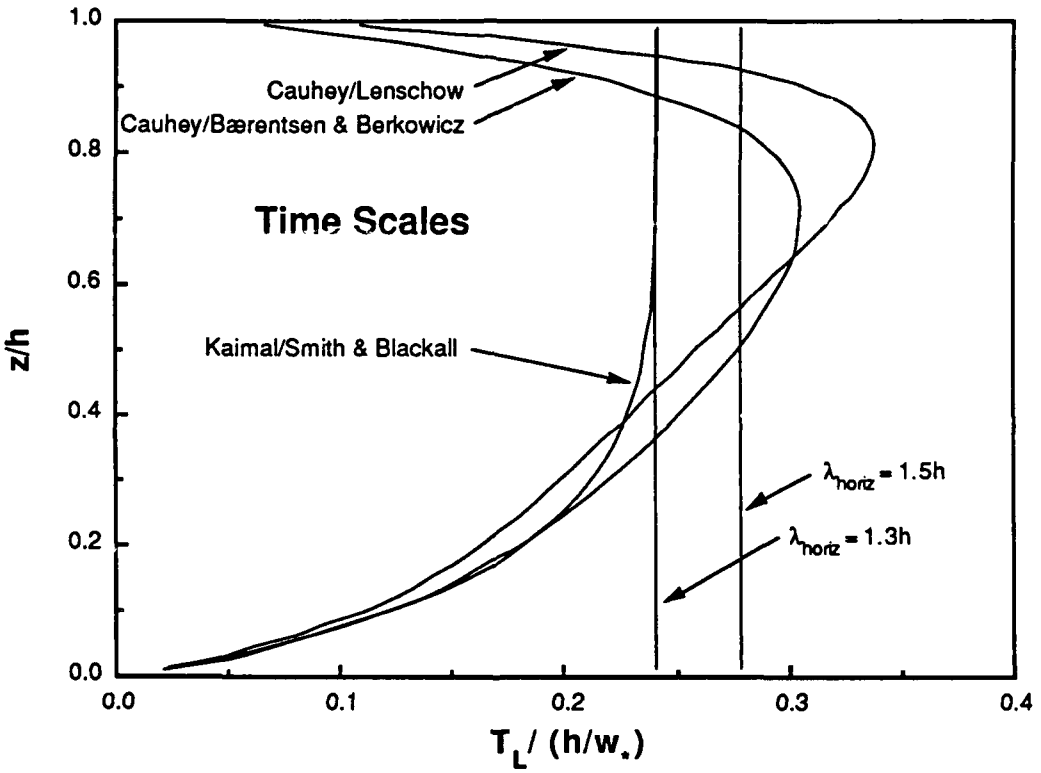

Figure 3.9 Comparison of Lagrangian time constants computed from various estimates of the peak wavelength and velocity variance according to Eq. (3.81).

The difference between the Kaimal/Smith & Blackall formulation (hereinafter KS) for which neither λ_m nor σ_w decline near the top of the boundary layer and those of Cauhey and either Lenschow (hereinafter CL) or Bærentsen & Berkowicz (hereinafter CB) for which both λ_m and σ_w decline near the top is apparent. It may well have been expected that since both λ_m and σ_w decline in CL and CB that $T_{L,w}$ would remain constant, or nearly so. However, in both cases λ_m declines faster than σ_w so that $T_{L,w}$ declines also. The most curious aspect of these results is that the maximum value of $T_{L,w}/(h/w_*)$ does not approach unity, reaching only a value of 0.24 to 0.34.

We must now obtain estimates for $T_{L,ij}$ for which $i \neq j$. Since we do not have estimates of λ_m for $\langle u_i u_j \rangle$, we must proceed in a different fashion than just discussed above. If we suppose that components whose energy-containing ranges are widely separated in frequency or wavenumber are independent and that components whose energy-containing ranges are close together interact, then we arrive at the following expression for T_{ij} ($= 1/T_{L,ij}$)

$$T_{ij} = \frac{1}{2}(T_{ii} - T_{jj}). \tag{3.86}$$

This is the formula for the envelope or "beat" frequency of two superimposed waves (Young 1976; page 161). Note that since the horizontal components have identical variances and peak wavelengths, $T_{12} \equiv T_{L,uv} = 0$.

3.3.3 The Mean Wind Profile

In the surface layer, the appropriate non-dimensional length and velocity scales are the roughness length z_0 and the friction velocity, defined according to $u_*^2 = \frac{\tau}{\rho} = -\langle uw \rangle$, τ is the shear stress at the surface. Thus we may scale the mean velocity near the surface as

$$U/u_* = f_x(z/z_0) \tag{3.87}$$

and

$$V/u_* = 0, \tag{3.88}$$

where f_x is a universal function. (The lateral component is zero because we have aligned the x-axis with the direction of the shear stress at the surface.) In order to arrive at an expression for the wind speed which is valid at large values of z/z_0, we must asymptotically match Eqs. (3.87) and (3.88) with expressions of the form

$$\frac{U - U_G}{u_*} = F_x(zf/u_*) \tag{3.89}$$

and

$$\frac{V - V_G}{u_*} = F_y(zf/u_*), \tag{3.90}$$

where F_x and F_y are universal functions, f is the Coriolis parameter and the subscript G denotes components of the geostrophic wind (i.e., the free stream velocity above the

boundary layer) caused by the earth's rotation. In the double limit as $z/z_0 \rightarrow \infty$ while $zf/u_* \rightarrow 0$ this process yields (Tennekes, 1984; page 43)

$$\frac{\kappa z}{u_*}\frac{\partial U}{\partial z} = 1, \tag{3.91}$$

where κ is the von Karman constant. Integrating Eq. (3.91) leads to the well known logarithmic wind profile for adiabatic conditions

$$\frac{U}{u_*} = \frac{1}{\kappa}\ln\left(\frac{z}{z_0}\right), \tag{3.92}$$

which is valid for $z/h << 1$ and $z/z_0 >> 1$.

In order to extend this to the actual planetary boundary layer, the effects of a heat-flux at the earth's surface must be accounted for. In such diabatic situations, the relevant length scale in the surface layer is the Monin-Obukhov length L. Thus the dimensionless wind shear Eq. (3.91) becomes

$$\frac{\kappa z}{u_*}\frac{\partial U}{\partial z} = \phi_m\left(\frac{z}{L}\right) \tag{3.93}$$

where, for consistency, $\phi_m(0) = 1$. Expressions for ϕ_m have to be determined empirically. Many forms have been proposed (Dyer and Hicks, (1970); Businger et al., (1971); Hansen, 1980; Dyer and Bradley, 1982); most use

$$\phi_m(\zeta) = \left(1 - b\left(\frac{z}{L}\right)\right)^{-1/4} \tag{3.94}$$

and offer different values for b and the von Karman constant κ. Thorough reviews are provided by Monin and Yaglom (1971) and Dyer (1974). In the present investigation we will use $b = 16$, $\kappa = 0.41$ as suggested by Dyer and Hicks (1970).

Integrating Eq. (3.93) leads to the diabatic mean wind profile

$$\frac{U}{u_*} = \frac{1}{\kappa}\left(\ln\left(\frac{z}{z_0}\right) - \Psi_m\left(\frac{z}{L}\right)\right), \tag{3.95}$$

where Ψ_m is given for unstable ($L < 0$) conditions by Paulson (1970) as

$$\Psi_m = 2\ln\left(\frac{1+x}{2}\right) + \ln\left(\frac{1+x^2}{2}\right) - 2\tan^{-1}x + \frac{\pi}{2}, \tag{3.96}$$

and $x = \phi_m^{-1}$. In order to use this formulation we will transform it to mixed layer scaling. Dividing by $w_*/u_* = (\zeta/\kappa)^{1/3}$ Eq. (3.95) becomes

$$\frac{U}{w_*} = \frac{1}{\zeta^{1/3}\kappa^{2/3}}\left(\ln\left(\frac{z}{z_0}\right) - \Psi_m\left(\frac{z}{L}\right)\right), \tag{3.97}$$

where $\zeta = h/-L$.

3.4 Interpreting Simulation Results

3.4.1 Estimating Mean Concentrations

The most general quantity which the stochastic model can predict is the mean concentration field. The mean concentration can be determined from an estimate of the transition probability $P(\mathbf{r}, t \mid \mathbf{r}', t')$:

$$C(\mathbf{r},t) = \int_{-\infty}^{\infty}\int_{0}^{t} P(\mathbf{r}, t \mid \mathbf{r}', t')\, S(\mathbf{r}', t')\, dt'\, d\mathbf{r}', \tag{3.98}$$

where $\mathbf{r} = (x,y,z)$ is the position vector of the "receptor" (the point at which the concentration prediction is desired) and S is the source distribution function. For a continuous point source $S(\mathbf{r}, t) = Q(t)\, \delta(\mathbf{r} - \mathbf{r}_0)$ Eq. (3.98) becomes

$$C(\mathbf{r},t) = \int_{0}^{t} P(\mathbf{r}, t \mid \mathbf{r}_0, t')\, Q(t')\, dt'. \tag{3.99}$$

Computationally, this is obtained using the discrete form for Eq. (3.99)

$$C(\mathbf{r},t) = \sum_{m=0}^{M} P(\mathbf{r}, M\Delta t \mid \mathbf{r}_0, m\Delta t)\, Q(m\Delta t)\, \Delta t. \tag{3.100}$$

Thus the concentration is obtained by summing over the contributions of M discrete "puffs" released at intervals Δt. If it is further assumed that each puff contains the same amount of material such that $Q\Delta t$ = constant and that the time-averaged wind speed and direction are stationary (constant) for the period $t = M\Delta t$, then $P(\mathbf{r}, M\Delta t \mid \mathbf{r}_0, m\Delta t) = P(\mathbf{r}, (M-m)\Delta t \mid \mathbf{r}_0, 0)$ and Eq. (3.100) becomes

$$C(\mathbf{r},t) = Q\sum_{m=0}^{M} P(\mathbf{r}, (M-m)\Delta t \mid \mathbf{r}_0, 0)\,\Delta t$$

$$= Q\sum_{m=0}^{M} P(\mathbf{r}, m\Delta t \mid \mathbf{r}_0, 0)\,\Delta t. \qquad (3.101)$$

This is now equivalent to summing up the contributions of just one puff over the period $0 \le t \le M\Delta t$. This greatly simplifies the computational effort required to determine the mean concentration since all that is now required is to compute the transition probability density for an instantaneous point source (i.e., a single "puff"). To accomplish this the computational domain is divided into sampling volumes $\Delta\mathbf{r} = \Delta x\Delta y\Delta z$ centered at $\mathbf{r} = (x, y, z)$. The number of particles $n(\mathbf{r}, m\Delta t)$ located in each volume at each time step m are counted. The transition probability is thus

$$P(\mathbf{r}, m\Delta t \mid \mathbf{r}_0, 0) = \frac{n(\mathbf{r},m\Delta t)}{N\,\Delta\mathbf{r}}, \qquad (3.102)$$

where N is the total number of particles in the "puff". The mean concentration is obtained by substituting Eq. (3.102) into Eq. (3.101)

$$C(\mathbf{r}, t=M\Delta t) = \frac{N}{\Delta t}\sum_{m=0}^{M}\frac{n(\mathbf{r},m\Delta t)}{N\,\Delta\mathbf{r}}\Delta t$$

$$= \sum_{m=0}^{M}\frac{n(\mathbf{r},m\Delta t)}{\Delta\mathbf{r}} = \frac{n_M(\mathbf{r})}{\Delta\mathbf{r}}, \qquad (3.103)$$

where $Q = N/\Delta t$. To verify that Eq. (3.102) is in fact a probability density function, integrate over all space

$$\int_{-\infty}^{\infty} C(\mathbf{r}, t' \mid \mathbf{r}_0, 0)\,d\mathbf{r} = Q\int_{-\infty}^{\infty} P(\mathbf{r}, t' \mid \mathbf{r}_0, 0)\,d\mathbf{r} = Q \qquad (3.104)$$

to recover the release rate Q and also integrate over time

$$\int_{-\infty}^{\infty} C(\mathbf{r}, t)\,d\mathbf{r} = Q\int_{0}^{t}\int_{-\infty}^{\infty} P(\mathbf{r}, t' \mid \mathbf{r}_0, 0)\,d\mathbf{r}\,dt' = Qt \qquad (3.105)$$

to determine the total amount released. Thus, using Eq. (3.102)

$$\frac{N}{\Delta t}\sum_{r}\frac{n(r,m\Delta t)}{N\,\Delta r}\,\Delta r = \frac{N}{\Delta t} = Q \tag{3.106}$$

and

$$\frac{N}{\Delta t}\sum_{m=0}^{M}\sum_{r}\frac{n(r,m\Delta t)}{N\,\Delta r}\,\Delta r\,\Delta t = \frac{N}{\Delta t}\,M\Delta t = Qt, \tag{3.107}$$

which provides the verification and also shows that mass is conserved. This will be scaled by $Q/(h^2U)$ which is the concentration that would result from a uniform distribution of particles. Thus

$$C^+(r,t) = \frac{C(r,t)}{Q/h^2U} = \frac{n_M(r)}{\Delta r}\frac{\Delta t}{N}h^2U$$

$$= \frac{n_M(r)}{N}\frac{h^3}{\Delta r}\frac{\Delta t}{h/w_*}\frac{U}{w_*}$$

$$= \frac{n_M(r)}{N}\frac{U^+\Delta t^+}{\Delta r^+}. \tag{3.108}$$

Using the method just described to estimate the concentration near the surface is problematic since the vertical coordinate of the centroid of the sampling volume Δr is located a distance $\Delta z/2$ from the surface. To measure concentrations very near the surface requires a very small sampling volume. This leads to either an unacceptably large sampling error (because only a few particles are to be found in any given sampling volume at a given time) or an impossibly large number of particles. In order to avoid these problems and to accurately estimate the surface concentrations, which are of primary interest in terms of pollutant dispersion in the atmosphere, we shall employ a kernal density estimation technique. Lorimer (1986) presents an introduction to the method of kernal density estimation. In an analogy to Eq. (3.102), the transition probability is estimated using

$$P(r, t \mid r_0, 0) = \frac{1}{N\sigma_N^3}\sum_{i=1}^{N} f\left(\frac{r_i - r}{\sigma_N}\right), \tag{3.109}$$

where σ_N is a time-dependent resolution bandwidth (analogous to the grid spacing), f is a smoothing kernal whose integral over the domain is unity and r_i is the position of

the i^{th} particle at time t. Boughton, DeLaurentis and Dunn (1987) employ such an estimator in their one-dimensional Monte Carlo model. They use a Gaussian kernal such that

$$P(z, t \mid z_0, 0) = \frac{1}{N\sqrt{2\pi}\,\sigma_N\,\phi(z/\sigma_N)} \sum_{i=1}^{N} \exp\left[-\frac{(Z_i - z)^2}{2\sigma_N^2}\right], \tag{3.110}$$

where σ_N is the resolution bandwidth computed from the instantaneous vertical spread of the particles about their centroid

$$\sigma_N = \frac{\sigma_z(t)}{N^{1/5}}, \tag{3.111}$$

$\phi(x)$ is the standard Gaussian distribution (i.e., $\phi(-\infty) = 0$, $\phi(0) = 0.5$ and $\phi(\infty) = 1$), and Z_i is the vertical location of the i^{th} particle. Because of the presence of the boundary at the surface, ϕ is required to ensure that the integral of the estimator over the domain is unity. Thus at ground level Eq. (3.110) becomes

$$P(0, t \mid z_0, 0) = \frac{1}{N\sqrt{2\pi}\,\sigma_N\,0.5} \sum_{i=1}^{N} \exp\left[-\frac{(Z_i)^2}{2\sigma_N^2}\right]. \tag{3.112}$$

In three dimensions Eq. (3.110) is given by

$$P(\mathbf{r}, t \mid \mathbf{r}_0, 0) = \frac{1}{N\,(2\pi)^{3/2}\,\sigma_{Nx}\,\sigma_{Ny}\,\sigma_{Nz}\,\phi(z/\sigma_N)}$$

$$X \sum_{i=1}^{N} \exp\left[-\frac{1}{2}\left\{\left(\frac{X_i - x}{\sigma_{Nx}}\right)^2 + \left(\frac{Y_i - y}{\sigma_{Ny}}\right)^2 + \left(\frac{Z_i - z}{\sigma_{Nz}}\right)^2\right\}\right] \tag{3.113}$$

with

$$\sigma_{Nx} = \frac{\sigma_x(t)}{N^{1/5}}, \quad \sigma_{Ny} = \frac{\sigma_y(t)}{N^{1/5}} \text{ and } \sigma_{Nz} = \frac{\sigma_z(t)}{N^{1/5}}. \tag{3.114}$$

In addition to providing improved concentration estimates near boundaries, the kernal method may require fewer particles in the simulation since it allows the contribution of each particle to the concentration at each receptor location to be computed. For simulations in which the turbulence is treated as Gaussian, this is an advantage;

however, for simulations such as ours in which the probability density of the turbulent velocity fluctuations is not Gaussian, this is not advantageous. In order for the extremes of our skewed velocity density function to be correctly realized, a large number of particles must be utilized. With a large number of particles and a large number of receptors, the computational requirements of the kernal method make it unfeasible. For this reason we shall only employ it near ground level.

3.4.2 Mean Statistics

In addition to the mean concentration field, other descriptive statistics are useful for comparison with data and with the results of other models. These include the position of the centroid of the cloud and the vertical and horizontal spread of the cloud as a function of travel time. The position of the centroid of the cloud at time $t = m\Delta t$ is given by

$$\langle \mathbf{r}(t) \rangle = (\langle X(t) \rangle, \langle Y(t) \rangle, \langle Z(t) \rangle) = \frac{1}{Q} \int_{-\infty}^{\infty} \mathbf{r}\, C(\mathbf{r}, t)\, d\mathbf{r}, \tag{3.115}$$

and in discrete form

$$\langle \mathbf{r}(t) \rangle = \sum_{\mathbf{r}} \mathbf{r}\, \frac{n(\mathbf{r}, m\Delta t)}{N\, \Delta \mathbf{r}}\, \Delta \mathbf{r}. \tag{3.116}$$

In the limit $N \rightarrow \infty$, this is equivalent to averaging over all the particles in the puff:

$$\langle \mathbf{r}(t) \rangle = \sum_{i=1}^{N} \mathbf{r}_i(t), \tag{3.117}$$

where $\mathbf{r}_i(t) = (X_i(t), Y_i(t), Z_i(t))$ is the position of the i^{th} particle at time $t = m\Delta t$. The horizontal and vertical spread are defined as

$$\sigma_Y^2(t) = \frac{1}{Q} \int_{-\infty}^{\infty} (y - y_0)^2\, C(\mathbf{r}, t)\, d\mathbf{r} \tag{3.118}$$

and

$$\sigma_Z^2(t) = \frac{1}{Q} \int_{-\infty}^{\infty} (z - z_0)^2\, C(\mathbf{r}, t)\, d\mathbf{r}; \tag{3.119}$$

or, for the puff

$$\sigma_Y^2(t) = \sum_{i=1}^{N} (Y_i(t)-y_0)^2 \tag{3.120}$$

and

$$\sigma_Z^2(t) = \sum_{i=1}^{N} (Z_i(t)-z_0)^2. \tag{3.121}$$

In the next section we will use these statistics to compare the results of our simulation with theoretical and experimental results.

4. MODEL VERIFICATION

In order to demonstrate that our model is able to correctly predict turbulent dispersion, simulation results will be compared with theoretical limits, experimental data gathered from both laboratory and atmospheric studies and with the results of other Monte Carlo models.

4.1 Theoretical Limits

The Taylor-series expansions, for $t/T_L << 1$, describing the rate of increase of the mean height and spread of the particles derived for a shear flow in an infinite boundary layer are given by Hunt (1984b, page 240). Integrating these leads to the following expressions for the mean height and spread

$$\langle Z-z_0 \rangle = \frac{-\overline{uw}}{U_0} t - \frac{t^2}{U_0}\left(\overline{w^2}\,\frac{dU}{dz} - U_0 \frac{d\,\overline{w^2}}{dz}\right) + O(t^3) \qquad (4.1)$$

and

$$\langle (Z-z_0)^2 \rangle = \sigma_w^2 t^2 + \left(\frac{1}{2}\frac{d\,\overline{w^3}}{dz} - \frac{\overline{w^3}}{U_0}\frac{dU}{dz}\right) t^3 + O(t^4), \qquad (4.2)$$

where $t = x/U$ has been substituted. All quantities are dimensionless and evaluated at the release height z_0/h. Van Dop et al. (1985) and deBaas et al. (1986) compare the results of their one-dimensional Monte Carlo simulations with simplified forms of (4.1) and (4.2):

$$\langle Z-z_0 \rangle = \left(\frac{d\,\overline{w^2}}{dz}\right) t^2 + O(t^3) \qquad (4.3)$$

and

$$\langle (Z-z_0)^2 \rangle = \sigma_w^2 t^2 + \frac{1}{2}\left(\frac{d\,\overline{w^3}}{dz}\right) t^3 + O(t^4), \qquad (4.4)$$

which assume a uniform mean wind and neglect the effect of the shear stress. For strongly convective conditions, these assumptions are justified.

For large travel times, $\langle Z \rangle \rightarrow 0.5$ since the marked fluid must eventually become uniformly distributed throughout the boundary layer. When the distribution reaches equilibrium and becomes uniform, the vertical spread is given by

$$Z_{eq}^2 \equiv \langle (Z-z_0)^2 \rangle = \int_0^1 (Z - z_0)^2 \, dZ = \frac{1}{3} - z_0 + z_0^2. \qquad (4.5)$$

4.2 Experimental Studies

In addition to comparing our results against these theoretical asymptotic limits, we will also utilize the results of the water tank simulations of dispersion in the convective boundary layer by Willis and Deardorff (1974, 1975, 1976a, 1978, 1981). In these experiments neutrally buoyant oil droplets 0.8 mm in diameter were deployed along a line parallel to the x-axis at initial heights of z_0/h = 0.067, 0.24 or 0.49 in a thermally stratified tank of water which was heated at the bottom (see Fig. 4.1). A camera was located at one end of the tank aimed along the x-axis such that the instantaneous line source formed by the droplets appeared as a point source. The position of the droplets was recorded at

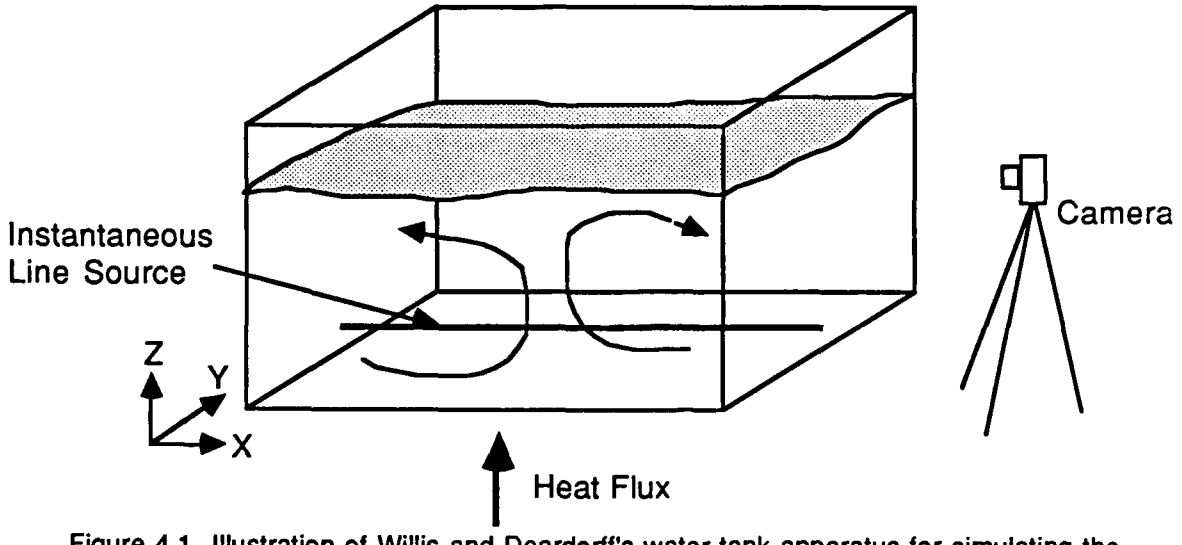

Figure 4.1 Illustration of Willis and Deardorff's water tank apparatus for simulating the convective planetary boundary layer.

3 to 5 second intervals. From these photographs, concentration distributions were estimated for the y-z plane. The distributions were averaged over an ensemble of trials. Thus a record of the dispersion as a function of time was obtained. Assuming x = Ut (i.e., neglecting streamwise diffusion) and integrating over the y-axis ("crosswind-integration") the data are presented as a function of the dimensionless downwind distance $X = (x/h)(w_*/U)$. This may also be written as $X = (x/U)(w_*/h)$ in which case it is

recognized as a dimensionless time (see §3.1.2). Willis and Deardorff (1976b) repeated their 1975 experiments with a continuous point source which was moved through the water tank and confirmed their earlier claim that their results are valid over the range $1.5 < U/w_* < 6$. At the lower limit streamwise diffusion can no longer be neglected; at the upper limit the effects of shear significantly affect the dispersion process. In order to compare our results with Willis and Deardorff's data, we must compute

$$C^y_{WD}(z,\frac{x}{U}) = \int_{-\infty}^{\infty}\int_{-\infty}^{\infty} C(x,y,z,\frac{x}{U})\,dx\,dy, \tag{4.6}$$

which is the numerical counterpart of Willis and Deardorff's representation. Essentially this amounts to neglecting the actual x-coordinate of a particle and instead using the position computed with $x = Ut$. The particles thus move downwind in a single cross section.

Because Willis and Deardorff's experiments were carried out in a water tank, the mean velocity U and the shear stress were zero. This corresponds to the limiting case where $\zeta\ (\equiv h/-L) \rightarrow \infty$. Since their results contradicted predictions of both Gaussian models and gradient diffusion models, it was of particular interest to test their results in a way that would include the effects of shear-produced turbulence. (Recall that in Chapter 1 we showed that a well-developed mixed layer can occur for values of $\zeta \approx 10$.) In order to investigate the combined effects of convection and shear arising from cases where $\zeta \approx 10$, Poreh and Cermak (1984, 1985) constructed a physical model of the convective boundary layer in a wind tunnel with a heated floor and carried out dispersion studies of neutrally buoyant plumes for $\zeta \approx 10$ and $U/w_* \approx 8$ at release heights $z_0/h = 0.02$, 0.25 and 0.61.

In addition to these laboratory studies, data gathered from field studies of atmospheric dispersion will also be presented for comparison with our simulation results. One such study, Project CONDORS (Convective Diffusion Observed by Remote Sensors), was designed to verify Willis and Deardorff's findings in the real convective boundary layer (Kaimal et al., 1986). It was comprised of sixteen trials conducted during the summers of 1982 and 1983 at the Boulder Atmospheric Observatory in Colorado. In these tests one or more of oil fog, aluminized mylar chaff and tracer gases were released either from near-surface or elevated positions into the convective boundary layer. The oil fog was tracked using lidar and the spatial concentration distribution determined by the amount of transmitted light scattered back

to the receiving telescope. The aluminized mylar chaff was tracked with doppler radar. Chaff concentration was computed from the strength of the reflected radar signal. The tracer gases were collected with bag samplers located at ground-level on an arc approximately one kilometer downwind from the release point.

We will also compare our results with data from Project Prairie Grass (Barad, 1956), the first comprehensive study of atmospheric dispersion. This was comprised of 70 ten-minute releases of gaseous sulfur dioxide carried out during the summer of 1956 in a mowed hayfield in north-central Nebraska. Measurements of time-integrated concentration (dosage) were made with an array of 599 chemical impingers ("bubblers") located downwind of a continuous ground-level source for a variety of meteorological conditions. The impingers were positioned at an elevation of 1.5 m on five semi-circular arcs located 50, 100, 200, 400 and 800 m from the source.

4.3 Model / Data Comparisons

For all of the cases discussed in this section, 10^4 particles were employed with the nondimensional time step $\Delta t^+ \equiv \Delta t/t_* = 0.005$ ($t_* = h/w_*$, the convective time scale) which is an order of magnitude less than that used by Van Dop et al., (1985) in their one-dimensional Monte Carlo model of the convective boundary layer. A smaller time step is necessary because we allow the nondimensional local integral scale T_{Lw}/t_* to increase with height, whereas Van Dop et al. assume that the integral scale is constant with height and equal to unity. Since the assumption that $\Delta t/T_L << 1$ is implicit in the Langevin equation as implemented, we must choose Δt small enough to ensure that this inequality is always true. Because the integral time scale T_{Lw} goes to zero as we approach the surface, we take all fluid statistics, such as T_{Lw} and σ_w, to be constant in a shallow layer $\delta/h = 0.0025$ near the surface so that Δt does not need to be infinitely small and so that no gradients become infinitely large in this region.

Van Dop et al., (1985) also use 10^4 particles whereas deBaas et al., (1986) use 2×10^4 in their one-dimensional Monte Carlo model. The use of a large number of particles is necessary not only to ensure the accuracy of the various statistical quantities derived from the results of the simulations, but also to ensure that the extremes of the skewed velocity distribution will be realized. The skewness of the particle velocity distribution is dependent on the time step: $Sk_\mu = \langle\mu^3\rangle/[\langle\mu^2\rangle]^{1/2} \sim (\Delta t^+)^{-1/2}$; a small time step results in a large skewness. Too few particles will result in an inaccurate representation of the skewness. We have tried using 2×10^4 particles and found that although the results are somewhat smoother, they exhibit the same trends

as those computed with fewer particles while requiring twice as long to execute (eight cpu-hours vs. four cpu-hours on a Sun-3/280).

In order to compare our model with the experimental data, we conducted stochastic simulations for release heights of z_0/h = 0.0025, 0.067, 0.24 and 0.49 and ζ = 500 and 50. Although the large value of ζ corresponds most nearly to that for Willis and Deardorff's experiments, the diabatic wind profile, Eq. (3.95), for this case puts U/w_* in the range 1.0-1.3. This is slightly less than Willis and Deardorff's stated lower limit of validity but matches U/w_* for the CONDORS tests well. The value of ζ = 50 yields $2.8 \leq U/w_* \leq 3.8$, for which streamwise dispersion should be negligible according to Willis and Deardorff. Both uniform and vertically varying mean wind profiles were tested to study the effect of a shear flow on the dispersion. For the uniform wind cases U/w_* was computed at the release height from the diabatic wind profile corresponding to the value of ζ for the run.

Comparisons will be made in terms of the mean height of the plume (Eq. 3.117), mean crosswind and vertical spread (Eqs. 3.120 and 3.121, respectively), crosswind-integrated concentration distribution (Eq. 3.108) and the ground-level crosswind-integrated concentration (Eq. 3.113). The volume elements which make up the computational network used to determine the concentration distribution are cubical having $\Delta x/h = \Delta y/h = \Delta z/h = 0.05$, except for the layer nearest the surface for which $\Delta z/h = 0.025$.

4.3.1 Mean Height and Vertical Spread

Figure 4.2(a) compares the mean height of the plume computed from the results of our stochastic model for ζ = 500, z_0/h = 0.067 and a uniform wind profile with the Taylor-series prediction of Hunt (1984b) given by Eq. (4.3) and with data from Willis and Deardorff (1975; hereinafter referred to as WD1). For $X << 1$, both the model and data agree well with Hunt's limit. At larger values of X both model and data diverge from the limiting behavior as larger scales of motion begin to affect the dispersion. Figure 4.2(b) shows a similar comparison for the vertical spread of the plume. Both the stochastic model prediction and the data from WD1 are in agreement and both agree with Hunt's limit for $X << 1$. Figure 4.3(a) shows that for both the mean height and vertical spread the model predictions and water tank data reach a maximum at about the same value of X, although the data indicate slightly larger values for the maxima. Both model and data reach the equilibrium limits for $X > 3$.

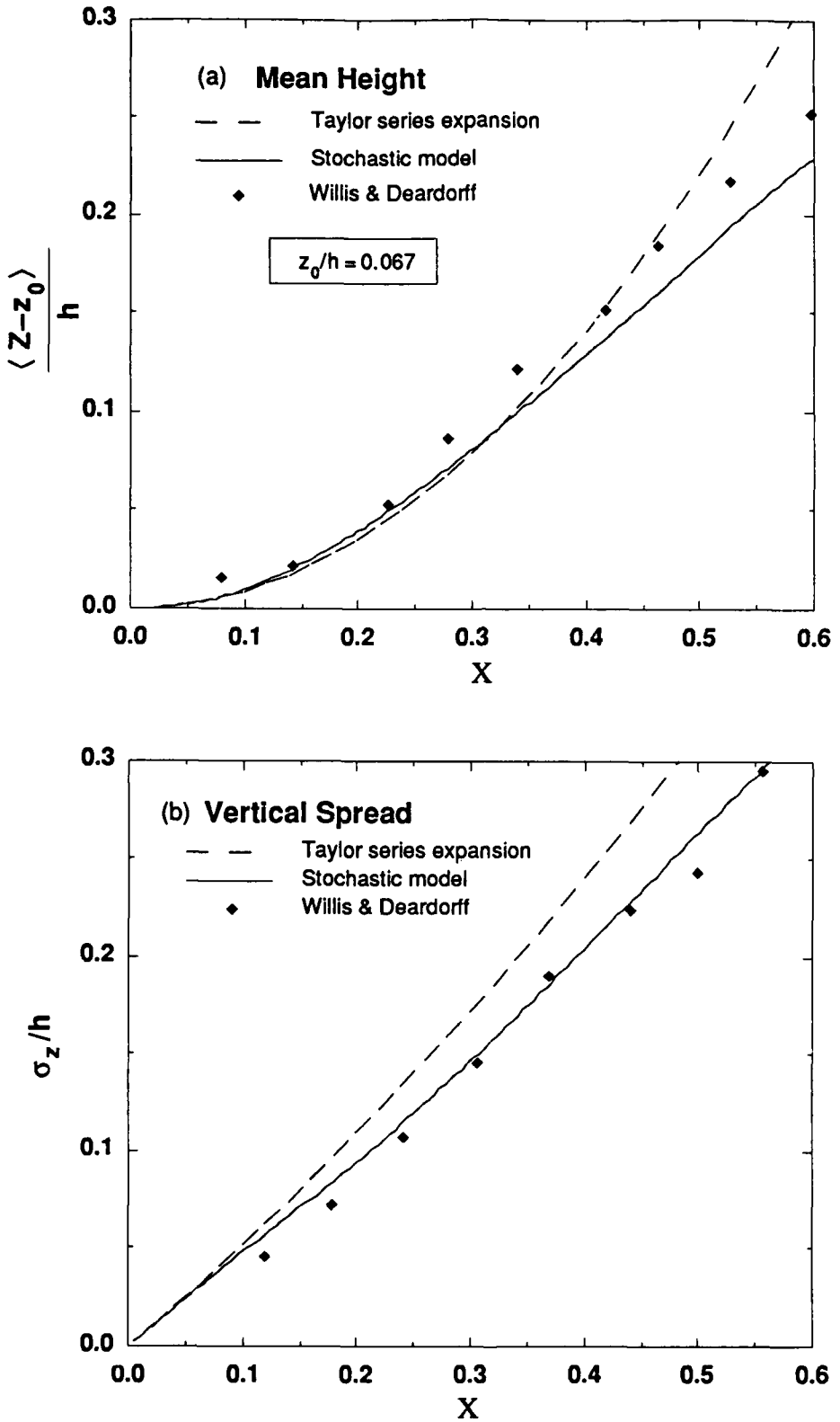

Figure 4.2 Mean height (a) and vertical spread (b) of particles as a function of downwind distance computed from the stochastic model results and compared with the prediction of the Taylor series expansion of Hunt (1982) for X < 1 as well as with data from Willis and Deardorff (1975).

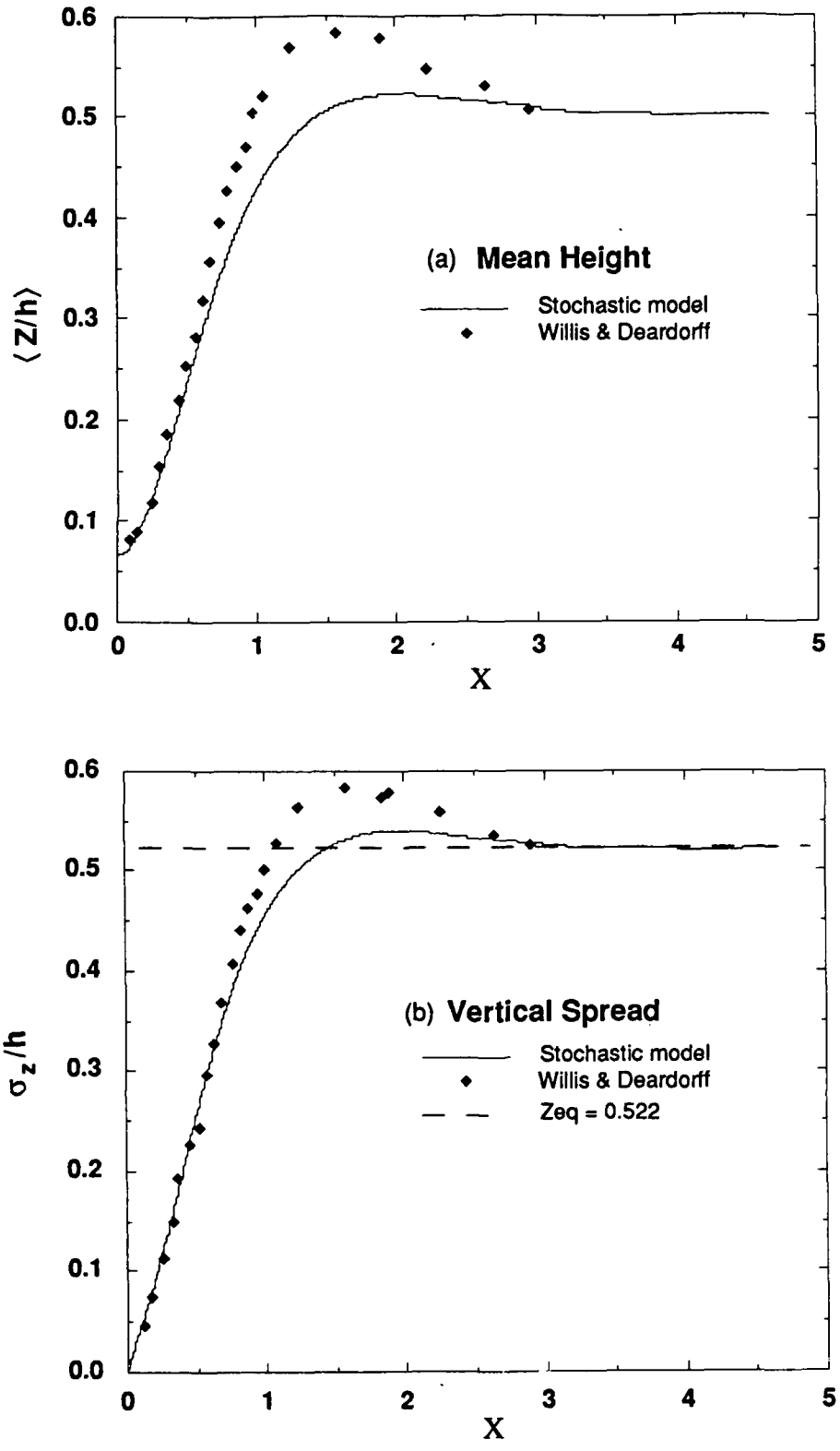

Figure 4.3 Mean height (a) and vertical spread (b) of particles as a function of downwind distance computed from the results of the stochastic model and compared with data from Willis and Deardorff (1975) as well as the equilibrium limits.

Figure 4.4(a) shows that for $z_0/h = 0.24$ the mean height of the plume predicted by the stochastic model agrees fairly well with the Taylor-series prediction for $X << 1$ but diverges from the limit sooner than the water tank data of Willis and Deardorff (1978; hereinafter WD2). The vertical spread predicted by the stochastic model given in Fig. 4.4(b) agrees well with the Taylor-series prediction for $X << 1$ and fairly well with the water tank data. As shown in Figs. 4.5(a) and 4.5(b), the stochastic model predictions increase to the equilibrium values before the water tank data but have nearly the same maximum values as the water tank results. Again, both the model predictions and the experimental data attain the theoretical equilibrium values.

The results for $z_0/h = 0.49$, presented in Figs. 4.6 and 4.7, also show about the same level of agreement between model and data (Willis and Deardorff, 1981; hereinafter WD3) for the mean height and vertical spread of the plume as did the lower release heights. Both model results and data follow the Taylor-series predictions closely; the equilibrium values for the mean height and spread are attained by both the stochastic prediction and the data from WD3. The mean height and vertical spread of the data in this case exhibit larger amplitude oscillations about the equilibrium values as did the data for $z_0/h = 0.067$.

The agreement between the mean plume height and vertical spread predicted by the stochastic model and the results of the water tank simulations of Willis and Deardorff primarily reflects the degree to which the formulations for the turbulent velocity moments employed in the model represent the turbulence in the water tank simulations. As Eq. 4.3 shows, the mean height of the cloud for $X << 1$ is primarily influenced by $\partial\sigma_w^2/\partial z$ evaluated at the release height. As $\langle Z\text{-}z_0 \rangle$ increases, the gradient $\partial\sigma_w^2/\partial z$ increases which causes the both model prediction and the experimental data to depart from the Taylor-series prediction. Differences between the stochastic model results and data regarding the mean height are indicative of differences in $\partial\sigma_w^2/\partial z$ (see Fig. 3.5). The mean vertical spread of the plume is primarily influenced by the variance of the vertical fluid velocity σ_w^2 and the gradient of the third moment of the fluid velocity $\partial\langle w^3\rangle/\partial z$ as Eq. 4.4 demonstrates. For $X << 1$, the value of these terms at the release height controls the initial behavior. As the mean height deviates from the release height so the mean vertical spread differs from the Taylor-series prediction. Thus differences between the model prediction and the data are largely due to differences in the value of these terms which grow as $X \rightarrow 1$.

Evidently, there must also be good agreement between the local integral time scales used in the stochastic model and the actual integral time scales in the water tank. In their one-dimensional Monte Carlo simulation of the convective boundary

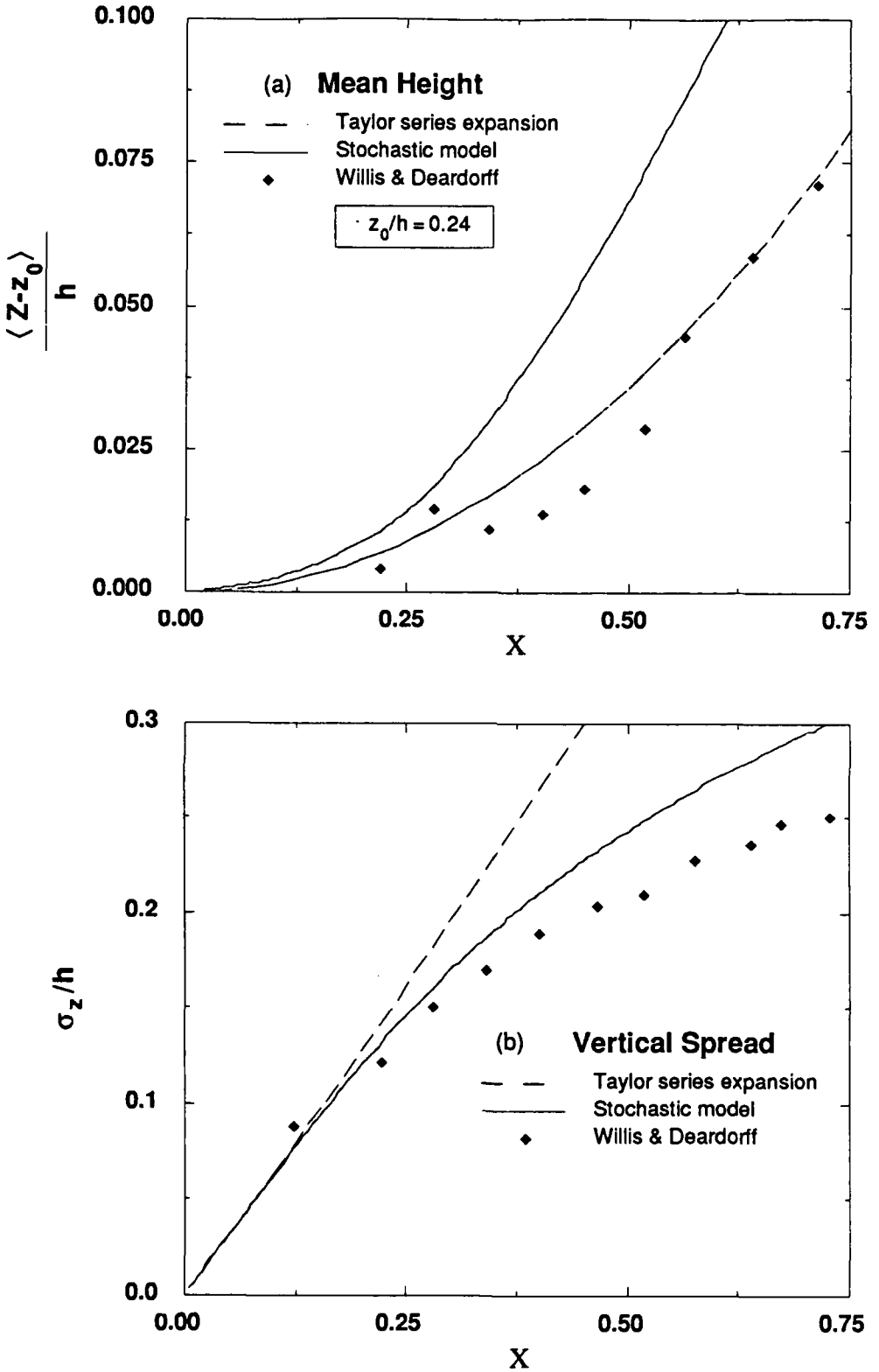

Figure 4.4 Mean height (a) and vertical spread (b) of particles as a function of downwind distance computed from the stochastic model results and compared with the prediction of the Taylor series expansion of Hunt (1982) for X < 1 as well as with data from Willis and Deardorff (1978).

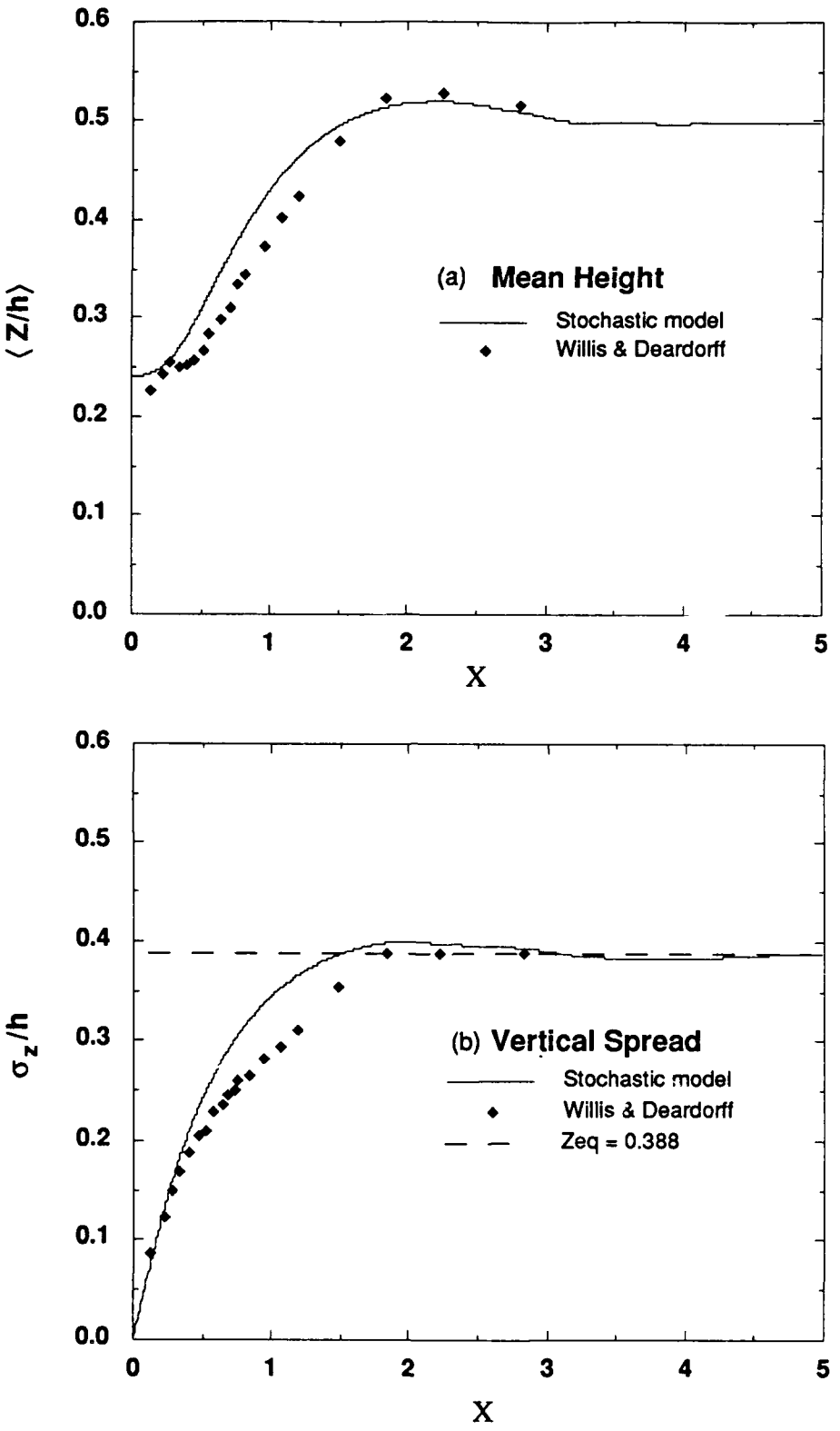

Figure 4.5 Mean height (a) and vertical spread (b) of particles as a function of downwind distance computed from the results of the stochastic model and compared with data from Willis and Deardorff (1978) as well as the equilibrium limits.

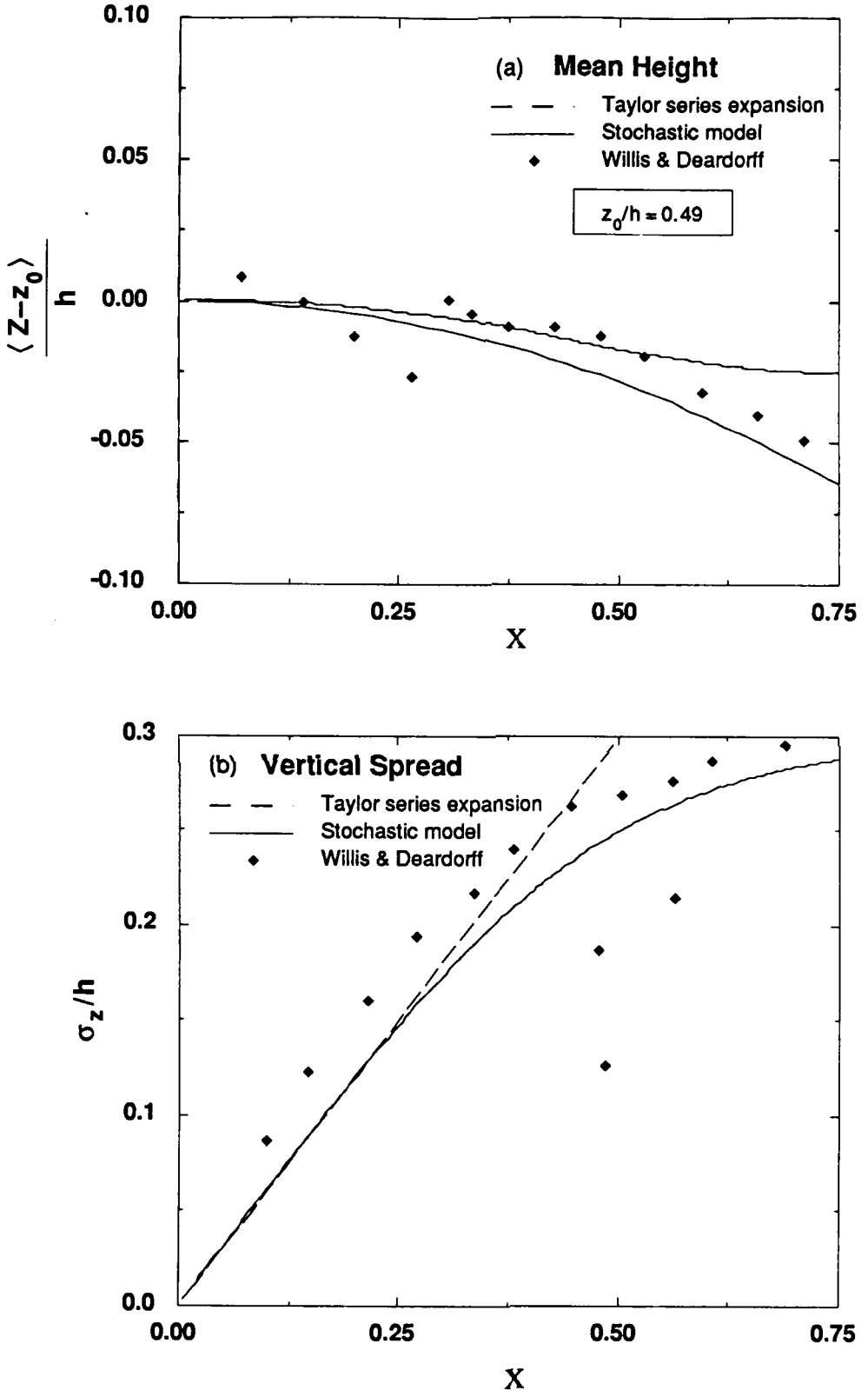

Figure 4.6 Mean height (a) and vertical spread (b) of particles as a function of downwind distance computed from the stochastic model results and compared with the prediction of the Taylor series expansion of Hunt (1982) for $X < 1$ as well as with data from Willis and Deardorff (1981).

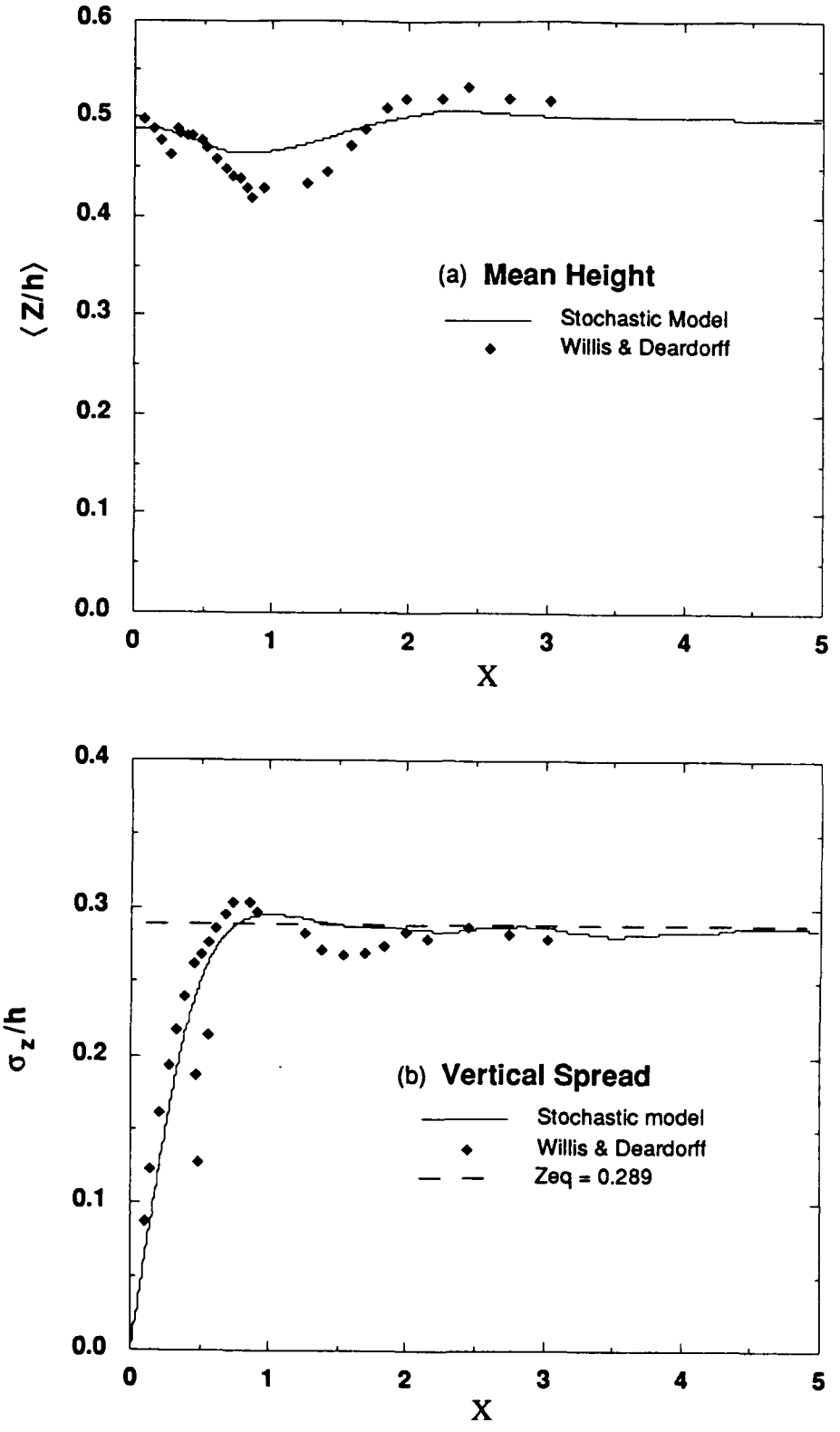

Figure 4.7 Mean height (a) and vertical spread (b) of particles with downwind distance computed from the results of the stochastic model and compared with data from Willis and Deardorff (1981) as well as with equilibrium limits.

layer deBaas et al. (1986) found it necessary to increase their (constant) value for T_{Lw}/t_* from somewhere in the range of 0.24-0.55 to unity in order to reproduce the water tank behavior. We have similarly found that we had to increase the vertical profile of T_{Lw}/t_* by a factor of three such that $T_{Lw}/t_* \rightarrow 1$ as $z/h \rightarrow 0.5$ in order to achieve agreement with Willis and Deardorff's measurements. This is quite reasonable since the local integral scale T_{Lw} should approach the time scale of the convective motions h/w_* in the middle of the convective boundary layer. Thus $a = 2$ in the empirical formula relating the Eulerian and Lagrangian integral time scales: $T_{Lw} = \beta T_{Ew}$ where $\beta = a/i$, i is the intensity of the turbulence and a is a proportionality constant.

Based on Hanna's (1981) recommendation we had initially used $a = 0.68$, which resulted in $T_{Lw}/t_* \rightarrow 1/3$ as $z/h \rightarrow 0.5$. Upon careful examination, the data presented by Hanna (1981, Fig. 6) hardly seem to support any linear relationship between β and $1/i$. This is because, for inhomogeneous turbulence, T_L cannot be regarded as a global integral time scale for the flow but rather should be considered to be a local time scale which Durbin (1983) calls the "decorrelation time," Eq. (2.81). Since the turbulence in the horizontal directions is very nearly homogeneous, the local integral time scales are essentially invariant. Therefore they obey the relationship between the Eulerian and Lagrangian reference frames given by Hanna (1981). However, in the vertical direction, Hanna's data reflect the path integral of $T_L(z)$ over each balloon's trajectory. Since each balloon was observed to follow a markedly different path, the large degree of scatter in the computed vertical integral scales should not be surprising. Clarke, Ching and Godowitch (1983) computed the proportionality constant a for convective atmospheric conditions from an analysis of "plume segments" (short duration point sources) using Pasquill and Smith's (1983, page 152) result for $t/T_L >> 1$

$$\sigma_y^2 = 4\sigma_v^2 T_L t = 4\sigma_v^2 \beta T_E t. \tag{4.7}$$

Clarke et al. determined σ_v^2 and T_E from tower-based turbulence measurements and σ_y^2 from aircraft-based measurements of tracer concentration averaged over one hour periods. They found $1.1 \leq a \leq 2.0$, depending on ζ, which is much greater than Hanna's result and more in line with our scaling arguments and model predictions.

Figures 4.8(a) and 4.8(b) compare the mean height and mean vertical spread predicted by the stochastic model for $\zeta = 500$ and $z_0/h = 0.0025$ with Project CONDORS data gathered during near-surface releases of oil fog and aluminized mylar chaff. Despite a large amount of scatter in the oil fog data for the 1983 tests, the

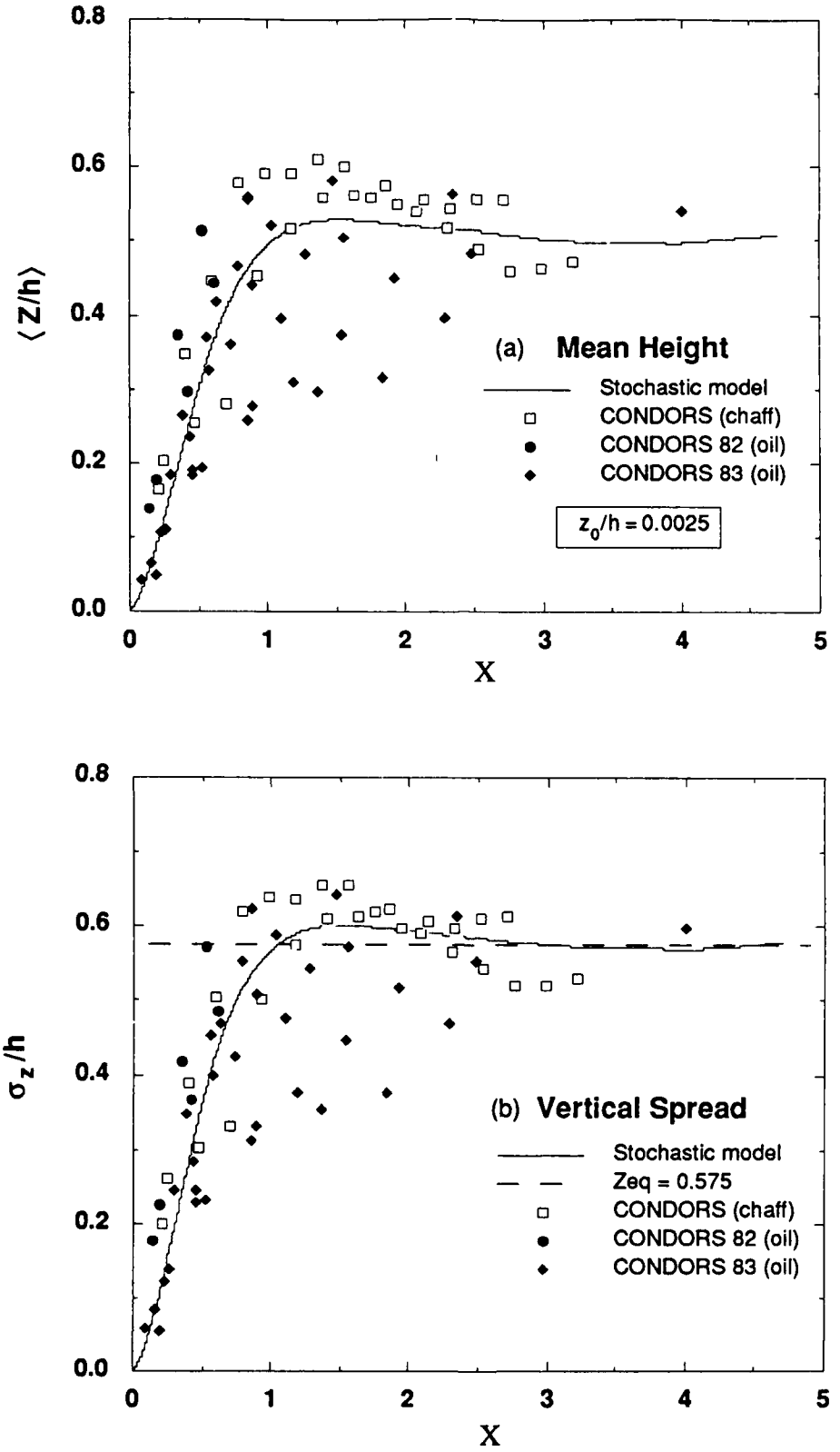

Figure 4.8 Mean height (a) and vertical spread (b) of particles with downwind distance computed from the stochastic model results and compared with results of Project CONDORS (Kaimal, et al., 1986) as well as equilibrium limits.

data agree rather well with the predictions. (The scatter in the 1983 oil fog data is due to ambiguity in the inversion height for three of the six tests included in this group which is used to normalize the data.) The chaff data reach a slightly greater maximum mean height and vertical spread than the model predictions. This was also observed to be the case for the water tank data. Only two chaff releases were performed from ground level during CONDORS 82 and none during CONDORS 83, primarily due to the appreciable settling velocity (0.3 m/s) and the difficulty in measuring chaff concentrations near the surface with the doppler radar. The significant settling velocity may be the reason for the decline in the mean height and vertical spread for $X > 2.5$. Nevertheless, the agreement between the model and data is encouraging.

4.3.2 Mean Crosswind Spread

In Fig. 4.9 the mean crosswind spread predicted by the stochastic model is compared with experimental data from WD1, Project Prairie Grass (reported by Nieuwstadt, 1980), and Project CONDORS for a ground-level release. Despite considerable scatter in the data, the agreement with the predicted spread is quite good. (Some of the CONDORS 83 oil fog data appears to be low due to the aforementioned uncertainty in the values of the inversion height used to normalize the data.) Since the crosswind spread is generally acknowledged to be essentially Gaussian and since the crosswind velocity fluctuations are modelled as Gaussian, such agreement is not surprising. It does, however, support our assumption of horizontal homogeneity. This is evident from the observation that for $X << 1$, $\sigma_y/h \sim X$, in agreement with Taylor's (1921) expression for dispersion in homogeneous turbulence at times much less than the Lagrangian integral time scale. Similarly, for $X >> 1$, the model and data obey $\sigma_y/h \sim X^2$, in keeping with Taylor's (1921) prediction for times much larger than the integral time.

4.3.3 Crosswind-Integrated Concentration

The crosswind-integrated non-dimensional concentration $\frac{C^y}{Q/hU}$ computed with the stochastic model, which includes the effects of streamwise diffusion, is presented in Fig. 4.10(a). This may be compared with C^y_{WD} computed by the stochastic model and presented in Fig. 4.10(b) for which streamwise diffusion is neglected (see Eq. 4.6). Isopleths of C^y_{WD} from WD1 are overlaid on Fig. 4.10(b) for comparison. Upon release, the particles encounter either an updraft and immediately begin to rise, or they encounter a downdraft and move essentially horizontally until eventually they

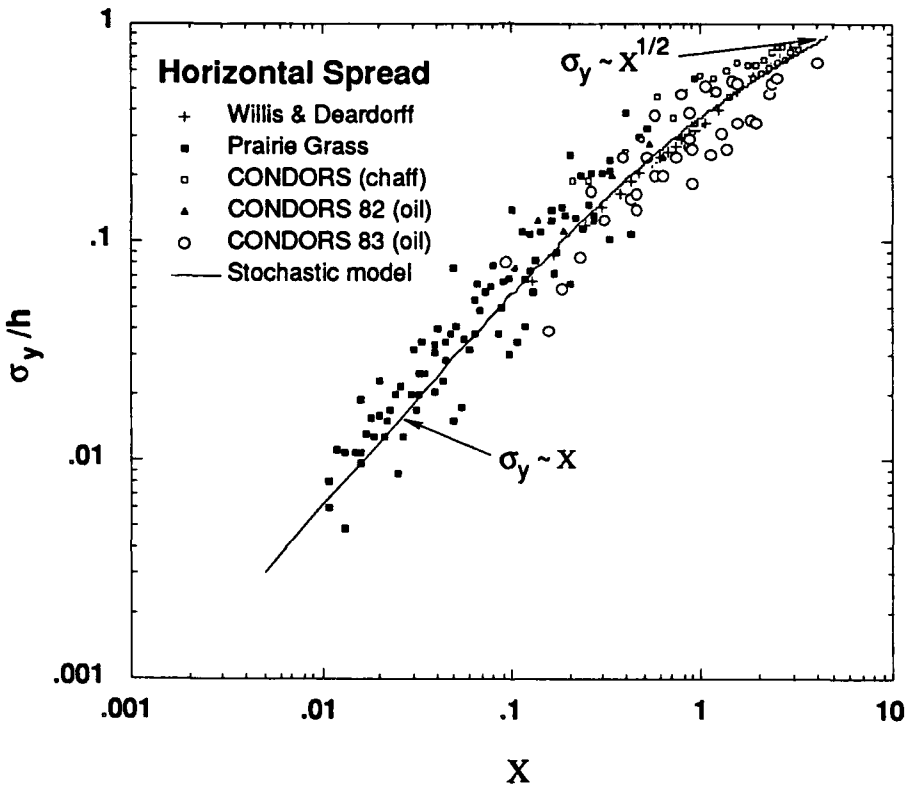

Figure 4.9 Horizontal (crosswind) spread of particles for near-surface release height computed from the results of the stochastic model and compared with data from Willis and Deardorff (1975), Project Prairie Grass (reported by Nieuwstadt, 1980) and Project CONDORS (Kaimal, et al., 1986). Limiting forms of Taylor's (1921) prediction are also indicated.

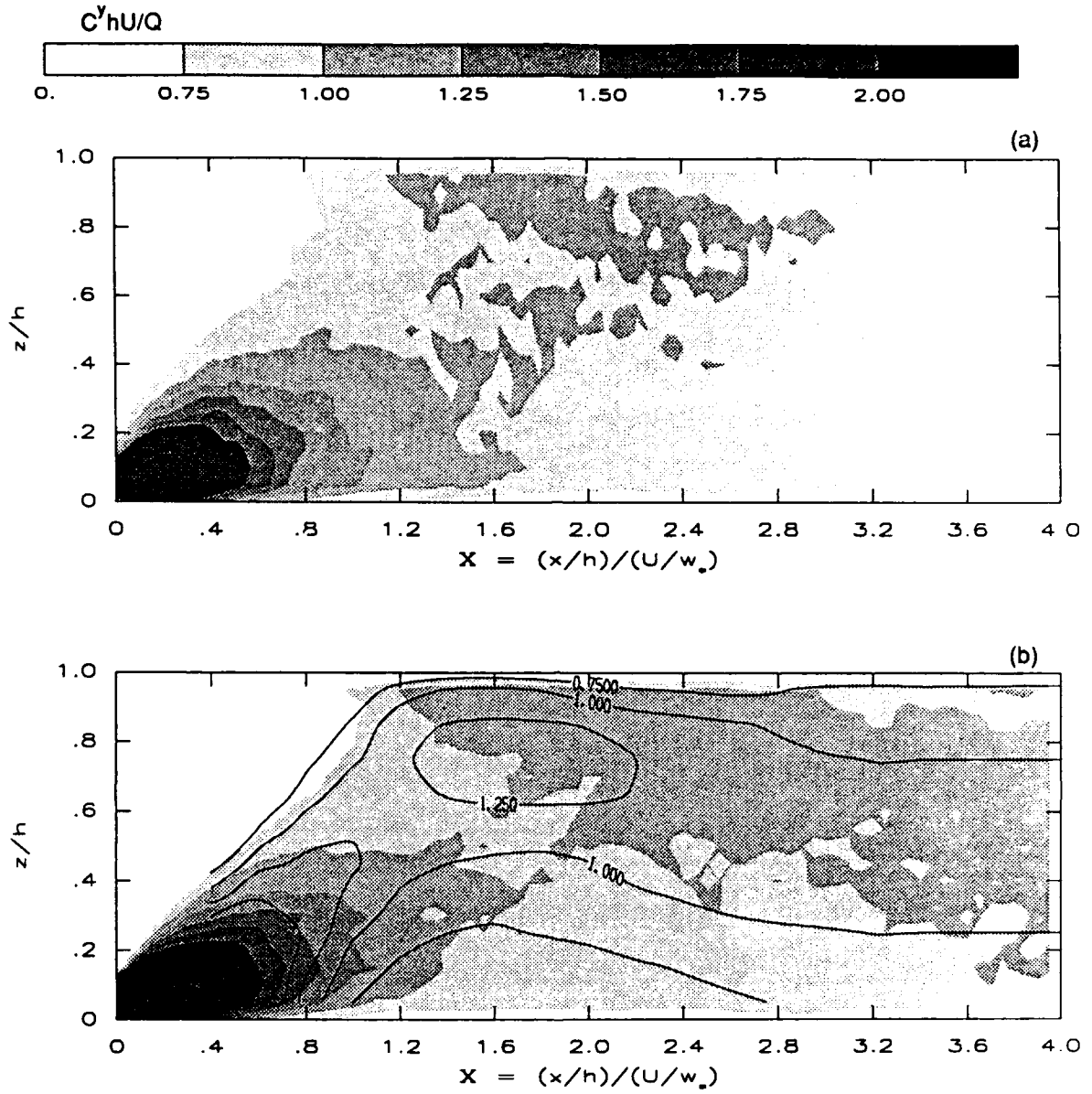

Figure 4.10 Non-dimensional crosswind-integrated concentration distributions computed from the stochastic simulation results for ζ = 500, U = constant and z_0/h = 0.067: (a) $C^y(x,z)hU/Q$ and (b) $C^y_{WD}(X,z)$ hU/Q. Willis and Deardorff's (1975) results are overlaid on (b).

encounter an updraft. The skewness of the vertical velocity fluctuations and their vertically increasing time scale causes the particles to be carried upward approximately to the inversion height before moving downward with the subsidence which, through interaction with rising thermals, causes the particles to spread throughout the boundary layer.

In Fig. 4.10, $z_0/h = 0.067$, $\zeta = 500$; the mean wind is uniform with height. $U/w_* = 1.2$ which is below the lower limit of validity for the tank data. Therefore, streamwise diffusion, which acts to reduce streamwise gradients, should be significant at such a low mean advection velocity. It is clear that the concentration gradients in Fig. 4.10(a) are indeed reduced in comparison with Fig. 4.10(b). Although the model prediction exhibits the same trends as the tank data, it does not show the sharp lift off apparent in the water tank results, nor is the elevated concentration as large. This difference was observed earlier in the comparison of the mean height and vertical spread. It was manifested in the oscillations of the water tank results about the equilibrium value. These differences are primarily due to differences between the turbulent velocity moments embodied in the empirical formulas utilized by the stochastic model and the values for these moments observed in the water tank and thus reflect the accuracy of the water tank simulation of the planetary boundary layer.

Figure 4.11 is identical to Fig. 4.10 except that the mean velocity is not held uniform but rather is given by Eq. 3.97 and varies from $U/w_* \approx 1$ near the surface to 1.3 at the upper boundary. The reference velocity is taken equal to the velocity at the release height $U(z_0)/w_* = 1.2$ as in Fig. 4.10. Comparing Figs. 4.10(a) and 4.11(a) reveals that the effect of shear is negligible for such strongly convective conditions except perhaps very near the surface.

The effect of reducing ζ is presented in Fig. 4.12. Here $\zeta = 50$, $U(z_0)/w_* = 3.5$ and $z_0/h = 0.067$ as before. For this case the effect of streamwise diffusion should be negligible according to the analysis presented in WD1. Comparison of the top and bottom isopleths demonstrates that this is indeed the case. (The top plot appears truncated because the dimensionless concentration is computed for a spatial network extending to $x^+ \equiv x/h = 4$. For $U/w_* = 3.5$, this corresponds to a maximum extent of $X = 1.15$.) Although the model plume does not lift off as quickly as the results of WD1, which are overlaid on the bottom plot, it does exhibit essentially the same trends as both WD1 and the case for $\zeta = 500$ (Fig. 4.11). The elevated maximum concentration has the same magnitude ($C^y hU/Q = 1.25$) as the water tank results. The predicted vertical concentration distribution does not become homogeneous by $X = 4$ (neither does the tank data). Although it may do so at some point farther downwind, the mean

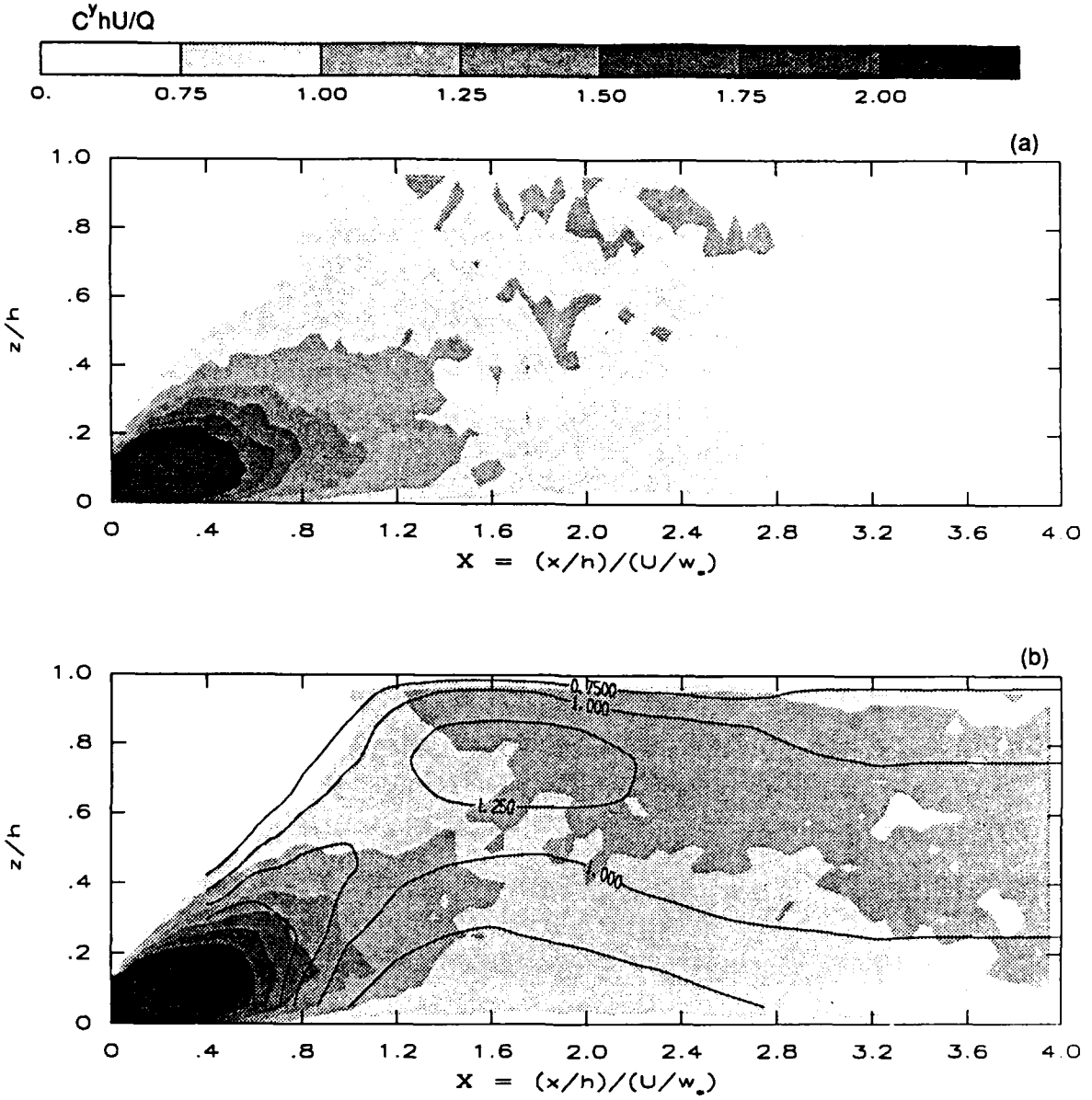

Figure 4.11 Non-dimensional crosswind-integrated concentration distributions computed from the stochastic simulation results for $\zeta = 500$, $U = U(z)$ and $z_0/h = 0.067$: (a) $C^y(x,z)hU/Q$ and (b) $C^y_{WD}(X,z)\ hU/Q$. Willis and Deardorff's (1975) results are overlaid on (b).

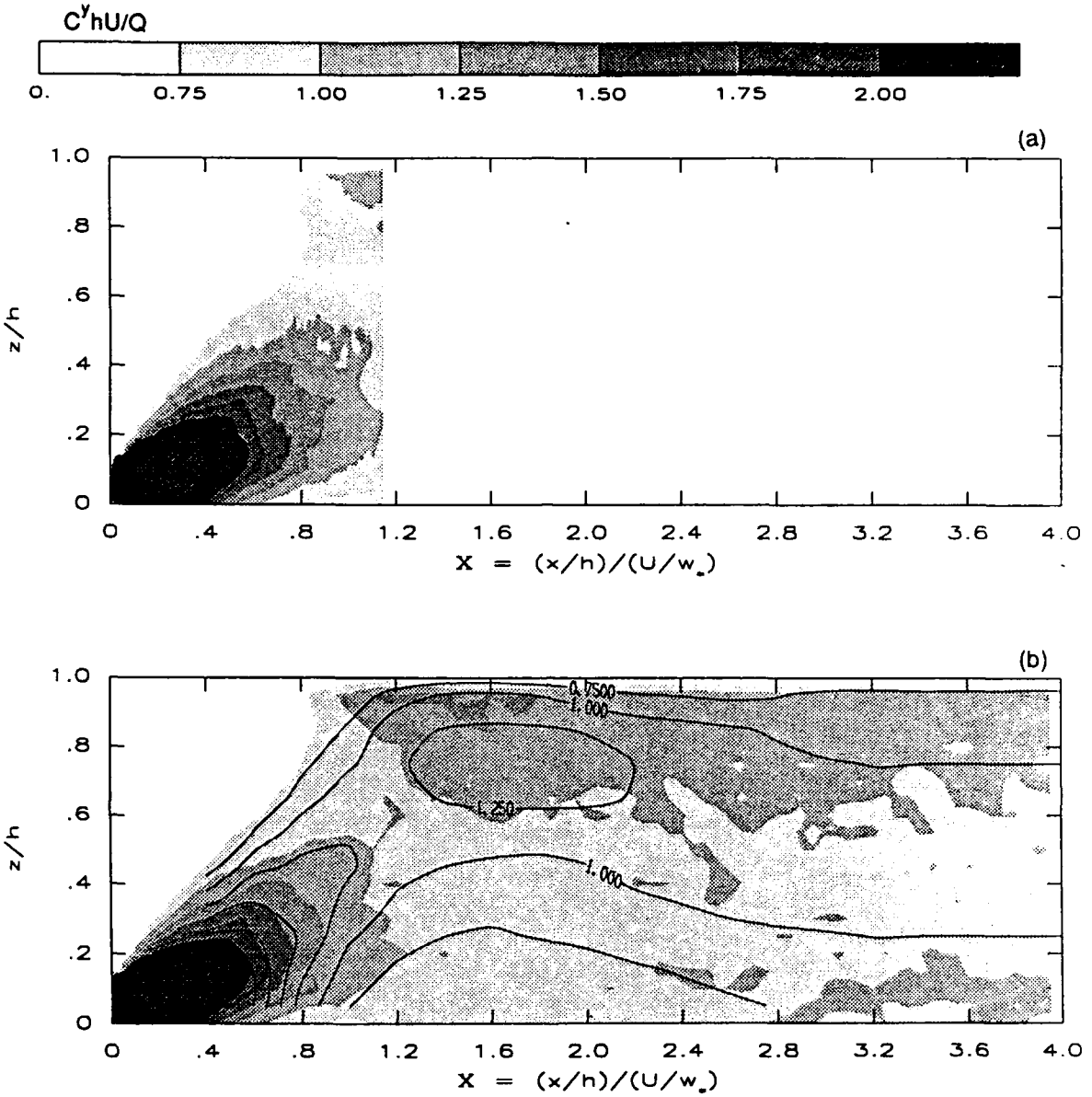

Figure 4.12 Non-dimensional crosswind-integrated concentration distributions computed from the stochastic simulation results for $\zeta = 50$, $U = U(z)$ and $z_0/h = 0.067$: (a) $C^y(x,z)hU/Q$ and (b) $C^y_{WD}(X,z)$ hU/Q. Willis and Deardorff's (1975) results are overlaid on (b).

height and vertical spread have already reach their equilibrium values. DeBaas et al. (1986) carried out a few of their one-dimensional simulations as far as X = 200 and still observed slight concentration gradients near the boundaries. Perhaps this is a consequence of treating the boundaries as perfectly reflective.

Figure 4.13 displays the results of our stochastic model for $\zeta = 5$, $U(z_0)/w_* = 8.8$ and $z_0/h = 0.067$. They show remarkable similarity to the earlier results for $\zeta = 500$ and $\zeta = 50$ considering that ζ has declined by two orders of magnitude and U/w_* has increased by almost ten times. This clearly demonstrates the value of the convective scaling, even in the presence of substantial shear.

In order to further illustrate the effects of the constant a in the relationship $\beta = a/i$, Fig. 4.14 presents the results of a model run for conditions identical to those in Fig. 4.13 except that a = 0.68 was used rather than a = 2 in relating the Eulerian and Lagrangian integral scales. The effects of the wind shear are more pronounced and the concentration near the inversion is significantly reduced. The concentrations near ground level also appear to be substantially affected beyond X = 2.

Figure 4.15(a) presents the results of the three-dimensional Monte Carlo simulation of Brusasca et al. (1987) for the case $\zeta = 200$, $U/w_* = 1.56$. Their results are in close agreement with both WD1 and our stochastic model. The model of Brusasca et al. does not use Thomson's (1984) formulation for the stochastic process; instead they follow the approach of Bærentsen and Berkowicz (1984) and model the convective boundary layer as a series of updrafts and downdrafts. They find that their model does not require the "drift" term shown by Thomson (1984), van Dop, Nieuwstadt and Hunt (1985) and Sawford (1986) to be necessary for modelling the convective boundary layer. However, they add a "mean updraft velocity" $w_u = 0.6\ w_*$ to ascending particles and subtract a "mean downdraft velocity" $w_d = 0.4\ w_*$ from descending particles such that $N_u w_u - N_d w_d = 0$ where N_u is the number of ascending particles and N_d is the number of descending particles. Brusasca et al. do not alter the relationship between the Eulerian and Lagrangian integral time scales given by Hanna (1981), as both deBaas et al. (1986) and we have found necessary. Rather, they again follow Bærentsen and Berkowicz (1984) and devise time constants for the updrafts and downdrafts in order to estimate the probability that particles will jump from an updraft to a downdraft and vice versa. These time constants are given by $h/w_u = 1.67\ t_*$ and $h/w_d = 2.5\ t_*$, respectively. The fact that these time constants are both greater than t_* probably compensates for their Lagrangian time scale which is substantially less than t_*.

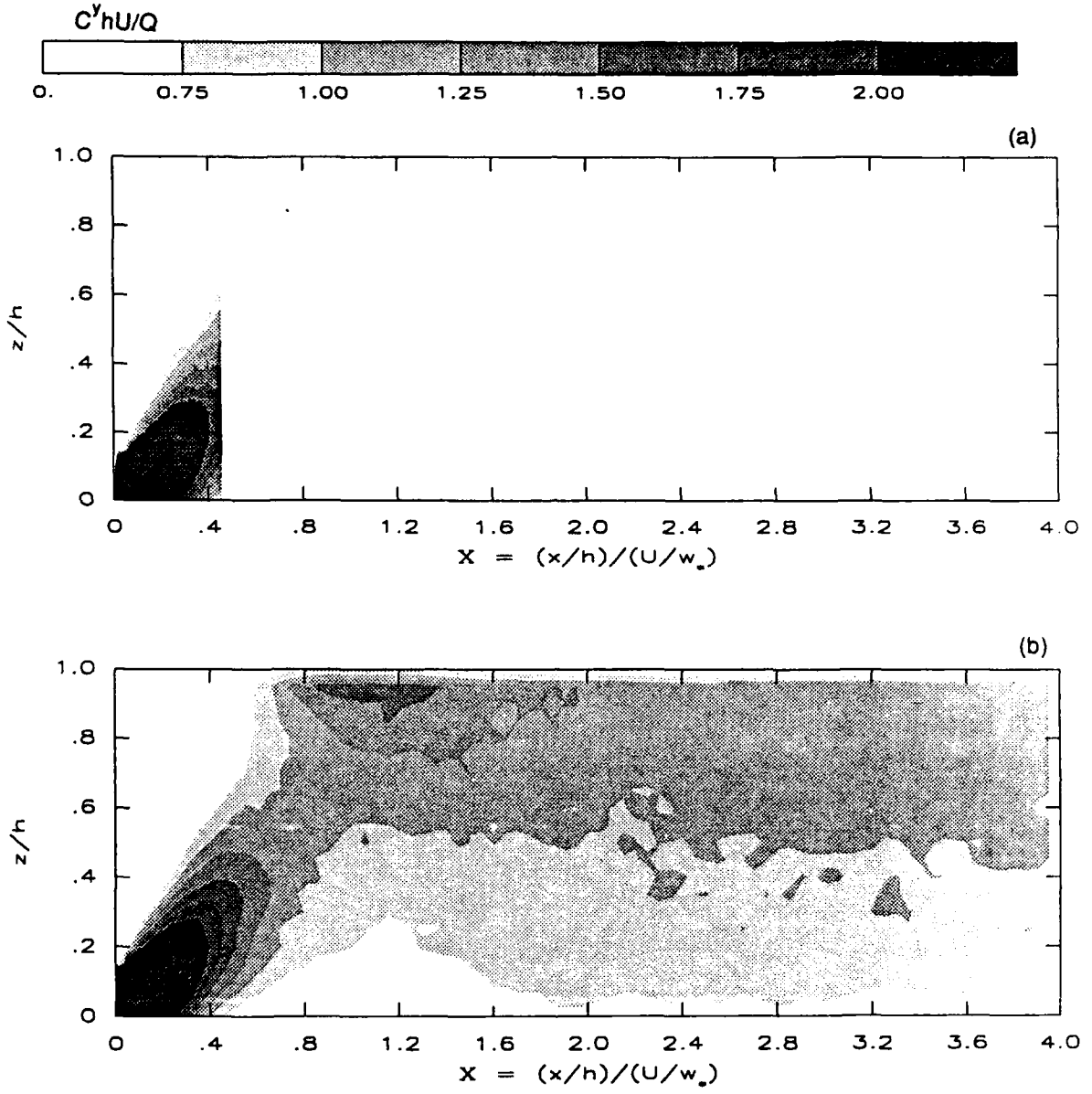

Figure 4.13 Non-dimensional crosswind-integrated concentration distributions computed from the stochastic simulation results for $\zeta = 5$, $U = U(z)$ and $z_0/h = 0.067$: (a) $C^y(x,z)hU/Q$ and (b) $C^y_{WD}(X,z)\ hU/Q$.

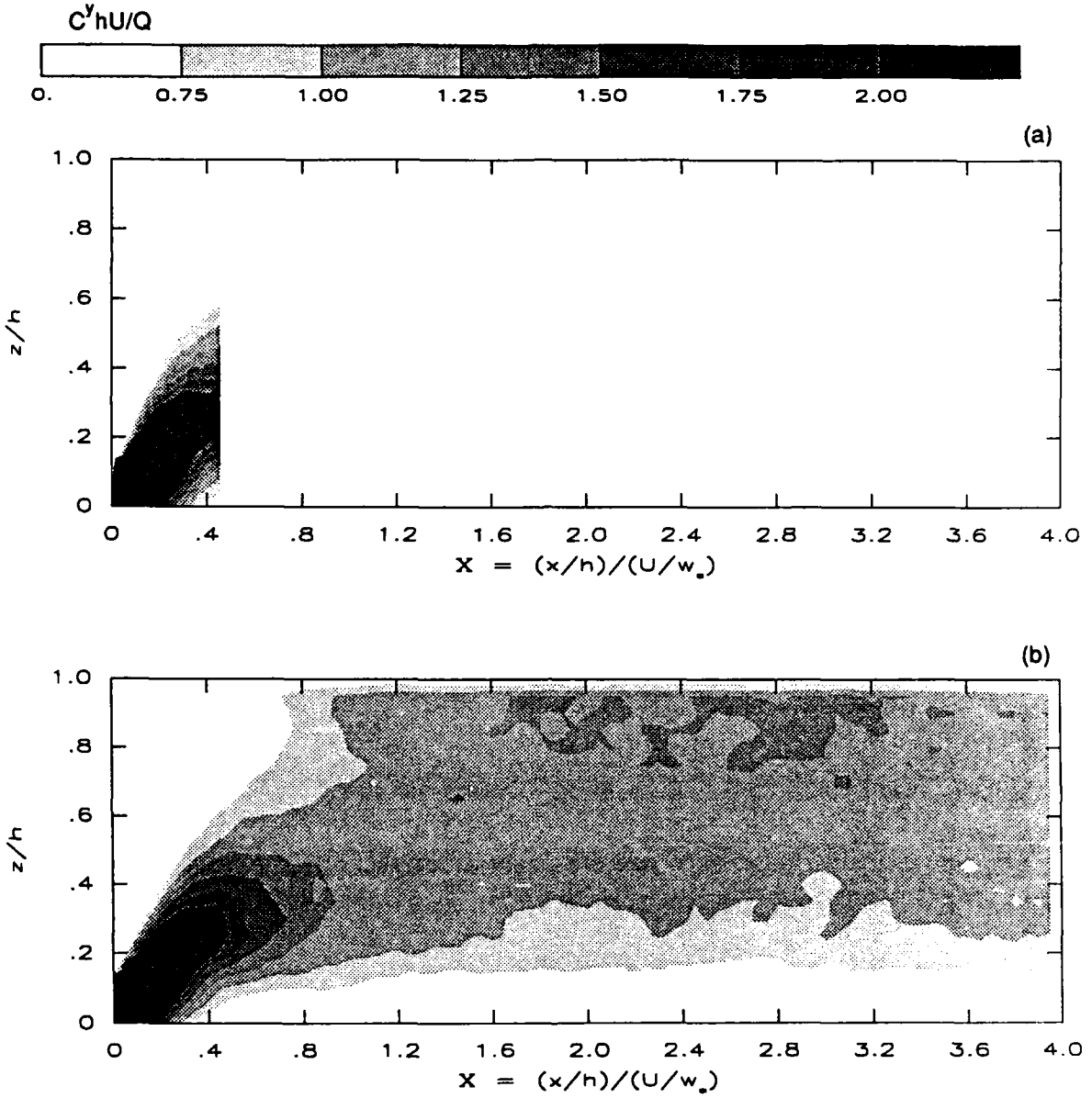

Figure 4.14 Identical with Fig. 4.13 except that in the relation $\beta = \frac{T_L}{T_E} = a/i$, a = 0.68 rather than a = 2.

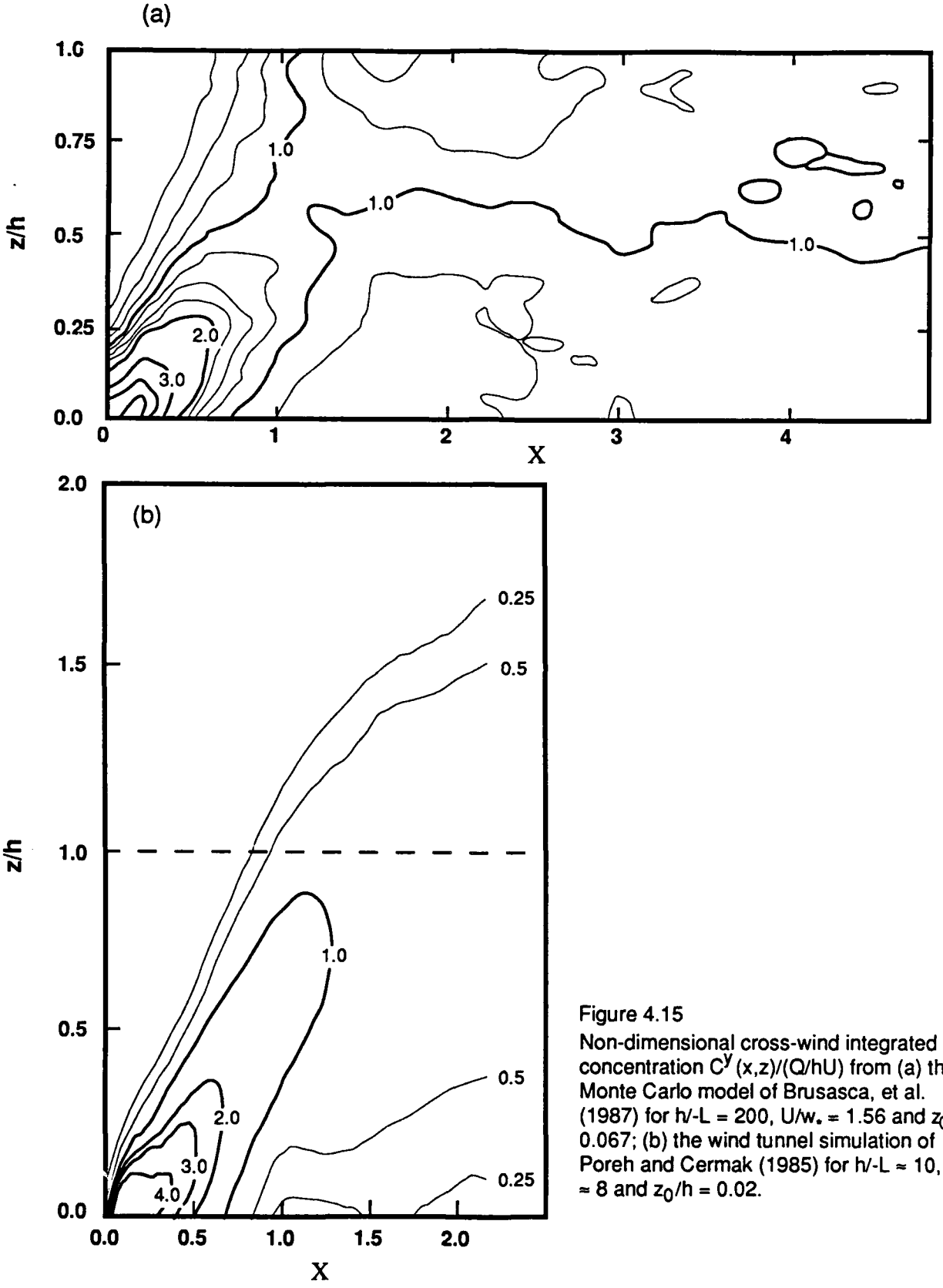

Figure 4.15
Non-dimensional cross-wind integrated concentration $C^y(x,z)/(Q/hU)$ from (a) the Monte Carlo model of Brusasca, et al. (1987) for $h/-L = 200$, $U/w_* = 1.56$ and $z_0/h = 0.067$; (b) the wind tunnel simulation of Poreh and Cermak (1985) for $h/-L \approx 10$, $U/w_* \approx 8$ and $z_0/h = 0.02$.

Figure 4.15(b) presents the experimental results of Poreh and Cermak (1985) from their physical simulation of the convective boundary layer in a wind tunnel. For this case, $\zeta \approx 10$ and $z_0/h = 0.02$. Their results agree reasonably well with both WD1 and our model calculations. The absence of dimensionless concentrations exceeding unity near the inversion height are most likely due to the difficulty Poreh and Cermak encountered in maintaining a strong inversion layer. As evidence of the latter problem, note that the plume rises above $z/h = 1$. A stronger inversion would have trapped the plume, leading to higher concentrations at the inversion height and probably resulted in better agreement with both WD1 and our model predictions.

The results of our model for $\zeta = 500$ are presented in Fig. 4.16 with a uniform mean wind velocity $U/w_* = 1.3$ and release height $z_0/h = 0.24$. Since subsidence occupies about 60% of the horizontal area (Lenschow and Stephens, 1980), most of the particles begin to descend after release and the maximum concentration occurs along a line from the release height to the surface. Once at the surface, the particles move horizontally until they encounter an updraft and rise to the inversion height where they again enter the subsidence and are mixed throughout the boundary layer. Figure 4.16(a) displays the effects of streamwise diffusion: streamwise material gradients are diminished relative to Fig. 4.16(b) wherein streamwise diffusion is neglected. The results for $\zeta = 50$ and $U(z_0)/w_* = 3.5$ at the same release height shown in Figs. 4.17(a) and (b) are quite similar to those for $\zeta = 500$ except that the effects of streamwise diffusion are no longer apparent. These results are in good agreement with the water tank results of WD2, presented in Fig. 4.18(a) and with the Monte Carlo predictions of Brusasca et al. (1987) in Fig. 4.18(b). The wind tunnel data from Poreh and Cermak (1985) for $z_0/h = 0.25$ are presented in Fig. 4.18(c). They show the same general trends as our results except that, without a strong inversion layer, the plume rises above $z/h = 1$ and the higher concentrations observed near the inversion height in the others results as well as ours are not present in Poreh and Cermak's data.

In Figs. 4.19(a) and (b) we present our results for $\zeta = 500$ with a uniform mean wind velocity $U/w_* = 1.3$ and a release height $z_0/h = 0.49$. As for the previous case, most particles encounter subsidence upon release and immediately begin to descend to the surface. Once at the surface they move horizontally until they are lifted to the inversion height by updrafts. From this point the particles are mixed by the subsidence and thermals throughout the boundary layer. Very similar results are obtained for the case where $\zeta = 50$ and the mean wind velocity profile increases with height ($U(z_0)/w_* = 3.8$), presented in Fig. 4.20. These results compare well with the results of WD3 shown in Fig. 4.21(a) with the exception that our results do not show as dramatic a

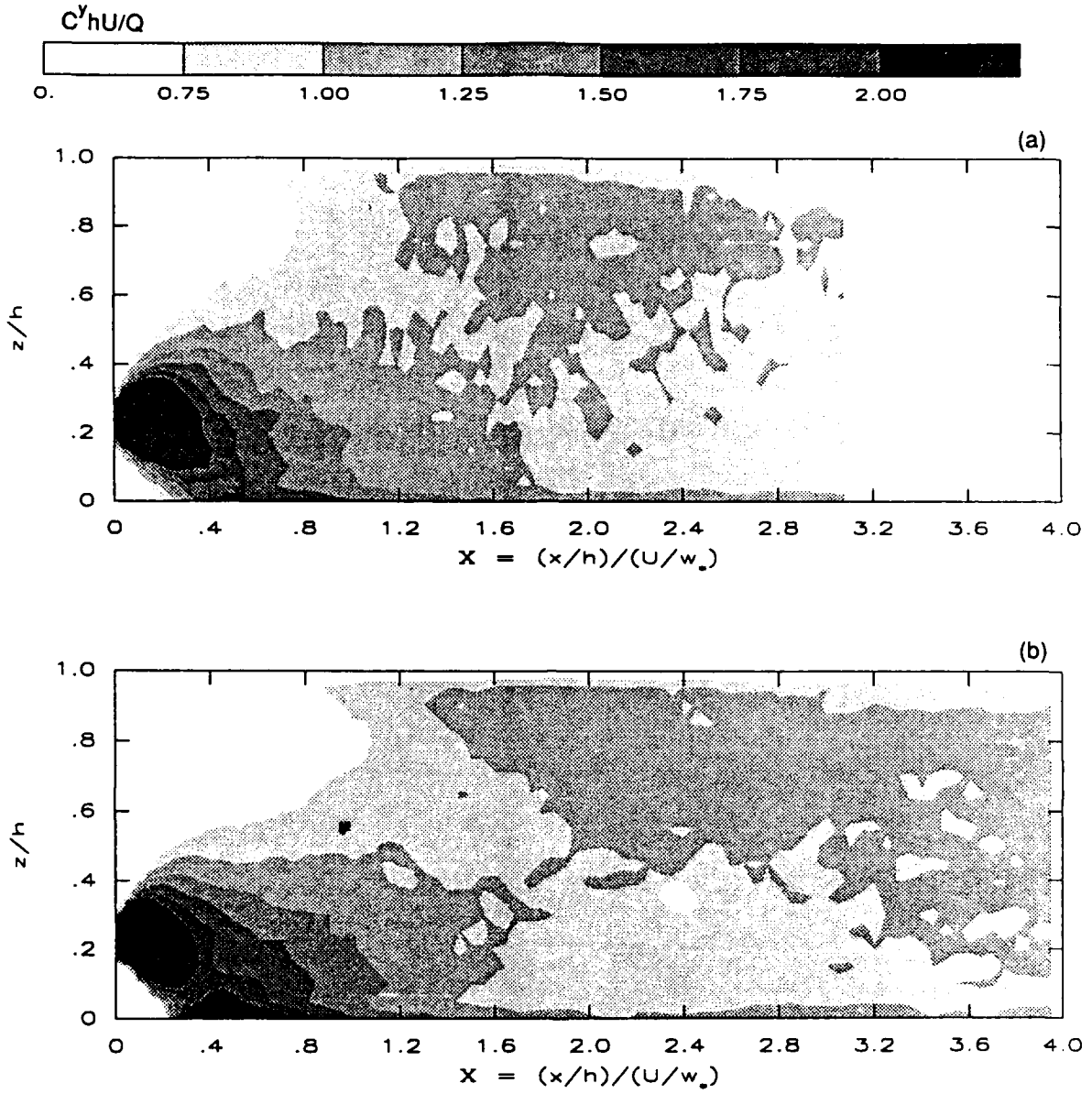

Figure 4.16 Non-dimensional crosswind-integrated concentration distributions computed from the stochastic simulation results for $\zeta = 500$, U = constant and $z_0/h = 0.24$: (a) $C^y(x,z)hU/Q$ and (b) $C^y_{WD}(X,z)$ hU/Q.

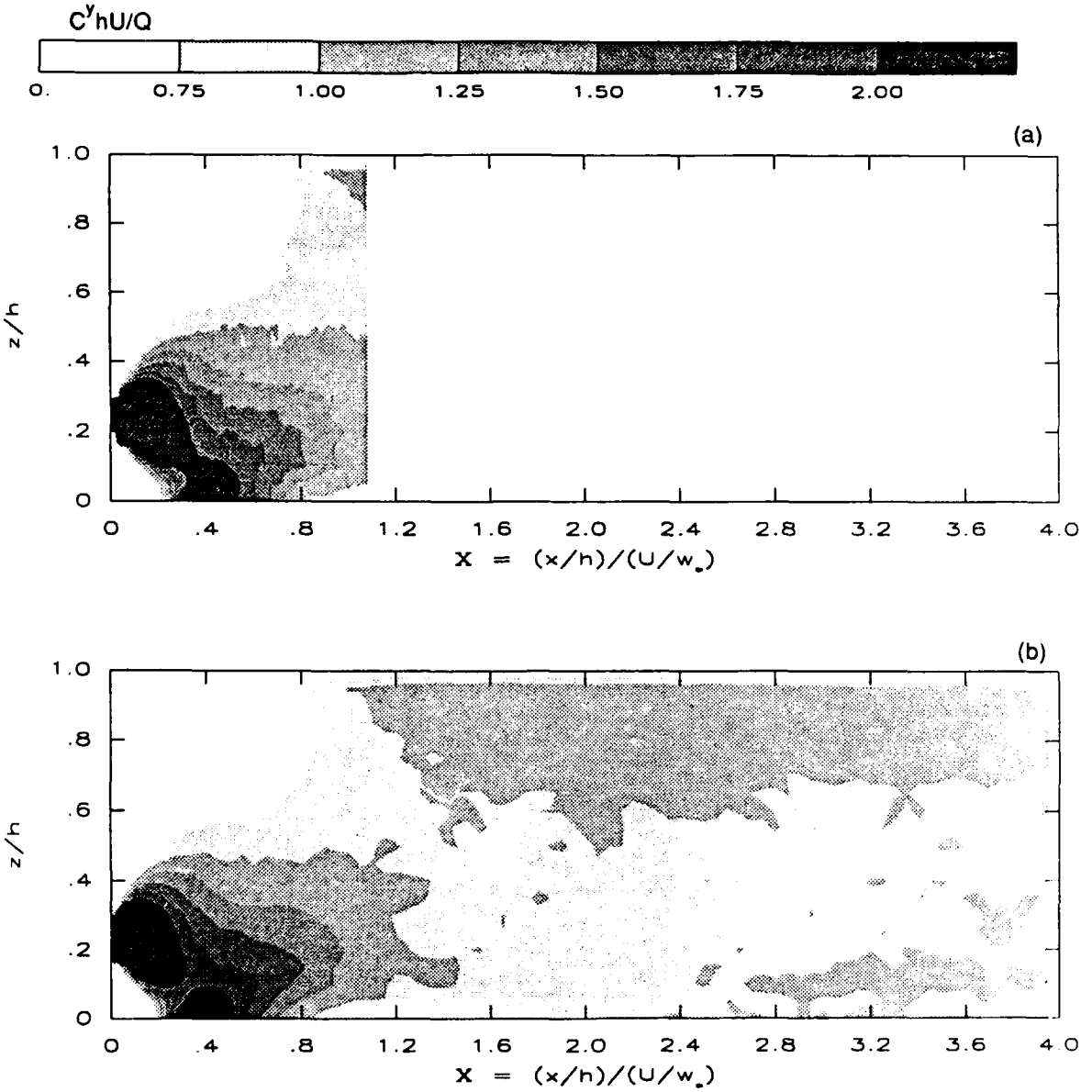

Figure 4.17 Non-dimensional crosswind-integrated concentration distributions computed from the stochastic simulation results for $\zeta = 50$, $U = U(z)$ and $z_0/h = 0.24$: (a) $C^y(x,z)hU/Q$ and (b) $C^y_{wD}(X,z)\ hU/Q$.

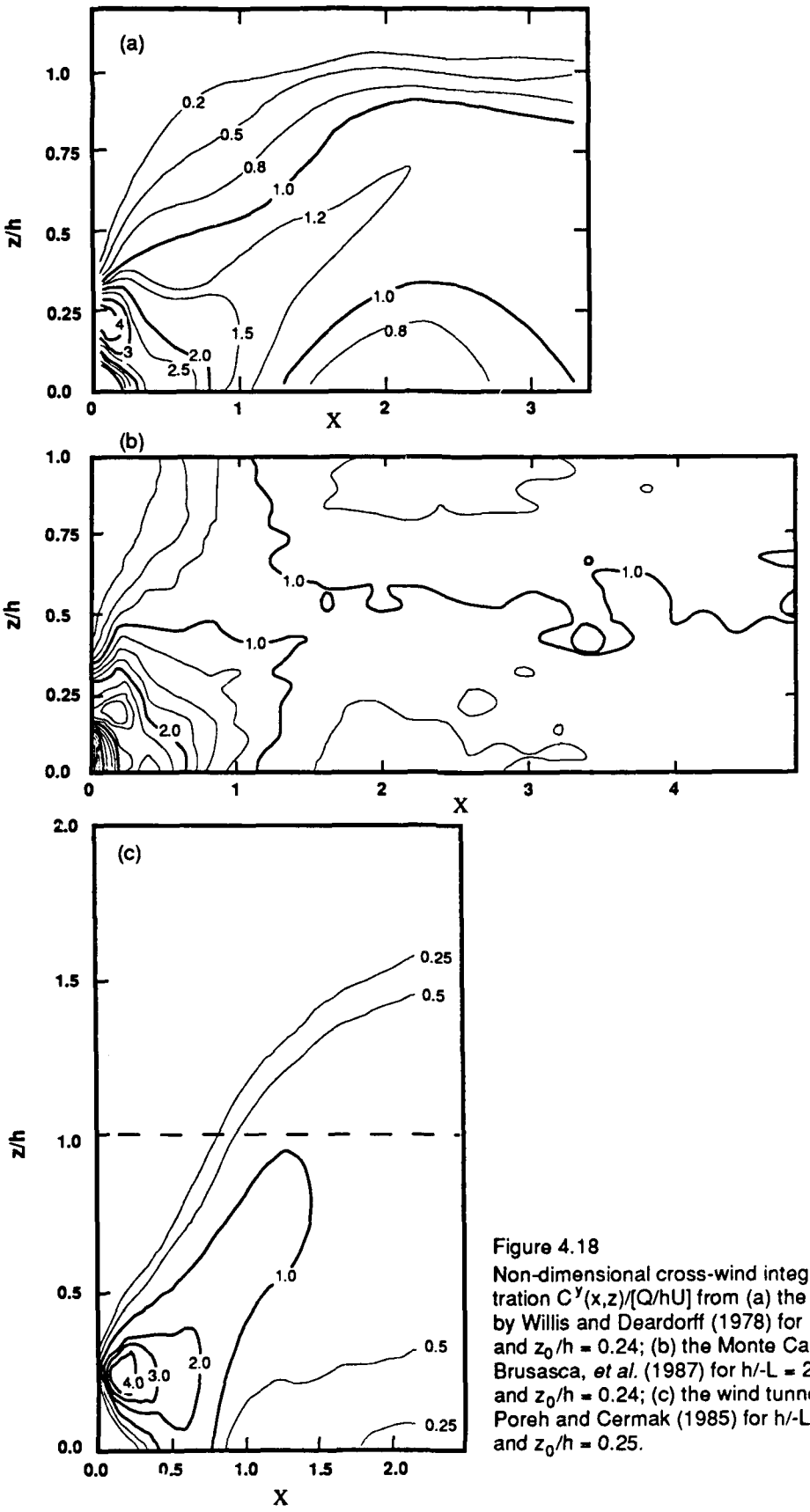

Figure 4.18
Non-dimensional cross-wind integrated concentration $C^y(x,z)/[Q/hU]$ from (a) the water tank study by Willis and Deardorff (1978) for $1.5 \leq U/w_* \leq 6$ and $z_0/h = 0.24$; (b) the Monte Carlo model of Brusasca, *et al.* (1987) for $h/-L = 200$, $U/w_* = 1.56$ and $z_0/h = 0.24$; (c) the wind tunnel simulation of Poreh and Cermak (1985) for $h/-L \approx 10$, $U/w_* \approx 8$ and $z_0/h = 0.25$.

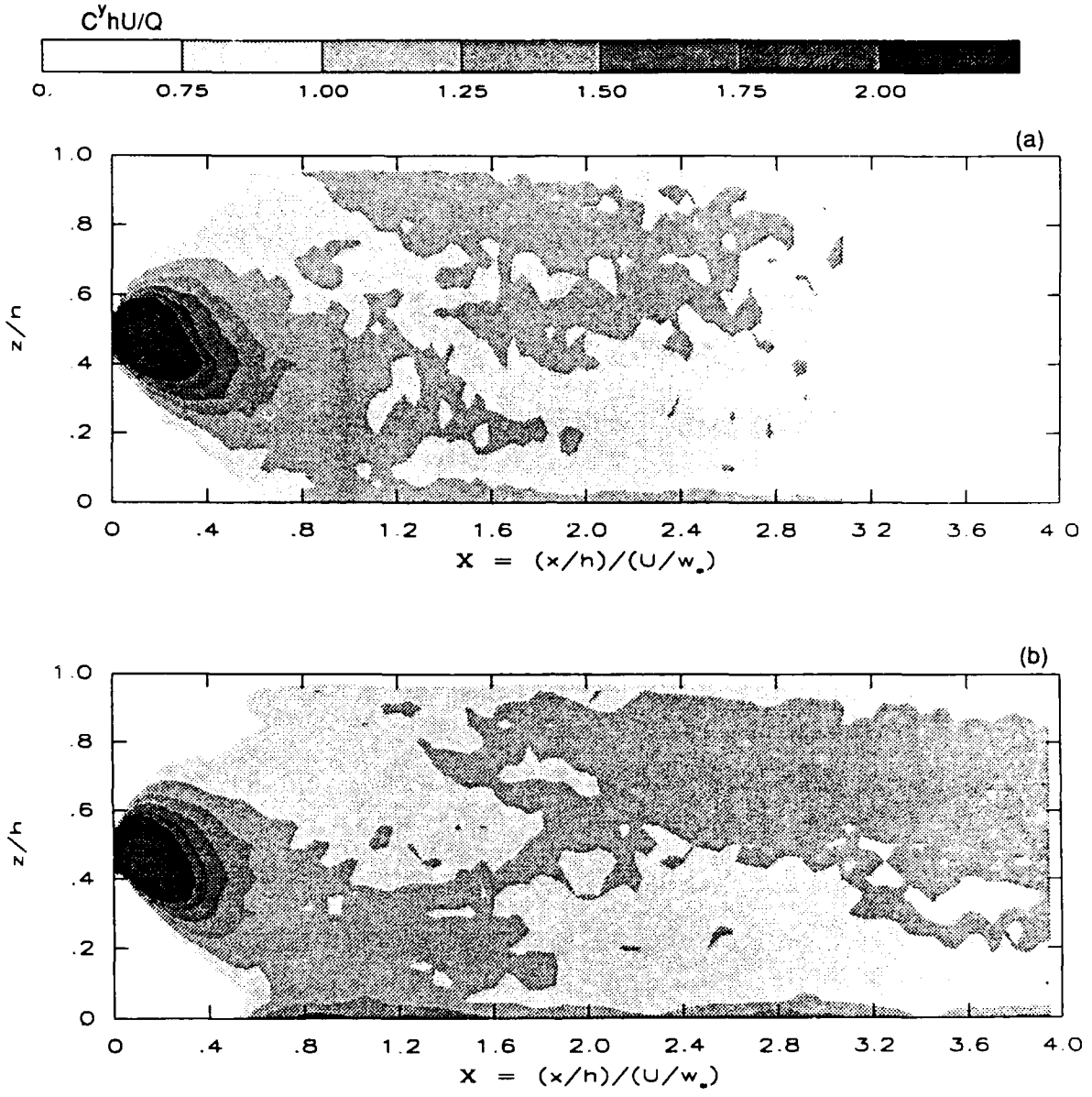

Figure 4.19 Non-dimensional crosswind-integrated concentration distributions computed from the stochastic simulation results for $\zeta = 500$, U = constant and $z_0/h = 0.49$: (a) $C^y(x,z)hU/Q$ and (b) $C^y_{WD}(X,z)\ hU/Q$.

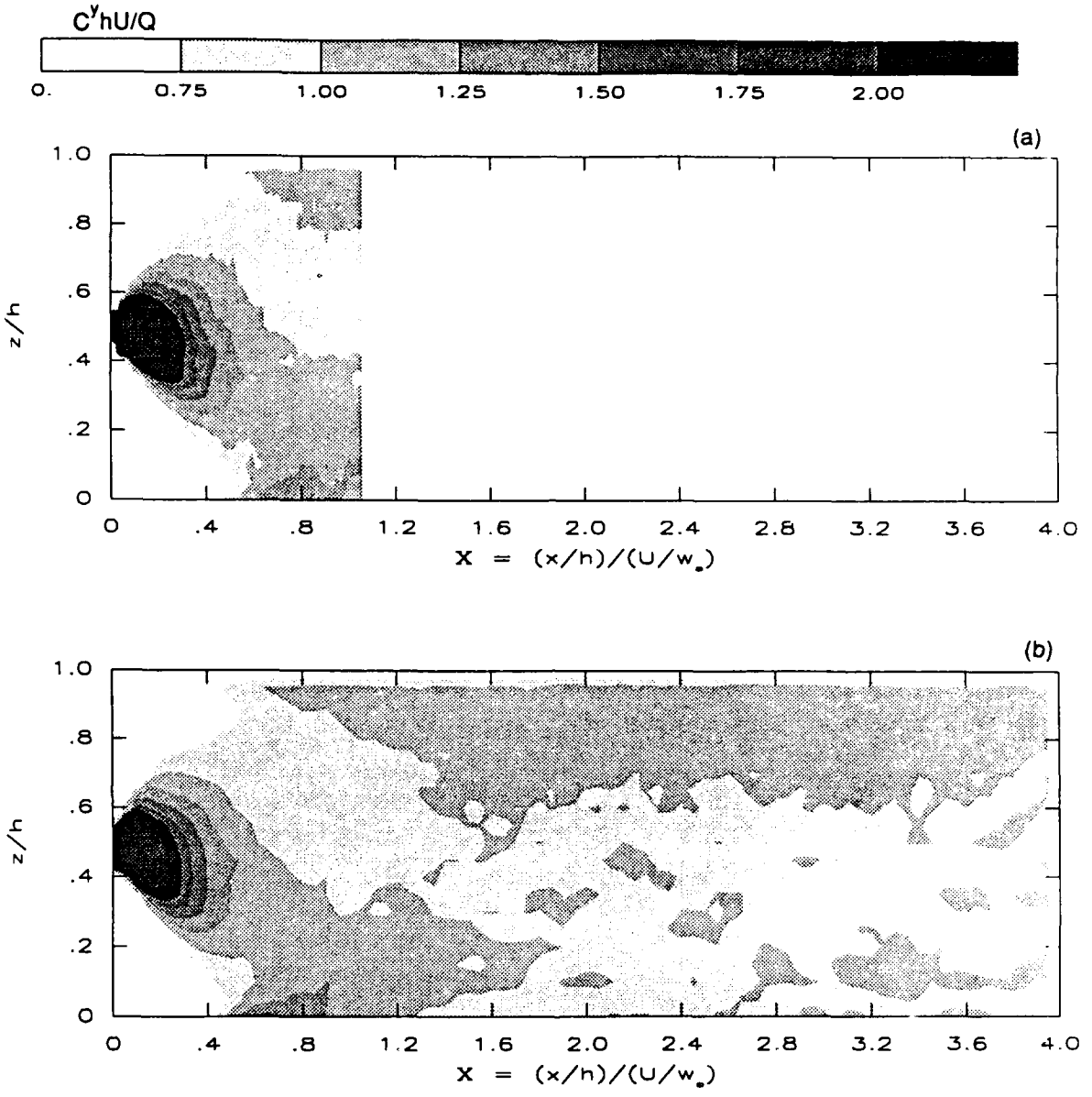

Figure 4.20 Non-dimensional crosswind-integrated concentration distributions computed from the stochastic simulation results for $\zeta = 50$, $U = U(z)$ and $z_0/h = 0.49$: (a) $C^y(x,z)hU/Q$ and (b) $C^y_{WD}(X,z)\ hU/Q$.

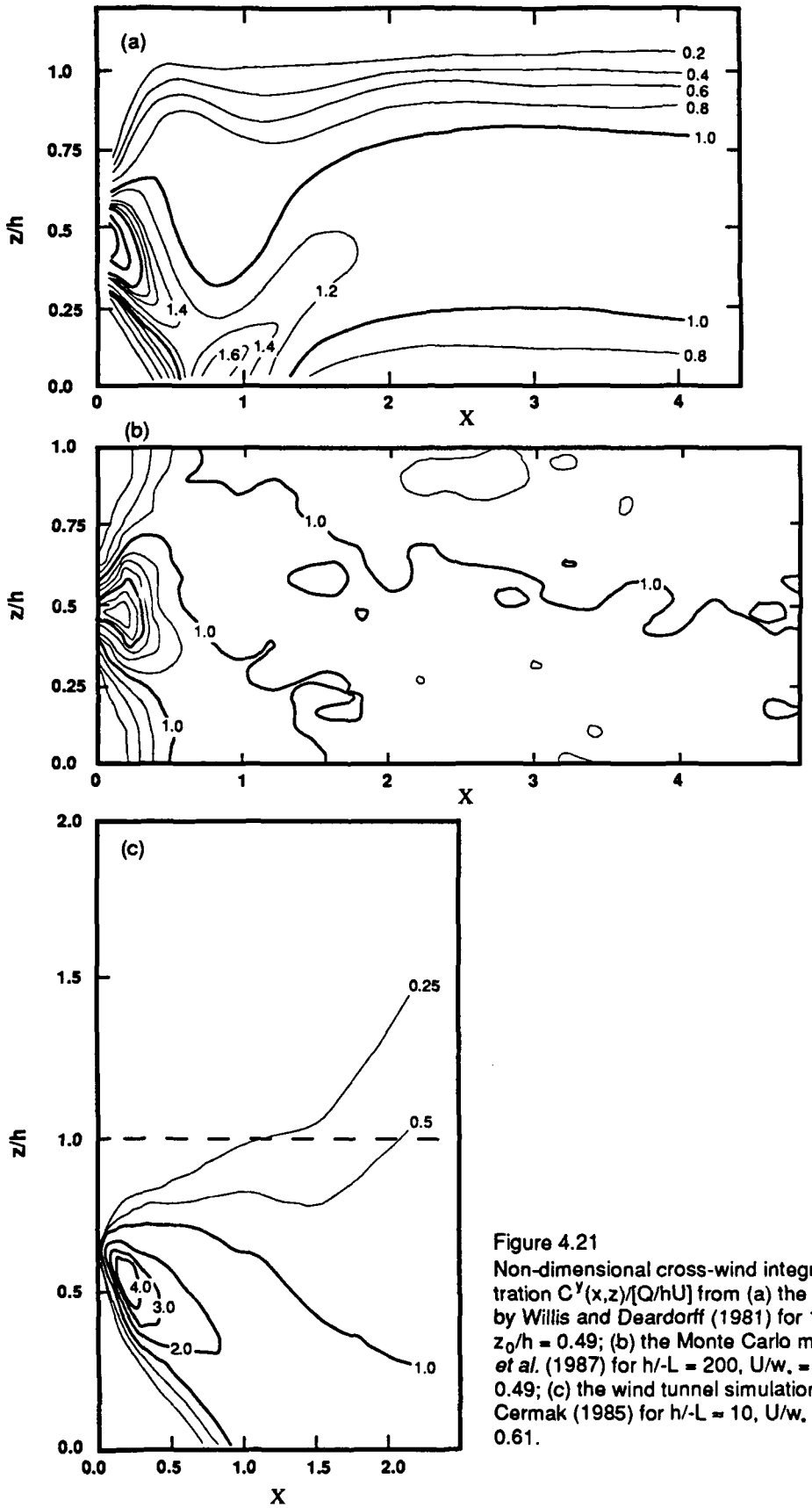

Figure 4.21
Non-dimensional cross-wind integrated concentration $C^y(x,z)/[Q/hU]$ from (a) the water tank study by Willis and Deardorff (1981) for $1.5 \leq U/w_* \leq 6$ and $z_0/h = 0.49$; (b) the Monte Carlo model of Brusasca, *et al.* (1987) for $h/-L = 200$, $U/w_* = 1.56$ and $z_0/h = 0.49$; (c) the wind tunnel simulation of Poreh and Cermak (1985) for $h/-L \approx 10$, $U/w_* \approx 8$ and $z_0/h = 0.61$.

secondary ascent once the plume has reached the surface. Both the Monte Carlo results of Brusasca et al. (1987) given in Fig. 4.21(b) for $z_0/h = 0.49$ and Poreh and Cermak's (1985) results, presented in Fig. 4.21(c) for a release height of $z_0/h = 0.6$, show the initial descent of the plume due to the subsidence but neither indicate a subsequent lift off as indicated by WD3.

In Fig. 4.22 we present crosswind-integrated concentrations computed with the stochastic model for $\zeta = 500$, a uniform mean wind $U/w_* = 1.0$ with a release height $z_0/h = 0.0025$. Figure 4.22(b) is overlaid with concentration isopleths computed from WD1, for which $z_0/h = 0.067$, since the trends exhibited by this case are very similar. In Fig. 4.22(a), for which streamwise diffusion is included, the particles move horizontally somewhat prior to ascending to the inversion height whereas in Fig. 4.22(b), neglecting streamwise diffusion, the particles appear to rise immediately. Streamwise gradients are much greater in Fig. 4.22(b) than in 4.22(a). Moving downwind, it is apparent that streamwise diffusion causes the particles to disperse more rapidly. Our results for this release height with $\zeta = 50$ and $U/w_* = 2.6$ are presented in Fig. 4.23. These results are quite similar to those for $\zeta = 500$ and to DW1.

These results can be further compared with crosswind-integrated concentrations of aluminized mylar chaff from the Project CONDORS data presented in Fig. 4.24. Figure 4.24(a) shows the results of Test 4-82 for which $U/w_* = 1.33$; the results of Test 5-82 having $U/w_* = 0.87$ are plotted in Fig. 4.24(b). The data indicate slightly higher concentrations than the model due to the fact that the chaff was not a conservative tracer. The total amount of chaff which was airborne declined with distance from the release point because of its relatively high settling velocity. In fact, the large near-ground concentrations at $X < 1$ are largely the result of the clumping and settling of the chaff. Nevertheless, the trends and the approximate magnitudes of the chaff data are quite similar to both WD1 and our model predictions.

4.3.4 Ground-Level Crosswind-Integrated Concentration

Because we are primarily interested in ground-level concentrations, we next consider comparisons of the crosswind-integrated dimensionless concentration at ground level predicted using our stochastic model with the results of various laboratory and atmospheric experiments. In order to determine the ground-level values with greater statistical accuracy, the results in this section were computed from simulations with 2000 particles using the estimator developed by Boughton et al. (1987).

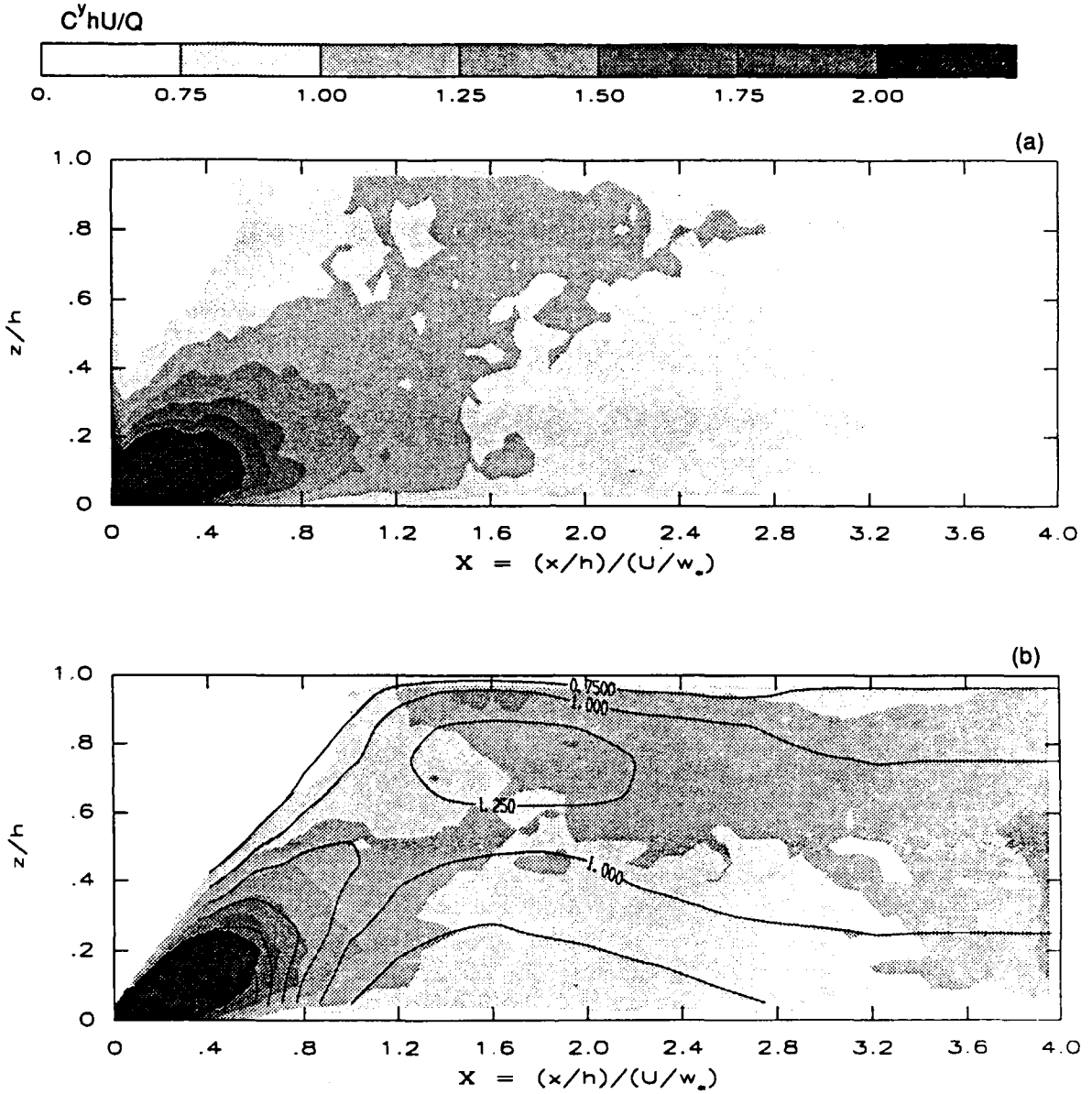

Figure 4.22 Non-dimensional cro swind-integrated concentration distributions computed from the stochastic simulation results for $\zeta = 500$, U = constant and $z_0/h = 0.0025$: (a) $C^y(x,z)hU/Q$ and (b) $C^y_{WD}(X,z)\ hU/Q$.

Dimensionless ground-level concentrations computed with our model for ζ = 500 are compared with data from WD1, WD2 and WD3 in Fig. 4.25 for (a) z_0/h = 0.067, (b) z_0/h = 0.24 and (c) z_0/h = 0.49. Note that the values attributed to Willis and Deardorff in Figs. 4.25(b) and (c) were actually determined by deBaas et al. (1986) using

$$C^y(x,z=0) = \int_{-\infty}^{\infty} C(x,y,0)\frac{dy}{h} = \int_{-\infty}^{\infty} C(x,0,0)\exp\left[-\frac{y^2}{\sigma_y^2}\right]\frac{dy}{h} = \sqrt{2\pi}\frac{\sigma_y}{h}C(x,0,0) \quad (4.8)$$

and the values of C(x,0,0) and $\frac{\sigma_y}{h}$ reported in WD2 and WD3. We have verified the calculations.

As the plume initially sinks to the surface, the ground-level concentration rises to a maximum at $X \approx 2\ z_0/h$. This has been observed in other data by Briggs et al. (1983). The value of the maximum concentration is reduced if the effect of streamwise diffusion is significant, as it clearly is for ζ = 500. As the plume ascends, the concentration declines. When the effect of streamwise diffusion is non-negligible the dimensionless concentration at the ground declines smoothly to unity, indicating a uniform vertical concentration distribution. If streamwise diffusion may be neglected, then the dimensionless concentration at the ground will fall below unity indicating a concentration maximum aloft. The model predictions for z_0/h = 0.067 and 0.24 agree moderately well with Willis and Deardorff's results. For z_0/h = 0.49 the model (neglecting diffusion) predicts a lower, broader maximum concentration than WD3. This is consistent with the slower secondary ascent or lift off noted in the discussion of Figs. 4.19, 4.20 and 4.21. Note, however, that since Willis and Deardorff computed concentrations by counting the number of particles in square bins measuring $\Delta z/h$ = 0.05 on a side, the lowest concentration is not actually at the surface, as the model predicts, but rather is positioned at the centroid of the counting volume, z/h = 0.025. For a typical convective boundary layer where h = 1000 m, this would correspond to an elevation of 25 m above the ground. Similarly, the lowest lidar scan of the oil fog plume during Project CONDORS was at an elevation of 50 m. Thus, one might expect higher, more sharply peaked estimates of C^y from these data.

The results of our model for z_0/h = 0.0025 and ζ = 500 and ζ = 50, both including and neglecting streamwise diffusion, are presented in Fig. 4.26 for comparison with data from fog oil releases of Project CONDORS. As discussed above, when the effects of streamwise diffusion are significant (ζ = 500), the maximum concentration is reduced and the concentration declines more slowly than when

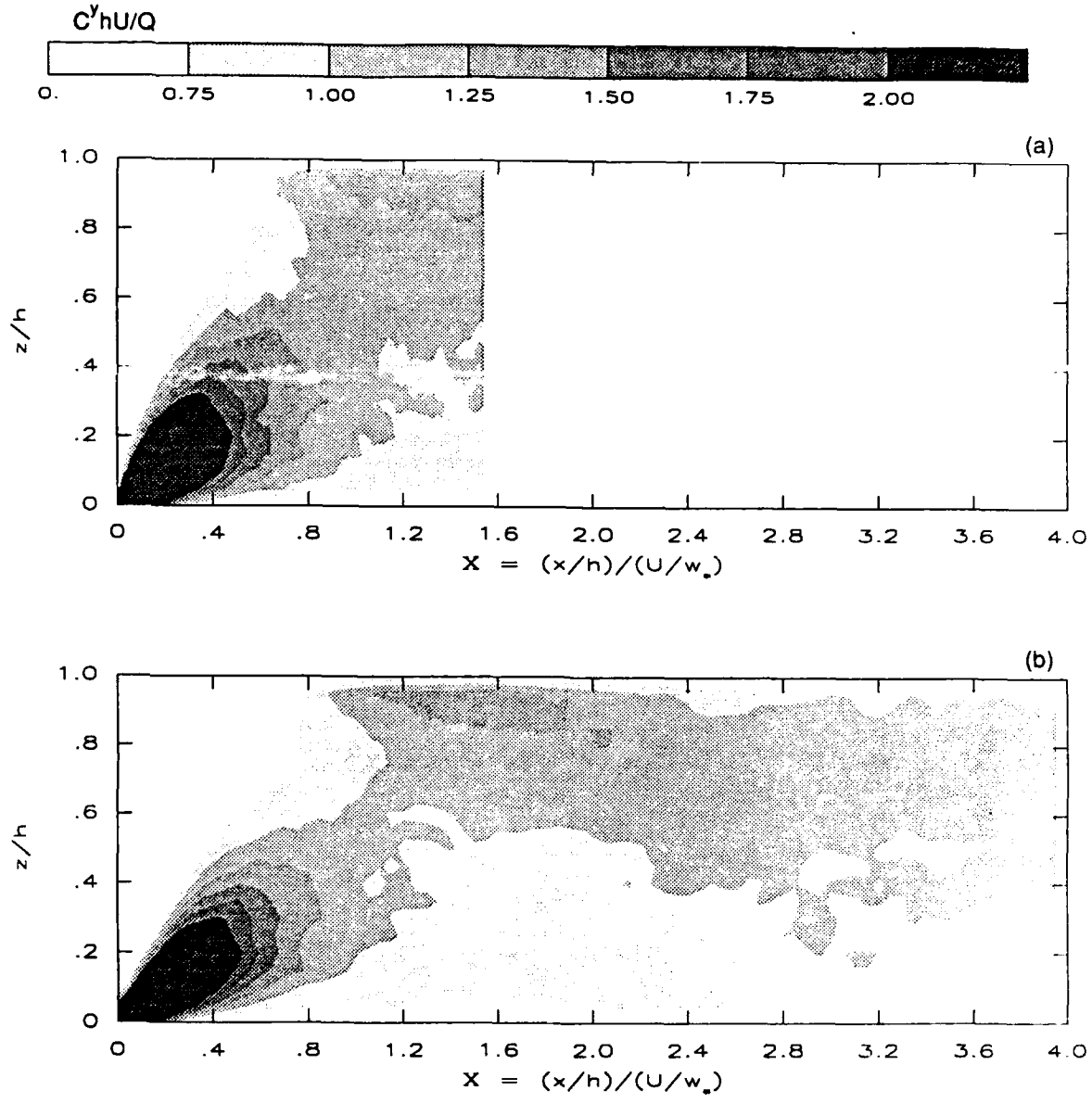

Figure 4.23 Non-dimensional crosswind-integrated concentration distributions computed from the stochastic simulation results for $\zeta = 50$, U = constant and $z_0/h = 0.0025$: (a) $C^y(x,z)hU/Q$ and (b) $C^y_{WD}(X,z)\ hU/Q$.

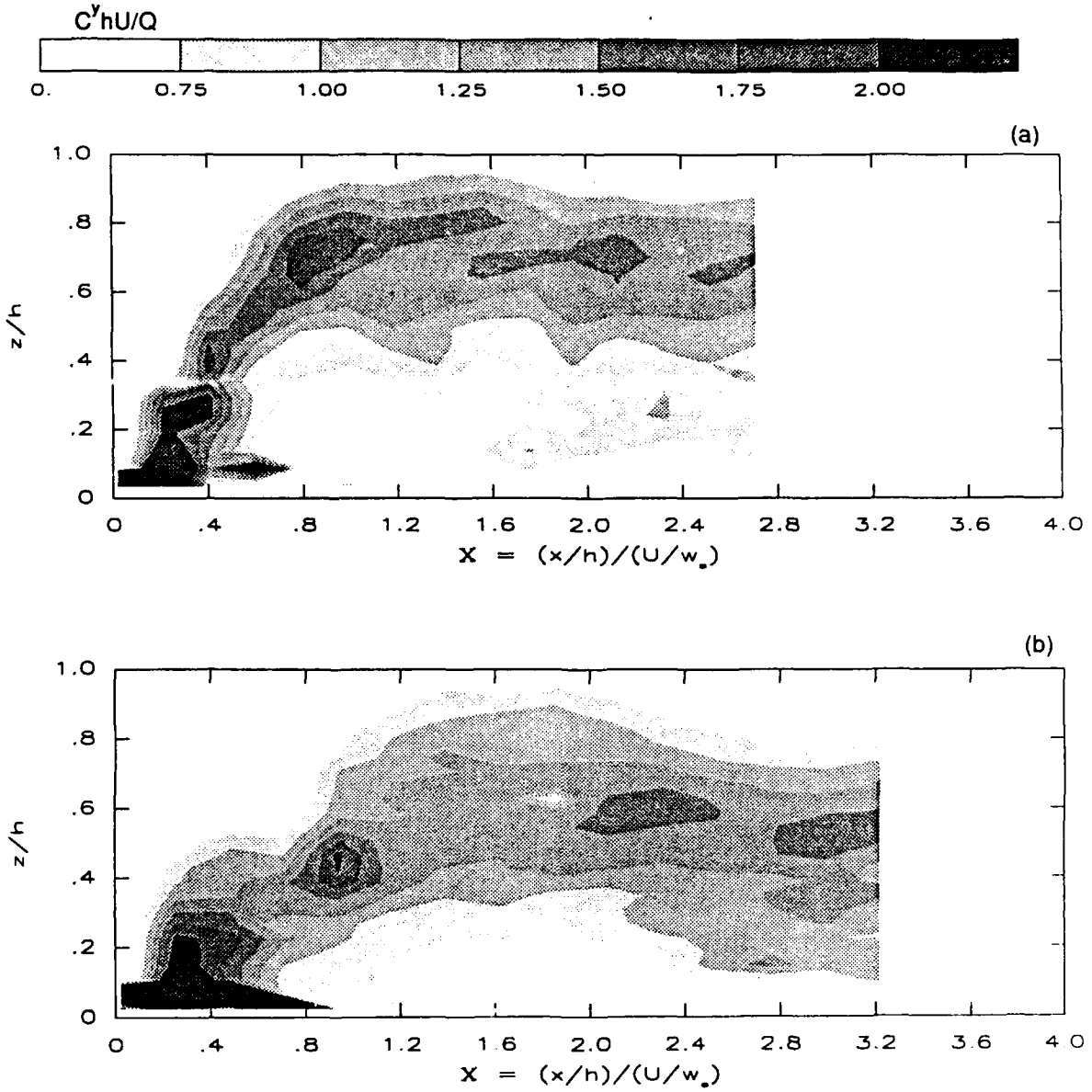

Figure 4.24 Non-dimensional crosswind-integrated concentration distributions from surface releases of aluminized mylar chaff from Project CONDORS for (a) test 4-82 and (b) test 5-82.

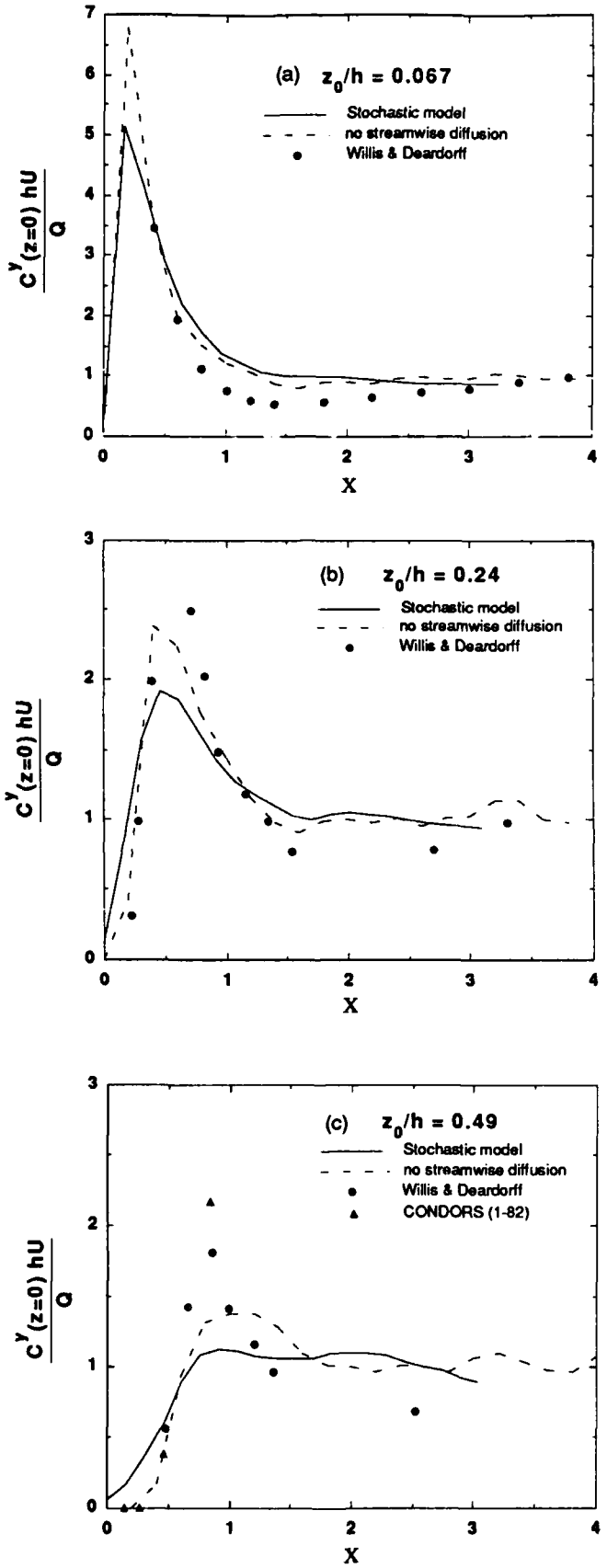

Figure 4.25 Dimensionless crosswind-integrated, ground level concentration for dimensionless release heights of (a) 0.067, (b) 0.24 and (c) 0.49. The results of the stochastic model for h/-L = 500 both including and neglecting the effects of streamwise diffusion are compared with data from Willis and Deardorff and Project CONDORS.

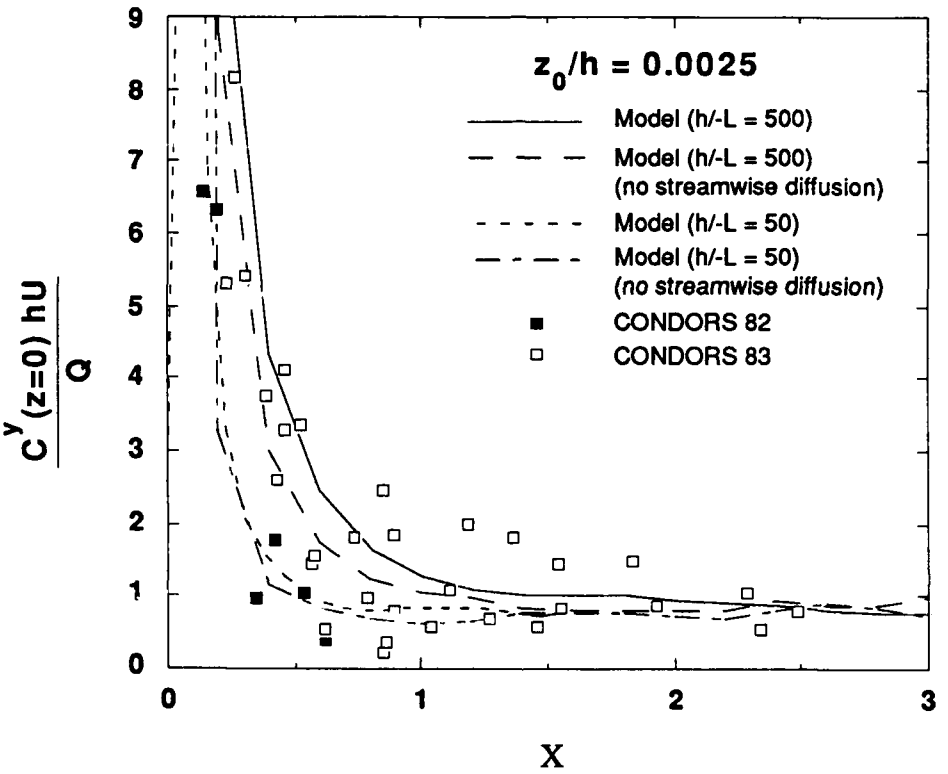

Figure 4.26 Dimensionless crosswind-integrated, ground level concentration as a function of dimensionless downwind distance for a near-surface release. Predictions of the stochastic model for h/-L = 500 and h/-L = 50 are presented both including and neglecting streamwise diffusion. Data from Project CONDORS for oil fog tracer tests during 1982 and 1983 are presented for comparison.

streamwise diffusion is neglected. However, when streamwise diffusion is relatively unimportant (ζ = 50) the concentration maximum is sharply peaked and declines rapidly to values less than unity indicating an elevated maximum as previously discussed.

The results for CONDORS 82 are distinguished from CONDORS 83 because the lower molecular weight oil used during the first summer was suspected of being non-conserving due to evaporation. This would cause the measured concentrations to decline with distance from the source more rapidly than might otherwise be expected. In fact, the concentration values from CONDORS 82 are less than those from CONDORS 83, although only slightly. The CONDORS data support the model predictions for the most part. The tests which appear to support higher concentrations than the model predicts were those for which substantial ambiguity existed in the inversion height data. Had a lesser value for the inversion height been used, as some of the temperature and humidity profile data suggest, the values computed for both the dimensionless concentration and the dimensionless downwind distance would have been reduced, resulting in superior agreement with the model results.

4.4 Summary

In this chapter we have verified the predictions of our stochastic dispersion model against 1) limiting cases derived from dispersion theory, 2) laboratory data from water tank and wind tunnel simulations of the convective planetary boundary layer, 3) experimental data from several field studies of atmospheric dispersion, and 4) other, more heuristic, Monte Carlo models. The comparisons were performed for both near-surface and elevated release heights (z_0/h = 0.0025, 0.067, 0.024 and 0.049) and covered a wide range of convective conditions ($5 \leq \zeta \leq 500$).

Comparisons of mean plume height and vertical plume spread with theoretical limits for both small ($X \rightarrow 0$) and large ($X \rightarrow \infty$) dimensionless travel time showed generally good agreement. Similar comparisons with laboratory data from water tank simulations conducted by Willis and Deardorff and with atmospheric data from Project CONDORS also supported the model predictions. Small differences between the model predictions and the water tank data could not be resolved by comparison with the CONDORS results owing to the scatter in the atmospheric data.

Our model predictions of crosswind plume spread were shown to be in good agreement with Willis and Deardorff's laboratory results as well as atmospheric data from Project Prairie Grass and CONDORS. The model predictions exhibited the

behavior predicted by Taylor's theory for homogeneous turbulence: initially the crosswind spread increased in proportion to travel time; eventually the rate of increase became proportional to the square root of travel time.

The vertical distributions of the crosswind-integrated concentration predicted by our model for near-surface and elevated releases exhibited the same trends as did laboratory data from Willis and Deardorff's water tank simulations. The effects of streamwise diffusion were seen to be important only at very low wind speeds ($\zeta = 500$, $U/w_* < 1.5$) as predicted by Willis and Deardorff. Comparisons with the wind tunnel simulations by Poreh and Cermak for $\zeta \approx 10$ were good at short range but eventually diverged due to the difficulty of achieving a strong capping inversion layer in the wind tunnel. Although the aluminized mylar chaff used as a tracer during Project CONDORS had a substantial settling velocity, comparisons of the data from two near-surface releases demonstrated encouraging qualitative agreement with model predictions.

Comparisons of crosswind-integrated ground-level concentrations computed by our model with those measured in both simulated and actual convective boundary layers are also in close agreement. The maximum model-predicted ground-level concentration occurs at $X \approx 2\ z_0/h$, in agreement with the data presented herein and with other data examined by Briggs (1983). The larger values for the maximum ground-level concentration indicated by the data may have resulted from the relatively large distance above the surface at which these "ground-level" values were measured.

This high level of agreement clearly demonstrates the power of the convective scaling since our model is totally predictive. That is, the stability parameter $\zeta = h/-L$ and the release height z_0/h are the only input quantities. Estimates of the turbulent Eulerian velocity moments, from which the Lagrangian velocity moments of the dispersing particles are computed, are determined from convectively scaled formulas summarizing extensive atmospheric turbulence research rather than from direct, on-site measurements. Thus, the degree to which these formulas are representative of convective turbulence in general is also indicated by the agreement between our model predictions and the various data with which they have been compared.

These results underscore the important role that convection plays in dispersing pollutants in the daytime planetary boundary layer. Moreover, the results demonstrate that convective behavior can control the dispersion from a ground-level source even for "slightly convective" atmospheric conditions, since $\zeta = 10$ in a typical boundary layer 1000 m deep corresponds to a Monin-Obukhov length $L = -100$. Thus convective dispersion can be significant even on relatively cloudy days. This is a valuable result

since convective effects such as the lift-off of the plume centerline were previously believed to be important only for low-wind, high-insolation situations.

5. THE ATTERBURY-87 DISPERSION STUDY

A major impediment in the development of both applied and research models is the lack of experimental data which adequately describe atmospheric dispersion. Although many experimental investigations of the phenomena have been performed, few provide complete, simultaneous descriptions of the characteristics of the prevailing meteorology and the material plume. Such complete data sets are essential to provide insight into the physics of atmospheric dispersion as well as for the development and validation of better modeling approaches.

In this chapter we describe the procedures and results of our field study at the Atterbury Reserve Forces Training Area during the autumn of 1987. This field study, which we will refer to as Atterbury-87, is one of three we have conducted as part of a larger effort by the US Army to assess the environmental impact of military obscurant smokes deployed during training exercises. The main objective of the Atterbury-87 study was to acquire a comprehensive database describing the dispersion of fog-oil and hexachloroethane (HC) smokes over flat terrain under a variety of atmospheric conditions.

The study was carried out over a five week period in October and November 1987 at the Atterbury Reserve Forces Training Center (ARFTC) near Columbus, Indiana. The five week period was divided into three phases. During the set-up phase comprising the first two weeks, the test site was surveyed, the sampling network was erected and the equipment was deployed. Releases of fog-oil smoke were performed during the first week of the testing phase; the second week of testing was devoted to HC smoke releases. The last week was spent tearing down the sampling network and removing the equipment from the field.

In all, four fog oil tests and five HC tests were carried out. The tests were designated by the date and test number on that date. For example, the test designated 1104872 was the second test executed on 4 November 1987. Of these nine tests, eight were completely successful. Sufficient data was acquired for environmental assessment purposes as well as for model evaluation and improvement. Despite operational difficulties with the M3A4 generator and meteorological data acquisition system, Test 1104871 was still marginally successful.

In order to provide a context for discussing our efforts we will begin by examining previous field studies. Rather than provide an exhaustive review, we will limit the discussion to those studies which are relevant to the current purpose.

5.1 Previous Experimental Studies

5.1.1 Project Prairie Grass

Project Prairie Grass (Barad, 1956), the first comprehensive study of atmospheric dispersion, was comprised of 70 experiments carried out during the summer of 1956 by a large team comprised of participants from several universities under the direction of the Air Force Cambridge Research Center. The experiments were conducted for the purpose of measuring time-average concentrations downwind from a continuous point source under a variety of meteorological conditions in order to provide as broad a database as possible for the study of atmospheric dispersion and for the evaluation and improvement of dispersion models.

The test site, a mowed hay-field in north-central Nebraska covering 2.6 km^2 (1 sq. mi.), was extremely flat having no more than a 1 m deviation from the mean elevation of 604 m above sea level over the area covered by the sampling network. The terrain surrounding the test site was nearly as flat: a small "hill" 800 m upwind of the release point rose only 6 m above the local terrain. After mowing, the site was covered with stubble 5 to 6 cm high.

For each test, gaseous sulphur dioxide (SO_2) was released into the atmosphere at rates of 40 to 100 g/s, depending on meteorological conditions, for a period of 10 minutes. For most of the tests the release height was 0.5 m although several experiments were conducted for a release height of 1.5 m.

Concentration measurements were performed with an array of 599 midget impingers (bubblers). The impingers were positioned at an elevation of 1.5 m on five semi-circular arcs located 50, 100, 200, 400, and 800 m from the source. They were spaced 2° apart on all but the 800 m arc where the spacing was reduced to 1°. Vertical dosage profiles were obtained from nine impingers located at elevations of 0.5, 1.0, 1.5, 2.5, 4.5, 7.5, 10.5, 13.5 and 17.5 m on each of six towers placed at 14° intervals on the 100 m arc. The impingers were aspirated at 1.0 liter/min (Lpm) on the 50 and 100 m arc and at 1.5 Lpm on the remaining arcs.

When air containing sulphur dioxide was bubbled through an impinger the SO_2 reacted with the 10 ml of dilute hydrogen peroxide in the impinger to form sulfuric acid. Subsequent to each test, the impingers were retrieved from the field and the electrical conductivity of the solution in each impinger was measured. This conductivity was then related to the airborne concentration of SO_2. Although the uncertainty in the

measured conductances was estimated to be less than 2%, the accuracy of the reported concentrations was estimated to be ±10% due chiefly to evaporation of the hydrogen peroxide solution during the course of a test.

Slow-response measurements of wind speed and direction fluctuations were performed with cup anemometers and wind vanes designed and built by participants from the Massachusetts Institute of Technology (MIT). The starting threshold for the cups was 0.8 m/s. These were mounted at an elevation of 2 m for two locations. One location was 25 m west of the source (along the baseline of the sampling network) and the other was 450 m north (downwind) and 30 m west of the network centerline. The reported ten and twenty-minute averages were computed from these data. Additional wind measurements were performed 900 m downwind with faster response instrumentation by participants from Texas A & M University. They measured wind speed at heights of 0.25, 0.5, 1, 2, 4 and 8 m. From these data covariances and spectra were computed. Air temperature profiles were also measured 900 m downwind with thermal radiation-shielded thermocouples mounted at elevations of 0.125 to 4 m.

Despite the short duration of these tests (10 minutes), the results of Project Prairie Grass have been utilized to evaluate three decades of atmospheric dispersion modelling efforts. The Pasquill-Gifford formulas (Gifford, 1961) relating the Gaussian plume parameters to atmospheric stability were developed from these data. Draxler (1976) used these data to relate the Gaussian plume parameters to on-site measurements of wind speed and the standard deviations of the horizontal and vertical velocity fluctuations.

5.1.2 The Hanford Series

Another more extensive series of dispersion experiments was carried out between 1959 and 1974 at the Hanford nuclear reservation near Richland, Washington by the Pacific Northwest Laboratory (PNL) for the Nuclear Regulatory Commission. The Hanford Series (Nickola, 1977; Nickola et al., 1983) is comprised of ten separate series totaling over 200 experiments. In the course of these tests a variety of particulate and gaseous tracers were released from ground-level and elevated point sources for a wide range of atmospheric conditions.

The site of the Hanford experiments was located in the southwest corner of the State of Washington. The elevation of the area covered by the sampling grid varied

between 200 and 230 m above mean sea level. The ground cover included sagebrush 1 to 2 m high interspersed with steppe grasses.

The sampling network at the Hanford test site was actually comprised of two grids, "S" and "U". The source of the U grid was located at the base of a 122-m meteorological tower. The source of the S grid, used only for ground-level releases, was displaced 100 m south of the U grid to avoid the wake of the 122-m tower. Both grids had sampling arcs at 100, 200, 300, 400, 500, 600, 800, 1600 and 3200 m from their source. Approximately 1000 samplers could be located along these arcs at an elevation of 1.5 m. Vertical profiles could be obtained from 365 sampler positions on 20 towers located on these arcs. Despite the large number of potential sampling positions available, only a portion of the sampling network was actually used for most experiments.

Meteorological measurements carried out on the 122-m tower included vertical profiles of the mean temperature, wind speed and wind direction as well as the standard deviation of the wind direction, all computed over the period of the release. Temperature measurements were accomplished with aspirated Foxboro RTDs at elevations of 0.9, 15.2, 30.5, 45.7, 61.0, 91.4 and 122 m. Wind speed and direction were measured with Aerovane propeller-vanes at 2.1, 15.2, 30.5, 45.7, 61.0, 91.4 and 122 m. The threshold speed for the propellers was ~1 m/s. The distance constants for speed and direction were 4.5 and 10 m, respectively. Wind speed and direction data were also available from a 25-m tower generally located near the point of release. These data were gathered using Beckman and Whitley cup anemometers and wind vanes mounted at 0.76, 1.5, 3.0, 6.1, 12.2 and 24.4 m.

The Hanford data can be organized into two groups. The Primary Series accounts for 195 experiments, in almost all of which fluorescent paint pigment ZnS was released. The Secondary Series accounts for the remaining 26 experiments and involved multiple tracers, one of which was always ZnS. The ZnS particulate had a mass median diameter of 4.1 microns and a specific gravity of 4.1. It was mixed with water (1-4 kg to ~150 liters) and dispersed into the atmosphere by mixing with the 400 °C air jet of an insecticide sprayer. The tracer was collected on aspirated PVC membrane filters with an exposed diameter of 41 mm. The exposed filters were subjected to a source of alpha particles which caused the ZnS to fluoresce. The scintillations were counted with a photodetector and related to airborne concentrations via prior calibration. Corrections for non-isokinetic sampling were based on wind tunnel studies conducted by Sehmel (1967).

Although apparently more extensive than the Prairie Grass database, the Hanford data has not been as extensively utilized, judging from citations in the literature. This may be due in part to the fact that the bulk of the data was not available until as recently as 1983 although PNL staff members have previously published analyses based on these studies (Doran, Horst and Nickola; 1978a, 1978b).

5.1.3 The Borris Field Experiment

The Borris Field Experiment (Mikkelsen, 1983), which constitutes a photographic study of atmospheric diffusion, was conducted to provide data for the evaluation of a specific Gaussian puff dispersion model (Mikkelsen, 1982). The experiments were conducted in a grassy meadow near Borris, Denmark. Hexachloroethane (HC) smoke was released at ground-level creating a dense white plume visible for ~1 km downwind. The visible contour of the smoke plume was recorded on photographs taken from an aircraft against a network of white contrast plates. These plates where placed on the ground along five transects located at 31.25, 62.5, 125, 250 and 500 m from the source.

During each of the ten experiments, approximately 20 photographs were taken at roughly 2-minute intervals from altitudes of 300 to 1800 m. The visible contours of the plume and the locations of the marker plates were digitized and the resulting data used to determine the instantaneous lateral position and the visible half-width of the plume. Assuming an instantaneous Gaussian displacement distribution function for the smoke particles, the lateral standard deviation of the instantaneous plume was computed using a method suggested by Gifford (1980).

Data regarding the prevailing meteorology were acquired with three-axis sonic anemometers/thermometers mounted on the top of four 10-m towers. Spectra, auto- and cross-covariances and mean values of the wind velocity components were computed from this data. In addition, direct monitoring of wind speed and direction were facilitated by a cup anemometer and vane mounted near the top of one of the towers.

5.1.4 Smoke Week Data

Data describing the dispersion of military obscurant smokes in the atmosphere were obtained from experiments conducted during annual Smoke Week field trials. The primary purpose of these experiments was to study the relationship between smoke concentration and obscuration performance as measured by transmission loss

along a line of sight passing through the plume. In a typical test, 40 to 50 concentration samplers were set out along two transects approximately normal to the expected plume centerline and roughly 100 m from the source. Transmission along each line of sight was measured using a transmitter/receiver pair spanning the transect. Each sampling station along the transect typically consisted of an aerosol photometer to measure instantaneous concentration and a chemical impinger to measure time-average concentration. In some cases the particle size distribution was measured at a single location, about 50 m from the source.

Because these tests focused on evaluating the obscuration performance of the smokes, little effort was devoted to defining the relationship between source characteristics and downwind concentrations. Accordingly, Policastro and Dunn (1985) concluded that the Smoke Week data were insufficient for environmental assessment and model evaluation purposes. However, despite their limitations the data proved useful in planning our field studies.

5.1.5 Summary of Previous Dispersion Studies

A thorough examination of the dispersion studies described above reveals several common aspects. All of these studies were restricted to dispersion phenomena in the atmospheric microscale, as defined in Chapter 1. Thus, the length scales of interest are limited to 2 km in the horizontal direction and the depth of the boundary layer in the vertical. Since there is a strong effect of the terrain on the microscale meteorology, the sites were carefully chosen so as to approximate as closely as possible the ideal boundary layer over a flat plate and thus facilitate comparison with theoretical predictions and laboratory measurements of ideal boundary layers.

The measurements which were performed during these studies were designed to define the four major aspects of the dispersion problem: 1) the source of the tracer, which determines the initial conditions, 2) the chemical and physical nature of the tracer (e.g.: particle size), 3) the micrometeorology of the boundary layer in which the tracer is dispersing and 4) the transport and dispersion of the tracer in terms of the material concentration distribution. Accordingly, the Atterbury-87 field study was designed to accurately quantify each of these areas in order to produce a high-quality database for environmental assessment as well as model evaluation and improvement. In the following sections we will describe the procedures employed and results obtained in order to fully describe each of these aspects of the problem.

5.2 The Test Site

5.2.1 The Interaction of Terrain and Meteorology

The effect of terrain on the microscale meteorology can best be described in terms of the uniformity of elevation and the covering vegetation. For the purpose of the present discussion we will consider the uniformity of the actual test site separately from the uniformity of the surrounding terrain. The test site will be termed "flat" if the variation of the local terrain about the mean elevation is less than 10 m; variations between 10 m and 100 m will be termed "gently rolling" and variations in excess of 100 m will be termed "complex" terrain. Although actual terrain spans a continuous range of horizontal homogeneity, these arbitrary classifications are useful for the discussion of terrain effects. The surrounding terrain spans a similar spectrum of uniformity ranging from flat-to-the-horizon to mountainous.

The vegetation or other roughness elements covering the terrain can also significantly affect the microscale meteorology by increasing the roughness and hence the shear stress at the surface. Typical roughness elements include short grass 2-3 cm high, tall grass 50-100 cm high, brush, trees and buildings. If the roughness elements are distributed homogeneously over a site, it is adequate to characterize them in terms of a "roughness height" marking the height above the ground surface where the wind speed vanishes.

We will use these descriptions of local and surrounding terrain as well as the roughness elements covering the terrain to categorize the interaction of terrain and microscale meteorology as "simple terrain/simple meteorology", "simple terrain/complex meteorology" or "complex terrain/complex meteorology".

For the simple terrain/simple meteorology case the site is uniformly flat in all directions to the horizon. In addition, it is covered with low, homogeneous roughness elements such that the roughness height is on the order of 1 cm. This extreme degree of horizontal homogeneity requires measurements only at a single location to adequately characterize the micrometeorology of the entire site. The mowed hay-field in which Project Prairie Grass was carried out satisfies these criteria and is a major reason for the enduring popularity of the Prairie Grass database. Taller or slightly less homogeneous vegetation only adds a small complexity to the site which can be easily accommodated by a larger value of the roughness height as long as the elevation

remains uniform. For this reason, the site of the Borris Field Study and the Smoke Week tests may also be included in this category.

As the terrain or vegetation deviate from the criteria discussed above, the micrometeorology becomes more complex. If the actual test site remains essentially flat but the upwind terrain is markedly different in elevation or vegetation we may classify the site as simple terrain/complex meteorology. In this case, an increased roughness height is insufficient to fully characterize the effect of the terrain on the meteorology. The influence of the terrain on the power spectra and statistics of the wind velocity fluctuations can be observed. However, the microscale meteorology does not vary significantly over the test site (i.e., statistics are horizontally homogeneous). The Hanford site falls into this category. The Hanford Reservation is located in a 40-km wide basin ringed with mountainous ridges rising roughly 900 m above the elevation of the test site. Although the elevation of the gently rolling terrain varies by approximately 30 m over the sampling network, the micrometeorology may be adequately characterized by measurements performed at a single location on the site.

Finally, as the elevation of the terrain varies significantly (more than about 100 m) the test site is classified as complex terrain/complex meteorology. Dispersion tests carried out over mountainous terrain fall into this category. In these cases measurements must be performed at a number of locations, (the number depending on the degree of variation of the terrain), in order to adequately characterize the the three-dimensional wind field.

As mentioned earlier, we have conducted three field studies of military obscurant smokes for the US Army. The first of these was conducted in March and April of 1985 at Dugway Proving Ground in Utah. The procedures and results of this study have been thoroughly described elsewhere (Liljegren et al., 1988) and will not be repeated here in detail although comparisons with the results of the Atterbury-87 study will be discussed. The Dugway test site was chosen because it satisfied the criteria for simple terrain/simple meteorology discussed above. Since it was located in a desert area, the terrain was flat and uniform in all directions. The terrain was homogeneously covered by a sagebrush-like shrub approximately 50 cm high.

The test sites for our Atterbury-87 and Meadowbrook-87 studies were significantly different from the Dugway site. The Atterbury-87 study was conducted in a grassy field in south-central Indiana which falls into the simple terrain/complex meteorology category because the terrain rises 50 m above the test site less than 1 km upwind of the sampling network. The Atterbury-87 site will be described in greater detail below.

The Meadowbrook-87 site, located 22 km northeast of Red Bluff, California, covers moderately complex terrain along a creek valley 300 m wide by 150 m deep (valley floor to main ridge). Our Meadowbrook-87 study was part of a mesoscale wind field study (Project WIND) jointly organized by the US Army Atmospheric Sciences Laboratory and the US Forest Service and will not be discussed here further.

5.2.2 The Climatology of the Atterbury-87 Test Site

The test site was located in Area 7A of the Atterbury Reserve Forces Training Center (ARFTC) in south-central Indiana near Columbus. The topology of the site and the surrounding terrain are presented in Fig. 5.1 which is taken from the US Geological Survey map "Ninevah, Indiana". As the figure shows, the site is positioned in a meadow among low hills which rise approximately 50 m above the mean site elevation of 218 m above sea level. The meadow was covered primarily with dense grass about 1 m high. The lower portions of the site, where water collected after a rainstorm, were covered with briars, brambles and reeds 1 to 2 m high in addition to grass. The surrounding hills were densely wooded with deciduous trees approximately 20 m high. Prior to the testing period, which spanned the first two weeks of November, the trees had dropped most of their leaves.

The timing of the Atterbury-87 tests and choice of the test site were based primarily on the climatology of the area within the limitations imposed by the availability of the ARFTC facilities and by our participation in Project WIND. An assessment of the climatology of south-central Indiana was performed using data collected by the National Weather Service (NWS) station at the Indianapolis International Airport, located 56 km north of Columbus, during the period 1979-1983. The data, recorded at 1-hr intervals, were analyzed to provide information regarding precipitation, ambient temperature and the prevailing wind speed and direction.

Precipitation was expected to have a severely adverse impact on testing. In addition to obviously precluding the initiation of a planned test or requiring the cancellation of a test in progress, precipitation would cause deterioration of the dirt roads at the ARFTC, hamper both pre-test and post-test field operations and present a potential hazard to the personnel and equipment. Therefore, timing the study for a period of low anticipated precipitation was particularly important.

The ambient temperature was a lesser, but still significant concern since the instruments and the computer equipment could be significantly affected. In addition, the increased viscosity of the SGF-2 fog oil at temperatures below 0°C requires that

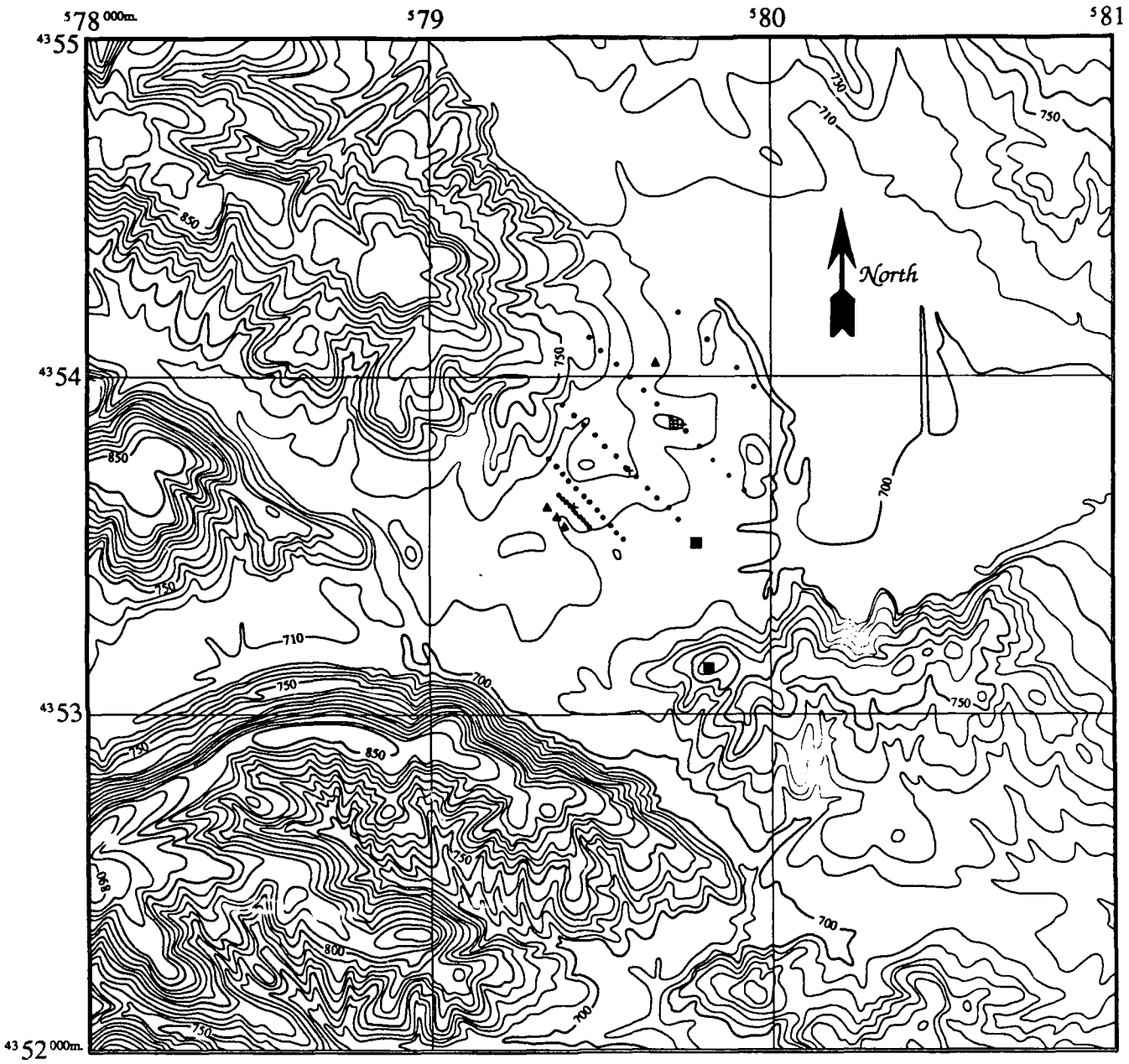

Figure 5.1 Topological map of the dispersion test site at Camp Atterbury. Elevations are in feet above sea level. North and East Universal Transverse Meridian (UTM) coordinates are given in meters. Sampling mast locations are indicated with filled circles [●]. Filled triangles [▲] indicate the various release points. Particle size measurements were carried out at locations marked by crosses [+]. The location of the 10 m meteorological instrument tower is indicated by the boxed cross [⊞]. The locations of the 2 m wind monitoring stations operated prior to the dispersion tests for the purpose of assessing the micrometeorology of the site are indicated by filled boxes [■].

kerosene be mixed with the oil in order to maintain the nominal release rate of the M3A4 fog-oil smoke generator (M3A4 Operator's Manual, 1985). We sought to avoid this situation because of the unknown effect it would have on the aerosol produced by the mixture.

Figure 5.2 presents the results of the analysis for precipitation and ambient temperature. For our purposes, "precipitation" included the NWS "present weather" categories 01: thunderstorms, tornados and squalls; 02: rain, rain showers and freezing rain; 03: squalls, drizzle and freezing drizzle; 04: snow, snow pellets and ice crystals; 05: snow showers, snow squalls and snow grains; 09: ice pellets (hail). The likelihood of precipitation, defined as that fraction of the total number of reporting periods in a month which indicate one or more of the precipitation categories listed above, as well as the monthly-mean dry bulb temperature are plotted on an annual basis in Fig. 5.2a. The data indicate that precipitation is least likely during June, July, August and September. The likelihood of precipitation increases steadily after September, reaching an annual maximum in December and January, whereas dry bulb temperature (and the number of hours of possible daylight) exhibit a complimentary behavior. In Fig. 5.2b the mean time between precipitation (i.e., the mean number of 1-hr reporting periods between precipitation events) and the mean precipitation duration (i.e., the mean number of contiguous periods indicating precipitation) are presented on an annual basis. The data indicate that summer storms occur less frequently and are more brief whereas storms occurring in the winter, spring and fall are more frequent and of greater duration. The summer months are therefore clearly preferable for field work in terms of favorable weather and maximum possible daylight. It is not surprising that Project Prairie Grass, the Borris Field Study, the Smoke Week studies and Project CONDORS (described in Chapter 4), which were all located in areas exhibiting similar climatological trends, were all carried out exclusively during the summer months. Unfortunately, during June and July, 1987 none of the ARFTC training ranges were available for five consecutive weeks as we required; August was completely unavailable since portions of the Pan American Games were held at ARFTC during that month. We were committed to participate in Project WIND during September and early October, 1987. Atterbury-87 was accordingly scheduled for October and November. Luckily, these turned out to be the driest October and November on record for the area. No tests were either postponed or cancelled due to precipitation.

Whereas precipitation and temperature patterns primarily affect the timing of the field study, knowledge of the prevailing wind direction is essential for choosing the

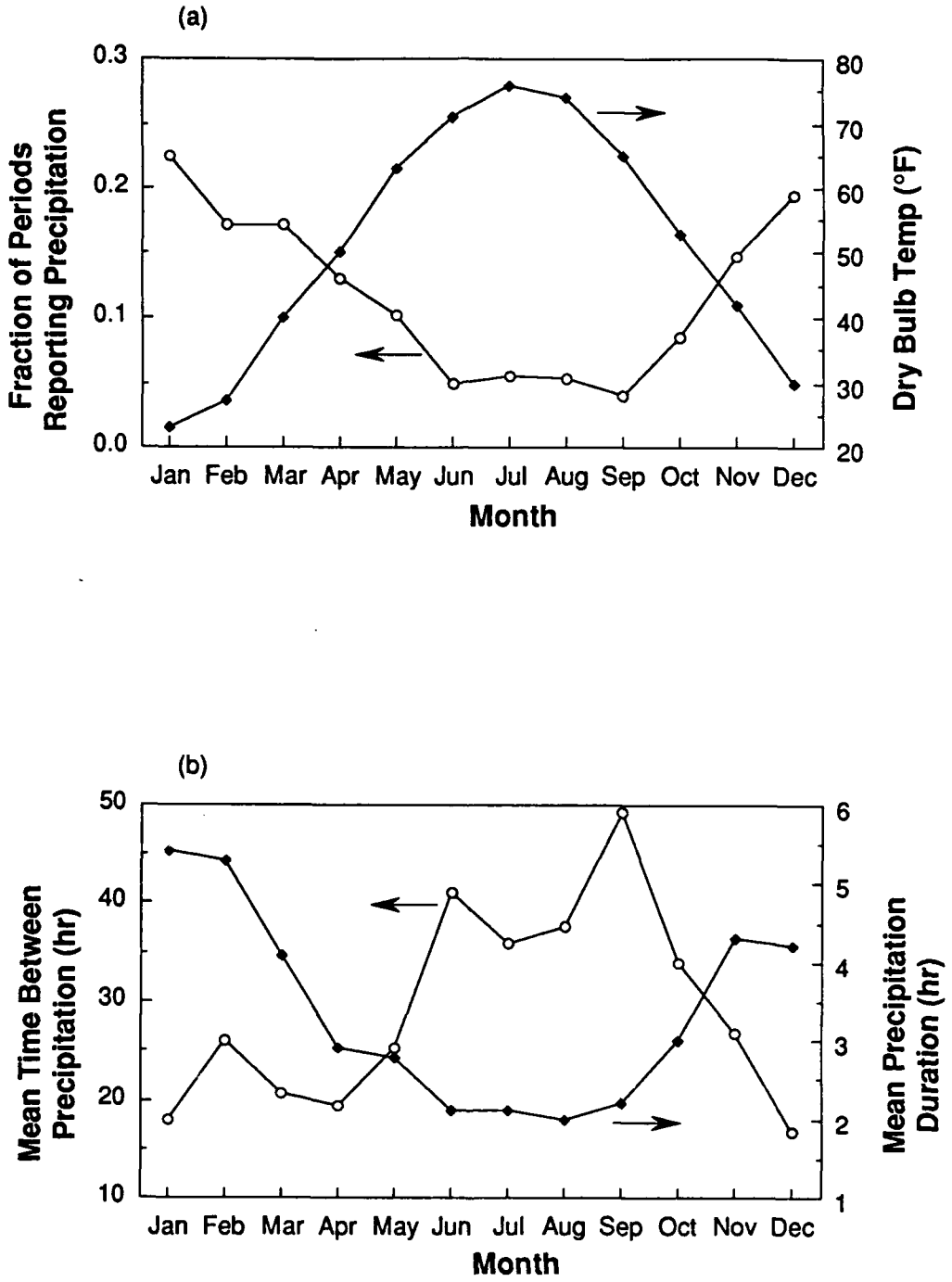

Figure 5.2 Results of precipitation analyses on NWS Indianapolis data; (a) monthly precipitation likelihood and mean dry-bulb temperature; (b) monthly mean time between precipitation and mean precipitation duration.

location of the test site as well as the design and orientation of the sampling network. Figure 5.3 presents windrose plots constructed from the NWS Indianapolis data for October and November divided into four periods: "Morning" (06:00 to 12:00), "Afternoon" (12:00 to 18:00), "Evening" (18:00 to 00:00) and "Night" (00:00 to 06:00). Periods for which the "present weather" variable indicated precipitation were excluded from these plots. These data indicate that during October and November the prevailing wind direction was predominantly from the southwest (225° east of north) in the afternoon. In addition, the mean wind speed was 5.5 m/s during the Afternoon and less than 2% of the reporting periods indicated calm conditions. During the other three periods the wind direction was more variable with mean wind speeds of 4.2, 3.7 and 3.7 m/s for the Morning, Evening and Night periods, respectively; calm conditions were observed respectively 8.5%, 5.4% and 12% of the time.

Based on this information, we sought a test site which would allow us to align our sampling network with the prevailing wind direction and which would be especially uniform to the southwest. Also, the desired even balance of test times, which would have enabled us to study dispersion during both stable nighttime conditions and unstable daytime conditions, was altered to favor daytime tests when the wind was more favorable.

ARFTC Area 7A, our ultimate choice, was not the primary candidate site. Area 2B, a more level site with more uniform terrain to the southwest, was preferred. However, as Area 2B was located immediately southeast of the main ARFTC complex, ARFTC officials felt that the risk of dense fog oil or hexachloroethane smoke entering the buildings and obscuring the roadways was unacceptable. Accordingly, Area 7A was selected.

In order to confirm the climatological information derived from the NWS data, we installed two automatic monitoring stations at Area 7A at the positions indicated in Fig. 5.1: one at the lowest elevation of the meadow, dubbed the "valley station", and one on the ridge of a 25 m hill to the southeast, dubbed the "hill station". These monitoring stations included a wind monitor (R. M. Young Co., Traverse City, MI; RMY model no. 05103) comprised of a combination propeller and direction vane for measuring wind speed and direction, as well as a temperature and humidity probe comprised of a thermistor and moisture-sensitive film (Campbell Scientific, Inc., Logan, UT; CSI model no. 207) enclosed in a solar radiation shield (CSI model no. 41002-3). These were mounted on a 2 m-high iron pipe and sampled at one-second intervals with a datalogger (CSI model no. 21X) mounted in a weather-proof enclosure (CSI model no. 022). From these data the datalogger computed one-minute means for the wind

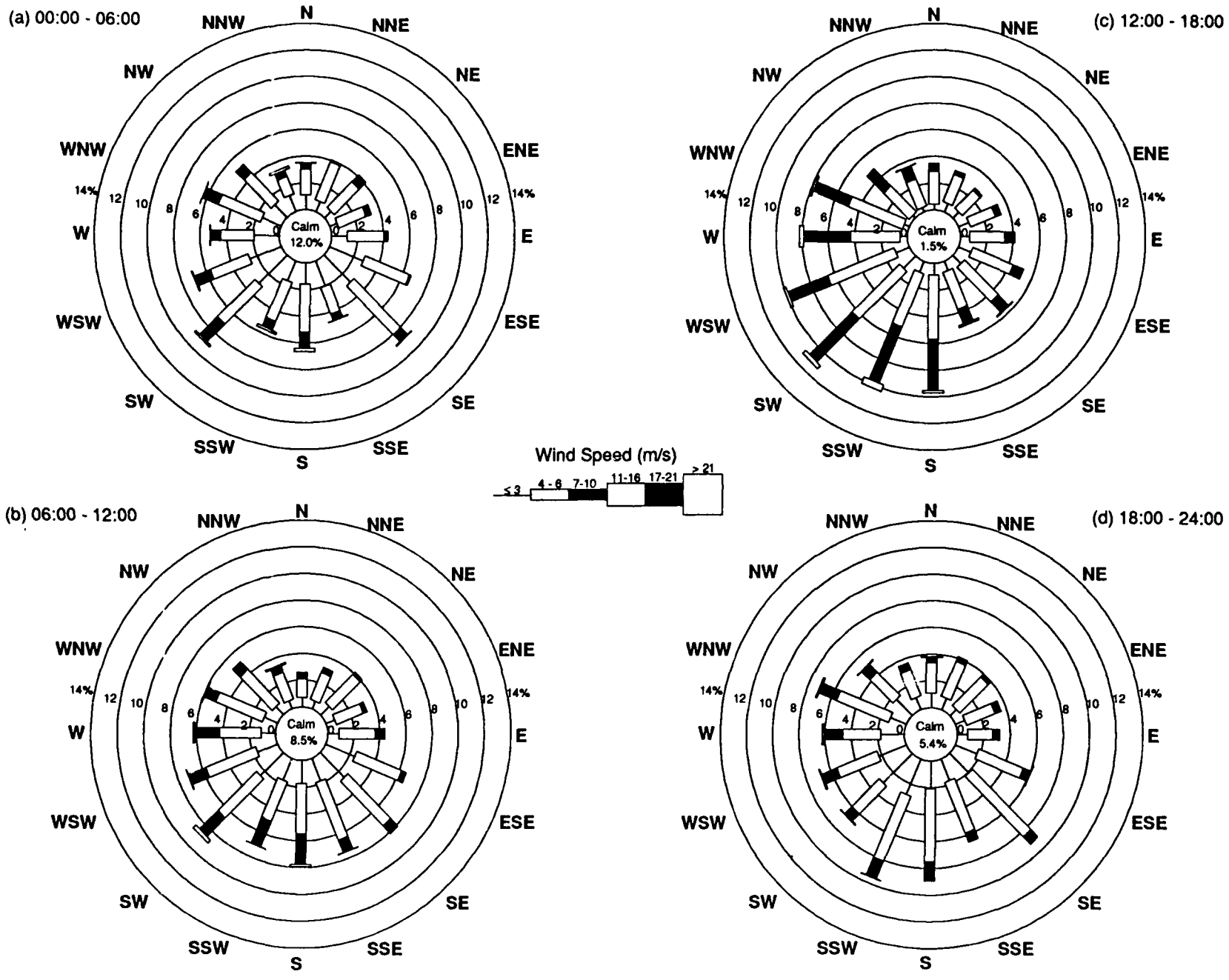

Figure 5.3 Windroses by time of day for October and November compiled from NWS Indianapolis data.

speed, wind direction, wind velocity vector magnitude, dry bulb temperature and relative humidity as well as the standard deviation of the wind direction. The datalogger was equipped with sufficient memory to collect and store data spanning a period of one week. These monitoring stations were installed shortly after our return from the Meadowbrook-87 study for Project WIND and the results collected one week later as we began field preparations for the Atterbury-87 study. Thus the data span the period from 18:00 on 13 October 1987 to 18:00 on 20 October 1987.

Windrose plots for the Morning, Afternoon, Evening and Night periods defined earlier are presented in Fig. 5.4 for the valley station and in Fig. 5.5 for the hill station. These results confirm that the prevailing wind is predominantly from the southwest. (The winds out of the northwest are associated with storm systems.) These plots show quite clearly that only during the Morning and Afternoon periods was the wind speed likely to be sufficient for testing. Because calm conditions prevailed during the Evening and Night periods, smoke releases conducted at night would not have yielded any useful data. Consequently, all tests scheduled to take place at night were rescheduled for the daytime in order to obtain as much useful data as possible.

5.2.3 The Atterbury-87 Sampling Network

In the Prairie Grass and Hanford studies the sampling network was arranged in semi-circular arcs around a fixed release point. In this manner almost any wind direction could be accommodated, but a large number of samplers had to be deployed. The sampling arcs were located at a geometric progression of distances from the release point since material concentration declines with downwind distance in a power-law manner. The sampling network we designed is located with respect to the topography of the site in Fig. 5.1 and schematically illustrated in Fig. 5.6. The filled circles indicate the positions of the masts supporting the concentration samplers. The network was comprised of 50 sampling locations on five linear transects oriented perpendicular to the anticipated prevailing wind direction (225° east of north). In order to resolve any near-ground concentration gradients, concentration samplers were deployed at elevations of 1, 2, 4 and 8 m on the first four transects and at elevations of 2 and 8 m on Transect 5 for a total of 192 samplers per test. The transects were arranged at distances of 50, 100, 250, 450 and 675 m from the baseline; an exact geometric progression was not possible. The third and fourth transects were displaced to avoid, respectively, a small stand of trees and a pioneer cemetery; the fifth transect was located 10 to 25 m upwind of a dense line of trees separating Area 7A

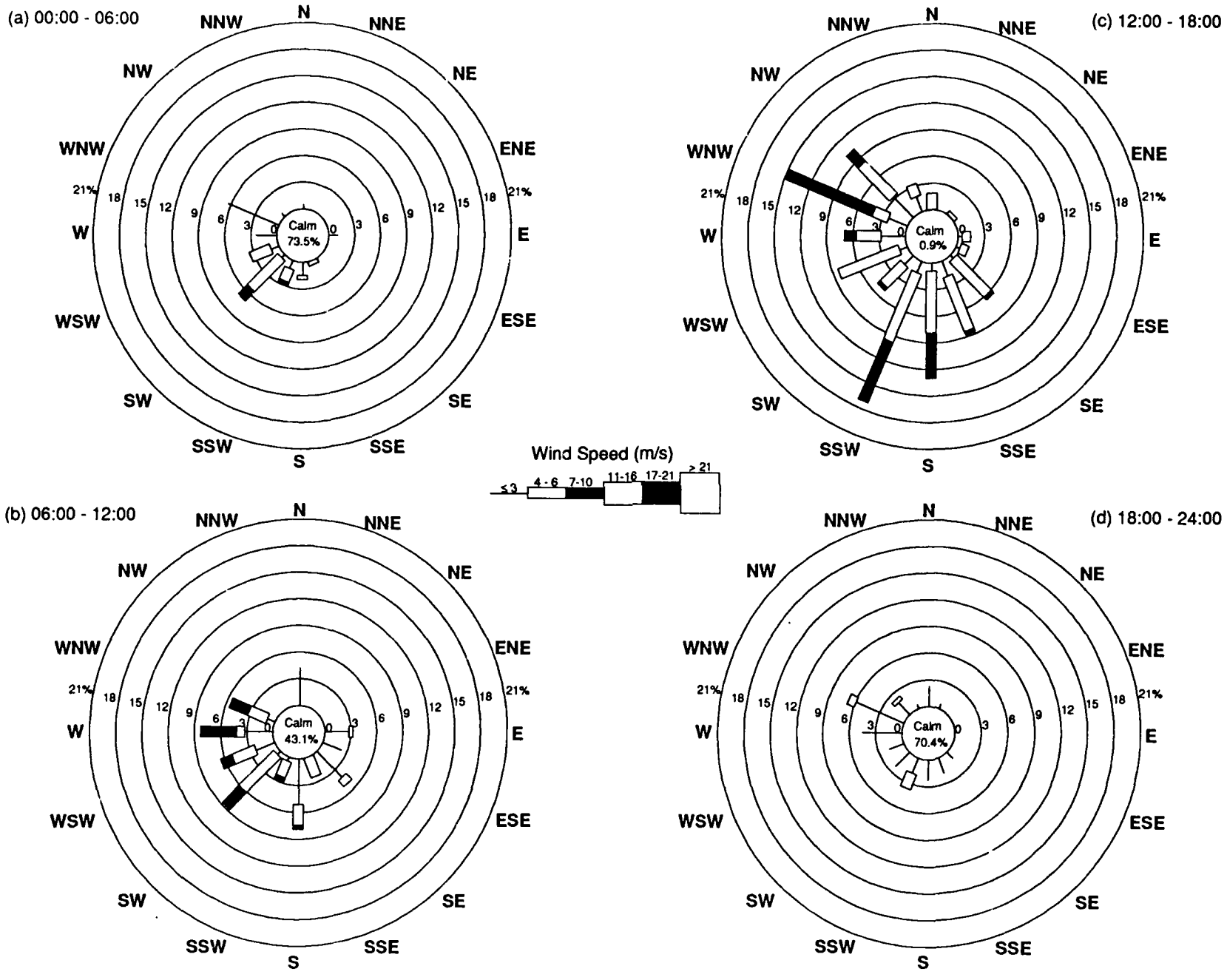

Figure 5.4 Windroses by time of day for the period 13-20 October, 1987 at the Atterbury-87 test site.

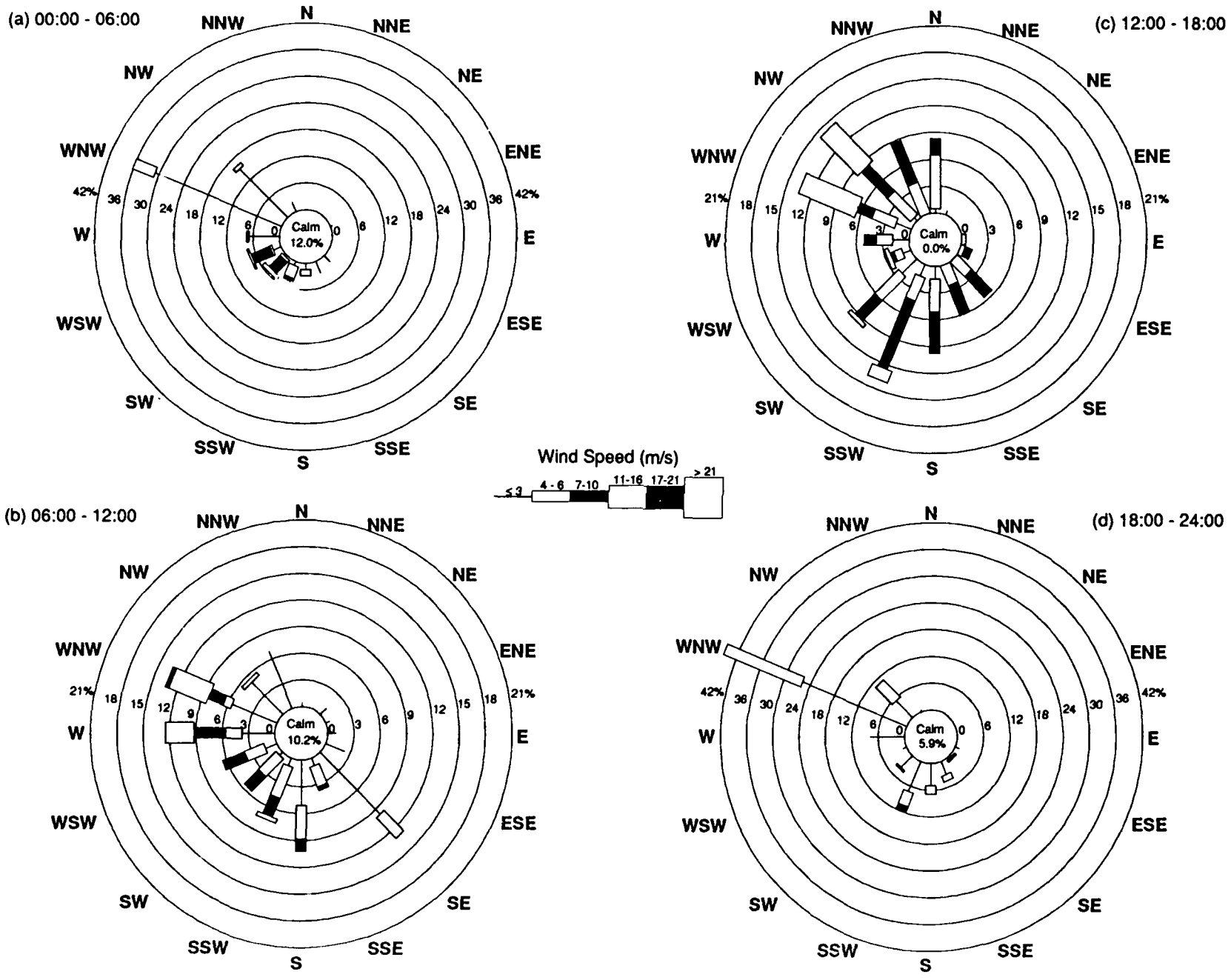

Figure 5.5 Windroses by time of day for the period 13-20 October, 1987 on a 25 m hill near the Atterbury-87 test site.

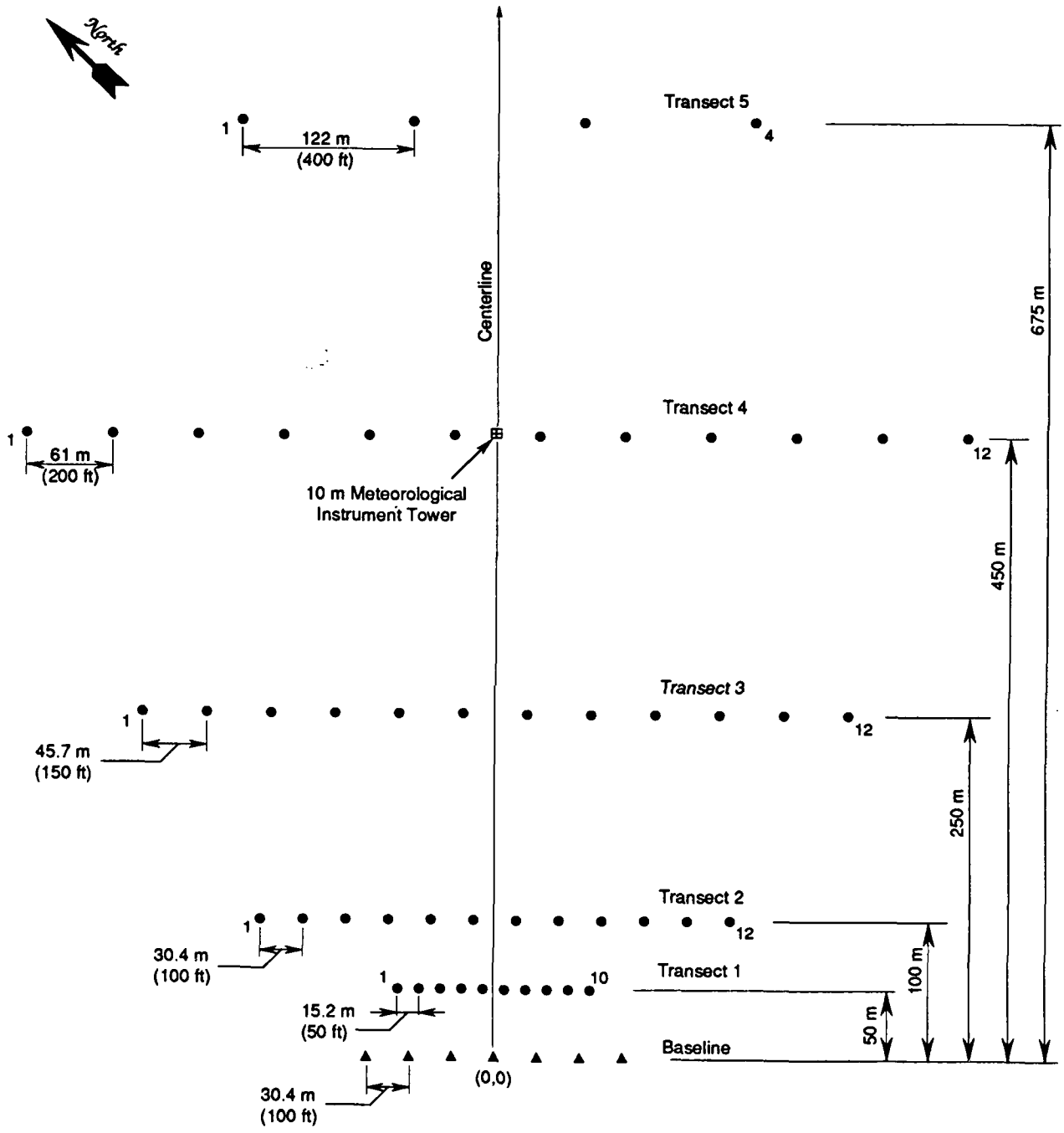

Figure 5.6 Nominal sampling network for Atterbury 87 dispersion field study. Symbols are the same as for Fig. 5.1.

and Area 1A. Because the plume was expected to spread linearly with distance as it traveled downwind from the source, the sampler spacing was increased on each transect in order to maintain approximately constant lateral resolution. The samplers were spaced at intervals of 15.2, 30.4, 45.7, 61.0 and 122.0 m, respectively on Transects 1-5.

Linear transects rather than arcs were employed during the Atterbury-87 tests as well as in the Borris Field Study and the Smoke Week tests. Transects are preferred since they require fewer samplers to accommodate variations in the prevailing wind direction by allowing flexibility in selecting the release point. Arcs arranged around a fixed release point require that many more samplers be laid out in order to ensure that the width of the smoke plume will be fully resolved. Accordingly, we also laid out potential release points along the baseline of the network (indicated by the filled triangles in Fig. 5.6) to allow us to choose the exact source location only a short time prior to the test.

The source location was chosen with the aid of a simple Gaussian plume model running on a battery-powered "laptop" computer (Zenith Data Systems Inc., St. Joseph, MI; model Z-181). Moving five-minute averages of the wind speed and wind direction as well as the standard deviation of the wind direction were first computed at one-minute intervals from data gathered by the meteorological monitoring station established at the network baseline. Using these values, estimates of the Gaussian plume spreading parameter σ_y were computed from Draxler's empirical formula (1976):

$$\sigma_y(x) = \sigma_\theta \, x \, f(x) \tag{5.1}$$

and

$$f(x) = \frac{1}{1 + 0.90\sqrt{x/(UT_i)}} \tag{5.2}$$

where x is distance downwind of the release point, U is the mean wind speed, σ_θ is the standard deviation of the wind direction and f(x) is a function which interpolates between the limits of Taylor's theory (1921) for homogeneous turbulence:

$$\begin{cases} \sigma_y \sim x, & x \to 0; \\ \sigma_y \sim \sqrt{x}, & x \to \infty. \end{cases} \tag{5.3}$$

T_i is a travel time (=x/U) such that f(x) = 1/2; based on his examination of the Prairie Grass data, Draxler recommends T_i = 300 s for horizontal spreading from a near-

surface release. Thus for a given source location, the computer model would display a plume comprised of a series of circles of radius $\sigma_y(x)$ moving with the current mean wind speed in the current mean wind direction overlaid on a map of the sampling network. This allowed us to quickly choose the most efficacious release point for the existing meteorological conditions (i.e., the one which would expose the greatest number of samplers to the plume.)

The value of this source locator was demonstrated quite clearly during the early part of the second week of the testing phase (HC smoke tests) when an advancing storm front caused the wind direction to shift to the north. Instead of having to completely cancel three of the five scheduled tests, we relocated the source to a position north of the fourth transect (see Fig. 5.1). The exact position was chosen based on the predictions of the source locator. Subsequently, we were able to keep the centerline of the plume on the sampling grid during all three HC tests conducted from this source position.

The locations of the sampling equipment for each test are given in Fig. 5.7 for the fog-oil tests and in Fig. 5.8 for the HC tests. In addition, the mean wind speed and direction are represented by a vector drawn from the location of the smoke source. Tests having a common source location are indicated on the same figure. The abscissa and ordinate indicate, respectively, the east and north coordinates of a point. The grid origin was arbitrarily chosen as the intersection of the centerline and baseline of the sampling network. When the coordinates of a specific position are given in this chapter, the coordinate system is that presented in Figs. 5.7 and 5.8.

Note that measurements of the particle size distribution were performed at only one location per test, generally near the 10-m meteorological tower but occasionally in other locations. When two locations are indicated, as in Fig. 5.7b, they are for different tests.

5.3 The Smoke Source

Accurate, detailed data which characterize the behavior of the smoke source are necessary for the accurate prediction of downwind concentrations as well as for the evaluation and improvement of models which predict such concentrations because they provide the initial conditions for the dispersion problem. These data can be divided into three broad areas: 1) *physical configuration*, including the description, number, location(s) and elevation(s) of the source(s) as well as the amount of material released and the duration of the release period; 2) *source operation* including the

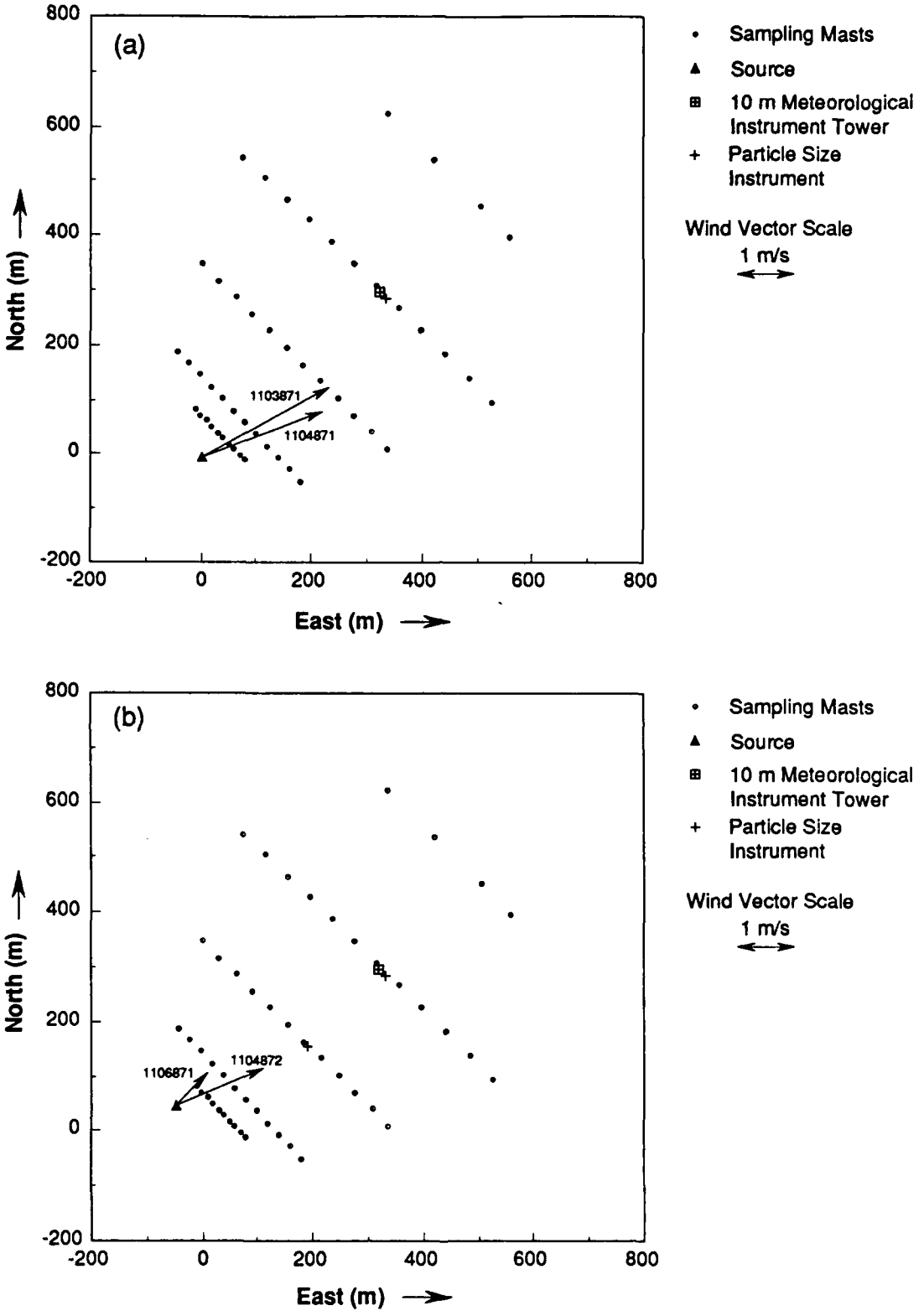

Figure 5.7 Enlargement of Fig. 5.1 showing equipment locations and average wind vector at source location for fog oil tests; (a) 1103871 and 1104871, (b) 1104872 and 1106871. Grid zero is arbitrary.

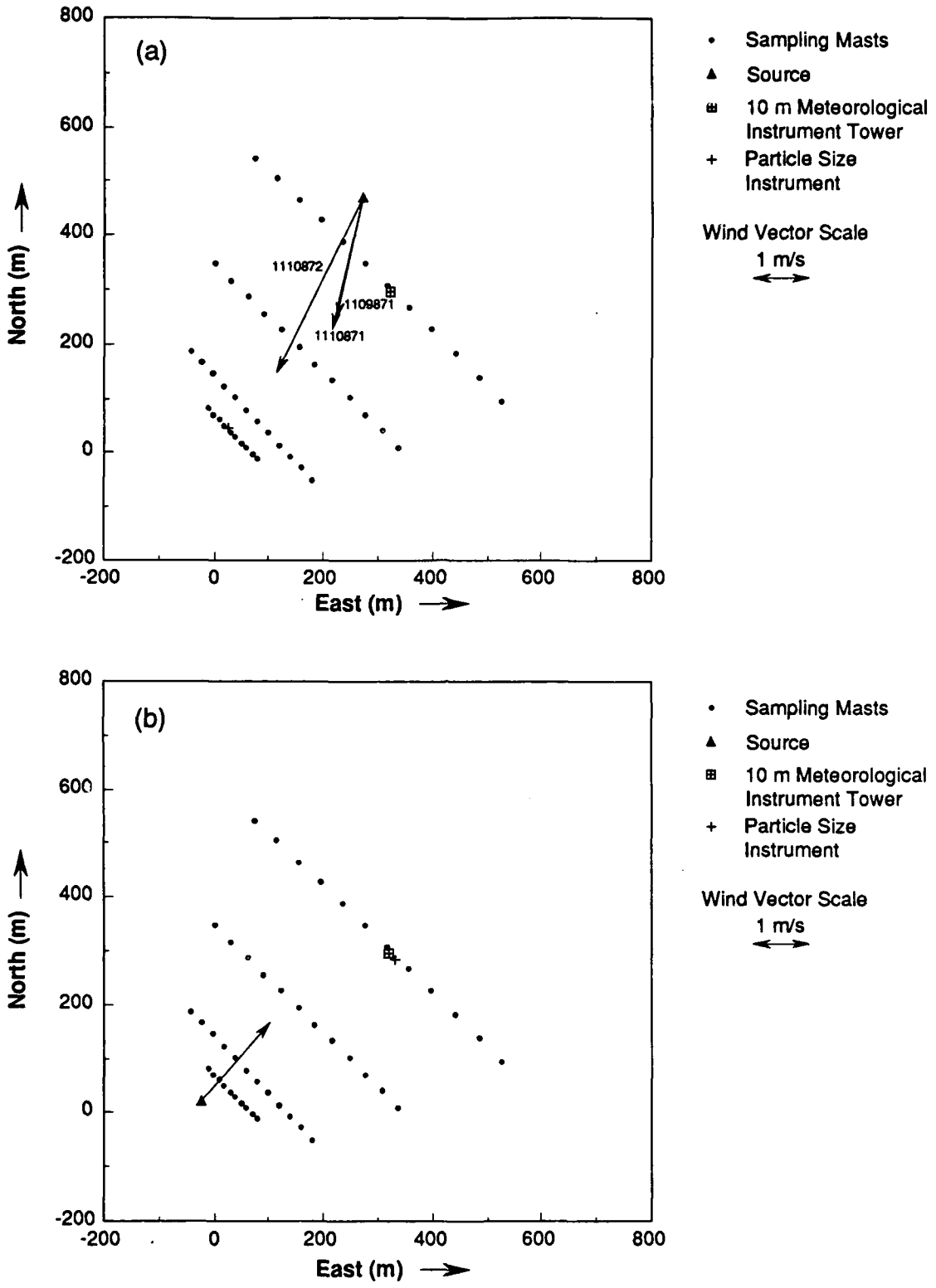

Figure 5.8 Enlargement of Fig. 5.1 showing equipment locations and average wind vector at source location for HC tests; (a) 1109871, 1110871 and 1110872 (b) 1112871 and 1113871. Note that for the HC tests the sampling masts on transect 5 were not operated and are omitted.

mass rate of release and exit temperature as functions of time; 3) *local meteorology* including the wind speed, wind direction, temperature and relative humidity at the release point, also as functions of time. In the present study of fog-oil and HC smoke, data of all three types were collected during the tests. This section describes the instruments and procedures employed to acquire and reduce these data in addition to providing a discussion and summary of the results obtained.

5.3.1 Configuration for Fog Oil Smoke

The M3A4 fog-oil smoke generator (NSN 1040-01-143-9506), illustrated in Fig. 5.9, produces smoke by vaporizing fog oil and ejecting it into the atmosphere at a nominal rate of 46 g/s (48 gal/hr) according to the M3A4 Operator's Manual (1985). A reciprocating pump driven by the high internal pressure of the M3A4 draws fog oil from an external supply and forces it into the engine tube of the gasoline-fired pulse-jet engine. The high temperature of the combustion gases causes the fog oil to vaporize. The vaporized oil is forced through three 19-mm (3/4-in) outlet nozzles at high velocity after which it rapidly mixes with air at ambient conditions and condenses to form a dense, white aerosol.

Two M3A4 smoke generators (serial numbers R26-0763 and R26-0764) were acquired from Letterkenny Army Depot for use in the present study. These were not new units but rather reconditioned M3A3 units which had been previously recalled by the manufacturer due to defective fog oil pumps. During the Meadowbrook-87 study, the oil pumps proved extremely troublesome. The pump on generator 0763 rarely functioned correctly and the pump on generator 0764 failed during the last test, causing its premature termination. Prior to the Atterbury-87 tests, a technician from the Letterkenny Depot traveled to the test site, replaced both pumps and tested both smoke generators. Subsequently, both generators exhibited much improved performance although during one test (1104871) the pulse-jet engine repeatedly shut down.

The M3A4 smoke generators were operated in accordance with the practices and procedures taught at the US Army Chemical School at Fort McClellan.

The two M3A4 units were never operated simultaneously. Rather, one smoke generator was employed during a test and the second unit was located nearby in order to provide redundant capability in the event the first unit failed during a test. The smoke generator to be operated was mounted in the bed of a "pickup" truck along with a 55-gallon drum of fog oil. The exit nozzles of the generator were thus positioned 1 m

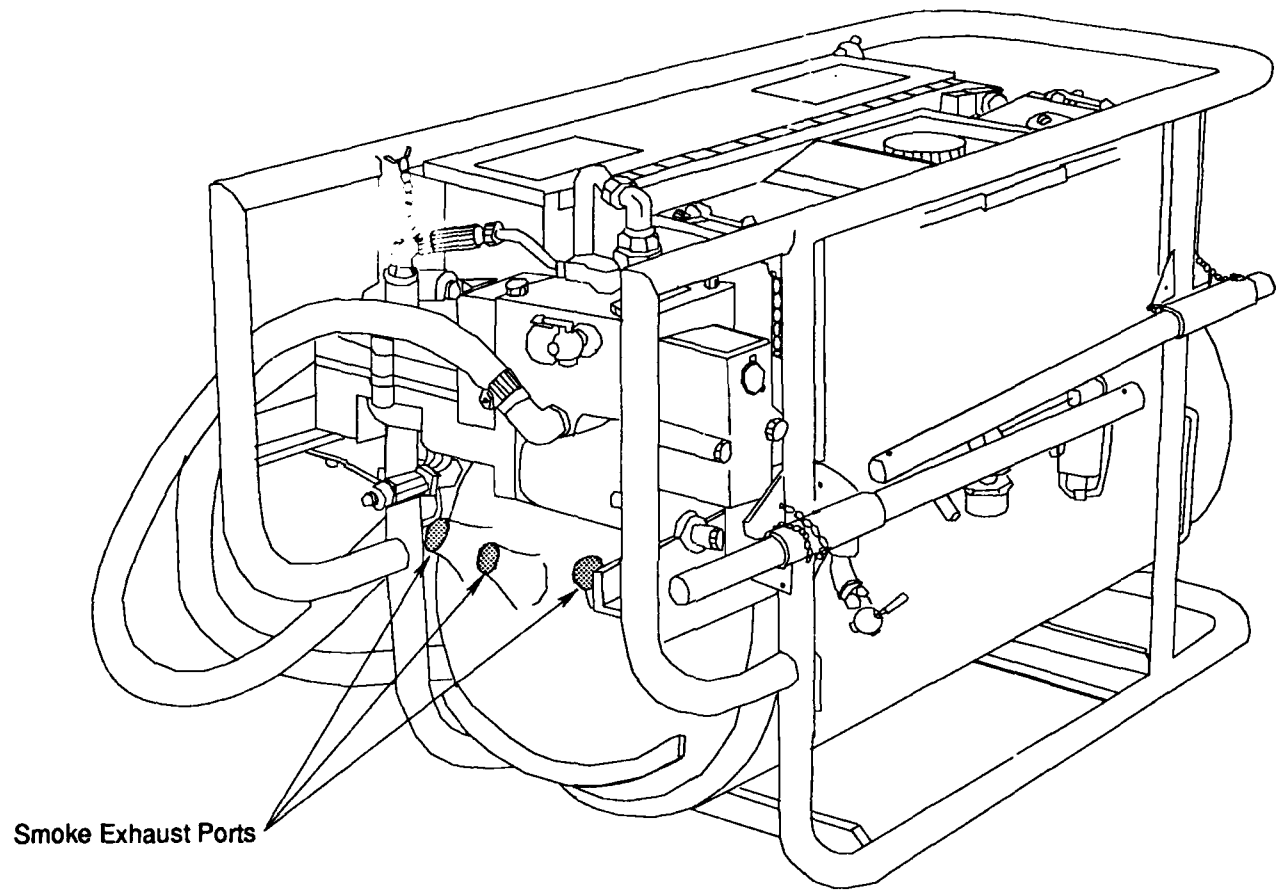

Figure 5.9 The M3A4 fog oil smoke generator.

from the ground. Mounting the source on a truck enabled the release point to be chosen based on the current mean wind speed and direction just prior to the test as well as to provide an additional precaution against fire.

The operation of a single smoke generator from a release height of 1 m provides a close approximation to a continuous, ground-level point source. This represents the most common source configuration for dispersion studies. All of the previous studies described above employed continuous point sources. The reason for this is most dispersion problems of practical interest can be treated as continuous point sources. US Army doctrine calls for smoke generators to be deployed and operated in groups of 8 to 48 units (Smoke Operations Manual, 1987). For strongly convective conditions, the combined smoke plume from a large number of generators can shield the ground from the solar heat flux, effectively altering the local microclimate. Although this could lead to greater ground-level concentrations than one would expect from the superposition of the concentration field associated with a single generator, the investigation of such phenomena is beyond both the scope and the resources of the present study.

5.3.2 Configuration for HC Smoke

The ABC-M5 30-lb HC smoke pot (NSN 1365-00-598-5207) produces a dense white smoke as a result of an exothermic chemical reaction of a mixture of reagents. Principally among these reagents are zinc oxide, aluminum metal and hexachloroethane (US Army Technical Bulletin, 1964). During the reaction, zinc chloride vapor is formed and expelled into the atmosphere, along with other reaction products, where it rapidly condenses. The resulting $ZnCl_2$ particulate is extremely hygroscopic and it is believed (Katz,*et al.*, 1980; Hansen, 1989) that these rapidly absorb water from the atmosphere to form the droplets which comprise the visible smoke. Hansen (1989) states that about 78% of the mass released from the smoke pot condenses to form the $ZnCl_2$ particles which are the basis for the HC smoke. Katz,*et al.* (1980) estimate that only 70% of the mass released forms $ZnCl_2$ particles.

One hundred M5 HC smoke pots were acquired for the Atterbury-87 study and stored in an ammunition bunker at ARFTC prior to use. Physically, the M5 smoke pot is approximately the size of a common one-gallon paint can with a tapered and rounded bottom to facilitate stacking. Each M5 smoke pot contains a charge of approximately 13.6 kg of material. The nominal "burn time" of a smoke pot varies from

12 to 22 minutes depending on configuration. (Multiple pots stacked one on top of another or placed side by side burn more quickly than do individual pots.)

Based on a 22 minute burn duration observed by Katz et al. (1980), an individual M5 smoke pot yields a release rate of 8 g/s of $ZnCl_2$. Therefore, to achieve a release rate comparable to that of an M3A4 fog oil generator, for which our sampling procedures were designed, and to achieve a test duration of about an hour, we used 19 to 20 smoke pots per test, arranged in five groups of four pots each. Except for the first HC test (1109871) the four groups were stacked on top of each other as recommended by US Army procedure (US Army Technical Bulletin, 1964).

The smoke pots were not placed on a pickup truck; rather they were stacked on a piece of fire-proof masonry overlaid on a wooden pallet that was in turn placed on the pan of a high-capacity scale which rested on the ground. The five stacks of smoke pots were surrounded with and attached to wire fencing which prevented them from collapsing and falling off the scale as they burned. The elevation of the top group of smoke pots was 1.5 m above the ground; this may be taken as the release height for all but the first test for which a release height of 0.4 m is appropriate.

5.3.3 Measurements

All of the sensors employed to measure time-dependent data were sampled at 1-s intervals with a Campbell Scientific, Inc. model 21X datalogger. The datalogger also applied any calibration information or computations necessary to transform the measured signals into values with the desired units. (An internal thermistor calibrated by the manufacturer provided the necessary reference temperature for the thermocouples.) The data were then transmitted in digital form to a Zenith model Z-181 computer. The data were held in the computer's random access memory so that they could be monitored during the test. Upon completion of a test the data were stored on flexible disks. Upon returning to the University of Illinois the data were transferred to a Sun-3/280, archived on 9-track magnetic tape and subjected to additional processing and analysis.

In order to effect time-dependent measurements of the exit temperature of the M3A4, 24-gauge chromel/alumel (type K) thermocouples were fixed in the exit plane of each of the three exhaust ports. From these data 1-minute averages were computed for each exhaust port. In addition, an overall average exit temperature was determined for the period of smoke generation based on combined measurements at each port.

Direct measurements of the fog oil release rate were impractical since some of the fog oil was used to cool the smoke generator and returned to the 55-gallon supply drum. Instead, the fog oil drum was placed on a 500 kg-capacity scale manufactured by Circuits and Systems (Rockaway, NY) which had been mounted in the bed of the pickup truck next to the smoke generator. The strain gauge in the scale had been previously calibrated in the laboratory; the calibration was checked prior to each test. In this manner the instantaneous mass of the fog oil and drum were recorded before, during and after each test. Because the vibrations produced by the smoke generator introduced fluctuations in the measured mass, the rate of release could not be determined by simply taking the difference between successive measurements and dividing by the time interval. Rather, the mass data were first digitally filtered using a recursive, first-order, low-pass filter with a time constant of 22 s. This time constant results in a 50% reduction of the signal power spectrum at the same frequency as does a simple 1-minute average (Pasquill and Smith, 1984; pages 24-29). The mass release rate was subsequently computed by taking the difference between filtered mass measurements at 30-s intervals and dividing by this time interval.

Measurements of the exit temperature of the HC smoke pots were carried out during Tests 1112871 and 1113871. However, it should be noted that during the course of these two tests a substantial amount of black, carbon-like material collected on the thermocouple and formed a spherical mass approximately 2 cm in diameter. This may have affected the exit temperature data by increasing the response time of the thermocouple.

The mass rate of release of the HC smoke was determined in the same way as for the fog-oil tests.

Measurements of the local meteorology near the source were performed with essentially the same equipment as previously described for monitoring the climatology of the site except that an improved version of the wind monitor was implemented. The Wind Monitor-AQ (R. M. Young Co., model 05305-1) is supplied with a carbon fiber propeller and a longer, lighter tail assembly for improved dynamic response. (The dynamic response of the meteorological instrumentation is discussed in Appendix B.) Measurements of the local wind speed, wind direction, air temperature and humidity at the 2-m level were initiated ten minutes prior to commencing smoke dissemination and were continued for ten minutes following termination of dissemination. From these measurements, 1-minute averages of the wind speed and direction were computed and plotted. In addition, averages over the period of data acquisition were computed

for each of the quantities measured as well as the standard deviation of the wind direction, σ_θ.

5.3.4 Results and Discussion

Averages of the source data for the fog oil tests are presented in Table 5.1. Because the Test 1103871 was ultimately terminated by a failure of the M3A4 smoke generator, the average exit temperature, computed from data gathered during the last five minutes of the test, may not be representative of the entire test.

Table 5.1. Summary of source data for fog oil tests conducted during Atterbury-87.

TEST:	1103871	1104871	1104872	1106871
Source Location (m)	3.0, –4.7	3.0, –4.7	–47.7, 47.7	–47.7, 47.7
Mass Released (kg)	115.9	44.0	117.8	193.0
Release Duration (min)	55.9	27.5	48.2	76.2
Release Rate (g/s)	34.6	26.7	40.7	42.2
Exit Temperature (°C)	486†	444	401	415
Wind Speed (m/s)	2.6	2.3	1.7	0.8
Wind Direction (°E of N)	241	249	247	224
σ_θ (°)	28.6	23.4	26.0	33.8
Temperature (°C)	23.4	20.0	25.3	8.0
Relative Humidity (%)	41	25	43	40

†Based on last five minutes of source data record.

Plots of the 1-minute averages of wind speed, wind direction, exit temperature and release rate are presented in Figs. 5.10-12 for Tests 1104871, 1104872 and 1106871, respectively. For Test 1104871, Fig. 5.10 reveals that the wind speed was highly variable although the wind direction was fairly constant. As a result, the material plume tended to move downwind in pulses rather than as a uniform cloud. Figure 5.10 confirms the previous statement that the M3A4 failed repeatedly during this test. Once the pulse-jet engine was started, the exit temperature climbed rapidly until the flow of fog oil was initiated. As the oil flow increased, the release rate increased as well and the exit temperature declined to a steady state value of approximately 450°C. About 18 minutes into the test, the pulse-jet engine failed for the first time, as indicated by the precipitous drop in exit temperature and release rate. The pulse-jet engine was restarted within one minute and the test continued. This

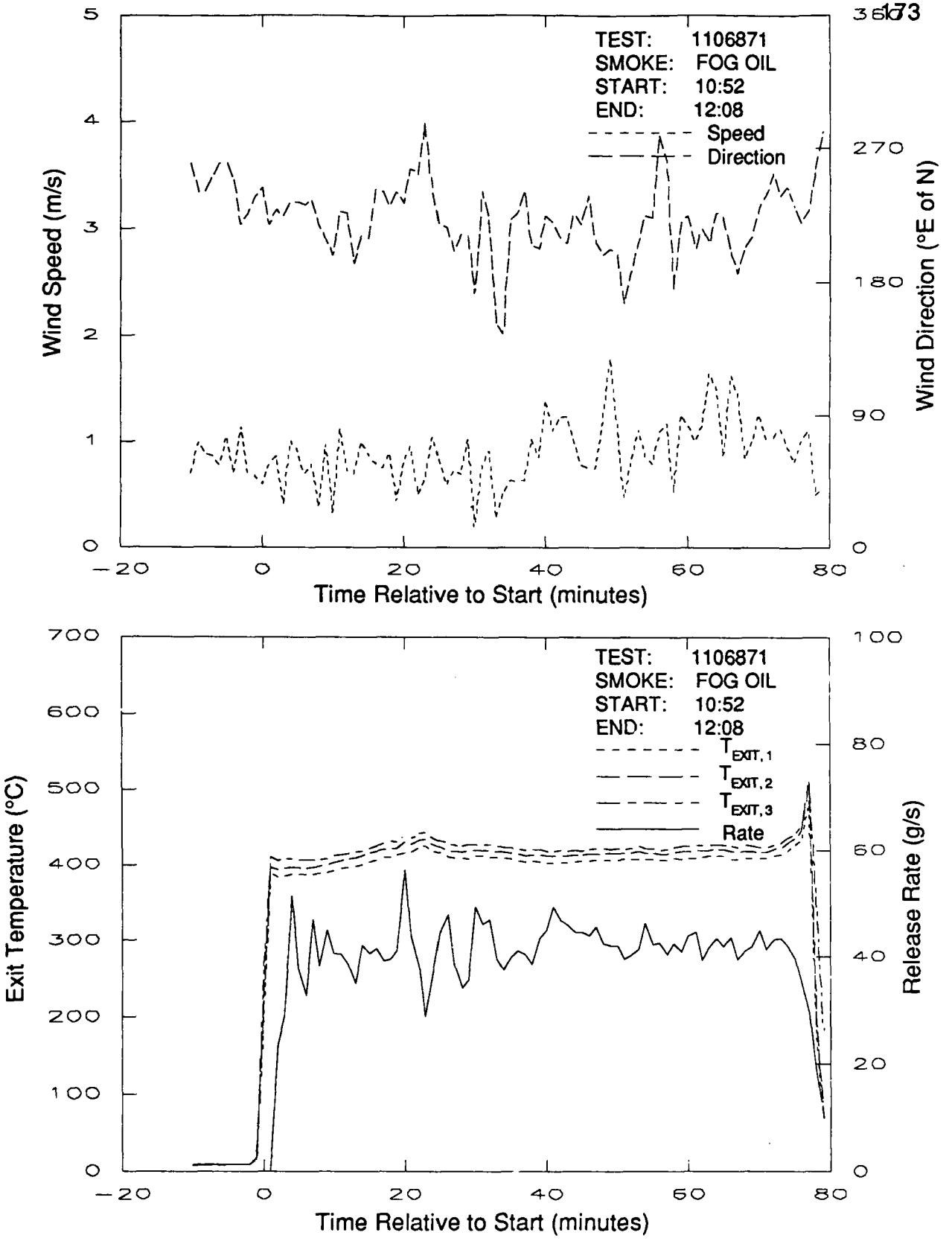

Figure 5.12 One-minute averaged source data for test 1106871. Top: wind speed and wind direction; bottorn: exit port temperatures and release rate.

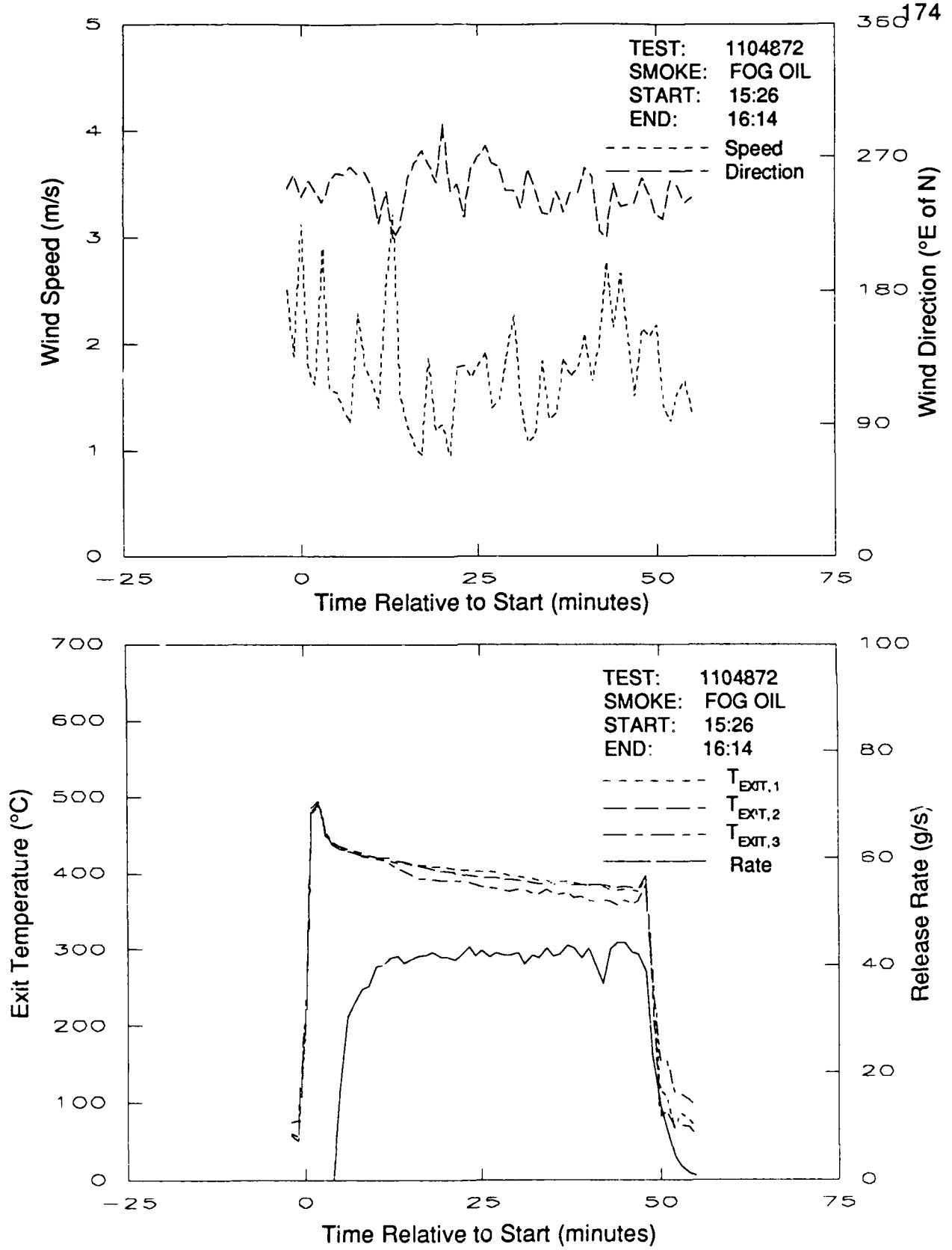

Figure 5.11 One-minute averaged source data for test 1104872. Top: wind speed and wind direction; bottom: exit port temperatures and release rate.

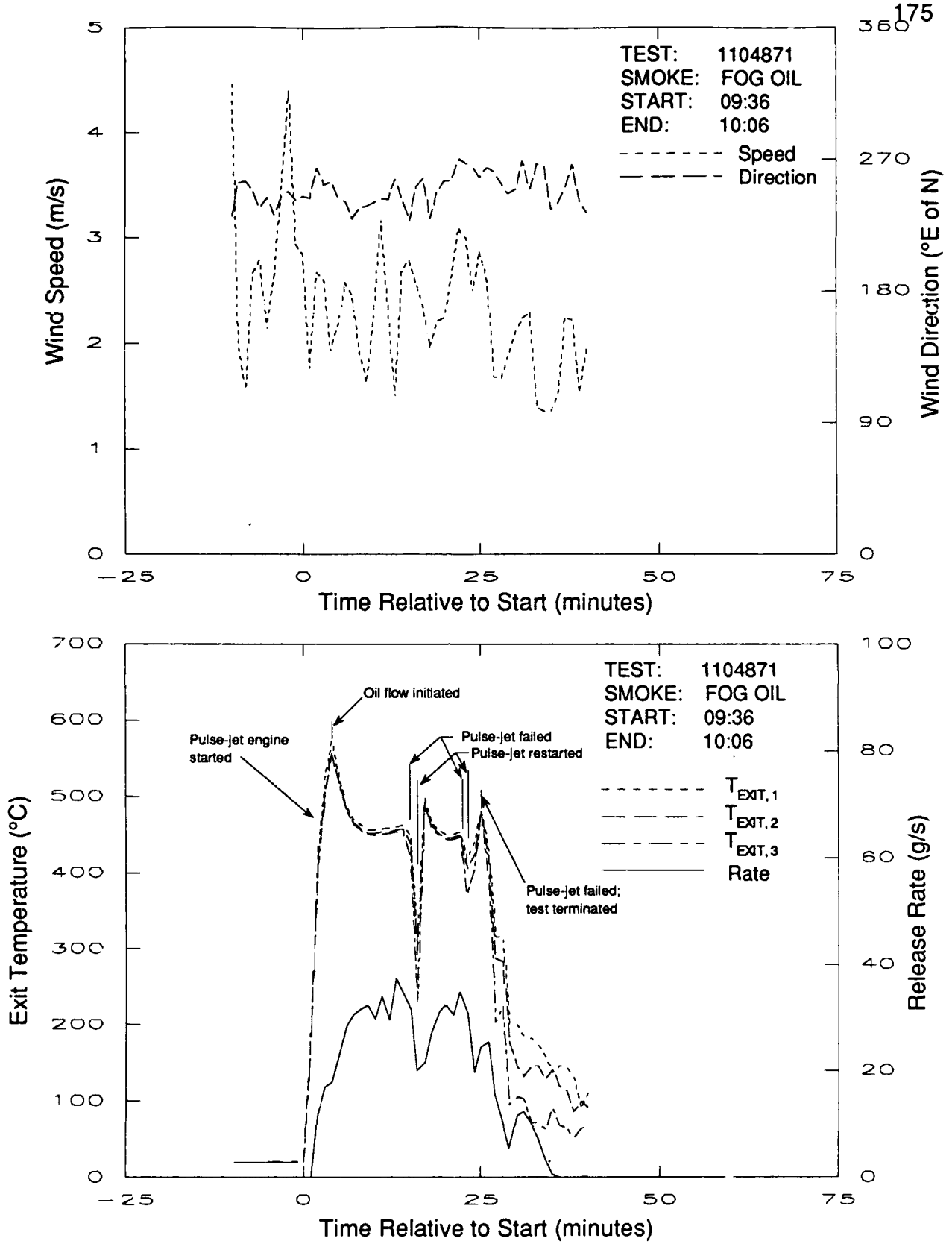

Figure 5.10 One-minute averaged source data for test 1104871. Top: wind speed and wind direction; bottom: exit port temperature and release rate.

pattern was repeated until after the third failure of the pulse-jet engine, whereupon the test was terminated.

As Fig. 5.11 indicates, Test 1104872 was more successful. The wind speed and direction were very similar to the earlier test but the M3A4 performed much better. As before, the exit temperature shows a sharp rise initially as the pulse-jet engine was started and allowed to warm up. Oil flow was initiated more slowly but increased gradually throughout the test, as indicated by the gradual decline in the exit temperatures.

The smoke generator performed flawlessly during Test 1106871. As Fig. 5.12 indicates, the wind speed was much lower than for the previous tests and the wind direction was highly variable and resulted in a much larger value for σ_θ in Table 5.1. Despite the variability of the wind direction, the smoke plume remained on the sampling network. Figure 5.12 reveals that oil flow was initiated very soon after starting the pulse-jet engine and the exit temperature stabilized rapidly. The data also reveal that release rate was much more variable during this test. This is due to the lower ambient temperature (8°C vs. 25°C) which correspondingly increased the viscosity of the fog oil. This in turn affected the ability of the fog oil pump to draw the oil from the supply drum and force it through a spray nozzle into the smoke generator. Interestingly, this does not seem to have had much affect on either the overall release rate or the overall exit temperature presented in Table 5.1.

The observed variation in the measured exit temperatures between the three exhaust ports is due to small variations in the proximity of the thermocouple measuring junction to the exit plane and do not reflect actual differences in exit temperature. Because the exhaust temperature declined rapidly with distance from the exit ports, slight variations in the thermocouple positions resulted in small variations in the measured temperatures.

Averages of the source data for the HC tests are presented in Table 5.2. The stated release rates have not been adjusted to reflect the 70% efficiency of $ZnCl_2$ production given by Katz,*et al.* (1980).

Plots of the 1-minute averages of wind speed, wind direction, exit temperature and release rate are presented in Figs. 5.13-16 for Tests 1109871, 1110871, 1110872 and 1112871, respectively. For Test 1109871, Fig. 5.13 indicates that the wind speed was variable although the direction was fairly steady. Since the wind direction for this test, as well as for Tests 1110871 and 1110872, was out of the north, the source was relocated to a position north of Transect 4 as shown in Fig. 5.8a. For this test, 19 smoke pots were arranged side-by-side in four rows. There were four pots in the first

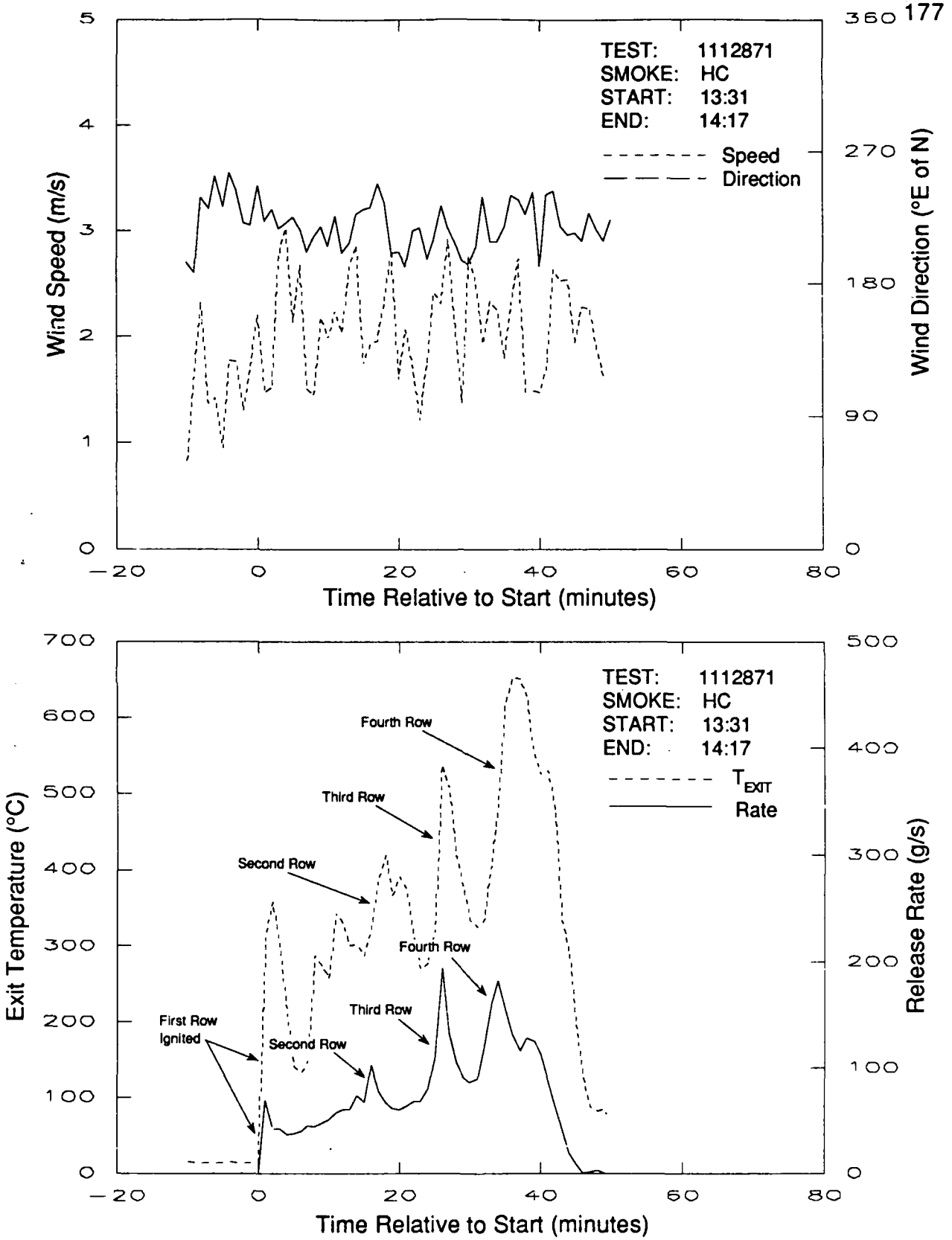

Figure 5.16 One-minute averaged source data for test 1112871. Top: wind speed and wind direction; bottom: exit temperature and release rate.

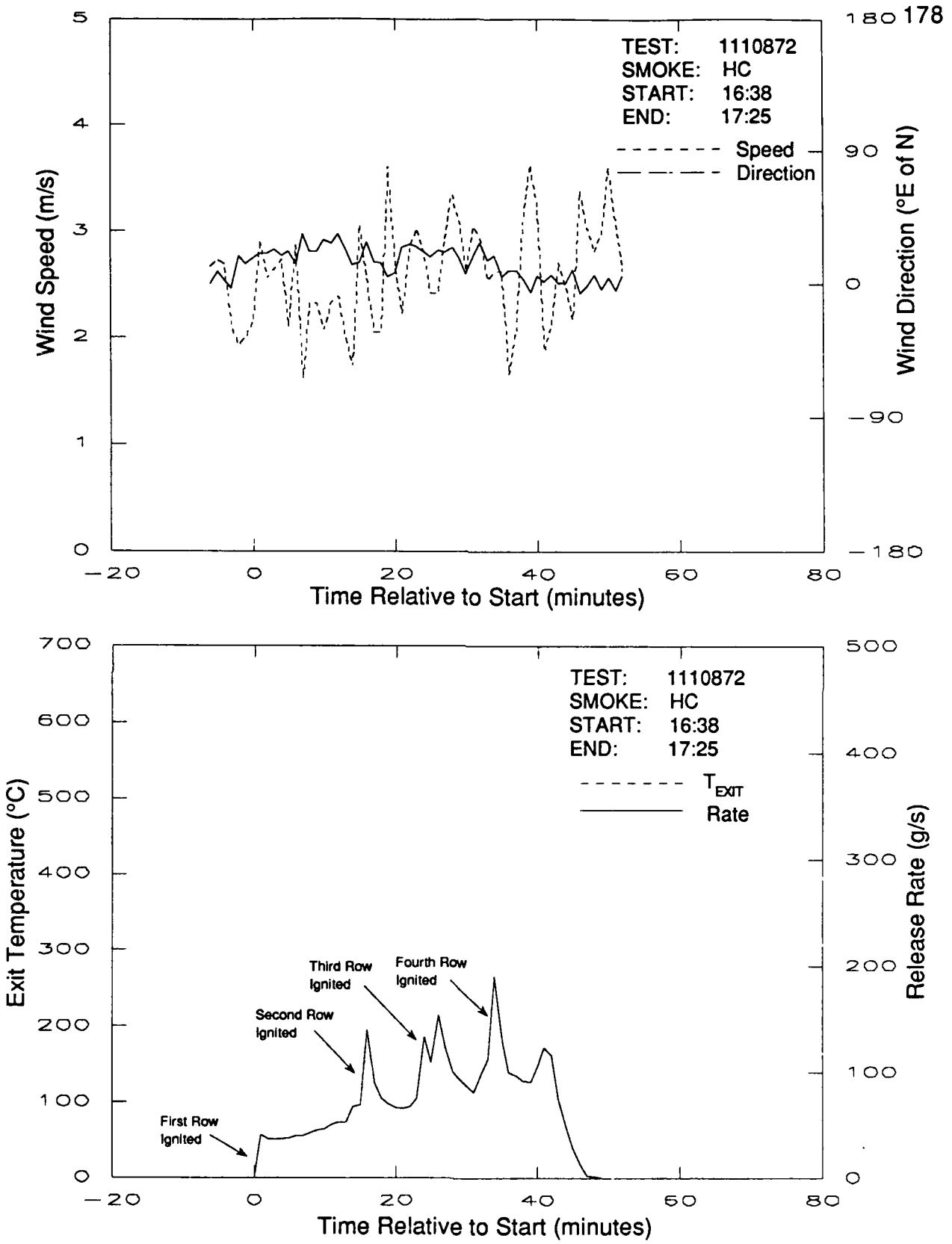

Figure 5.15 One-minute averaged source data for test 1110872. Top: wind speed and wind direction; bottom: release rate.

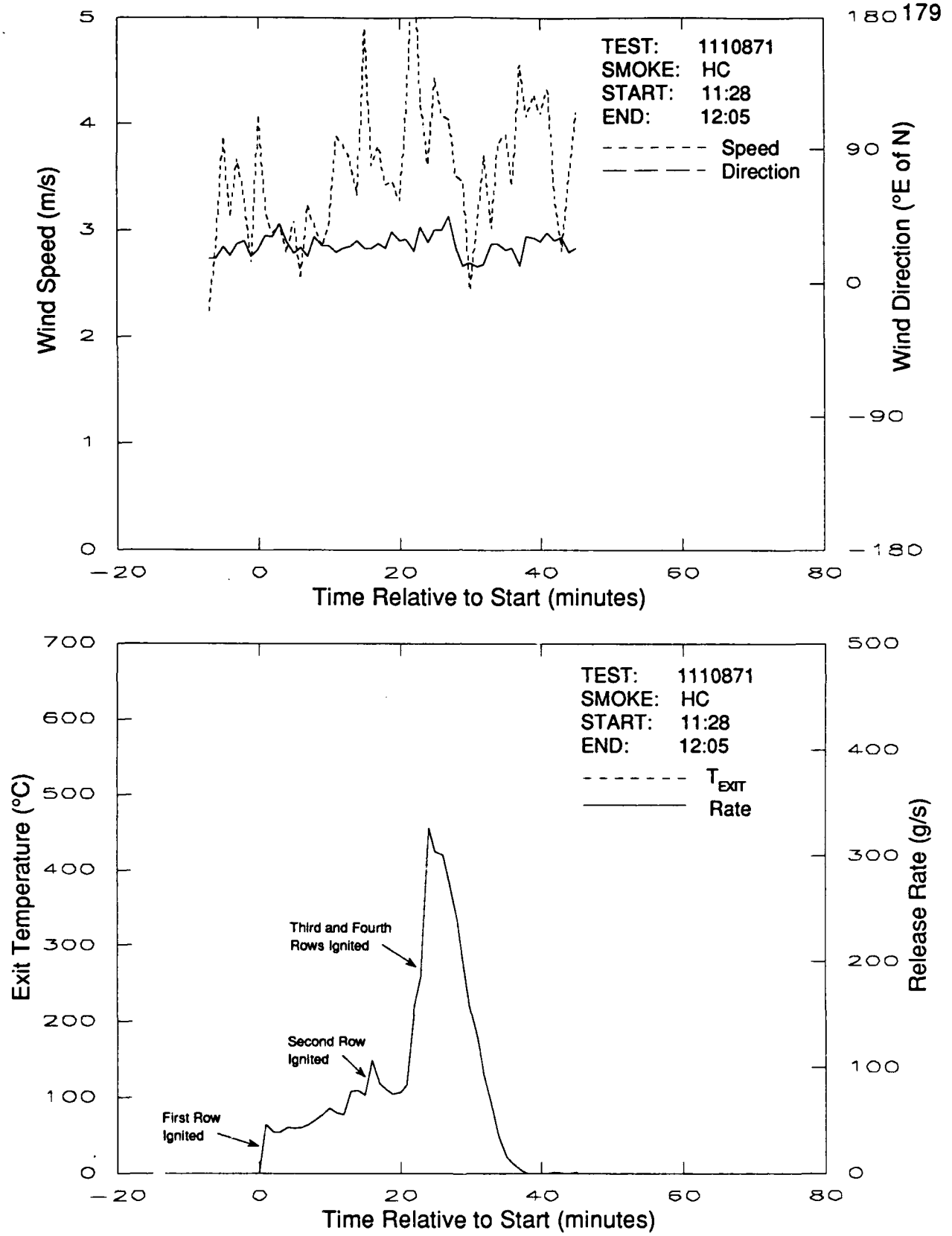

Figure 5.14 One-minute averaged source data for test 1110871. Top: wind speed and wind direction; bottom: release rate.

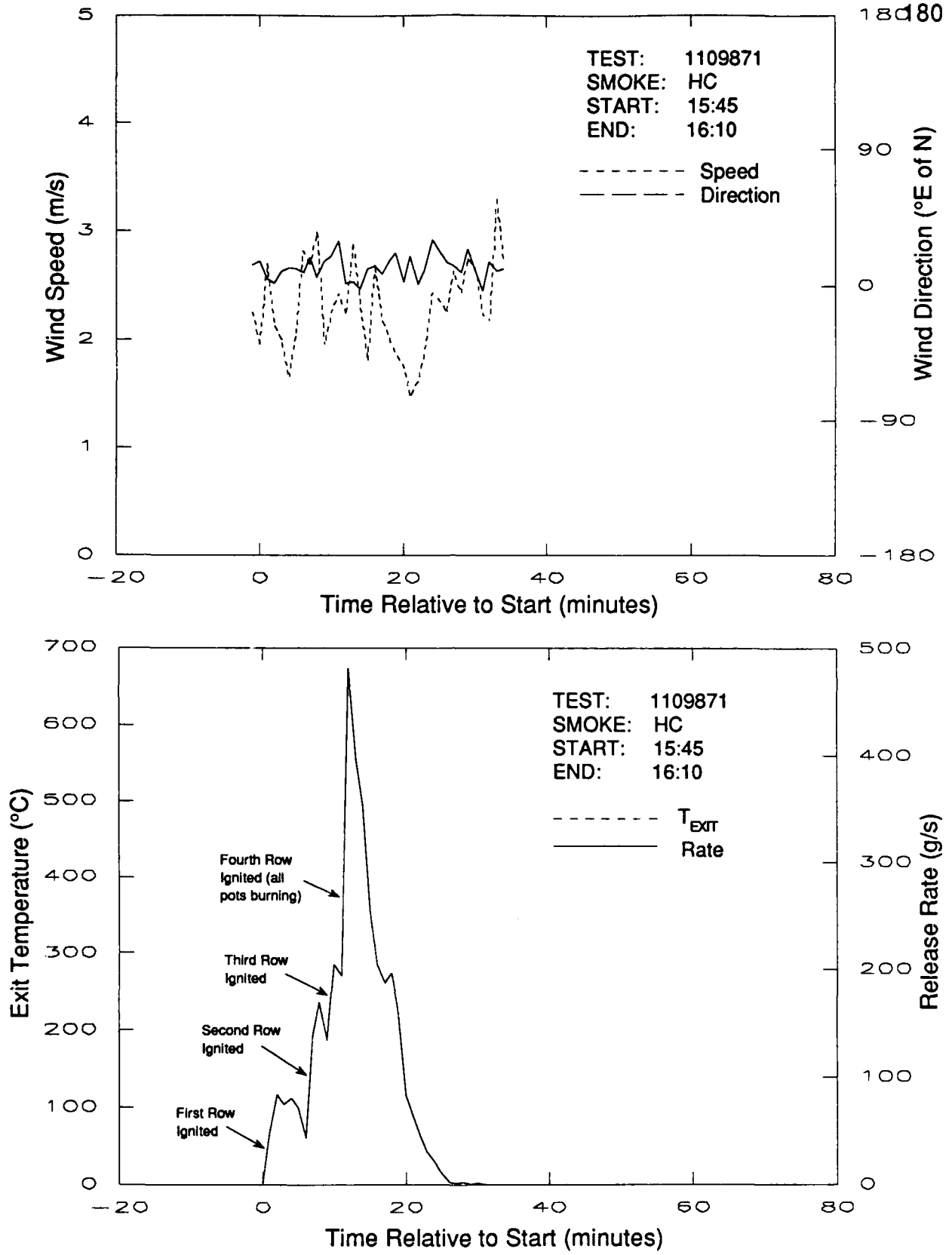

Figure 5.13 One-minute averaged source data for test 1109871. Top: wind speed and wind direction; bottom: release rate.

row and five in the other three. All pots in each row were connected electrically so that they could be ignited sequentially, i.e., after the first row had burned the second would be ignited and so on. Unfortunately, the heat generated by the first row of pots quickly caused the second row to ignite. Within approximately ten minutes, all 19 smoke pots were burning simultaneously. The test lasted only about 25 minutes and the release rate was far from uniform, as Fig. 5.13 shows, with a peak of 500 g/s.

Table 5.2. Summary of source data for HC tests conducted during Atterbury-87.

TEST:	1109871	1110871	1110872	1112871	1113871
Source Location (m)	270.3, 470.8	270.3, 470.8	270.3, 470.8	-21.1, 21.1	-21.1, 21.1
Mass Released (kg)	222.1	229.3	219.5	218.5	202.0
Release Duration (min)	25	36.5	47.3	45.7	43
Release Rate (g/s)	148.1	104.7	77.3	79.7	78.3
Exit Temperature (°C)	–	–	–	376	–
Wind Speed (m/s)	2.3	3.6	2.5	1.9	1.9
Wind Direction (°E of N)	12	26	13	220	221
σ_θ (°)	18.7	19.7	19.9	28.6	31.2
Temperature (°C)	5.9	3.2	3.0	13.8	12.9
Relative Humidity (%)	69	61	49	35	45

To prevent this self-ignition from recurring, during all subsequent HC tests the pots were stacked in five columns. For Test 1110871, 20 pots were stacked in five columns of four pots each. The columns were arranged in a "star" pattern with one center stack surrounded by the other four stacks. During this test, we observed that the burn rate of the M5 smoke pot was highly temperature dependent. The stack of pots in the center of the group were consumed much more quickly than the others. Eventually, this resulted in more than five pots burning simultaneously, with the corresponding jump in the release rate shown in Fig. 5.14. In fact, each pot burned non-uniformly; the side facing into the wind and thus cooled by it burned much more slowly than the side facing downwind.

For Test 1110872, 20 smoke pots were stacked in 5 columns of 4 pots each. This time the columns were arranged in a circle and a much more uniform release rate was achieved, as Fig. 5.15 indicates. The occasional jumps in the release rate observed in the data record mark the ignition of the next lower level of pots: for a short period two levels of smoke pots are burning simultaneously and the release rate soars briefly.

These jumps in the release rate were less evident in earlier tests because of the non-uniform manner in which different stacks of pots burned.

As the data record in Fig. 5.16 reveals, the wind direction for Test 1112871 returned to the southwest. The source position was relocated accordingly, as shown in Fig. 5.8b. Twenty smoke pots were arranged in the same manner as for Test 1110872. The exit temperature, presented in Fig. 5.16, increased throughout the test. The reason for this upward trend is unclear. Since the release rate appears to have been very similar to that of Test 1110872, the exit temperature behavior is probably not anomalous. The large amount of carbon-like material which collected on the thermocouple during the test may have acted as a thermal insulator as well as serving to increase the response time. Because the exit temperature is very irregular, the average exit temperature given in Table 5.2 is not representative of the overall test. The same is true for the release rate. This demonstrates the critical need for time-dependent data concerning the source behavior.

Test 1113871 was conducted with only 18 smoke pots arranged in three stacks of four pots each and two stacks of three. The five stacks were placed in the circular pattern used during Tests 1110872 and 1112871. The test conditions and source behavior were nearly identical to those which prevailed for Test 1112871.

In order to provide data on the characteristics of M5 smoke pots burned individually, we conducted two tests for which only the exit temperature and mass release rate were recorded. In order to investigate the effects of physical orientation, one pot was placed upright during the test whereas the other was placed on its side. Both of these configurations are described in US Army documentation (US Army Technical Bulletin, 1964). The results of these measurements are summarized in Table 5.3 and the time-dependent data plotted in Fig. 5.17.

Table 5.3. Characteristics of individual M5 smoke pots.

TEST:	UPRIGHT	ON SIDE
Mass Released (kg)	10.7	10.2
Release Duration (min)	18	17
Release Rate (g/s)	9.9	10.0
Exit Temperature (°C)	922	618

The data presented in Fig. 5.17 indicate that a substantial difference in exit temperature arises depending on the orientation of the smoke pot. However, the release rate does not appear to be substantially affected. In addition, the exit

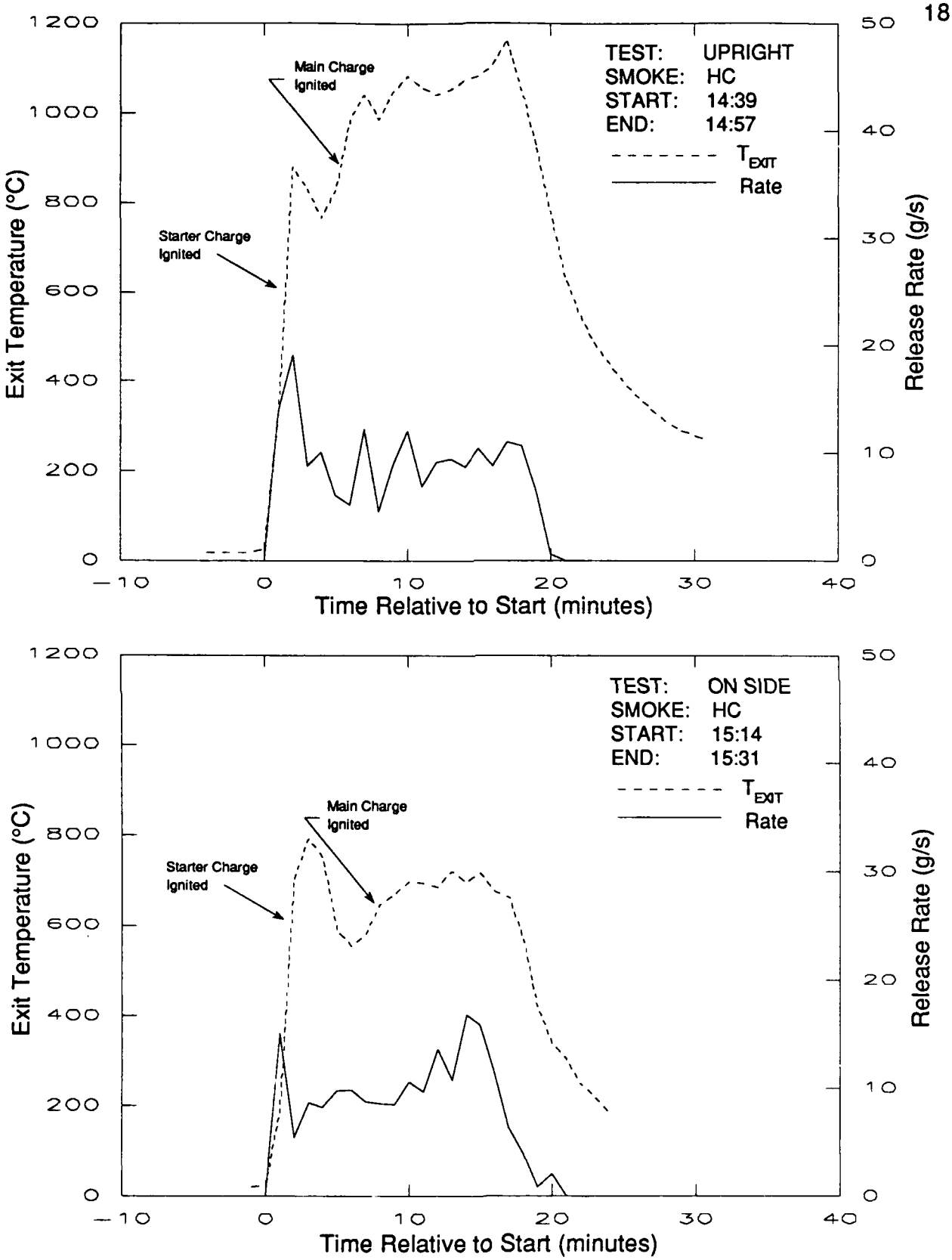

Figure 5.17 One-minute averaged exit temperature and release rate for individual M5 smoke pots; top: pot in upright position; bottom: pot laid on side.

temperature of the single upright smoke pot significantly exceeded the exit temperature measured during test 1112871. It is interesting to note that the release rate of the individual smoke pots also displayed a non-uniform behavior, indicating that they burned unevenly.

From these measurements it is possible to determine the extent to which the initial buoyancy and momentum of the jet which issues from the fog-oil smoke generator or HC smoke pot affects the trajectory of the smoke plume. Table 5.4 summarizes the key dimensional and nondimensional parameters governing the initial behavior of the jet for the three discharge geometries used in the present study: 1) the fog-oil smoke generator, 2) HC smoke pots burned five at a time (designated "HC-5") and 3) 19 HC smoke pots burned roughly all at once (designated "HC-19"). In the table, V_{EXIT} is the exit velocity, D_{EXIT} is the diameter of the exit, T_{EXIT} is the exit temperature, N_{EXIT} is the number of exit ports for the M3A4 or the number of smoke pots for the HC and θ_{EXIT} is the angle between the exit jet and the horizontal plane.

The exit velocity of a prototype of the M3A4 smoke generator (the M3A3E3) was measured during our Dugway-85 field study to be 78 m/s (Liljegren et al., 1988). For the HC tests, no exit velocity measurements were attempted for practical and safety reasons. However, the exit velocity may be estimated from the measured mass flux and exit temperature:

$$V_{EXIT} = \frac{Q}{\rho_{EXIT} \frac{\pi}{4} D_{EXIT}^2}, \tag{5.4}$$

where ρ_{EXIT} is the fluid density at the exit. For the nominal M3A4 mass flux of 45 g/s and assuming ρ_{EXIT} = 587.9 g/m^3, the density for air at an exit temperature of 500 K, V_{EXIT} = 83 m/s which is very close to the measured exit velocity. For a mass flux of 75 g/s, as in Tests 1112871 and 1113871, and an approximate exit temperature of 1000 K, $V_{EXIT} \approx 10$ m/s.

The two relevant nondimensional parameters are the densimetric Froude number Fr, and the ratio of the exit velocity to the mean wind speed U:

$$Fr = \sqrt{\frac{\rho_\infty V_{EXIT}^2}{\Delta\rho\, g\, D_{EXIT}}}, \qquad R = \frac{V_{EXIT}}{U}. \tag{5.5}$$

Here $\Delta\rho = \rho_\infty - \rho_{EXIT}$, where ρ_∞ is the ambient fluid density, and g is the gravitational acceleration. In the table, the subscripts "S" and "M" designate, respectively, the "single-jet" and "merged-jet" values of the exit diameter and densimetric Froude number. The merged-jet diameter is simply the single-jet diameter multiplied by the square root of N_{EXIT}, the number of jets (i.e., the number of exit ports or smoke pots). The actual densimetric Froude number may be expected to lie between the single-jet and merged-jet values. For all the densimetric Froude number calculations, the ambient temperature is taken to be 300 K and the wind speed is assumed to equal 2 m/s.

Table 5.4. Summary of dimensional and nondimensional parameters for three smoke release configurations.

Case	V_{EXIT} (m/s)	$(D_{EXIT})_S$ (m)	$(D_{EXIT})_M$ (m)	T_{EXIT} (K)	N_{EXIT}	θ_{EXIT} (°)	F_S	F_M	R
FO	55	0.019	0.033	800	3	45	166	126	27.5
HC-5	10	0.075	0.167	1000	5	90	14	9.3	5
HC-19	10	0.075	0.326	1000	19	90	14	6.7	5

Experimental investigations of jet behavior which cover the range of parameters defined by Table 5.4 include the studies of Fan (1967), Wright (1977), Petersen (1978), Dunn, Leylek and Chittenden (1982) and Leylek (1984). From these results one can determine the downstream and vertical distances to which the influence of the jet extends and the residual temperature difference between the plume and the ambient fluid. Because the relevant portions of these investigations are limited to vertical jets in a crossflow (i.e., $\theta_{EXIT} = 90°$), only the vertical component of the fog-oil jet is considered in this analysis. Thus in Table 5.4 $V_{EXIT} = 78 \cos(45) = 55$ m/s. These results are summarized in Table 5.5 for the three exit configurations used in our dispersion experiments.

Table 5.5. Jet Characteristics at the end of the region of influence based on the results of laboratory studies.

Case	Downstream Extent of Jet Influence (m)	Vertical Extent of Jet Influence (m)	Residual Temperature Difference (K)
FO	12	3.6	0.4
HC-5	25	4.2	0.1
HC-19	26	3.9	0.15

These results are confirmed by video and still photographs of the initial jet region of the smoke plume taken during our dispersion experiments.

5.4 The Smoke Aerosol

A chemical and physical description of the aerosol produced by the M3A4 fog oil smoke generator and the M5 HC smoke pot is necessary for a complete understanding of the behavior of the smoke plume. The chemical composition determines, for example, how the aerosol is partitioned between the droplet and vapor phases as well as the extent to which evaporation is significant. It substantially influences the size distribution of the droplets. This is especially true for HC smoke since the resultant $ZnCl_2$ droplets are believed to be extremely hygroscopic. The size distribution plays a major role in the behavior of the smoke plume. Removal mechanisms such as settling and deposition are primarily influenced by the size and density of the droplets. In addition, the extent to which the droplets are respirable by animals and humans is also dependent on the droplet size distribution.

5.4.1 Chemical Composition

A detailed study of the chemical composition of SGF-2 fog oil was performed by Katz, Snelson, Butler, Farlow, Welker, Mainer and Rajendran (1980) of the Illinois Institute of Technology Research Institute (IITRI). They determined that "the fog oil and the fog [oil smoke] contained almost equal amounts of aliphatic and aromatic hydrocarbons ..." and that "of the several hundred identifiable species, aliphatic hydrocarbons were in the $C_{14} - C_{22}$ range." Using gas chromatography and a parallel analysis of the fog oil and a series of n-paraffins in the $C_{12} - C_{29}$ range, DeVaull (1988) determined the equivalent molecular weight distribution of the fog oil. Table 5.6 presents these results along with the molecular weight, density and vapor pressure compiled by the American Petroleum Institute (1958).

DeVaull (1988) examined the vapor/droplet partitioning of the fog-oil aerosol by connecting a filter and an adsorbent-filled tube in series. He found that less than 1% of the aerosol by mass existed as a vapor. This is in contrast to the diesel fuel-based aerosol produced by the US Army Vehicle Engine Exhaust Smoke System (VEESS), of which approximately 20% exists in the vapor phase (Jenkins Gayle, Wike and Manning, 1982). The vapor phase for the VEESS aerosol was determined by Jenkins et al. to contain those constituents of the initial diesel fuel having a boiling point less than tridecane ($n\text{-}C_{13}H_{28}$). This supports DeVaull's conclusion regarding fog-oil

smoke since the liquid fog oil contains negligible amounts of such light molecular weight compounds, as Table 5.6 indicates.

Table 5.6. Equivalent molecular weight distribution of fog oil and selected property values.

C_n	Molecular Weight	Density (kg/m^3)	Vapor Pressure (kPa)	Fog Oil Fraction (%)
12	170.34	748.69	9.71E-03	0 00
13	184.37	756.22	2.71E-03	0.00
14	198.39	762.75	7.24E-04	1.90
15	212.42	768.30	1.89E-04	3.42
16	226.45	773.44	4.62E-05	5.32
17	240.48	777.90	1.27E-05	7.98
18	254.50	781.80	3.15E-06	9.13
19	268.53	785.40	7.76E-07	12.93
20	282.56	788.60	1.49E-07	12.17
21	296.58	792.98	4.21E-08	11.03
22	310.61	797.44	1.04E-08	9.51
23	324.64	802.54	2.59E-09	7.60
24	338.66	808.47	6.68E-10	6.08
25	352.69	815.45	1.78E-10	4.94
26	366.72	823.67	4.99E-11	3.80
27	380.75	833.32	1.48E-11	2.28
28	394.77	844.60	4.73E-12	1.14
29	408.80	857.71	1.64E-12	0.76

The IITRI staff also performed a chemical analysis of the M5 smoke pot (Katz et al., 1980). The smoke pots were found to contain two layers of mixtures of hexachloroethane (HC), zinc oxide (ZnO) and aluminum (Al) in the mass fractions given in Table 5.7. The higher aluminum content of the upper layer facilitated its ignition and increased its burn rate. This accounts for the non-constant release rates observed for the individual M5 smoke pots presented in Fig. 5.17. In addition, the IITRI study found that the starter mixture contained silicon, potassium nitrate, charcoal, iron oxide, grained aluminum, cellulose nitrate and acetone. That this mixture is similar to both thermite and black power probably accounts for the explosive nature of the ignition phase.

Table 5.7. Composition of M5 smoke pot (Katz,et al, 1980).

REAGENT:	UPPER LAYER	LOWER LAYER
HC	45.5	46.6
ZnO	47.5	48.3
Al	7.0	5.2

$ZnCl_2$ was found to be the predominant constituent of the aerosol along with small amounts of Al_2O_3 (1.7%) and traces of lead and cadmium chlorides.

In their analysis of the trace gases given off by the M5 smoke pot, Katz et al. (1980) found carbon monoxide, phosgene, trichloroacetyl chloride, carbon tetrachloride, tetrachloroethylene, hexachloroethane and hexachlorobenzene. In order to prevent the inhalation of these trace gases as well as the hygroscopic $ZnCl_2$ particles, which the Surgeon General of the US Army has ruled toxic and hazardous to human health (Hansen, 1989) all field personnel were required to wear face masks fitted with both glass fiber and activated charcoal filters.

5.4.2 Particle Size Analysis

The particle size analysis was carried out using a Model PC-2 quartz crystal microbalance (QCM) cascade impactor manufactured by California Measurements, Inc. (Sierra Madre, CA). The cascade impactor of the PC-2 is comprised of ten aerodynamic inertial impactors arranged in series. Figure 5.18 is a schematic illustration of the QCM. The aerosol is drawn into the instrument at 240 cm^3/min by a small pump. The aerosol stream is then accelerated through a nozzle in a small high-speed jet and impinges on a quartz crystal plate mounted close to the jet exit and normal to the direction of flow. The effect of the plate is to form an abrupt 90° bend in the streamlines. Particles with sufficient inertia are unable to follow the streamlines and thus impact on the crystal plate. The crystal plates were coated with Apiezon L grease in order to prevent the HC particles from bouncing off; this was not necessary for the fog-oil droplets. Smaller particles which are able to follow the streamlines avoid hitting the plate and are carried on past it. The ten stages are identical except that they have progressively smaller nozzle diameters which cause the air jets to have progressively higher speeds. In this manner, increasingly smaller particles are deposited on successive stages.

As the particles collect on the crystal plate the oscillating frequency f_S of the crystal decreases. Immediately behind the sensing crystal and shielded from the impinging air stream is an identical reference crystal whose frequency f_R does not change since no particles are impacted on it. Both crystals have resonant frequencies of 10 MHz, but the frequency of the reference oscillator is purposely set about 3 kHz higher than the sensing crystal oscillator. The two frequencies are then mixed; the beat frequency output by the mixer f_{OUT} represents the frequency difference between the sensing and reference crystals. The purpose of the reference crystal is to cancel

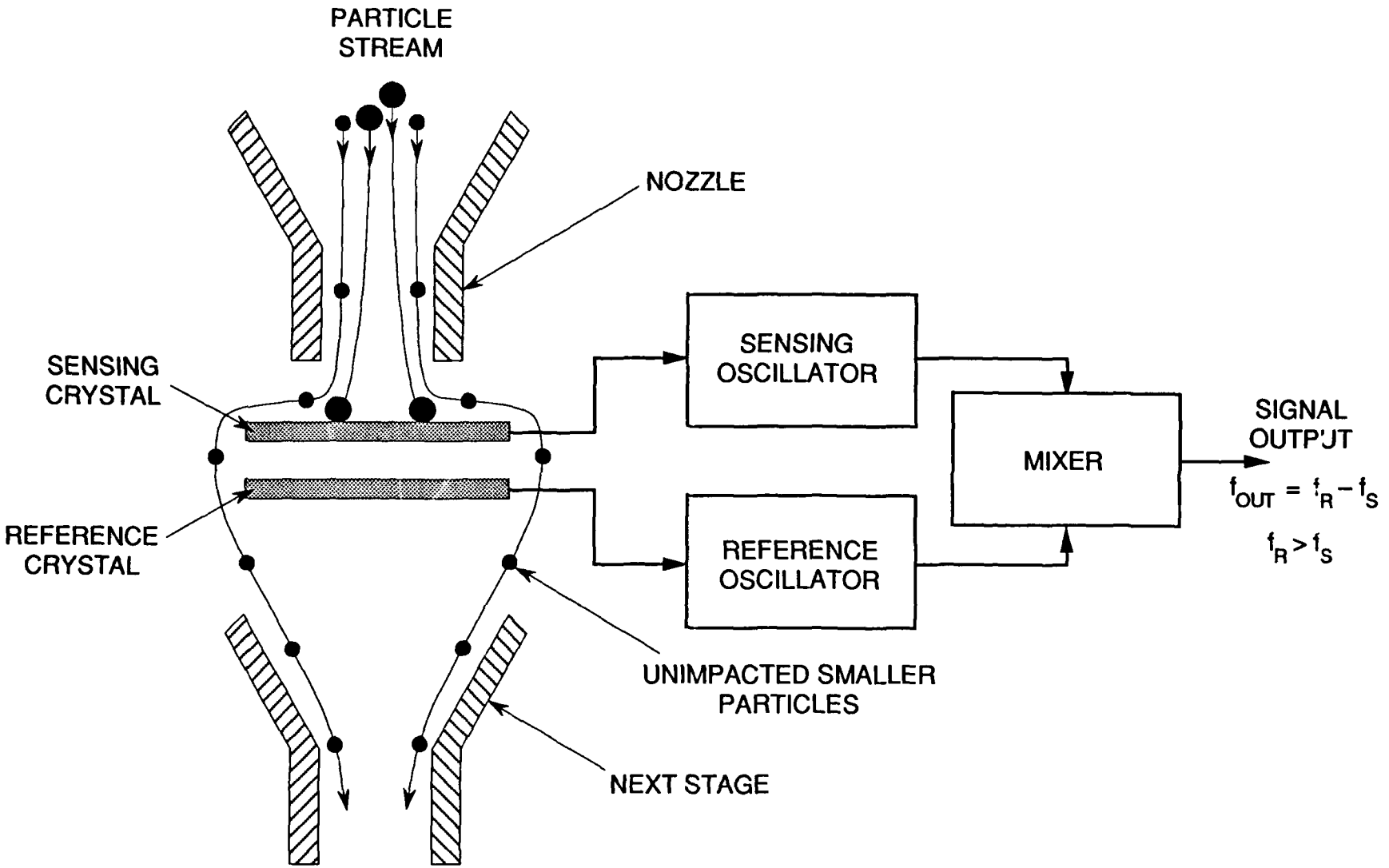

Figure 5.18 A typical quartz crystal microbalance impactor stage.

out any frequency changes due to changes in temperature and humidity variations in the air stream. Since both crystals will experience an identical frequency shift due to changes in temperature and humidity, their effect will not be present in the mixed beat frequency.

As particles impact on the sensing crystal and mass accumulates, f_S decreases and $f_{OUT} = f_R - f_S$ increases. By measuring f_{OUT} before and after aerosol collection, the amount of mass deposited on the sensing crystal plate may be determined with a high degree of accuracy. In addition, the extreme sensitivity of the technique means that only a small amount of mass need be collected and so the aerosol need only be sampled for periods of several seconds. This is an important consideration in field sampling of smoke plumes since the instrument may only be exposed to the smoke for brief periods due to the meandering nature of the plume.

The probability that a particle will impact on a stage, referred to as the *collection efficiency*, is governed by the Stokes number (Hinds, 1982; page 114)

$$Stk = \frac{2\ T_R\ V_j}{D_j}, \tag{5.6}$$

where V_j is the jet velocity, D_j is the jet diameter and T_R is the *relaxation time* of the particle:

$$T_R = \frac{\rho_p d_p^2\ C_c}{18\ \eta}. \tag{5.7}$$

Here ρ_p and d_p are the particle density and diameter, respectively and η is the viscosity of the air. C_c is the Cunningham correction factor (Hinds, 1982; page 45):

$$C_c = 1 + \frac{2.52\ \lambda_{mfp}}{d_p}, \tag{5.8}$$

where λ_{mfp} is the mean free path of the air molecules. (For air at 1 atm and 20 °C, λ_{mfp} = 0.066 μm.) The Cunningham correction factor accounts for non-continuum effects that arise as the particle size approaches the mean free path of the air molecules.

Impactors which exhibit a "sharp cutoff" efficiency curve closely approximate the ideal step-function efficiency curve for which all particles greater than a certain aerodynamic diameter are impacted and all smaller particles pass through. (The aerodynamic diameter is the diameter of the unit density sphere that has the same

settling velocity $V_s = T_R g$ as the particle under study.) Well-designed impactors are generally assumed to be ideal and their efficiency curves characterized by a single number Stk_{50}, the Stokes number that gives 50% collection efficiency. As shown in Fig. 5.19, this is equivalent to assuming that the mass of particles larger than the cutoff size that get through (upper shaded area) equals the mass of particles below the cutoff size that are collected (lower shaded area).

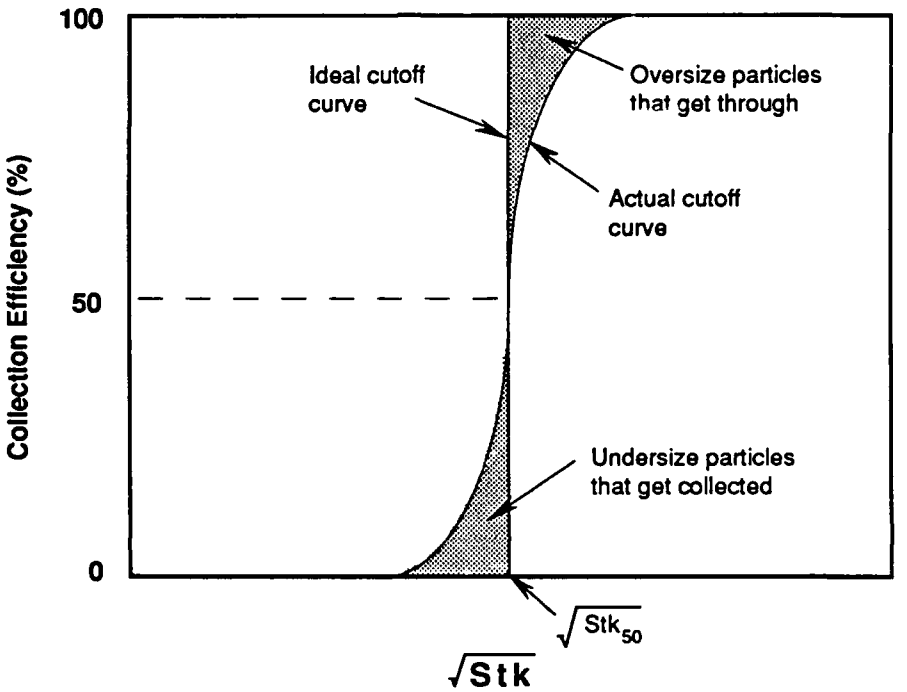

Figure 5.19 Actual vs. ideal collection efficiency for inertial impaction. Adapted from Hinds (1982).

The cutoff sizes stated by the manufacturer for each of the ten stages of the PC-2 cascade impactor are given in Table 5.8 for particles with $\rho_p = 2.0$ g/cm^3. Thus Stage 1 collects particles for which $d_p \geq 25.0$ μm, Stage 2 collects particles in the range $12.5 \leq d_p < 25.0$ μm, etc. The midsize given in the third column of Table 5.8 represents the assumed average size of the particles collected on that stage. This value is used in determining the mass mean particle size; it is simply the arithmetic average of the endpoints of the size range for the stage.

Table 5.8. Cutoff sizes for California Instruments PC-2 QCM cascade impactor for particles with $\rho = 2$ g/cm^3.

STAGE	CUTOFF SIZE (μm)	MIDSIZE (μm)
1	25.0	–
2	12.5	18.75
3	6.4	9.45
4	3.2	4.80
5	1.6	2.40
6	0.80	1.20
7	0.40	0.60
8	0.20	0.30
9	0.10	0.15
10	0.05	0.075

The sizes given in Table 5.8 must be adjusted for the fog oil analysis since the density of the fog oil is 0.9 g/cm^3 (Katz et al., 1980). This adjustment is based on the observation that for a given stage the Stk_{50} value must remain constant. Thus,

$$Stk_{50} = \frac{\rho_{oil}\, d_{oil}^2\, V_j\, C_c}{9\eta D_j} = \frac{\rho_{nominal}\, d_{nominal}^2\, V_j\, C_c}{9\eta D_j} \tag{5.9}$$

and so

$$d_{oil} = d_{nominal}\sqrt{\frac{\rho_{nominal}}{\rho_{oil}}} = 1.4907\, d_{nominal}\,. \tag{5.10}$$

Table 5.9 presents the cutoff sizes and mid sizes appropriate for fog oil.

Table 5.9. Cutoff sizes for California Instruments PC-2 QCM cascade impactor for fog oil (ρ = 0.9 g/cm^3).

STAGE	CUTOFF SIZE (μm)	MIDSIZE (μm)
1	37.3	–
2	18.6	28.0
3	9.5	14.1
4	4.8	7.2
5	2.4	3.6
6	1.2	1.8
7	0.60	0.9
8	0.30	0.45
9	0.15	0.22
10	0.075	0.11

The values for the cut size and mid size given in Table 5.8 were used for the HC particle size analysis since the density of HC particles was taken to be 2 g/cm^3. Katz et al. (1980) also used this value for the particle density in their analysis of HC particle size carried out with an earlier model of the PC-2 QCM cascade impactor. Although this is the density of the material in the smoke pot prior to ignition (Katz et al., 1980) and not necessarily equal to the density of the aerosol particles, it was used because no better estimate of the actual particle density was available. However, the particle density can be bounded. If the particles were pure $ZnCl_2$, their density would be about 3 g/cm^3. If, on the other hand, the particles were essentially water droplets with very small $ZnCl_2$ nuclei, then their density would be approximately 1 g/cm^3. For ρ_p = 3 g/cm^3, the cut sizes and mid sizes given in Table 5.8 would have to be adjusted by a factor of 0.816; for ρ_p = 1 g/cm^3, the adjustment would be 1.414. The actual density must lie between these two bounds; the estimated density of 2 g/cm^3 seems reasonable. Nevertheless, the uncertainty in the density will affect the accuracy of the results.

The arithmetic mass mean $\bar{d}$, geometric mass mean d_g and geometric standard deviation σ_g were computed from the data gathered during each test as follows. For the arithmetic mass mean,

$$\bar{d} = \frac{\sum_{i=1}^{S} m_i d_i}{\sum_{i=1}^{S} m_i}, \tag{5.11}$$

where S is the number of stages in the cascade impactor, d_i is the mid size of the i^{th} stage and $m_i = \sum_{j=1}^{N} m_{ij}$, the total mass collected on each stage during the test. N is the number of particle size measurements carried out during the test and m_{ij} is the mass collected on the i^{th} stage during the j^{th} measurement. The geometric mass mean diameter is given by

$$\ln d_g = \frac{1}{M} \sum_{j=1}^{N} \sum_{i=1}^{S} m_{ij} \ln d_i , \tag{5.12}$$

where $M = \sum_{j=1}^{N} \sum_{i=1}^{S} m_{ij}$, is the total mass collected on all stages during the test. The geometric standard deviation is computed according to

$$(\ln \sigma_g)^2 = \frac{1}{M} \sum_{j=1}^{N} \sum_{i=1}^{S} m_{ij} (\ln d_i - \ln d_{g,j})^2$$

$$= \frac{1}{M} \sum_{i=1}^{S} m_i (\ln d_i)^2 - (\ln d_g)^2 , \tag{5.13}$$

where $d_{g,j}$ is the geometric mass mean diameter computed from the results of the j^{th} measurement. (Note that since the total mass collected M is five to six orders of magnitude greater than the mass of an "average" particle m_{avg}, the number of "average" particles collected $N_{avg} \equiv M/m_{avg} \cong N_{avg}-1$ and the sample variance and population variance are essentially equal. Thus normalizing Eq. (5.13) with the total mass M rather than $m_{avg}(N_{avg}-1)$ is sufficient.)

5.4.3 Results

The arithmetic mass mean diameter, geometric mass mean diameter and geometric standard deviation for fog-oil Tests 1103871, 1104872 and 1106871 are presented in Table 5.10. The geometric standard deviation $(\sigma_g)_{H\text{-}C}$ computed from the

mass mean diameter and the geometric mass mean diameter using the Hatch-Choate equation (Hinds, 1982; page 91) for a lognormal distribution is also given in Table 5.10.

Table 5.10. Particle size distribution statistics for fog oil (ρ = 0.9 g/cm^3). The uncertainties represent a 95% confidence limit.

TEST:	1103871	1104872	1106871	Katz et al.	
LOCATION (m)	316.4, 298.4	316.4, 298.4	184.0,164.5	—	
DISTANCE FROM SOURCE (m)	436	436	259	—	
T_{EXIT} (°C)	486†	401	415	371	572
$\bar{d}$ (μm)	1.02±0.13	0.71±0.06	1.07±0.09	0.98	0.74
d_g (μm)	0.91±0.10	0.60±0.03	0.96±0.03	0.90	0.64
σ_g	1.55±0.09	1.71±0.09	1.53±0.11	1.53	1.36
$(\sigma_g)_{H-C}$	1.61	1.79	1.59	1.51	1.71

†Based on last five minutes of source data record.

Note that for Test 1104871, a fog-oil concentration sufficient to yield a statistically valid measurement of the particle size distribution was never present at the cascade impactor location due to the meandering of the smoke plume. Also tabulated are the distances from the release point to the location at which the particle size measurements were carried out and the average exit temperature of the M3A4 smoke generator. As previously explained, the value of the exit temperature given in the table for Test 1103871 may not be representative of the actual conditions during the test.

The results of Tests 1103871 and 1106871 agree with the findings of Katz et al., (1980) for an exit temperature of 371°C. Katz et al., (1980) also observed a decrease in particle size at a higher exit temperature of 572°C. Although their results appear to suggest that the exit temperature for Test 1104872 was higher than normal, our data indicate that it was not. These results are also in agreement with our earlier findings during the Dugway-85 field study (Liljegren et al., 1988).

Log-probability plots of the measured size distribution for Tests 1103871, 1104872 and 1106871 are presented in Figs. 5.20-22, respectively. The error bars indicate the 95% confidence limits in the data. (A detailed error analysis is presented in Appendix A.) The particle size is plotted along the horizontal axis on a logarithmic scale and the cumulative mass fraction is plotted along the vertical axis on a Gaussian or normal scale. A lognormal distribution (a distribution of values x for which y=ln(x) is normally distributed) with the same geometric mean and standard deviation as the

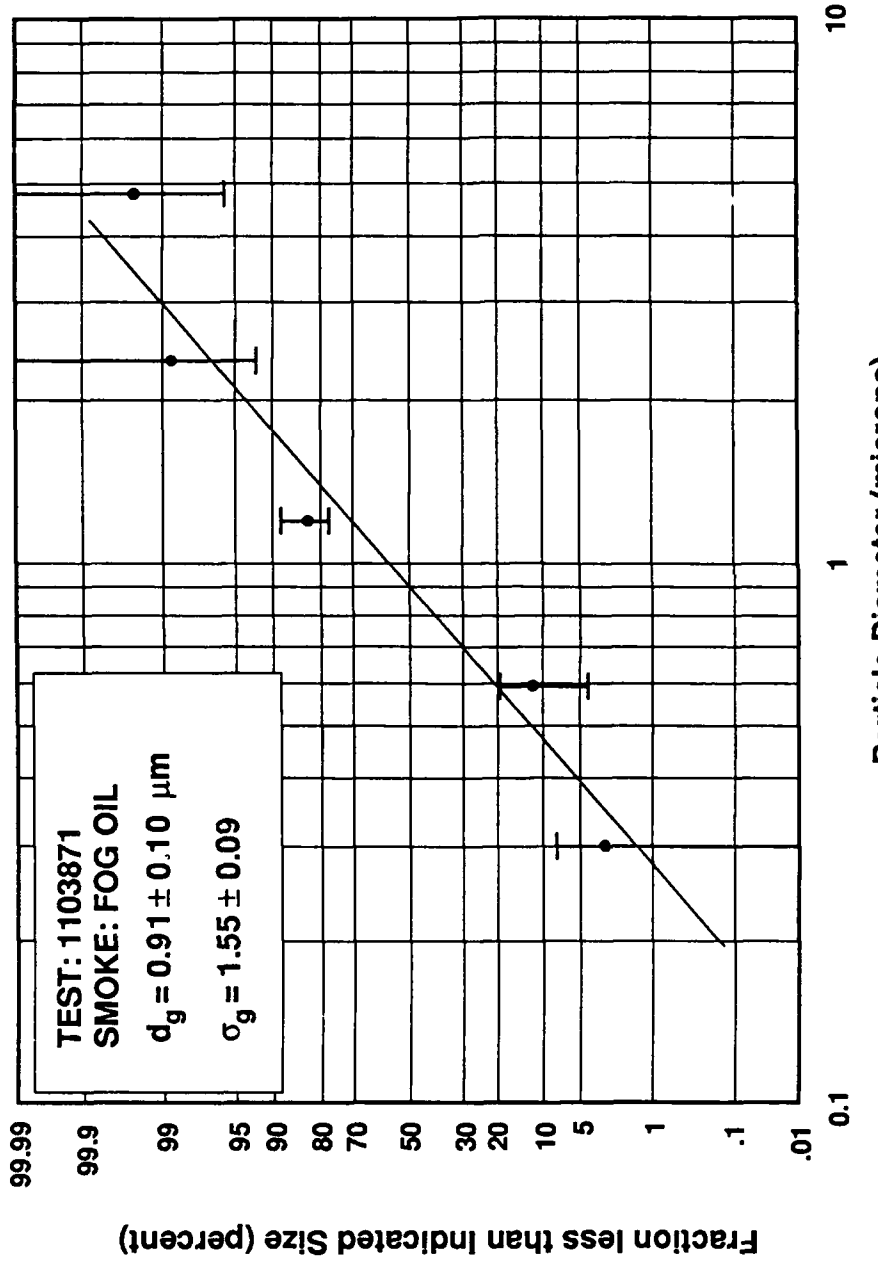

Figure 5.20 Particle size distribution of fog oil smoke from test 1103871.

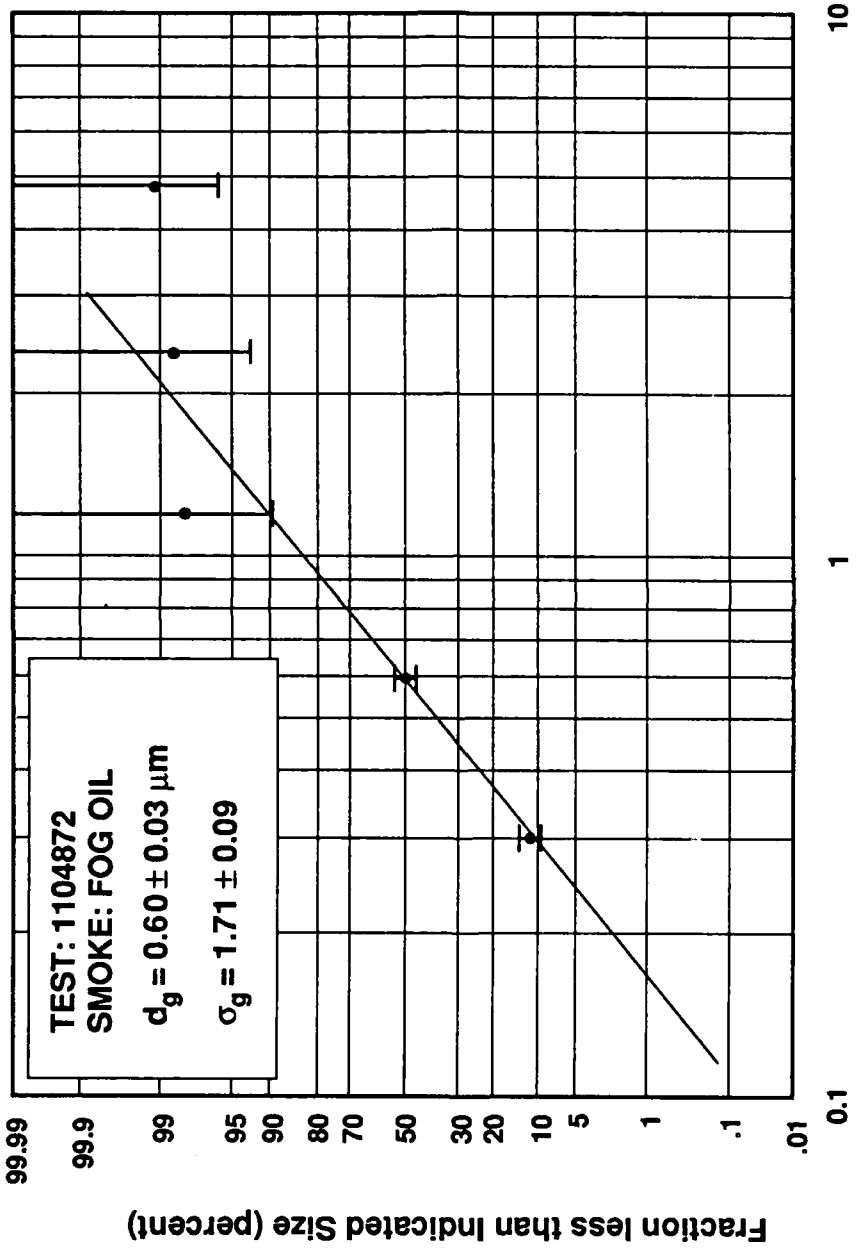

Figure 5.21 Particle size distribution of fog oil smoke from test 1104872.

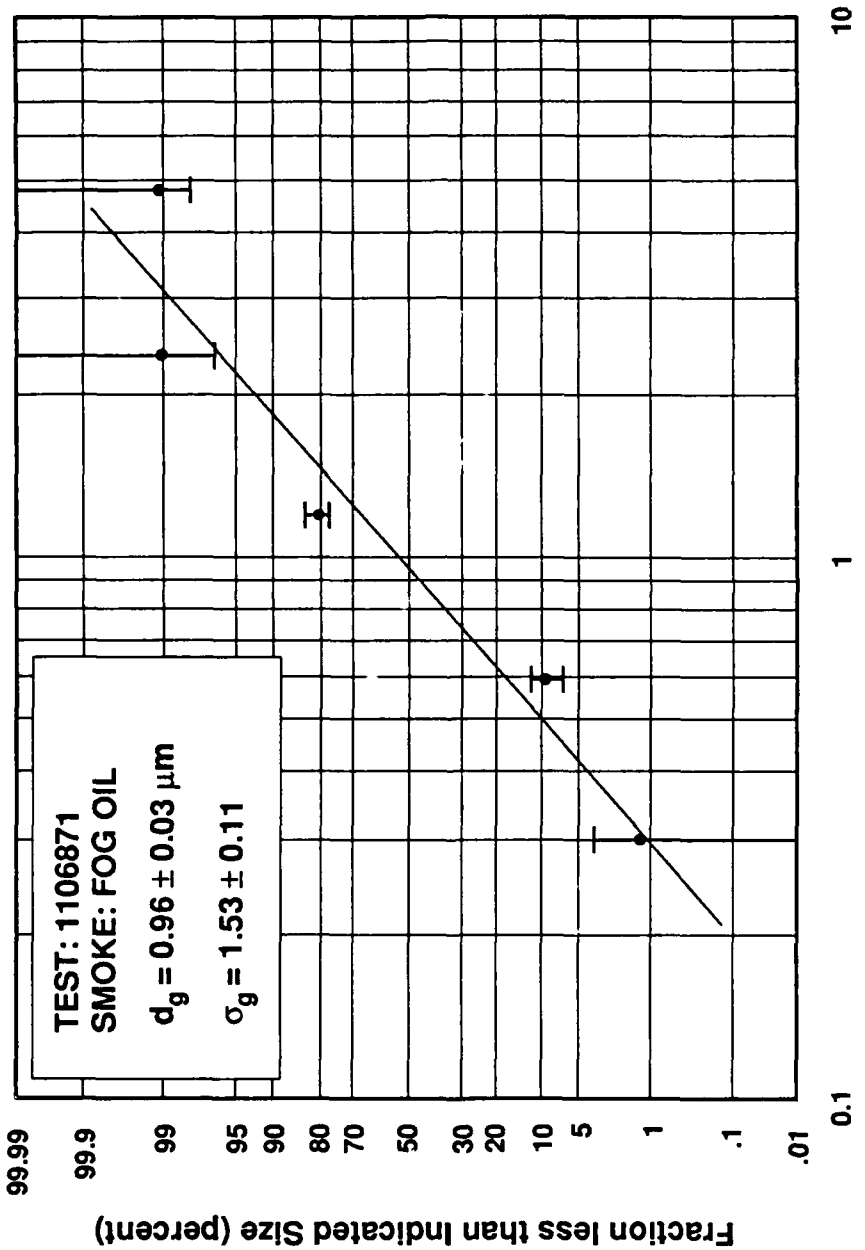

Figure 5.22 Particle size distribution of fog oil smoke from test 1106871.

data is thus indicated as a straight line. For the lognormal distribution the geometric mean diameter is equal to the median diameter. Thus if the oil fog size distribution may be approximated as lognormal, the computed geometric mass mean also represents the mass median diameter; that is, the diameter for which 50% of the mass is at larger diameters and 50% is at smaller diameters. Although the figures give the impression that the data are lognormally distributed, a more quantitative indication is desirable. The Hatch-Choate equation (Hinds, 1982; page 91) can be used to relate the mass mean diameter, mass median diameter and geometric standard deviation for a lognormal distribution:

$$(\sigma_g)_{H\text{-}C} = \exp\left[\sqrt{2 \ln\left(\frac{\bar{d}}{d_g}\right)}\right]. \qquad (5.14)$$

Using the values for $\bar{d}$ and d_g from Table 5.10, Eq. (5.14) yields the values for $(\sigma_g)_{H\text{-}C}$ given in Table 5.10. Note that the computed values of $(\sigma_g)_{H\text{-}C}$ all fall within the 95% confidence limits for the measured values of σ_g for the tests. Although this is not a conclusive proof of the lognormal hypothesis, it strongly suggests that the size distribution of the oil fog aerosol is lognormal.

The arithmetic mass mean diameter $\bar{d}$, geometric mass mean diameter d_g and geometric standard deviation σ_g for HC Tests 1109871, 1110871, 1110872, 1112871 and 1113871 are presented in Table 5.11. The geometric standard deviation which would result from a lognormal distribution having the same values of $\bar{d}$ and d_g, as calculated from the Hatch-Choate equation, is also given in the table.

Table 5.11. Particle size distribution statistics for HC. The uncertainties represent a 95% confidence limit (90% confidence for 1109871).

TEST:	1109871	1110871	1110872	1112871	1113871
LOCATION (m)	23.8, 45.0	23.8, 45.0	23.8, 45.0	316.4, 298.4	316.4, 298.4
DISTANCE FROM SOURCE (m)	492	492	492	431	431
RELATIVE HUMIDITY (%)	69	61	49	35	45
ABSOLUTE HUMIDITY (mol/m^3)	0.28	0.21	0.16	0.24	0.29
$\bar{d}$ (μm)	1.22±0.13	1.07±0.06	1.07±0.11	1.50±0.16	1.18±0.10
d_g (μm)	1.05±0.32	0.77±0.05	0.83±0.06	1.11±0.16	0.93±0.08
σ_g	1.78±0.45	2.36±0.20	2.07±0.18	2.41±0.17	2.05±0.12
$(\sigma_g)_{H\text{-}C}$	1.85	1.52	1.50	2.35	1.82

These results suggest that, within the experimental uncertainty, Tests 1109871, 1112871 and possibly 1113871 were lognormally distributed. Tests 1110871 and 1110872 had a much larger geometric standard deviation than a corresponding lognomal distribution would give. A careful study of the log-probability plots of the size distribution for the HC tests, given in Figs. 5.23-27, shows that for all HC tests more material was collected on the smallest stages of the impactor than a lognormal distribution would indicate, with Tests 1110871 and 1110872 showing the greatest deviation from lognormal. Since particle size measurements conducted prior to these tests did not reveal the presence of significant background aerosols, it may be concluded that the actual size distribution of HC particles is bimodal.

These results may be compared with those obtained by Katz et al., (1980) as summarized in Table 5.12. The comparison is complicated by the fact that Katz et al. constructed "minipots" containing small amounts of material from the M5 HC pots and carried out their tests in a confined chamber with a volume of 96.5 m^3. Although their approach yielded repeatable and reliable data, their results are difficult to reconcile with data collected in our field studies. For example, the airborne concentration in the chamber ranged from 800 to 8000 mg/m^3 whereas the concentrations measured in the field study at the distance from the release point where the size distribution measurements were performed was ~1 mg/m^3. As a result, the confined aerosol showed a significant increase in mean diameter over the period of confinement (approximately 30 minutes) due to agglomeration whereas no such growth was observed for our field study.

Table 5.12. Particle size distribution statistics for HC reported by Katz et al. (1980).

TEST NO.:	3-5	6-7	8-9	10	11-29
Pot Type	1	2	3	4	1
Volume (cm^3)	12	25	50	500	12
$\bar{d}$ (μm)	0.42	0.53	1.07	1.40	0.41
d_{av} (μm)	0.41	0.48	0.59	0.71	0.30
σ_g	~1.7†	—	—	—	—
$(\sigma_g)_{HC}$	1.09	1.18	1.56	1.61	1.38

†Determined from Figure 4 in Katz et al. (1980).

Table 5.12 presents the mass mean diameter $\bar{d}$, the number mean diameter d_{av} and the geometric standard deviation reported by Katz et al., (1980) for four different

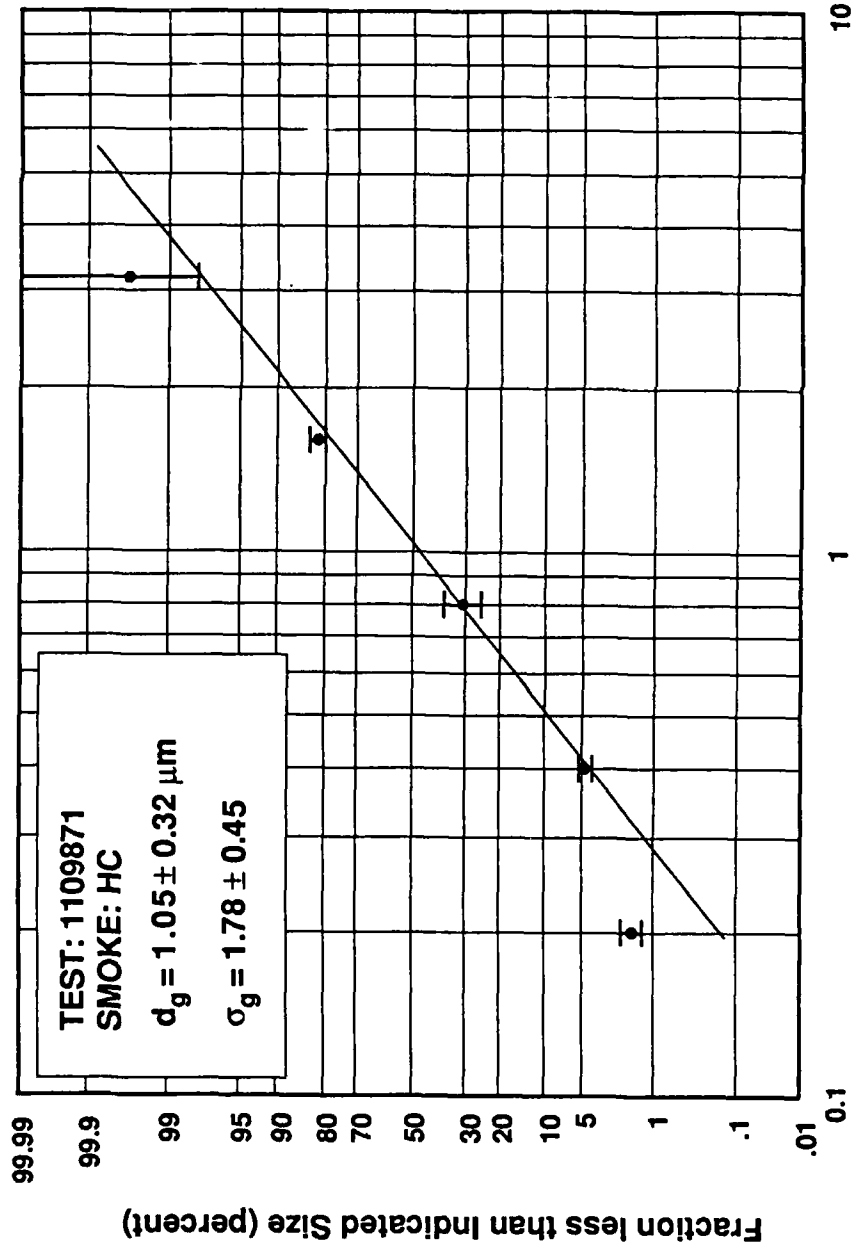

Figure 5.23 Particle size distribution of HC smoke from test 1109871.

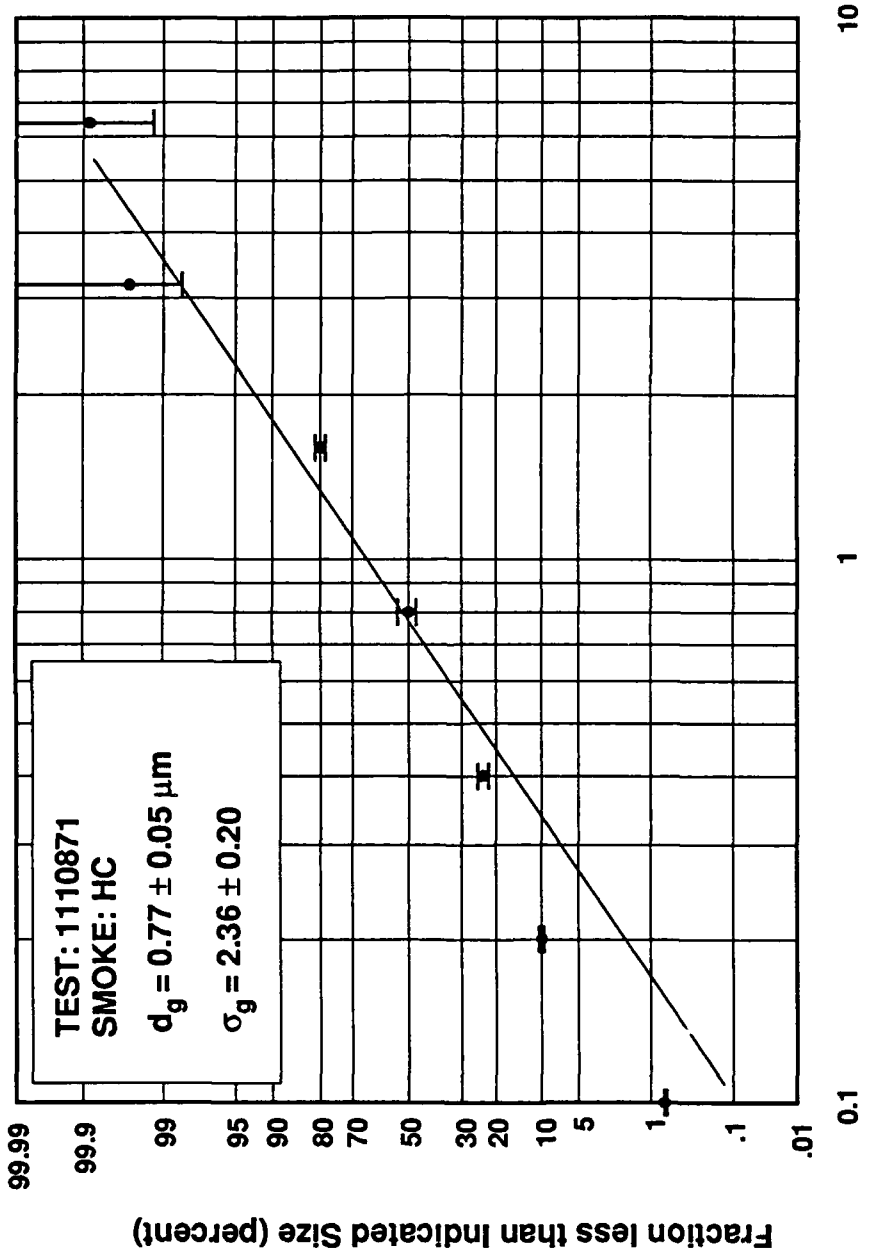

Figure 5.24 Particle size distribution of HC smoke from test 1110871.

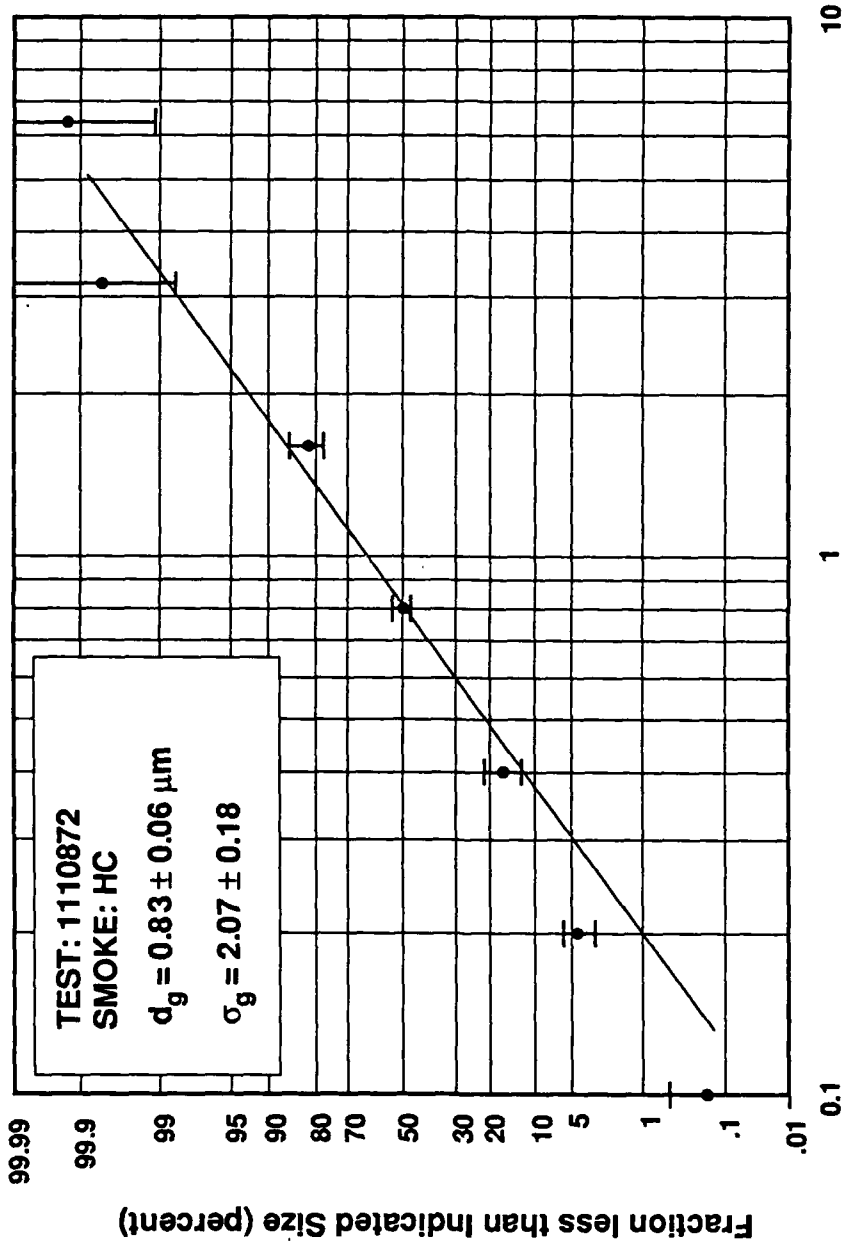

Figure 5.25 Particle size distribution of HC smoke from test 1110872.

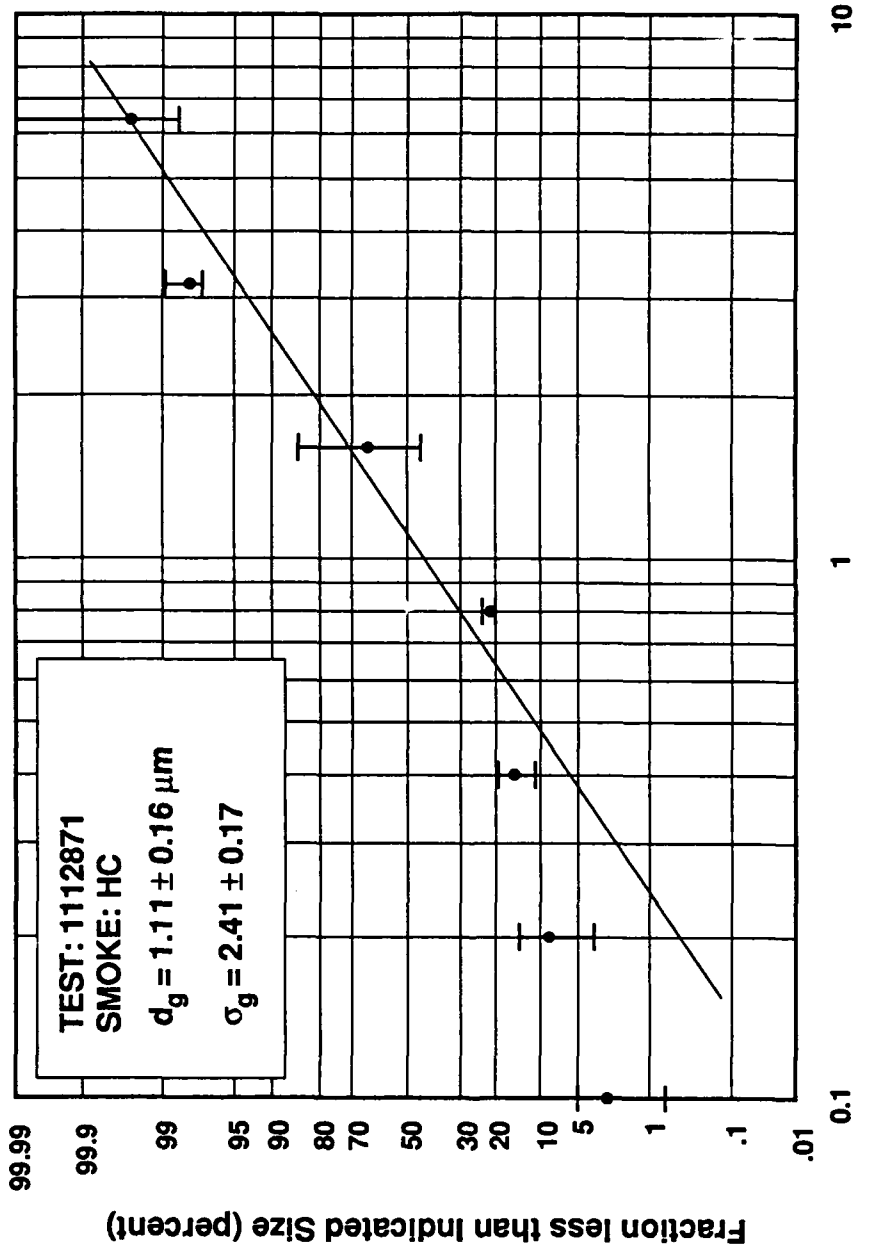

Figure 5.26 Particle size distribution of HC smoke from test 1112871.

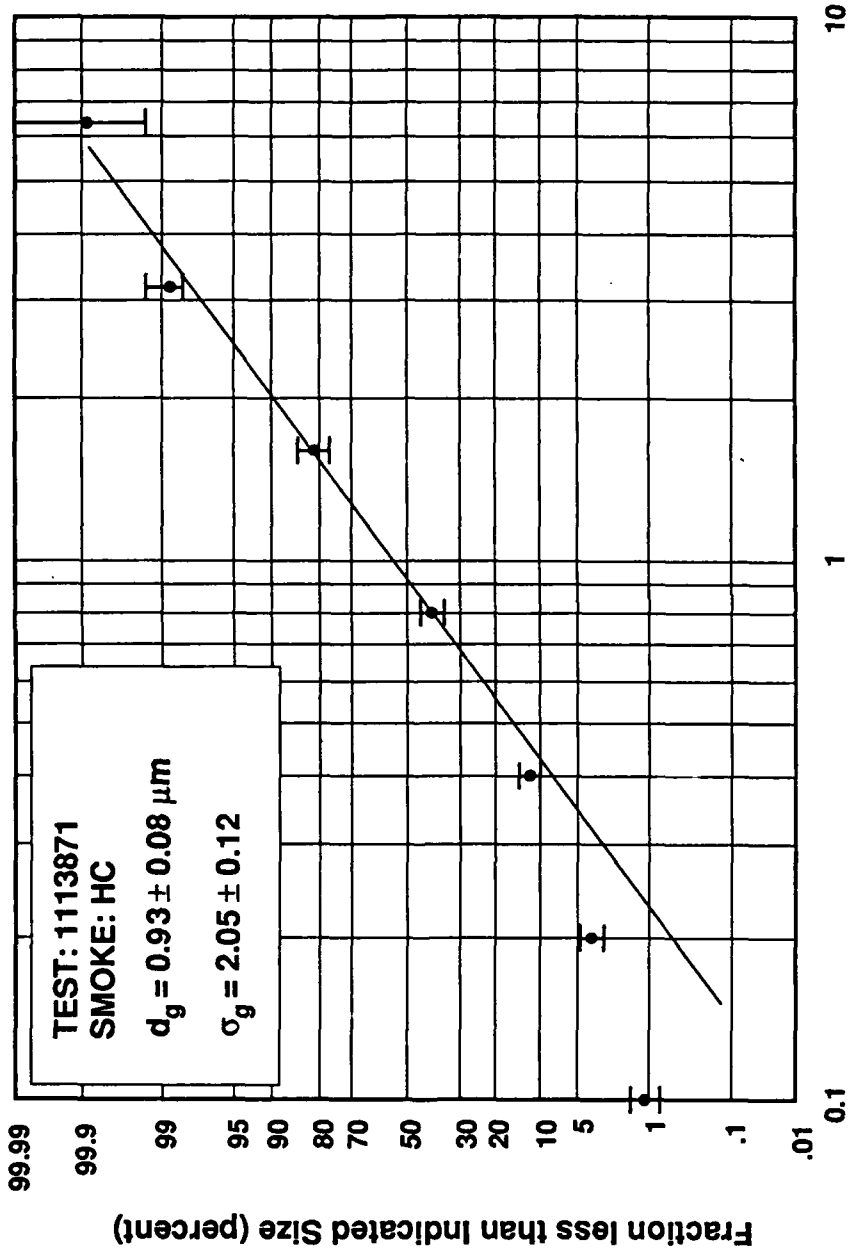

Figure 5.27 Particle size distribution of HC smoke from test 1113871.

size minipots as well as the geometric standard deviation for a lognormal distribution having the reported values of $\bar{d}$ and d_{av} calculated using the Hatch-Choate equation. Clearly the size of the pot significantly affects the mean statistics and the distribution does not appear to be lognormal.

Although these results differ significantly from those based on their own data for an actual M5 HC smoke pot, their tests 8 and 9 do show some quantitative agreement with our data. In addition, their measurements also indicated that the HC smoke was bimodally distributed with one mode at less than 0.2 μm and the other mode at 0.7-1.1 μm. The contribution of the 0.2 μm mode to the mass-weighted statistics would be very small since the mass of a particle is proportional to the cube of its diameter. Despite the nearly negligible contribution of the small particles to the total mass of the aerosol, our measurements did indicate their presence, as evidenced by the departure of the cumulative distributions we measured from lognormal at small sizes.

Katz et al. also investigated the effects of relative humidity in the range 9.5-75% at 25 °C which corresponds to absolute humidity in the range 0.12-0.96 mol H_2O per m^3 air. Although they found a strong effect of humidity on the burn rate, they could find no effect on the size distribution. This was unexpected since $ZnCl_2$ is extremely hygroscopic. Our HC tests also revealed no significant variation in the particle size distribution with relative humidity although our tests encompassed a much narrower range of humidity (relative: 35-61%; absolute: 0.16-0.29 mol/m^3).

5.4.4 Discussion

Several important aspects of the behavior of the fog-oil plume can be deduced from the results of the particle size analysis. First, the relaxation time or response time of the particles can be computed using Eq. (5.7). For $d_p = 1$ μm, $\rho_p = 0.9$ g/cm^3 and $\eta = 1.82 \times 10^{-5}$ kg/m·s, $C_c = 1.16$ and thus $T_R = 3.2 \times 10^{-6}$ s. This may be compared with the Kolmogorov time scale T_K which is characteristic of the smallest fluid motions (Tennekes and Lumley, 1972; page 20):

$$T_K = \left(\frac{\nu}{\varepsilon}\right)^{1/2}, \qquad (5.15)$$

where ν is the kinematic viscosity of the air and ε is the viscous dissipation rate. In the atmosphere, $T_K \approx 10^{-2}$ s, which is considerably larger than the response time of the fog-oil droplets. From this it may be concluded that the fog-oil droplets can respond to

the smallest motions in the atmosphere and can thus be accurately modelled as a passive tracer (i.e., the plume may be regarded as "marked" fluid).

The magnitude of the error in the measurement of airborne fog-oil concentrations arising from anisokinetic sampling can also be estimated once the droplet size is known. Anisokinesis occurs when the aerosol is sampled at a velocity (speed and direction) other than the free stream velocity. One of the appropriate dimensionless parameters in this case is the Stokes number:

$$\mathrm{Stk} = \frac{T_R V_s}{D_s}, \tag{5.16}$$

where V_s is the velocity of the air flow in the sampler and D_s is the diameter of the sampler inlet. We sampled the smoke with 37 mm filter cassettes aspirated at 23.6 liters per minute (50 ft^3/hr). These give V_s = 36.6 cm/s; with $T_R = 3.2 \times 10^{-6}$ s, the Stokes number becomes $\mathrm{Stk} = 3.2 \times 10^{-5}$. The other parameter is ratio of the free stream velocity to the sampling velocity U/V_s. Belyaev and Levin (1974) give a formula relating the Stokes number and the velocity ratio to the aspiration coefficient $A = C/C_\infty$ where C is the measured concentration and C_∞ is the concentration in the free stream:

$$A = 1 + \left(\frac{U}{V_s} - 1\right)\left(1 - \frac{1}{1 + (2 + 0.62\, V_s/U)\mathrm{Stk}}\right). \tag{5.17}$$

With their formula, and using $U/V_s = 10$, A = 1.005, indicating essentially perfect sampling. In addition, Durham and Lundgren (1979) and Hinds (1982, page 190) indicate that, in general, perfect sampling results for Stk < 0.01; this condition is well satisfied for our measurements.

Deposition of the aerosol to the ground surface and covering vegetation may be examined in terms of filtration theory by treating the vegetation as fibers in a filter. For the purposes of this discussion the predominant vegetation, grass about 1 m tall, will be considered to have a diameter of 1 mm and a spacing of 25 mm between stalks. Five mechanisms for deposition can thus be identified: 1) interception, 2) inertial impaction, 3) diffusion, 4) gravitational settling and 5) electrostatic attraction.

Collection by interception occurs when a particle follows a gas streamline that happens to come within one particle radius of the surface of a fiber. The particle hits the fiber and is captured because of its finite size. The single-fiber efficiency due to interception is given in terms of $R = d_p/d_f$, the ratio of the particle diameter to the diameter of the fiber (Hinds, 1982; page 175):

$$E_R = \frac{1}{2Ku}\left(2(1+R)\ln(1+R) - (1+R) + \frac{1}{1+R}\right) \qquad (5.18)$$

where Ku is the Kuwabara hydrodynamic factor which accounts for the distortion of the flow field around a fiber due to the presence of nearby fibers. It is a function of the solidity α (= 1 – porosity) only (Hinds, 1982; page 175):

$$Ku = -\frac{\ln\alpha}{2} - \frac{3}{4} + \alpha - \frac{\alpha^2}{4}. \qquad (5.19)$$

Assuming $d_f \approx 1$ mm and $\alpha = 0.04$ (for 25 mm spacing between roughness elements), then for our particles ($d_p \approx 1\mu m$) $R = 10^{-3}$, Ku = 0.9 and $E_R = 1 \times 10^{-6}$; deposition by interception is negligible.

Collection by inertial impaction occurs when a particle, because of its inertia, is unable to adjust sufficiently quickly to the abruptly changing streamlines in the vicinity of the fiber and so crosses those streamlines and hits the fiber. As we have seen, the Stokes number is the relevant parameter in this situation:

$$Stk = \frac{T_R\, U}{d_f}, \qquad (5.20)$$

where U is the free stream velocity. For $\tau = 3.2 \times 10^{-6}$, $d_f \approx 1$ mm and U = 2 m/s, Stk = 6.4×10^{-3}. The collection efficiency due to inertial impaction is given by (Hinds, 1982; page 176):

$$E_I = \frac{Stk \cdot J}{2Ku^2}, \qquad (5.21)$$

where $J = (29.6 - 28\alpha^{0.62})R^2 - 27.5R^{2.8}$ for $R < 0.4$. Using the values for Stk and Ku gives $E_I = 1 \times 10^{-7}$; deposition due to inertial impaction may be neglected.

The Brownian motion of very small particles is sufficient to greatly enhance the probability of their hitting a fiber while traveling past it on a non-intercepting streamline. According to Hinds (1982, page 177) the single-fiber efficiency due to diffusion is a function of the Peclet number only:

$$Pe = \frac{d_f\, U}{\mathcal{D}} \qquad (5.22)$$

where $\mathcal{D}$ is the diffusion coefficient. $\mathcal{D}$ is given by

$$\mathcal{D} = \frac{kTC_c}{3\pi\eta d_p} \tag{5.23}$$

where k is Boltzmann's constant, T is absolute temperature, C_c is the slip correction factor and η is the viscosity of the air. At 20°C, $\mathcal{D} = 2.7 \times 10^{-7}$ cm^2/s and Pe = 7.4×10^7 (for U = 2 m/s). The single-fiber efficiency is given by Hinds (1982) as

$$E_D = 2Pe^{-2/3}. \tag{5.24}$$

For our case $E_D = 1 \times 10^{-5}$; diffusion has a negligible effect on deposition.

Deposition due to gravitational settling is described by the ratio of the terminal settling velocity V_s to the free stream velocity:

$$G = \frac{V_s}{U} = \frac{T_R g}{U}. \tag{5.25}$$

Since gravity acts perpendicular to the air flow, the single-fiber efficiency due to gravitational settling is given by Hinds (1982) as $E_G \approx G^2$. For U = 2 m/s and g = 9.8 m/s^2, $V_s = 3.1 \times 10^{-3}$ cm/s, $G = 1.5 \times 10^{-5}$ and $E_G = 2.4 \times 10^{-10}$. From this analysis one may conclude that deposition due to gravitational settling is negligible. This conclusion is supported by the experimental work of Clough (1973) who measured the rate of deposition of solid particles to smooth extended surfaces and horizontal filter paper in a large wind tunnel. His results also support the theoretical work of Sehmel (1973) who predicted that deposition was exceedingly small for particles in the range 0.1-1.0 μm. Clough also presents data from a study of deposition to grass by Chamberlain which shows that although the settling velocity has a minimum in the range 0.1-1.0 μm, it is larger (by as much as ten times) than that indicated by Sehmel or Clough. This is probably due to impaction on the upright blades of grass. Garland (1982) discusses more recent field studies resulting in similar conclusions. In addition, during our field study at Dugway Proving Ground we attempted to measure deposition on both horizontally and vertically oriented, non-aspirated, glass-fiber filters (125 mm diameter) at distances from 25 m to 400 m from the release point. No statistically significant amounts of fog oil were detected on any deposition filter; however, measurements within 10 m of the smoke generator exit at ARFTC in 1986 did reveal some deposition. This is probably due to large, incompletely vaporized oil droplets which settle out very rapidly. In addition, within approximately 10 m of the HC release point black, carbon-like deposits were observed on the upper portions of the

vegetation. This is also probably due to the rapid settling of large particles; the remaining aerosol is thus comprised of small, non-depositing particles.

The effect of electrostatic attraction on the deposition of the particles is difficult to quantify since neither the charge on the particles nor the charge on the vegetation is known. However, in the absence of other charging mechanisms it may be assumed that the Boltzmann equilibrium charge distribution is achieved. For a 1 μm particle Hinds (1982, page 303) gives the average number of charges $n_{avg} = 2.34$. Thus the terminal electrostatic velocity V_E can be determined using (Hinds, 1982; page 288):

$$V_E = \frac{neE_T C_c}{3\pi\eta d_p} \tag{5.26}$$

where e is the charge on an electron (1.6×10^{-19} Coulombs), E_T is the strength of the terrestrial electric field (1.8 V/cm), C_c is the slip factor (1.16 for a 1 μm particle) and η is the viscosity of the air (1.8×10^{-5} kg/m·s). Thus $V_E = 4.6 \times 10^{-5}$ cm/s, which is very small compared with the free stream velocity (200 cm/s). In the absence of additional information regarding the actual charge on the particles, deposition due to electrostatic attraction appears to be negligible.

Since all of these five mechanisms act independently, the total single-fiber efficiency is equal to their sum: $E_\Sigma = E_R + E_I + E_D + E_G \cong 10^{-5}$. The overall filter efficiency is thus (Hinds, 1982; page 173):

$$E = 1 - \exp\left(\frac{-4\alpha E_\Sigma t}{\pi d_f}\right) \tag{5.27}$$

where t is the filter thickness. Recalling that we are considering the ground cover to act as a filter, for $E_\Sigma = 10^{-5}$ the aerosol would have to enter and remain within the grass for more than 200 m before even 10% of the particles were captured! Clearly deposition is insignificant and the boundary condition at the ground may be accurately modelled as reflective (as for a gas).

5.5 The Meteorology

The dispersion of material in the atmosphere is carried out by both mean transport and turbulent diffusion. The mean wind (i.e., speed and direction), is primarily responsible for the transport of the material. The spreading of the material, both vertically and horizontally transverse to the mean wind direction, is due principally to the diffusion induced by the turbulence. Hence, a plume of material

emanating from a continuous point source is transported by the mean wind and spreads under the action of turbulent diffusion. Thus a knowledge of both the transport and diffusion are essential to understanding atmospheric dispersion. Accordingly, measurements of the mean and fluctuating components of the wind are required in order to provide the most basic description of the dispersion phenomena.

Both the mean and fluctuating components of the wind speed generally increase with height above the ground. The resulting wind shear and vertical momentum flux can have a significant effect on the dispersion. Additionally, the vertical heat flux caused by solar heating during the daytime and radiative cooling at night gives rise to vertical gradients in temperature and density of the air, especially near the ground. These gradients play a dominant role in the dispersion process. Accordingly, measurements of ambient temperature, wind speed and wind direction must be performed at several elevations above the ground.

All of these variables, and hence dispersion as well, are directly influenced by the prevailing meteorology of the planetary boundary layer. The strong diurnal variation in the meteorology results in a corresponding and dramatic alteration in dispersion. The need to relate observed wind speeds, directions and temperatures to the "state" of the boundary layer is paramount.

Extensive research in the planetary boundary layer has produced a coherent description in terms of several key length and velocity scales. As described in Chapter 1, these include the friction velocity u_*, the Monin-Obukhov length L, the convection velocity w_*, the top of the boundary layer h and the roughness height z_o. Thus determining the values of these scales essentially defines the state of the boundary layer meteorology. It also allows the data acquired during one test to be compared with the results of another test in a meaningful manner. In this way the relationship between dispersion and the prevailing meteorological conditions may be quantified and generalized. Unfortunately, these scales are generally difficult, expensive and in some cases impossible to measure directly. Rather, they must be inferred from other, more easily measured quantities. These measured quantities must therefore be determined accurately and with precision.

Our objective concerning the meteorological measurements was to define the state of boundary layer as it existed during the dispersion tests. We sought to provide data not only for the purpose of evaluating existing models but also to facilitate the development of better models. In the following sections we describe the equipment and methods used to acquire the data necessary to achieve our objective.

Subsequently, the procedures and results of the data analysis will be presented and the significant findings discussed.

5.5.1 Measurements

Measurements of the wind speed, wind azimuth (horizontal angle or direction), wind inclination (vertical angle) and temperature were carried out at four levels on a 10-m instrument tower. The tower, model HDBX-32 manufactured by Rohn Inc. (Frankfort, IN) had a triangular frame 30-50 cm on a side. In order to provide data representative of the test site, the instrument tower was located along the centerline of the sampling network on Transect 4, as shown in Fig. 5.6. A battery-powered flashing light was mounted on top of the tower in order to provide a warning to low-flying military aircraft on training flights in the vicinity of the test site.

Wind speeds were measured at 2, 4, 6 and 10 m above ground level with R. M. Young (RMY) model 12102D-20 three-cup anemometers. The anemometers were mounted at the end of 1.8 m retractable instrument booms (RMY model 16106). The booms extended northwest of the tower and were oriented parallel to the transects so that they could not possibly be in the wake of the tower during potential test conditions. The anemometers employed a phototransistor and light chopper to produce a pulse-train output whose frequency was linearly proportional to the wind speed. The 20-slot light chopper was selected to provide the maximum resolution of 0.05 m/s at the expense of a restricted maximum speed of 12 m/s (26.75 mph) due to the 8-bit counters in the datalogger. This choice was based on the climatological study which revealed that during the afternoon the median (50%) 1-minute mean wind speed was 4.5 m/s and that 99.9% of the 1-minute mean wind speeds were less than 9.7 m/s.

Wind azimuth and inclination were measured at 4, 6 and 10 m above ground level with R. M. Young model 17003 bivanes. The bivanes were mounted midway (0.9 m) between the tower and the end of the instrument boom in order to minimize wake effects from the cup anemometers. The bivanes were designed and developed specifically for micrometeorological research by Professor G. C. Gill of the University of Michigan. With each gust, the light vane moves up and down and from side to side in order to equalize the dynamic pressure on the horizontal and vertical polystyrene tail fins. These motions are transmitted to two precision conductive plastic potentiometers. With a constant voltage applied by the datalogger, the voltage outputs are directly proportional to the wind azimuth and inclination angles.

Wind azimuth was measured at the 2 m level using an R. M. Young model 12302 microvane, also designed by G. C. Gill. It operates in the same manner as the bivane except, of course, that it only indicates the wind azimuth.

Measurements of ambient dry-bulb temperature were performed at 2, 4, 6 and 10 m above ground level using Campbell Scientific Inc. (CSI) model 107 temperature probes. These probes consisted of a thermistor (Fenwal Electronics model UUT51J1) and associated bridge circuitry. The CSI bridge circuit uses high precision (0.1%), thermally stable resistors; the linearization error in the fifth-order polynomial supplied with the CSI model 21X datalogger to transform the measured voltage into a temperature is less than 0.1°C. The thermistor specification guarantees an interchangeable accuracy of 0.2°C. CSI documentation states that individual units have a greater accuracy of 0.1°C which may be achieved by a single-point calibration to eliminate the offset error. The probes were accordingly calibrated in the laboratory. In order to ensure that true air temperature was measured, the temperature probes were mounted in R. M. Young model 43408 aspirated thermal radiation shields. The radiation shields were mounted on extendible booms which were oriented to the south of the tower.

Relative humidity was measured at the 2-m level using a CSI model 207 temperature and relative humidity probe. This probe is comprised of the same thermistor as the model 107 probe used to measure temperature alone and a Phys-Chemical Research PCRC-11 moisture-sensitive film resistor along with the necessary bridge circuitry. According to CSI documentation, the error in the indicated humidity is less than 5% in the range 12 – 100 % relative humidity. The probe was mounted in a Gill-designed, multiplate, wind-aspirated plastic thermal radiation shield (R. M. Young model 41002-5) to prevent solar heating.

The choice of instrumentation reflects a balance between durability and sensitivity. The durability of the instrumentation was important since, once installed on the tower, the equipment would be exposed to the weather for a period of three to four weeks. Thus, research-grade equipment specifically designed to yield accurate measurements despite prolonged exposure to extreme temperatures, precipitation and lightning was essential.

Since our objective was to characterize the state of the boundary layer, instrumentation designed to provide hourly data for routine meteorological monitoring, which could thus resolve only mesoscale motions, would not provide sufficient dynamic response to adequately define the turbulence in the planetary microscale.

Guidelines for choosing research-grade instrumentation capable of adequately resolving the turbulent motions of the microscale have been issued by the American Meteorological Society (Randerson, 1984). All of the meteorological equipment employed in the Atterbury-87 field study exceeded the American Meteorological Society recommendations. A comparison of these recommendations with the specifications of our sensors, and a thorough analysis of the dynamic response of our wind speed and direction probes, is presented in Appendix B. No corrections for instrument response were necessary.

The meteorological instrumentation mounted on the tower were scanned at 1-s intervals using a CSI model 21X datalogger mounted in an electrically-isolated, weather-proof enclosure. Appropriate measures were taken to ensure proper grounding of the sensors, cable shields and datalogger in order to avoid ground loops and to provide protection against lightning. The data were transmitted in digital format to a Zenith model Z-181 battery-powered "laptop" computer for monitoring and storage on a flexible disk. Upon returning to the University of Illinois, the data were transferred to a Sun-3/280 computer for reduction and analysis. The data were also archived on 9-track magnetic tape.

A tethersonde manufactured by Atmospheric Instrumentation Research (Boulder, CO) was acquired in order to gather meteorological data throughout the depth of the boundary layer to provide a direct estimate of the inversion height marking the top of the boundary layer. Because military aircraft regularly used the ARFTC airspace for low-level flight training, use of the tethersonde was restricted to Mondays and before 10:00 on Tuesdays. However, operational difficulties caused by wind speeds aloft in excess of the 10 m/s maximum which the tethersonde could safely sustain prevented the acquisition of upper air data at these times. This was not a significant problem since the inversion height was adequately estimated from upper air data collected by the National Weather Service stations at Peoria, Illinois and Dayton, Ohio (no upper air data were available for Indianapolis).

5.5.2 Results and Discussion

The two major factors complicating the analysis of atmospheric turbulence are the extreme range of scale and the non-stationary character of the flow. Even on the planetary microscale, the scales of motion range from small viscous motions of about 1 mm to large convective motions on the order of the depth of the boundary layer. As a result, the statistics of the flow are very sensitive to the duration of the sampling

period. Worse yet, due to diurnal changes in insolation and changes in the weather systems on the meso- and macro-scales, atmospheric flows are generally non-stationary. (A stationary flow is one whose statistics are invariant with time.) This renders most statistical methods of analysis theoretically invalid.

However, it is possible to separate the short-term stationary signal of interest from the longer-term non-stationary signal by a filtering process. This is the purpose of "trend removal" (Bendat and Piersol, 1977; page 288). Low frequency (long wavelength) components with a period greater than the duration of the smoke release are approximated by a mean value or linear trend and subtracted from the signal prior to analysis. In terms of our previous discussion, it is these low frequency components which comprise the "mean wind" responsible for the transport of material in the atmosphere whereas the high frequency components arising from the locally-stationary turbulence produce the diffusive spreading of material. The latter are usually characterized in terms of variances about the mean.

Although means and variances of the data provide sufficient input for most current predictive models of atmospheric dispersion, our analysis also provides estimates of the relevant scaling lengths and velocities derived from vertical profiles and variance ("power") spectra of the data for use in developing improved dispersion models.

Estimates of the means and variances of the data were computed as time averages. If the turbulence is homogeneous and stationary along a given spatial coordinate, then such a time average should converge to the ensemble average encountered in turbulence theory providing the averaging time is long enough. However, the inhomogeneous and non-stationary nature of the atmosphere implies that such time averages may not converge since longer averaging times include lower frequency motions. The importance of this issue is discussed by Chatwin and Allen (1985). It therefore seems worthwhile to examine the averaging process to discover the nature and magnitude of the errors introduced.

Pasquill and Smith (1983) provide an extensive discussion of the effects of finite sampling and averaging times. They state that since finite sampling times partially exclude slow variations and since instrument response affects fast fluctuations (essentially averaging them over a short but finite period), "the mean velocity is thus recognized as a purely arbitrary quantity." Clearly this is true not only for velocity but for all time-varying quantities. Pasquill and Smith demonstrate that the effect of finite sampling and averaging times is to apply low-pass and high-pass filters, respectively, to the data. Thus our division of the dispersion phenomena into "mean transport" and

"turbulent diffusion" is recognized to be based on the arbitrary definition of the atmospheric microscale: length scales up to 2 km and time scales less than 1 hour.

Values of the time-average wind speed U, wind vector magnitude $\bar{u}$, azimuth $\bar{\theta}$, inclination $\bar{\phi}$, temperature $\bar{T}$ and relative humidity were computed over the period beginning ten minutes prior to smoke initiation until ten minutes after smoke termination, by which time the smoke had traveled beyond Transect 5. Over this same period, the standard deviations of the wind speed σ_s, azimuth σ_θ, inclination σ_ϕ as well as the horizontal components (parallel σ_u and perpendicular σ_v to the mean azimuth) and vertical component of the wind vector σ_w. These were computed from the horizontal wind speed s, indicated by the cup anemometers, and the azimuth θ and inclination ϕ indicated by the bivanes as follows.

The horizontal wind speed was first resolved into perpendicular components

$$u_1 = s\cos(\theta), \tag{5.28}$$

and

$$u_2 = s\sin(\theta). \tag{5.29}$$

The mean wind direction was determined from the time-averaged values of u_1 and u_2 according to the relation

$$\bar{\theta} \equiv s\tan^{-1}\left(\frac{\overline{u_2}}{\overline{u_1}}\right). \tag{5.30}$$

This is the speed-weighted wind direction: periods of low wind speed contribute less to the mean direction than periods of greater wind speed. This is the wind direction of interest for transport and diffusion. If the wind speed were steady, then $\bar{\theta}$ would equal the non-speed-weighted direction.

The mean wind speed is simply $U \equiv \bar{s}$; the mean wind vector magnitude is given by

$$\bar{u} = \sqrt{\overline{u_1}^2 + \overline{u_2}^2}. \tag{5.31}$$

By definition, the transverse mean velocity is zero: $\bar{v} \equiv 0$. Clearly, $\bar{u} < U$; the equality would prevail if the wind direction were constant in the mean direction. The horizontal components of the wind vector (u,v), respectively parallel and perpendicular to the mean wind direction, are given by

$$u = s\cos(\theta - \bar{\theta}) \tag{5.32}$$

$$v = s\sin(\theta - \bar{\theta}). \tag{5.33}$$

The vertical component of the velocity vector was computed using

$$w = s\tan(\phi). \tag{5.34}$$

Once the mean values had been determined, the standard deviations could be computed in the usual manner; e.g.: $\sigma_w^2 = \overline{(w - \bar{w})^2}$. The results of these computations are presented in tabular form for each test in Appendix C. Note that the wind direction is reported following the meteorological convention. Thus 0° indicates that the mean wind was blowing from north to south ("out of the north"), 90° indicates a mean wind out of the east, 180° indicates a south wind and 270° indicates a west wind.

In addition to the means and standard deviations of the data, the exponent of the power law fit to the vertical profiles of mean wind speed and mean vector magnitude are also given in Appendix C. These exponents are used directly by K-theory dispersion models although they are more commonly used as approximate indicators of the stability of the boundary layer. For a roughness height of 20 cm (which we found representative of the Atterbury-87 test site) Panofsky and Dutton (1984, page 138) calculate the power law exponent to range from 0.20 for neutral conditions (zero surface heat flux), to 0.145 for a Monin-Obukhov length equal to -100 m (slightly convective conditions). For the Atterbury-87 tests, exponents in the range 0.103 to 0.183 were computed, indicating that atmospheric conditions ranged from near-neutral to moderately convective.

Figure 5.28 presents a comparison of the normalized horizontal and vertical variances of the wind velocity data with values predicted by integrating the spectral model of Højstrup (1982). This model is based on atmospheric turbulence data gathered during the Kansas and Minnesota boundary layer meteorology studies that were described in Chapter 3. The error bars represent the 95% confidence limits on the data for test 1103871. These were determined by assuming that the errors in the data were described by a student-t distribution having N degrees of freedom where N is not the total number of samples but rather the number of *independent* samples in the data record (Bendat and Piersol, 1971). N was estimated by dividing the total

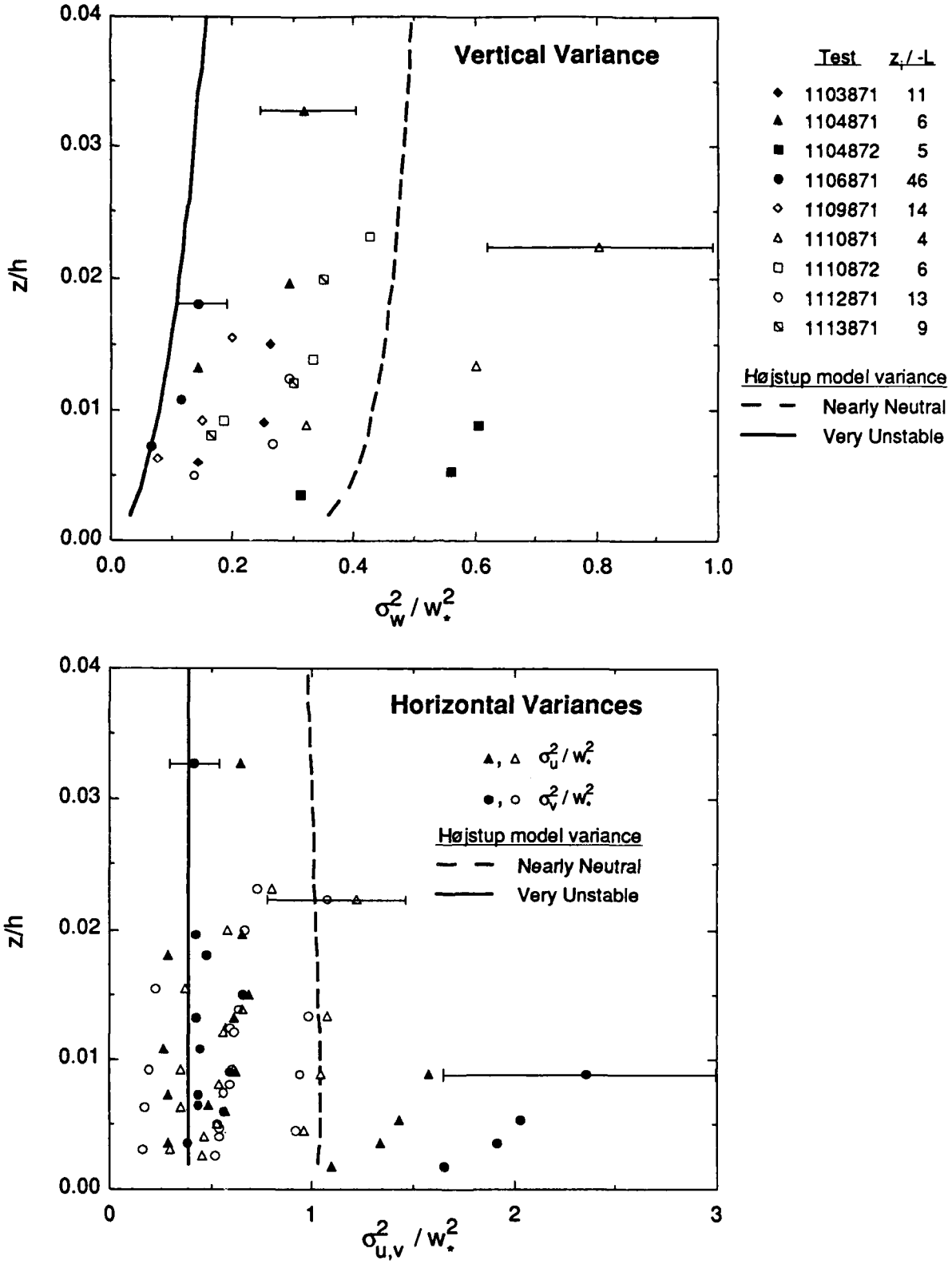

Figure 5.28 Variances of (a) vertical and (b) horizontal velocity fluctuations measured during the Atterbury 87 field study compared with limiting forms of the Højstrup model (1982) variances. The filled symbols denote for-oil tests whereas the hollow symbols denote HC tests. The error bars represent the 95% confidence limits.

record length by the time over which the data were significantly correlated, estimated as three times the integral time scale of the data. (The estimation of the integral scales is described later in the discussion of the power spectra.) Error estimates for the other tests were very similar. Thus the *expected* scatter in the data is also large; this presents a fundamental difficulty in the study of atmospheric turbulence because the length of the data record must be limited to include only microscale phenomena.

Our data fall mostly fall within these limiting cases. The data from the most unstable case, Test 1106871 for which $z_i/-L = 46$, fall close to the unstable limit whereas the more nearly neutral cases fall closer to the near-neutral prediction. Although some data appear to depart significantly from the predicted values, a re-examination of Figs. 3.5 and 3.7 indicates that the data upon which the spectral model is based also exhibited considerable scatter due to the fundamental limitation identified above. Therefore, our results are probably within the uncertainty inherent in the spectral model. Despite this uncertainty, the Atterbury-87 data may reflect actual effects of the terrain; the sites of the Kansas and Minnesota studies corresponded closely to the simple terrain/simple meteorology category described earlier whereas the Atterbury-87 test site departed somewhat from this ideal. This may explain why the vertical variances are slightly larger than the predictions. However, the uncertainty in both the Kansas and Minnesota data as well as the Atterbury-87 data prevent a definite conclusion from being drawn with regard to the effects of terrain on the velocity variances.

The horizontal velocity variances may be slightly lower than predicted because the duration of the smoke releases, over which the variances were computed, was often less than one hour whereas the variances computed from the Kansas and Minnesota data were for one hour periods. The effect of a limited sampling time is to exclude the contributions of the lower frequencies. As the spectra will show, motions at these low frequencies contributed significantly to the horizontal variances but much less to the vertical variances. Based on an analysis by Olesen, Larsen and Højstrup (1984), the horizontal variances computed from a 20-minute data record could be 10-20% lower than the 1-hour values depending on the atmospheric stability. This is supported to some extent by the observation that the largest horizontal variances are for the fog-oil tests which lasted from 48 to 76 min whereas the shortest variances are for the HC tests which lasted from 25 to 47 min.

Atmospheric turbulence is generated by mechanical forces due to the momentum flux caused by the shear stress at the surface and by convective forces due to the heat

flux caused by insolation. The friction velocity u_* is a measure of the shear stress τ at the surface

$$u_*^2 = \tau/\rho = \langle u'w' \rangle, \tag{5.35}$$

where ρ is the air density. The kinematic heat flux Q_o describes the convection:

$$Q_o = \frac{q}{\rho\, c_p} = \langle T'w' \rangle . \tag{5.36}$$

q is the sensible heat flux at the surface: $q = -k_T\, dT/dz$, where k_T is the thermal conductivity of the air and dT/dz is the temperature gradient at the surface. The Monin-Obukhov length L is a measure of the relative contributions of shear and convection to the turbulence:

$$L = -\frac{u_*^3}{\kappa\, (g/T)\, Q_o} \tag{5.37}$$

where κ is von Karman's constant ($\approx$0.4), g is the gravitational acceleration and T is the average (absolute) temperature in the surface layer.

Values of the friction velocity, Monin-Obukhov length, and the temperature scales T_* and T_o were determined from the mean wind speed and temperature by fitting the integrals (Paulson, 1970) of the following scaling relations to the data.

$$\frac{\kappa z}{u_*}\frac{dU}{dz} = \phi_m\left(\frac{z}{z_o}, \frac{z}{L}\right) \tag{5.38}$$

$$\frac{\kappa z}{T_*}\frac{dT}{dz} = \phi_h\left(\frac{z}{z_o}, \frac{z}{L}\right) \tag{5.39}$$

Here ϕ_m and ϕ_h are the ostensibly universal functions for momentum and heat flux, respectively, which have been determined empirically by Businger et al. (1971), Dyer and Hicks (1970) and Hansen (1980) for simple terrain/simple meteorology. T_* is defined according to the relation

$$T_* = -\frac{\langle T'w' \rangle}{u_*} = -\frac{Q_o}{u_*} \tag{5.40}$$

and T_o is the effective temperature at $z = z_o$.

This method, suggested by Nieuwstadt (1977) and improved by Boughton (1983) minimizes the combined mean square error in fitting the speed and temperature profiles simultaneously. An estimate of the roughness height z_o, defined as the height at which the wind speed drops to zero, is required to fit the data to the profiles in this way. The fitting procedure is iterative: a small roughness height, say 1 cm, is used to provide a first estimate of L and u_*; a large roughness height of 1 m is then used to provide an upper bound. By examining the behavior of the residual error in the fit as the roughness height is changed, a reasonable value of the roughness height is obtained along with the corresponding Monin-Obukhov length and friction velocity.

This method was used to reduce the wind speed and temperature data gathered during our Dugway-85 study and yielded excellent results. The 2 cm value of the roughness height deduced from this procedure was in the range estimated by Waldron (1977) for Dugway Proving Ground (2-4 cm). For each test, the fitted Monin-Obukhov length agreed with the Pasquill-Gifford stability class estimated by Dugway Proving Ground meteorologists.

The results of this fitting procedure for the Atterbury-87 data are presented in Figs. 5.29-32 for z_o = 20 cm. Because the 10-m instrument tower was on a small knoll which rose slightly more than 1 m above the surrounding terrain, 1 m was added to the instrument heights in order to achieve a satisfactory fit. Although most of the data were well-fitted, for Test 1104872 in Fig. 5.29 the agreement between the potential temperature data and the fitted function is clearly contradictory since the positive temperature gradient at the surface is indicative of a positive Monin-Obukhov length whereas $L < 0$ is computed with the fitting scheme. The temperature at the 10-m level of the tower is significantly higher than those at the 4 and 6-m levels, possibly indicating a low-lying temperature inversion. This behavior is problematic for the fitting scheme which is applicable only to situations where the potential temperature gradient is monotonically increasing, decreasing or zero. The corresponding mean wind speed profile is well-fitted, however.

Although the Nieuwstadt-Boughton fitting method produced estimates of the surface layer scales which were generally consistent with other empirical measures of atmospheric stability, such as the power law exponent, the effects of the vegetation and terrain were evident. For example, the roughness height of 20 cm which characterized the Atterbury-87 site was ten times greater than that determined for the desert site of the Dugway-85 study. The friction velocities were also greater than those determined for the Dugway-85 tests, consistent with the increased surface shear stress due to the greater roughness. The Monin-Obukhov lengths fell in a narrow range (-4.7

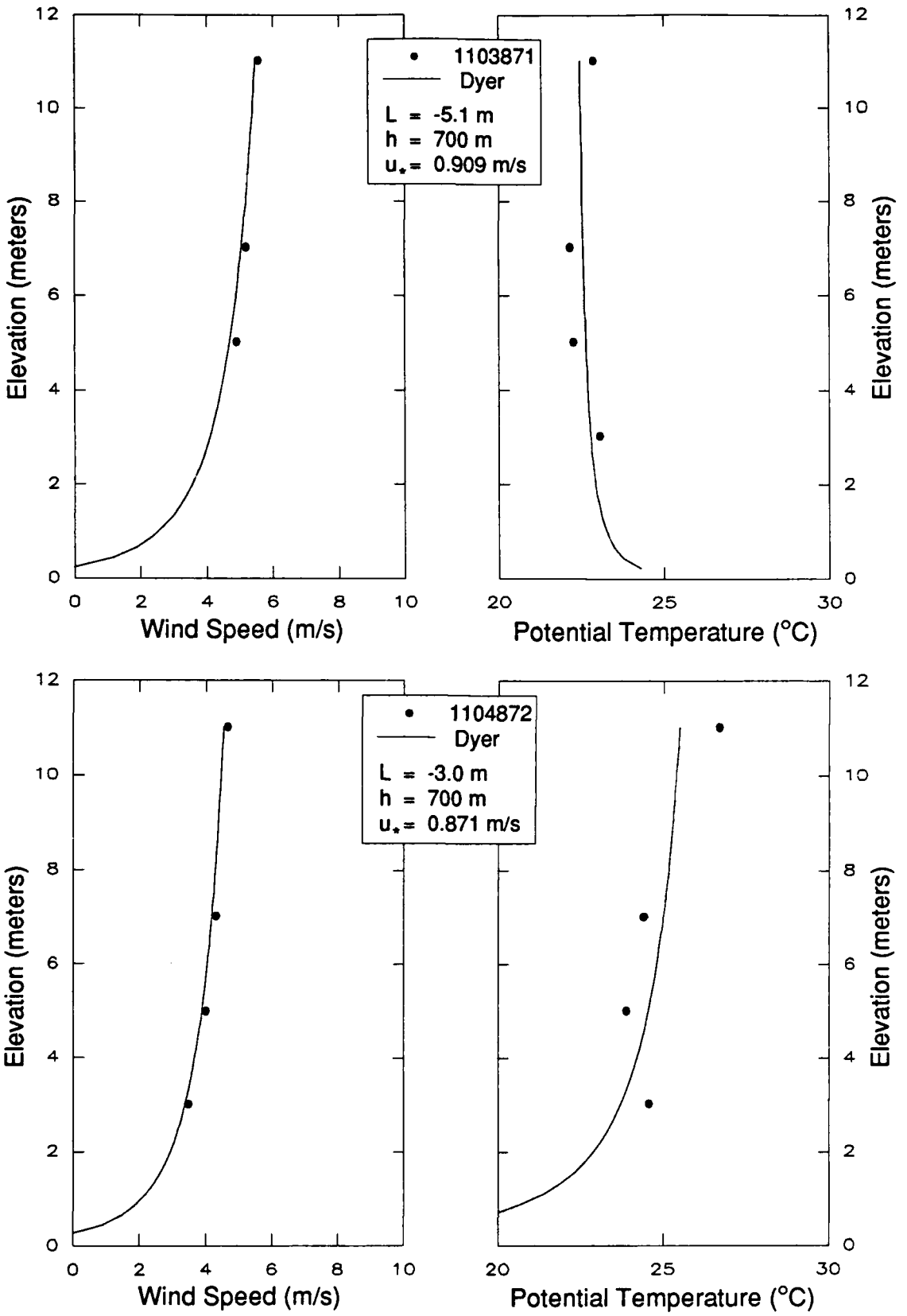

Figure 5.29 Vertical profiles of wind speed and potential temperature data from (a) 1103871 and (b) 1104872 along with the best-fit curve to the flux-profiles of Dyer (1980) and the resulting values of Obukhov length L and friction velocity u_* .

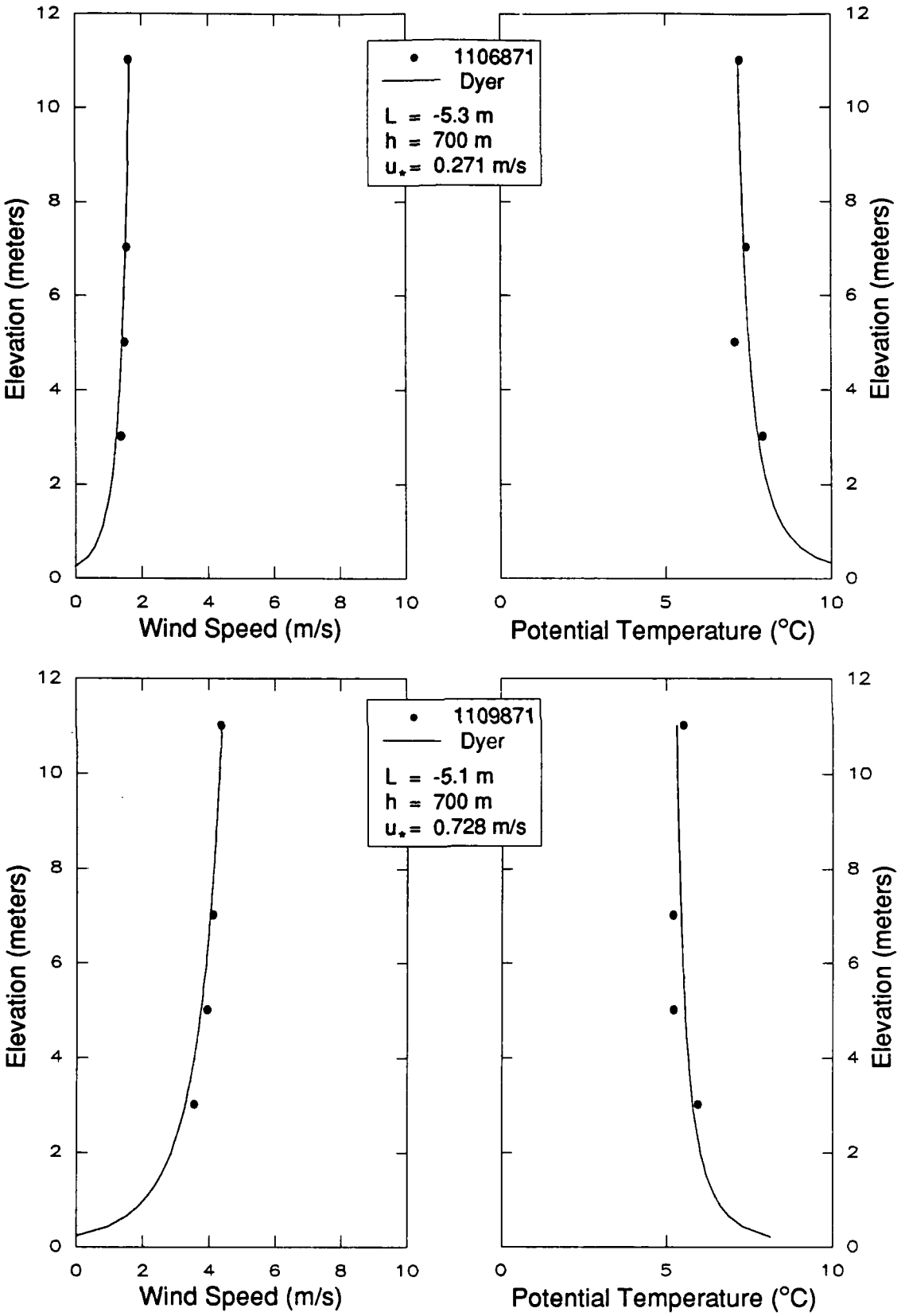

Figure 5.30 Vertical profiles of wind speed and potential temperature data from (a) 1106871 and (b) 1109871 along with the best-fit curve to the flux-profiles of Dyer (1980) and the resulting values of Obukhov length L and friction velocity u_* .

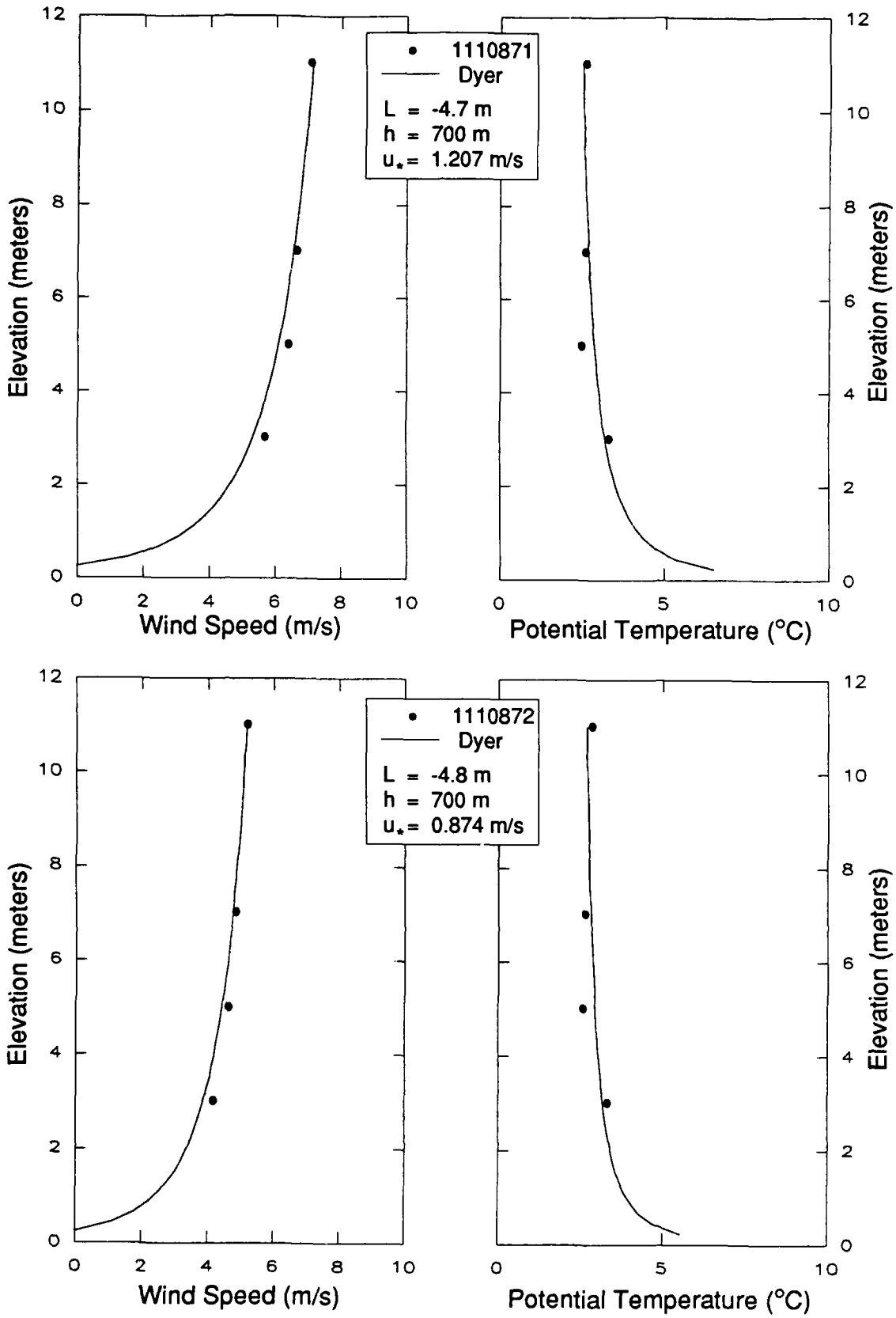

Figure 5.31 Vertical profiles of wind speed and potential temperature data from (a) 1110871 and (b) 1110872 along with the best-fit curve to the flux-profiles of Dyer (1980) and the resulting values of Obukhov length L and friction velocity u_* .

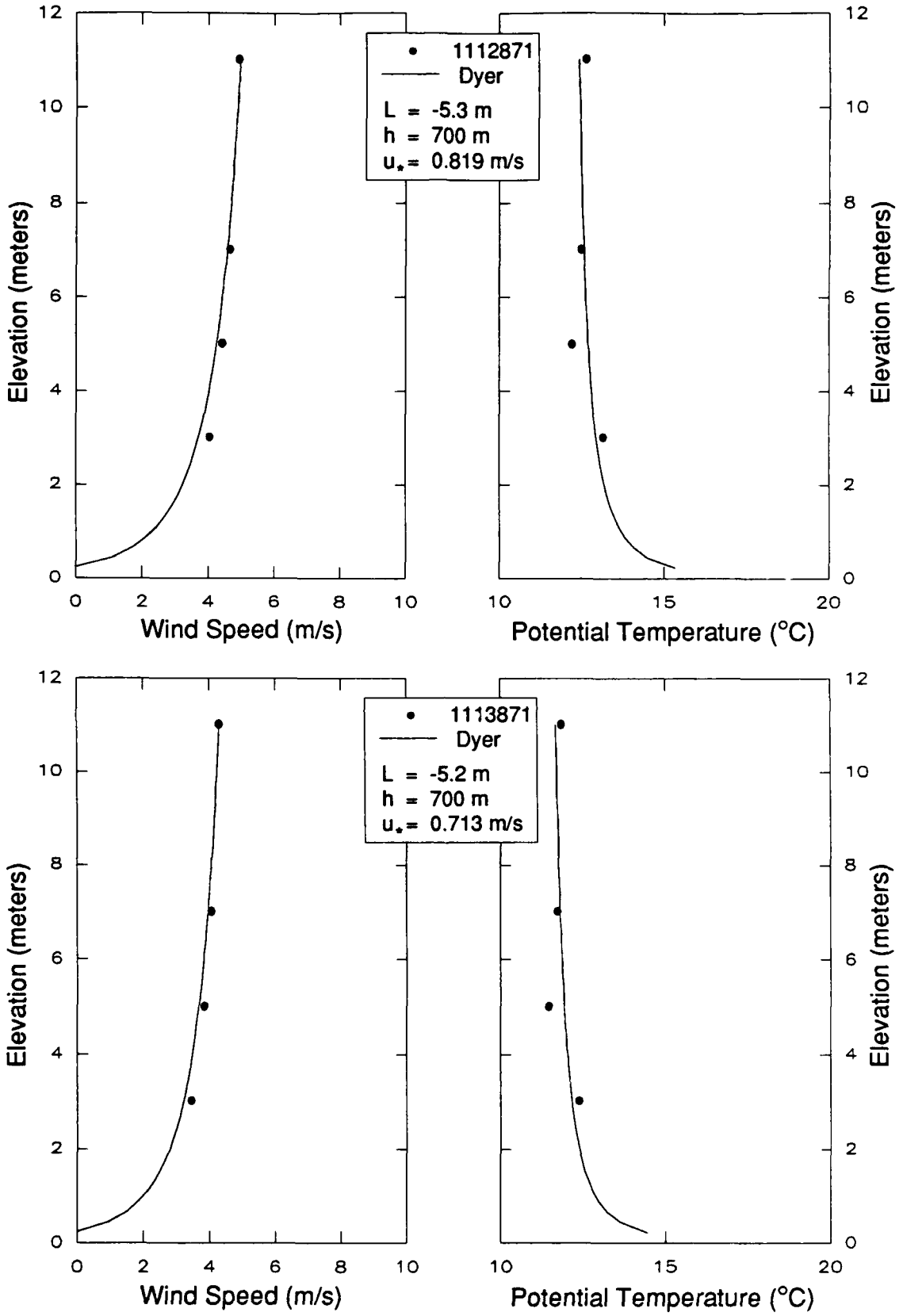

Figure 5.32 Vertical profiles of wind speed and potential temperature data from (a) 1112871 and (b) 1113871 along with the best-fit curve to the flux-profiles of Dyer (1980) and the resulting values of Obukhov length L and friction velocity u_* .

to -5.3) apparently indicating that strongly convective conditions prevailed during all tests. A somewhat broader, less convective range of conditions was indicated by the power law exponent of the wind profile, as discussed earlier. This may reflect the fact that wind speed and temperature measurements were performed at 2, 4, 8, 16 and 32 m during Dugway-85 and only at 2, 4, 6 and 10 m for Atterbury-87. It is more likely due to the fact that the empirical forms for the flux-profiles (Eqs. 5.38-39) to which the data were fitted were determined from measurements for uniformly flat, "simple terrain/simple meteorology" conditions, whereas the meteorology of the Atterbury-87 site was more complex.

The friction velocity and Monin-Obukhov length are the relevant velocity and length scales in the surface layer, which extends roughly to an elevation $z = |L|$ above the ground. For increasingly convective conditions $|L| \rightarrow 0$ and the relevant scaling parameters are the mixed layer scales: the convection velocity w_* and the boundary layer height h. The mixed layer and surface layer scales are related as follows

$$\left(\frac{w_*}{u_*}\right)^3 = -\left(\frac{z_i}{\kappa L}\right) \tag{5.41}$$

Values of the convection velocity w_* were estimated from the data by solving Eq. (5.41): $w_* = u_*(z_i/-L\kappa)^{-1/3}$ and substituting in the estimated values of u_*, z_i and L.

In order to examine the internal consistency of the scaling parameters, the results of several approaches for atmospheric stability estimation are presented in Table 5.13. The first approach, the fitting scheme of Nieuwstadt and Boughton described above, provides an estimate of L. Then, using Golder's nomograms (1972) the corresponding Turner stability classes have been estimated for a roughness height of 20 cm. The Turner classes are essentially updated and improved versions of the Pasquill-Gifford categories which classify the atmospheric stability during the daytime as either 1) extremely convective, 2) moderately convective, 3) slightly convective or 4) nearly neutral. The second approach uses Turner's method (Panofsky and Dutton, 1984, page 140) based on the position of the sun in the sky, the cloud cover and the surface wind speed to determine the "actual" Turner stability class for each test; the Golder nomograms are then used to provide a corresponding estimate of L. The third method uses the standard deviation of the wind direction σ_θ computed for the 10-m height to estimate the Turner class based on the relationship given by Barr and Clements (1984) for which the Turner class decreases as σ_θ increases. A method suggested by Irwin and Binkowski (1980) based on the bulk Richardson number $Ri_B = (z_2\, g\, \Delta T/T_2)/u_2^2$

where $\Delta T = T_2 - T_1$ provides the last method of estimating the Monin-Obukhov length and friction velocity. The subscript 2 denotes the value of the quantity at the 6-m level and the subscript 1 indicates the 2-m level value. The expression $z_2/L = \kappa Ri_B F^2/G$ is solved iteratively for L; here F and G are expressions resulting from the integration of the flux profiles, Eqs. (5.38) and (5.39) such that $F = u/u_*$ and $G = \Delta T/T_*$. Since Irwin and Binkowski recommend underestimating the roughness height when using this method, a value of 10 cm, rather than 20 cm, was employed. The corresponding Turner class was estimated from Golder's nomograms.

Table 5.13. Comparison of Monin-Obukhov length and Turner Class determined by various methods.

METHOD:	Nieuwstadt/Boughton		Turner/Golder		σ_θ	Irwin and Binkowski	
	Class	L	Class	L	Class	Class	L
1103871	1	-5	3	-50	3	3	-63
1104871	1	-6	3	-50	4	3	-51
1104872	1	-3	4	-200	3-4	4	-243
1106871	1	-5	2	-20	1	2	-12
1109871	1	-5	4	-200	4	3	-46
1110871	1	-5	3-4	-100	3	3-4	-110
1110872	1	-5	4	-200	3	3	-68
1112871	1	-5	3	-50	3	3	-63
1113871	1	-5	3	-50	3	3	-53

These results indicate that the "actual" Turner class values determined using Turner's scheme are consistent with the values of Turner class estimated using σ_θ or the Ri_B method and Golder's nomograms. The fact that substantially different values of L yield the same Turner class underscores the primary objection to these relatively arbitrary classification schemes.

The second, third and fourth approaches indicate a wider range of atmospheric stability which are less convective than the Nieuwstadt/Boughton fitting approach. The reason for this discrepancy has been briefly mentioned above: the empirical forms for ϕ_m and ϕ_h to which the data were fitted were derived from "simple terrain/simple meteorology" cases whereas the meteorology of the Atterbury-87 site is more complex due to the surrounding terrain. As a result, the value of L computed from the fitting procedure should not be regarded as the "true" Monin-Obukhov length, but rather as an "effective" Monin-Obukhov length that relates the Atterbury-87 meteorology to

simple terrain/simple meteorology. This means that much more convective atmospheric conditions would be required in order to observe the same vertical fluxes of momentum and heat at a simple terrain/simple meteorology test site as were observed at the Atterbury-87 test site. The physical basis for this behavior will be examined in the discussion of the spectra.

For convective conditions the top of the boundary layer is defined as the elevation of the lowest temperature inversion; thus $h \equiv z_i$. Because the inversion height could not be determined directly from upper air data gathered at the test site, it was instead estimated from upper air data gather by the National Weather Service stations at Peoria, Illinois and Dayton, Ohio using a method suggested by Benkley and Schulman (1979). The estimates of z_i from each of these locations were generally within 15% of each other. These values were also supported by an estimate obtained from the power spectra of the velocity components. This procedure and the velocity spectra are discussed next; the estimates of the scaling lengths and velocities are presented in Table 5.14 along with the means and variances from the 10-m level in a summary of the data for each test.

Estimates of the single-side power spectra S(n) of the fluctuating components of the wind vector were computed using the Fast Fourier Transform (FFT) as implemented by Rabiner (1979). The data record was first divided into overlapping segments of 512 points. Pasquill and Smith (1983) show that overlapping the data segments in this manner reduces aliasing and the accompanying distortion of the high-frequency end of the spectrum. The choice of a 512-point segment length reflected a compromise between precision and accuracy. The precision of the spectral estimate is improved by increasing the number of segments which make up the ensemble; the accuracy is improved by ensuring that the longest wavelengths in the signal are not excluded from the estimate through the use of too-short segments.

Values for the mean and variance are then computed for each segment and the mean subtracted from the data comprising that segment. A "Hanning" weighting function was applied to each segment prior to the transformation via the FFT in order to reduce "leakage" from one spectral band into adjoining bands (Brigham, 1974). The ensemble average of the FFTs of these segments provides a raw estimate of the power spectrum. (This raw estimate may be inverse transformed to yield an estimate of the auto-correlation.) The raw spectral estimate is then normalized by the ensemble average of the segment variances. The ensemble average of the segment variances is used in order to account for the filtering effects of limiting the sample size to 512 points.

Table 5.14 Summary of Atterbury-87 Data

Test	1103871	1104871	1104872	1106871	1109871	1110871	1110872	1112871	1113871
Smoke Type	Fog Oil	Fog Oil	Fog Oil	Fog Oil	HC	HC	HC	HC	HC
Begin Test (CDT)	10:31:06	09:36:33	15:25:50	10:51:50	15:45:00	11:27:30	16:37:41	13:31:20	10:21:00
End Test (CDT)	11:27:00	10:06:00	16:14:00	12:08:00	16:10:00	12:04:00	17:25:00	14:17:00	11:04:00
Transects in Operation	1-5	1-5	1-5	1-5	1-4	1-4	1-4	1-4	1-4
Source									
Location [x(m),y(m)]	3.0, -4.7	3.0, -4.7	-47.4, 47.4	-47.4, 47.4	270.3, 470.8	270.3, 470.8	270.3, 470.8	-21.1, 21.1	-21.1, 21.1
Mass Released (kg)	115.9	44.0	117.8	193.0	222.1	229.3	219.5	218.5	202.0
Test Duration (min)	55.9	27.5	48.2	76.2	25	36.5	47.3	45.7	43
Rate of Release (g/s)	34.6	26.7	40.7	42.2	148.1	104.7	77.3	79.7	78.3
Wind Speed (m/s)	2.6	2.3	1.7	0.8	2.3	3.6	2.5	1.9	1.9
Wind Direction (°E of N)	241	249	247	224	12	26	13	220	221
σ_θ (°)	28.6	23.4	26.0	33.8	18.7	19.7	19.9	28.6	31.2
Ambient Temperature (°C)	23.4	20.0	25.3	8.0	5.9	3.2	3.0	13.8	12.9
Relative Humidity (%)	41	25	43	40	69	61	49	35	45
Particle Size									
Location [x(m),y(m)]	316.4, 298.4	316.4, 298.4	316.4, 298.4	184.0,164.5	23.8, 45.0	23.8, 45.0	23.8, 45.0	316.4, 298.4	316.4, 298.4
Mass Mean Diameter (μm)	1.02	--	0.71	1.07	1.22	1.07	1.07	1.50	1.18
Geometric Mean Diameter (μm)	0.91	--	0.60	0.96	1.05	0.77	0.83	1.11	0.93
Geometric Std. Deviation	1.55	--	1.71	1.53	1.78	2.36	2.07	2.41	2.05
Meteorology									
Wind Speed (m/s)	5.5	5.1	4.7	1.6	4.4	7.1	5.2	4.9	4.3
Wind Direction (° E of N)	239	249	261	240	25	34	24	226	241
σ_θ (°)	16.2	11.0	18.6	35.4	11.0	13.2	14.4	15.3	15.5
σ_ϕ (°)	8.8	8.2	8.2	14.9	8.0	9.3	8.3	9.8	9.9
σ_u (m/s)	1.52	1.17	1.26	0.70	1.03	1.74	1.28	1.32	1.08
σ_v (m/s)	1.49	0.94	1.54	0.90	0.80	1.63	1.22	1.34	1.15
σ_w (m/s)	0.94	0.82	0.78	0.49	0.75	1.41	0.93	0.94	0.83
10 m - 2 m ΔT (°C)	-0.41	--	1.89	-0.89	-0.68	-0.95	-0.70	-0.76	-0.74
Wind Speed Power Law Exponent	0.143	0.149	0.183	0.103	0.130	0.132	0.132	0.121	0.137
Scaling Parameters									
Turner Stability Class	3	3	4	2	4	4	4	3	3
Monin-Obukhov Length (m)	-63	-51	-243	-12	-46	-110	-68	-63	-53
Friction Velocity (m/s)	0.61	0.59	0.44	0.26	0.51	0.72	0.57	0.54	0.49
Roughness Height (cm)	20	20	20	20	20	20	20	20	20
Convection Velocity (m/s)	1.83	1.46	1.00	1.30	1.68	1.57	1.42	1.73	1.41
Inversion Height (m)	668	305	1135	557	649	448	434	816	500

Notes

1. All values are averaged over the period BEGIN-10 to END+10 minutes.
2. Source wind data for the 2 m level; meteorology data for the 10 m level except relative humidity.
3. Only last 5 minutes of source data record is available for tests1103871 & 1113871.
4. Only last 20 minutes of met record is available for test 1104871.

The resulting spectral estimate was subsequently smoothed in the frequency domain. Smoothing was accomplished by averaging over a frequency range Δn centered on the frequency of interest. The range Δn was varied with frequency such that $\Delta n/n$ remained approximately constant. Bendat and Piersol (1971) have shown that frequency smoothing is essential to reduce the substantial random error and to make the estimate consistent, that is, to make the estimate convergent in the limit of an infinite sampling period. A more detailed discussion of the errors occurring in estimates of power spectra, and quantities derived from power spectra such as correlations and integral scales, is presented in Appendix B of our report describing the Dugway-85 tests (Liljegren et al., 1988).

The frequency-weighted, normalized power spectra of the three components of the wind velocity measured at the 10-m level during the Atterbury-87 study are presented in Fig. 5.33-40. They are presented on logarithmic axes owing to the large range of frequencies they span. As a result, the spectra are frequency weighted in order to preserve the property that the area under the curve between specified frequency limits is proportional to the fraction of the variance or "power" contributed by that range of frequencies since $nS(n)d(\ln n) = S(n)dn$. The error bars indicate the 90% confidence limits based on the analysis presented in Appendix B of our Dugway-85 report and the error analysis of Bendat and Piersol (1971), assuming the errors conform to a chi-square distribution.

The data are compared with the spectral model of Højstrup (1982) which is based on data from the Minnesota boundary layer turbulence study. The model consists of two components: a high-frequency component which models the mechanical turbulence and a low-frequency component which models the convective turbulence. The mechanical component scales with the Monin-Obukhov length; the convective component scales with the boundary layer height z_i. Using the "effective" Monin-Obukhov length determined previously, the boundary layer height may be estimated by an iterative process in which the model prediction is compared with the spectral estimates computed from the data. This method provided satisfactory estimates of z_i for the Dugway-85 study. For all Atterbury-87 tests the boundary layer height estimated in this manner was within 50% of the value determined from the NWS upper air data.

The spectra of Tests 1103871, 1104872, 1106871, 1112871 and 1113871, for which the wind was out of the southwest, exhibit very similar behavior. The axial (u) spectra display the -2/3 slope characteristic of inertial subrange behavior above the peak frequency. (The slight attenuation at high frequencies is due to the roll-off in the

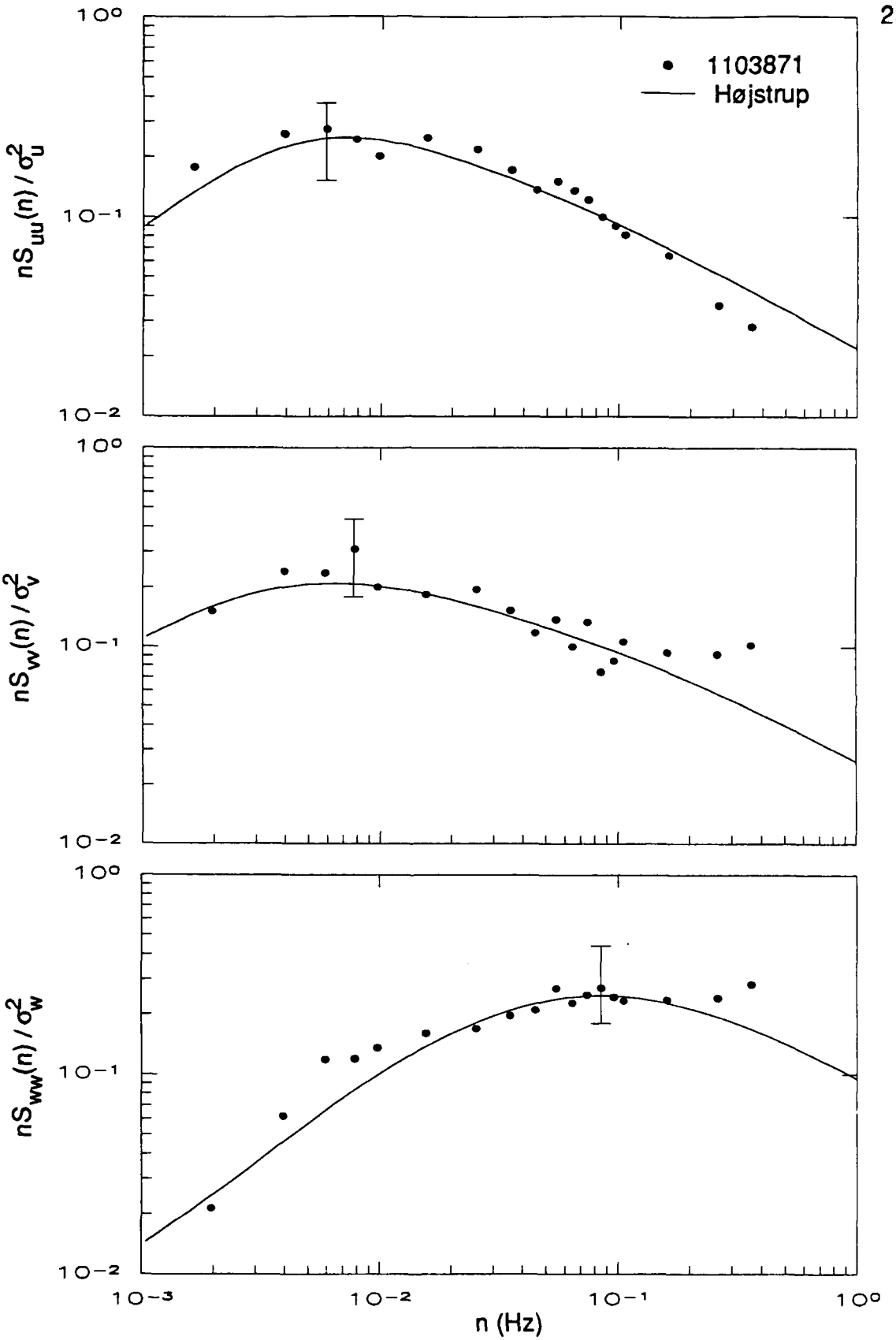

Figure 5.33 Frequency-weighted power spectra of the wind velocity fluctuations at the 10-m level for test 1103871 compared with a spectral model by Højstrup (1982). Error bars indicate the 90% confidence limits.

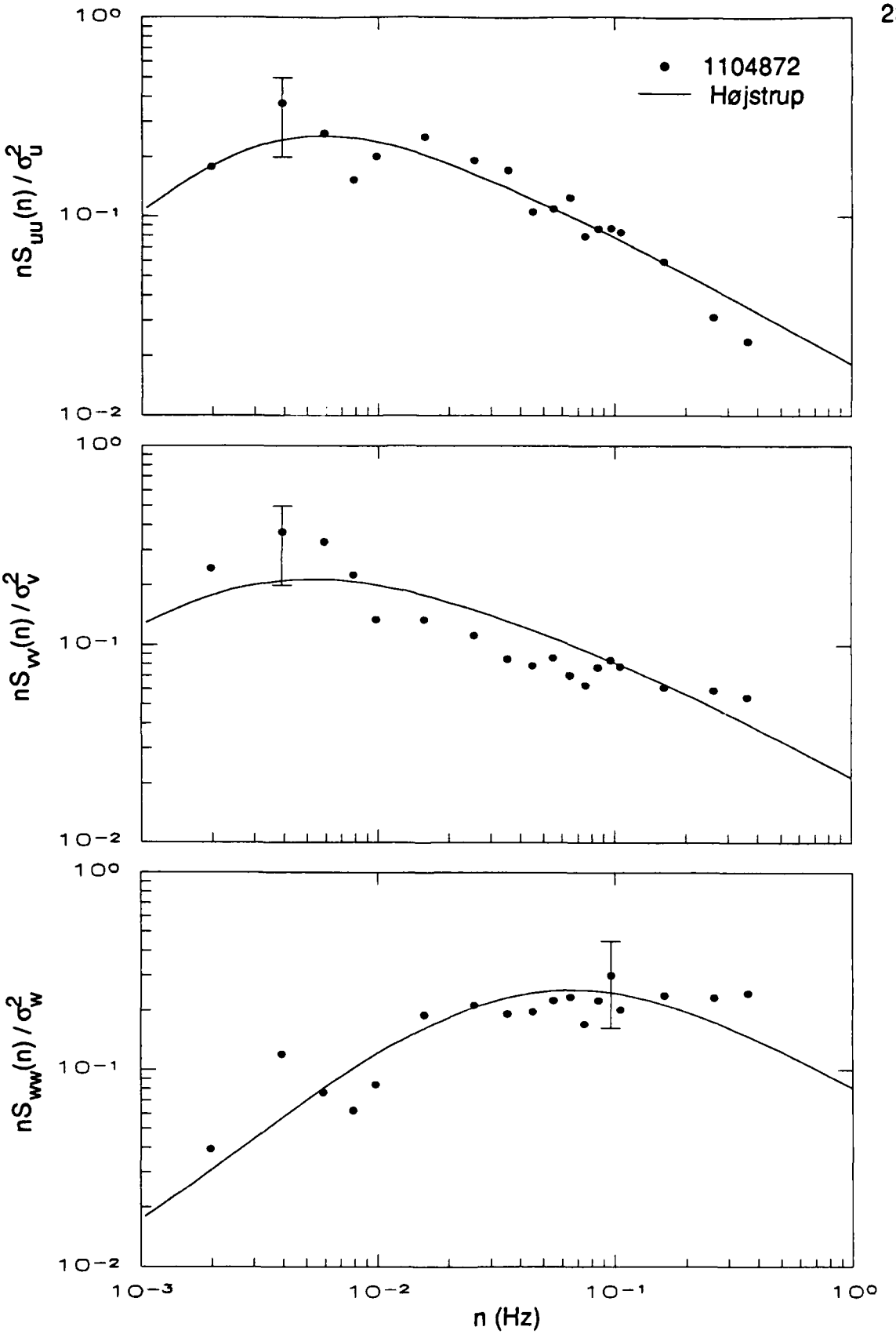

Figure 5.34 Frequency-weighted power spectra of the wind velocity fluctuations at the 10-m level for test 1104872 compared with a spectral model by Højstrup (1982). Error bars indicate the 90% confidence limits.

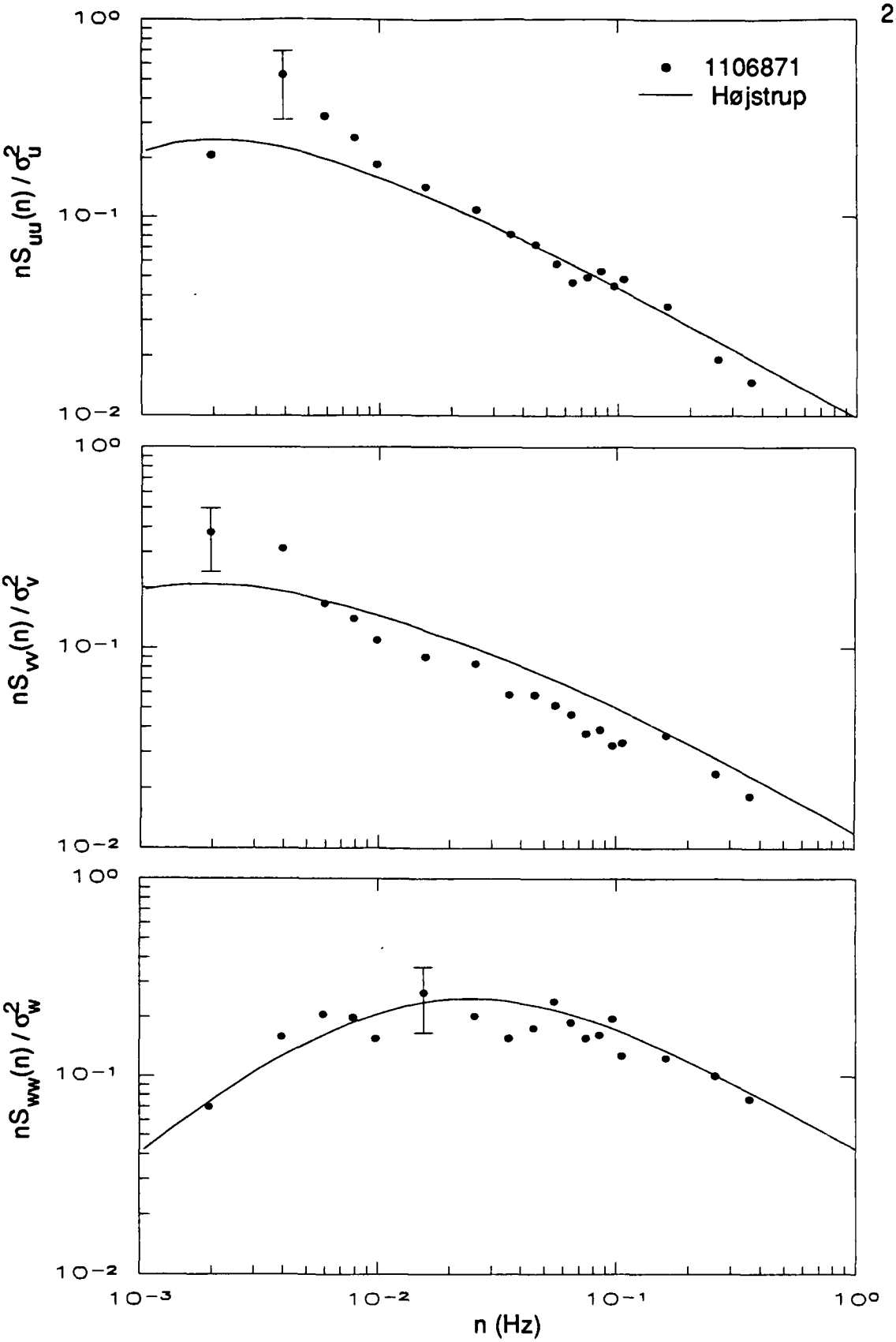

Figure 5.35 Frequency-weighted power spectra of the wind velocity fluctuations at the 10-m level for test 1106871 compared with a spectral model by Højstrup (1982). Error bars indicate the 90% confidence limits.

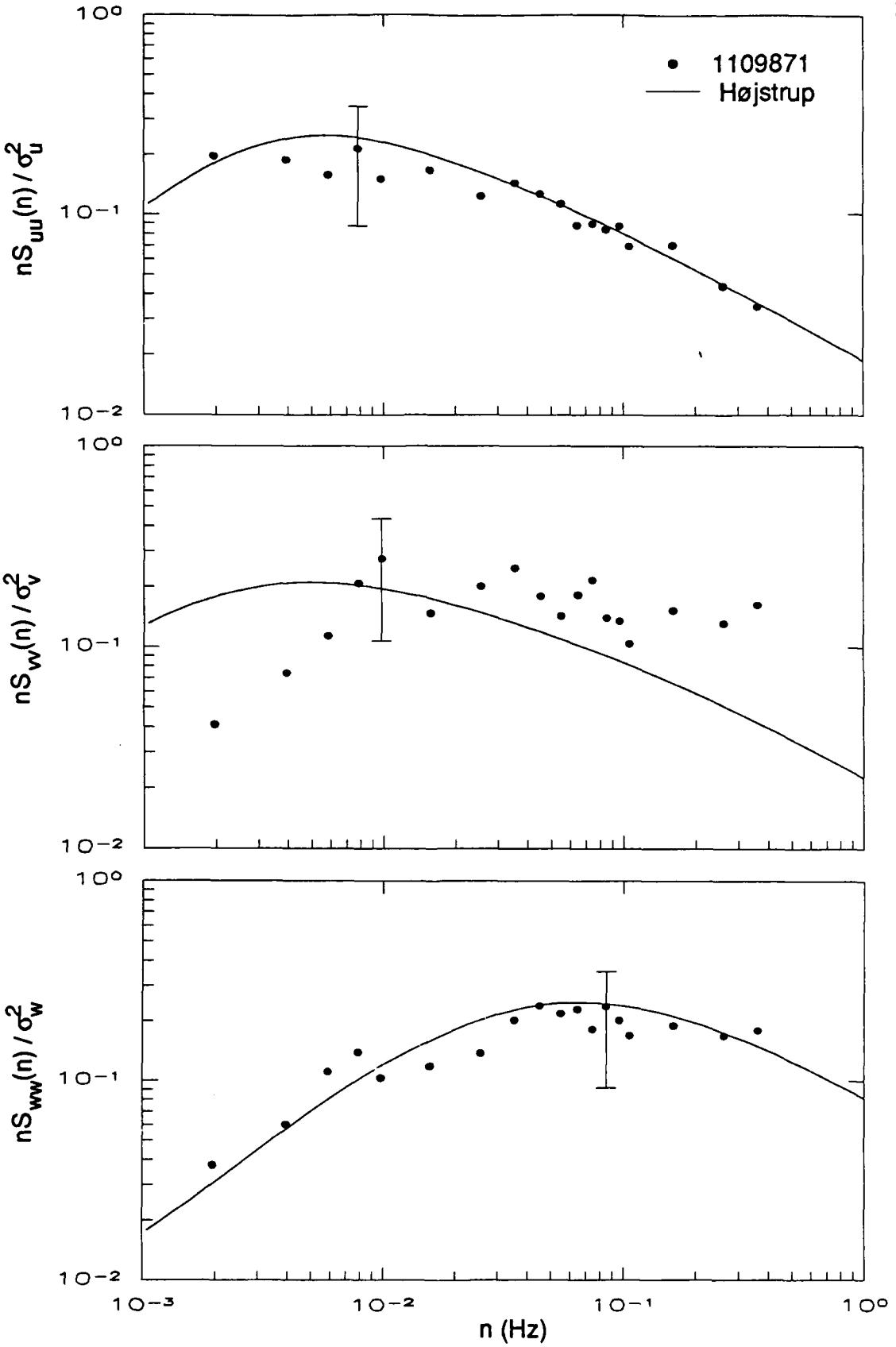

Figure 5.36 Frequency-weighted power spectra of the wind velocity fluctuations at the 10-m level for test 1109871 compared with a spectral model by Højstrup (1982). Error bars indicate the 90% confidence limits.

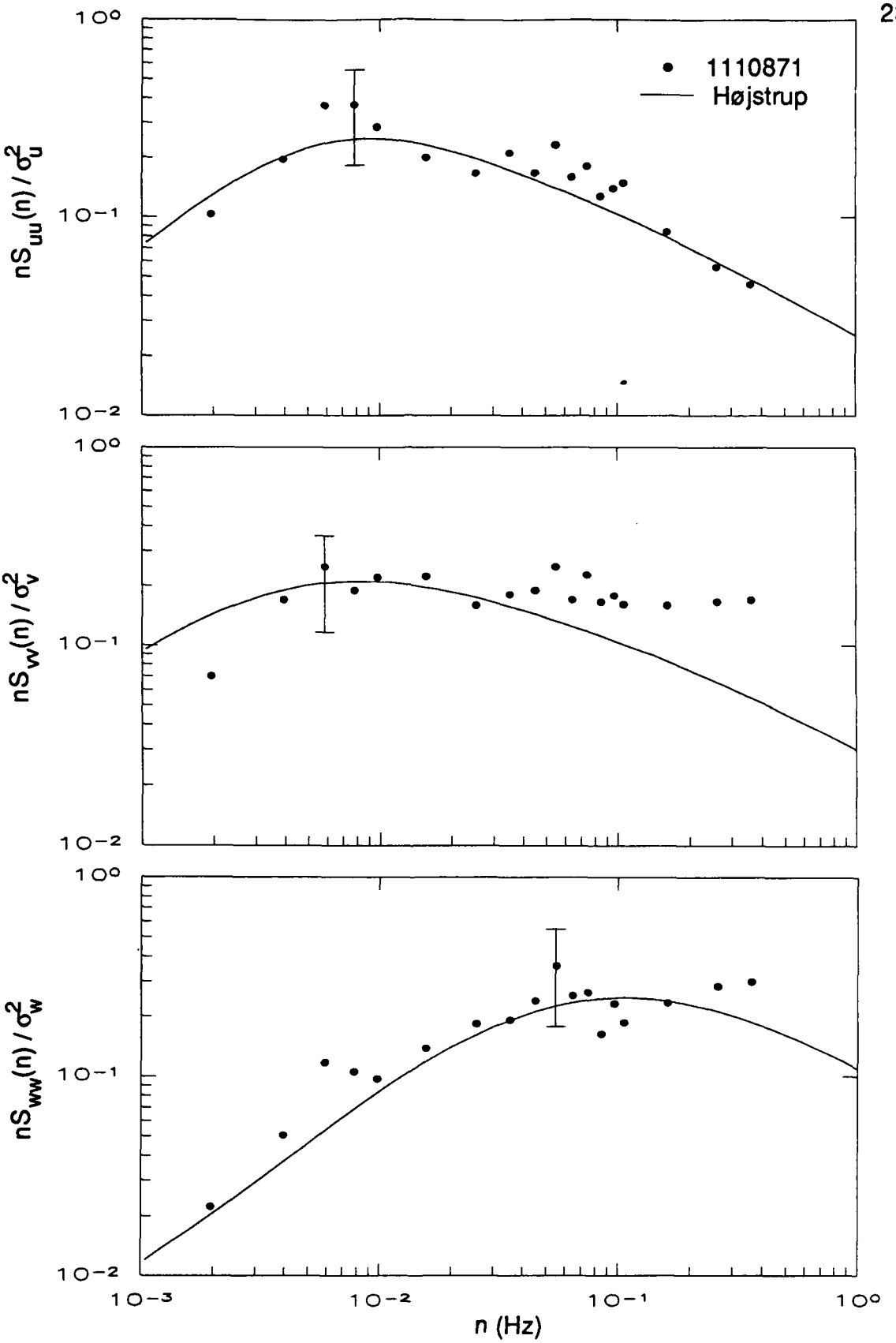

Figure 5.37 Frequency-weighted power spectra of the wind velocity fluctuations at the 10-m level for test 1110871 compared with a spectral model by Højstrup (1982). Error bars indicate the 90% confidence limits.

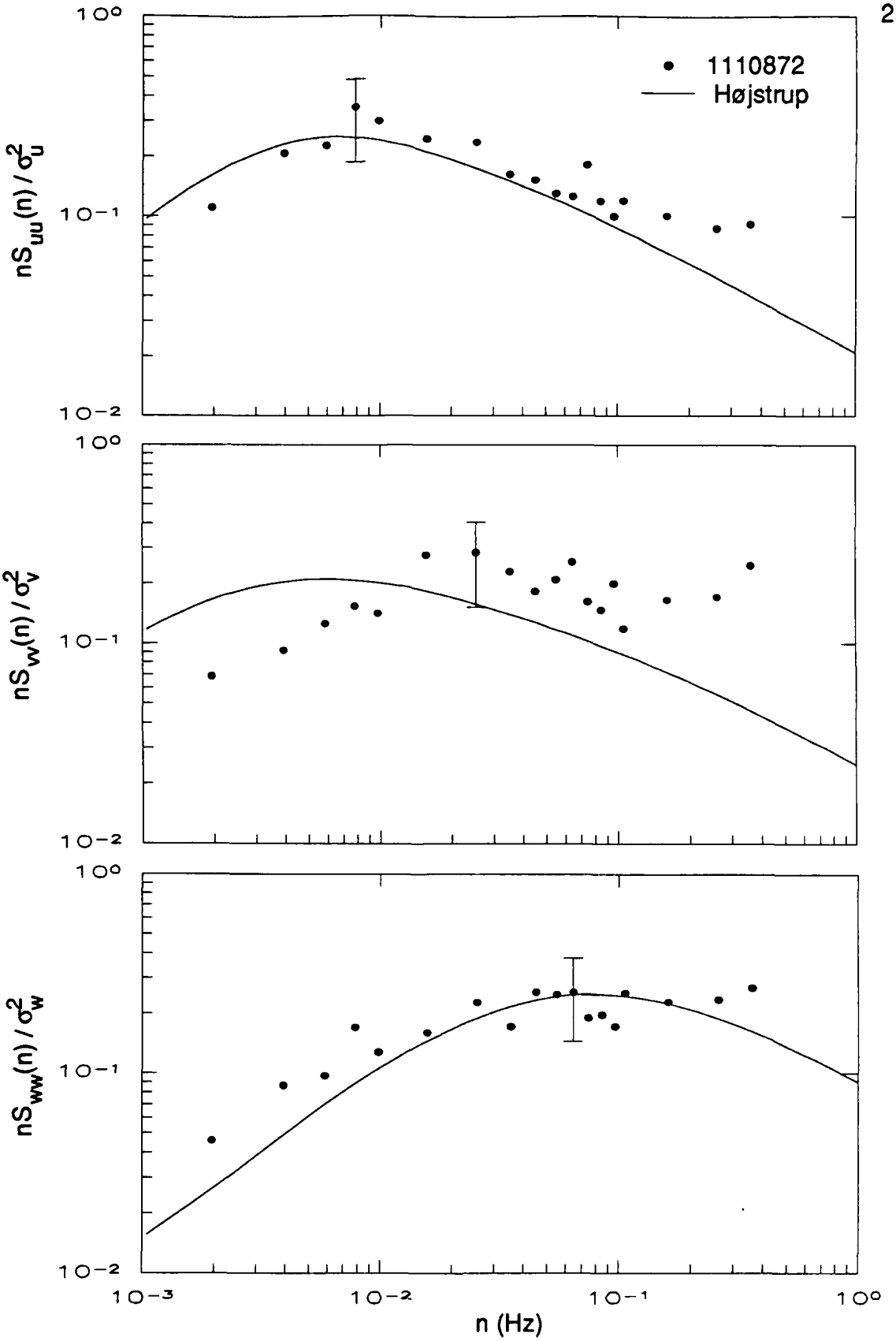

Figure 5.38 Frequency-weighted power spectra of the wind velocity fluctuations at the 10-m level for test 1110872 compared with a spectral model by Højstrup (1982). Error bars indicate the 90% confidence limits.

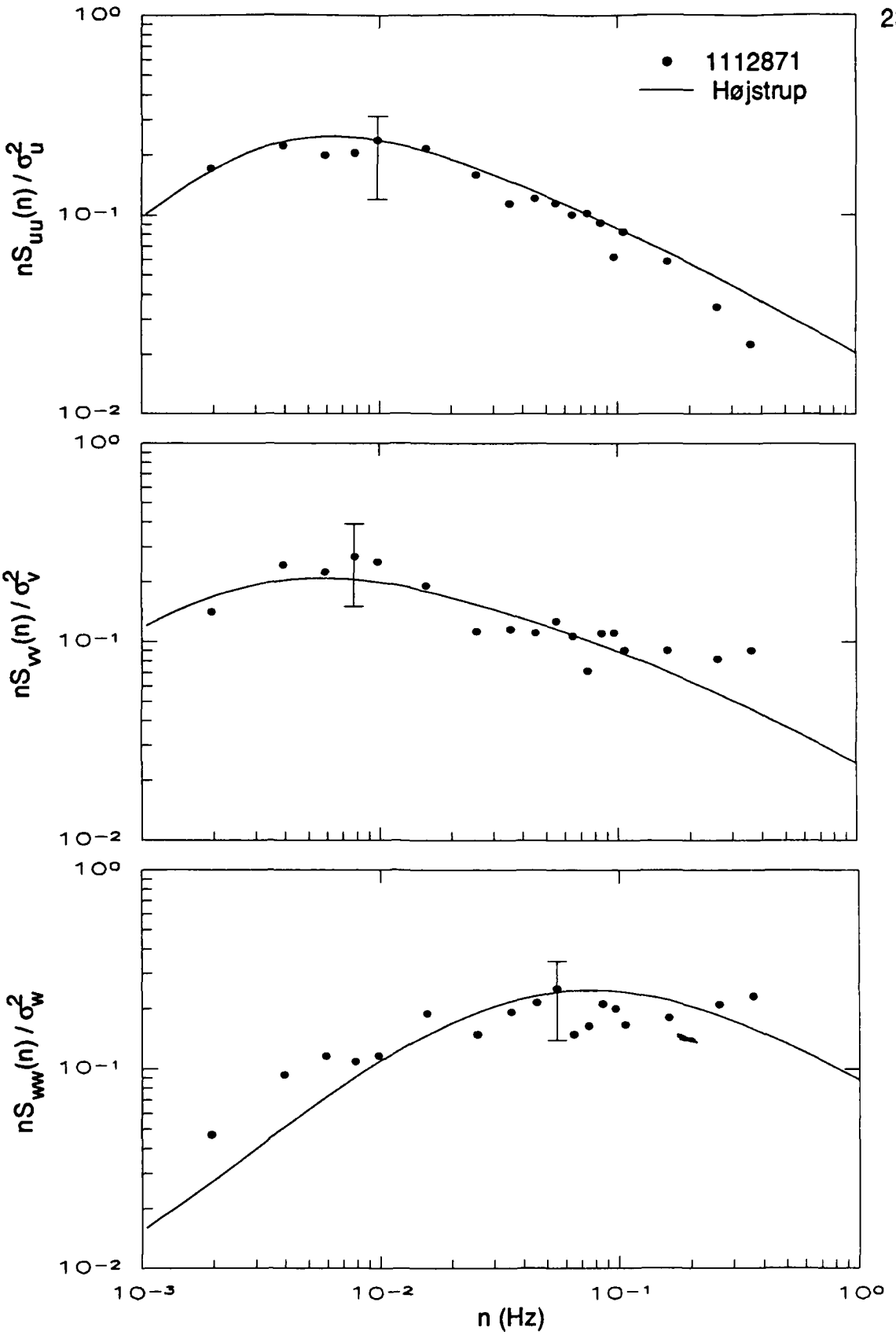

Figure 5.39 Frequency-weighted power spectra of the wind velocity fluctuations at the 10-m level for test 1112871 compared with a spectral model by Højstrup (1982). Error bars indicate the 90% confidence limits.

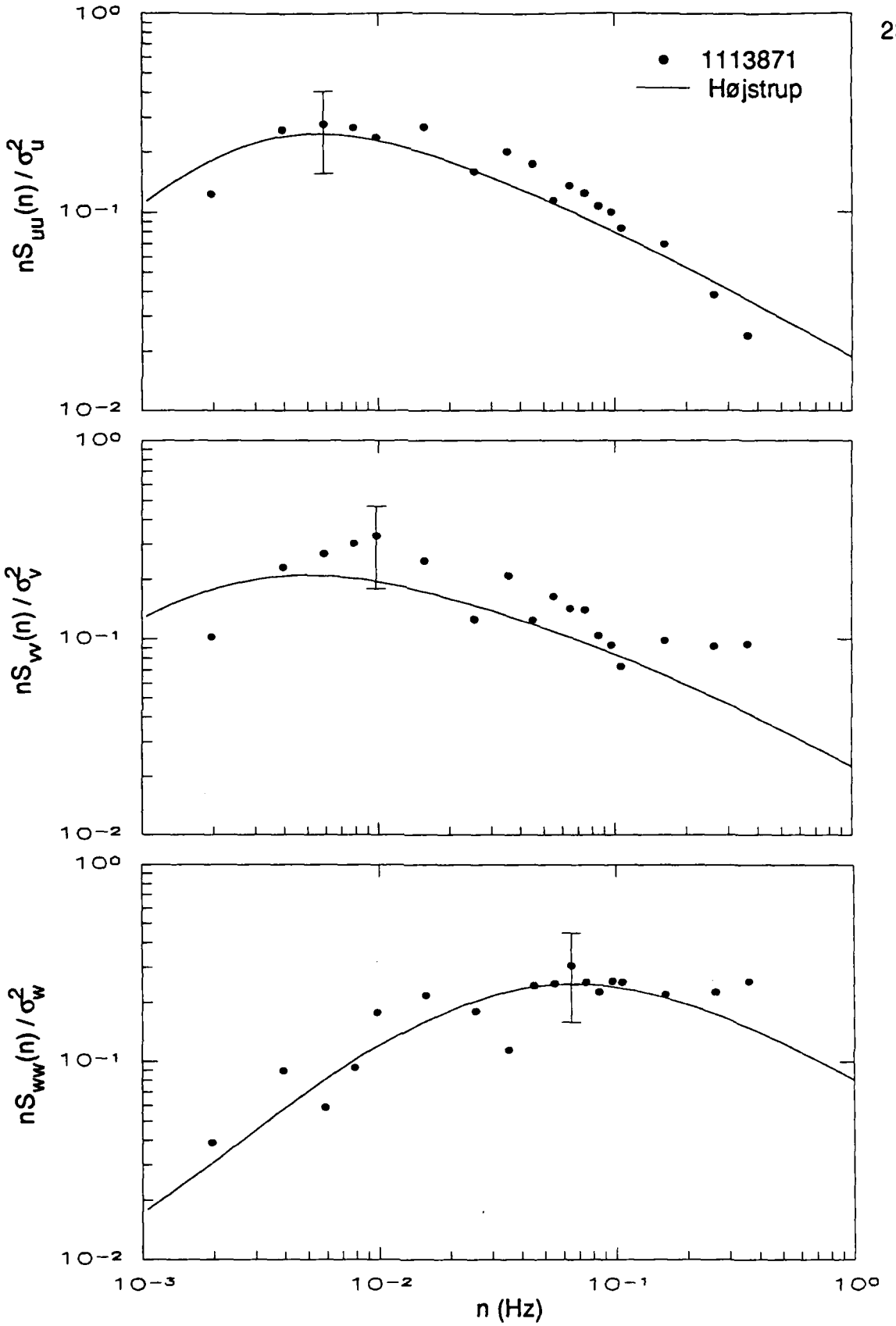

Figure 5.40 Frequency-weighted power spectra of the wind velocity fluctuations at the 10-m level for test 1113871 compared with a spectral model by Højstrup (1982). Error bars indicate the 90% confidence limits.

dynamic response of the cup anemometers.) The transverse (v) and vertical (w) spectra for this group of tests also show general agreement with the model. However, for all but the low wind speed test, 1106871, the spectra increase at high frequencies. This may be due to the increased high frequency motions induced by the relatively tall vegetation. Spectra from the Dugway-85 tests, and those from the low-speed test 1106871, showed no such increase.

The transverse (v) spectra for Tests 1109871, 1110871 and 1110872, for which the wind was out of the north, displayed a different behavior. The transverse spectra were attenuated at low frequencies and amplified at higher frequencies. However, a lower estimate for the boundary layer height was not justified since the location of the peaks of the axial and vertical spectra agree very well with the model for z_i = 700 m. It may be that the dense line of mature, leafless deciduous trees located approximately 200 m north of the meteorological instrument tower acted as "flow straighteners", passing the axial and vertical motions essentially intact while attenuating the low-frequency lateral motions and transferring the energy to higher frequencies.

The aforementioned differences aside, the velocity spectra appear fairly similar in all cases: the maximum occurs at very nearly the same frequency and has about the same magnitude. In addition, the data are in generally good agreement with Højstrup's model spectra determined from simple terrain/simple meteorology data. This supports the use of the "effective" Monin-Obukhov length to relate more complex meteorological situations to the simple terrain/simple meteorology ideal for which much data exists. More importantly, the agreement between the data and the Højstrup model spectra indicates that for most of the Atterbury-87 tests there is more energy at low frequencies than would otherwise be expected based on the Turner stability class estimates given in Table 5.13. (The Turner classes do not consider roughness or terrain effects.) This additional low-frequency energy is manifested in the small values of the "effective" L determined with the Nieuwstadt-Boughton fitting procedure because the only mechanism for producing such low-frequency motions over uniformly flat terrain is thermal convection.

The most likely source of the large-scale motions required to produce this low-frequency energy is the hilly upwind terrain. Although these large-scale motions would be produced mechanically by the flow of the wind over the upwind hills rather than by thermal convection, the resulting energy would nevertheless be at low frequencies and would have the same effect on the spectra and mean vertical profiles as would strong convective motions for simple terrain/simple meteorology cases. For example, the spectra for Test 1106871, which has a Turner class of 2 and a mean 10-

m wind speed of 1.6 m/s, are very similar to the spectra for Test 1104872 which was has a Turner class of 3 and a 10-m wind speed of 4.7 m/s despite the fact that the low-frequency energy for Test 1106871 was primarily due to thermal convection and the low-frequency energy for Test 1104872 had a substantial contribution from mechanical turbulence.

The implications of this rather startling result are that the effects of the upwind terrain on the local meteorology can be related to the ideal case of simple terrain/simple meteorology by using the effective Monin-Obukhov length determined using the Nieuwstadt-Boughton fitting approach. This may prove valuable since much data exist for the simple terrain/simple meteorology case and most models assume this ideal terrain.

Integral time scales may be computed as the integral of the auto-correlation or from the value of the power spectrum at zero frequency. However, since much of the energy in the atmosphere is at low frequencies, both of these values are extremely sensitive to the manner in which the high and low frequency components are separated (i.e., the duration of the sampling period and the period over which the mean values are computed.) As a result, the integral scales may be greatly in error. In fact, Panofsky and Dutton (1984) recommend against using integral scales for this reason.

Hanna (1981) has suggested two alternative methods of determining integral scales. Both of these methods require the assumption that the auto-correlation is an exponential function. Neumann (1978) shows that this assumption is consistent with dispersion data and Tennekes (1979) shows that this is a theoretically valid assumption in the inertial subrange. However, one disadvantage of the exponential correlation function is that its slope is infinite at the origin, which restricts its application to large Reynolds number flows such as are found in the atmosphere.

In the first method, Hanna (1981) derives the following relationship between the frequency n_{MAX} or the wavelength $\lambda_{MAX} = U/n_{MAX}$ at which the peak of the frequency-weighted spectrum nS(n) occurs and the Eulerian (fixed-point) integral scale: $T_E = (2\pi n_{MAX})^{-1} = \lambda_{MAX}/(2\pi U)$. In the second method, Hanna takes the integral scale to be the time lag at which the correlation falls to e^{-1} of its initial value. Hanna finds agreement between these approaches to within 10%. Since we have essentially fit the Højstrup model spectra to the data, we can determine the integral scale from the peak frequency or wavelength predicted by the model. It should be noted that these peak wavelengths agree with the findings of Kaimal et al. (1976) and Cauhey and Palmer (1979), discussed in Chapter 3. Because the peak frequencies for all of the Atterbury-

87 tests are nearly identical within the precision of the spectral estimates, the corresponding integral scales are approximately the same as well. Thus, within the precision of the data, $T_{E,u} \approx T_{E,v} \approx 30$ s; $T_{E,w} \approx 2$ s for the 10-m level.

5.6 The Material Plume

In this section, the results of the in-plume measurements of time-average concentration will be presented and discussed for the fog-oil tests only. The results for HC smoke will be presented elsewhere.

5.6.1 Measurements

In order to quantify the mean transport and turbulent diffusion of the fog-oil plume, the average concentration of fog-oil smoke was determined at the 50 locations indicated in Fig. 5.6. The average concentration was determined from the total mass of material collected on aspirated Nuclepore (Pleasanton, CA) model 210817, grade "AAA", glass fiber filters 37 mm in diameter. According the the manufacturer, these filters were capable of sustaining a high mass loading without a significant increase in pressure drop and were capable of collecting 99.99% of a 0.3 μm mono-disperse DOP reference aerosol. This was sufficient to capture the fog-oil droplets, as the particle size analysis confirmed.

The filters were housed in acrylic cassettes (Nuclepore model 321315) as illustrated in Fig. 5.41. Because the filters were relatively fragile, they were supported on 37 mm pads (Nuclepore model 240810), also indicated in Fig. 5.41. The cassettes were attached to the sampling masts by mean of silicon-rubber surgical tubing. The silicon-rubber tubing remains flexible at temperatures below 25 °C and provides a tight seal between the cassette and the sampling mast. Less expensive vinyl tubing does not perform satisfactorily below room temperature.

The sampling masts consisted of 8-m long, thin-walled aluminum tubes to which pipe fittings had been welded at 1-m intervals. These were fabricated by the Hastings Irrigation Pipe Co. (Hastings, NE). The filter cassettes were attached at the 1, 2, 4 and 8-m levels on Transects 1-4, as shown in Fig. 5.42, and at 2 and 8 m on Transect 5. (The remaining fittings were plugged.) The masts were attached to and supported by 2-m steel fence posts.

Aspiration was provided to each mast by a 450 W AC-powered air pump (Gast Mfg., Inc.) and the air flow regulated with a Dwyer Instruments Corp. rotameter. The filters on Transects 1-4 were aspirated at 23.6 Lpm (50 ft^3/hr) whereas those on

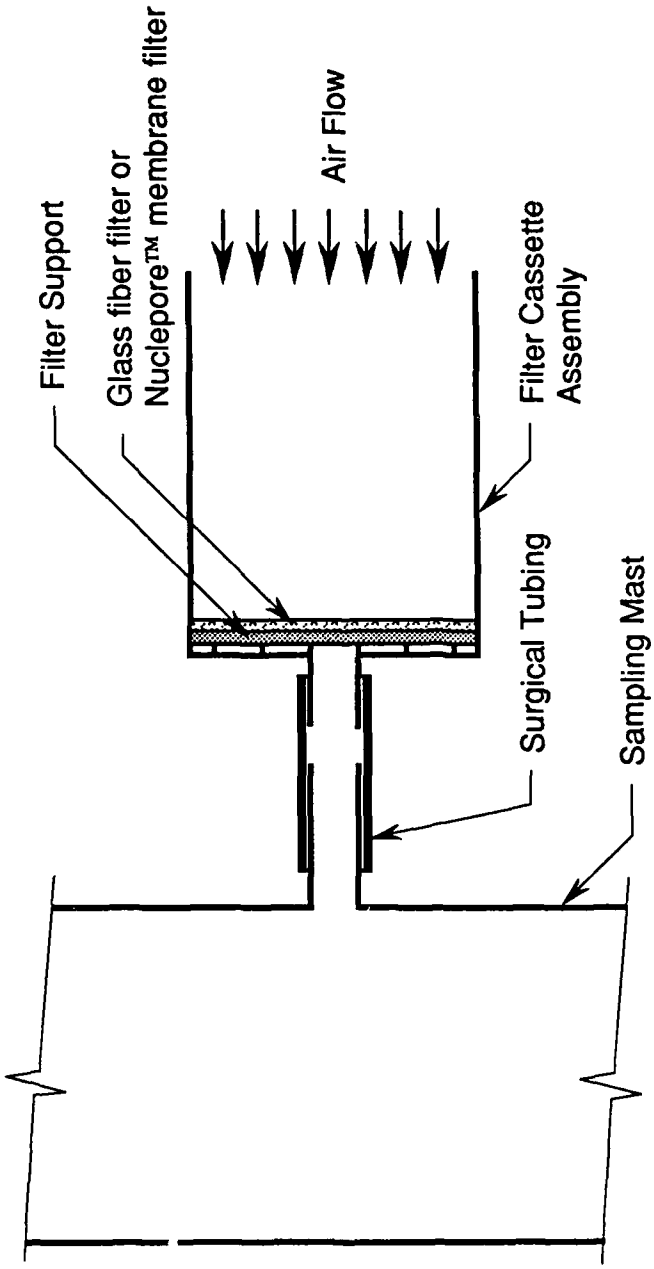

Figure 5.41 Schematic illustration of the filter cassette assembly.

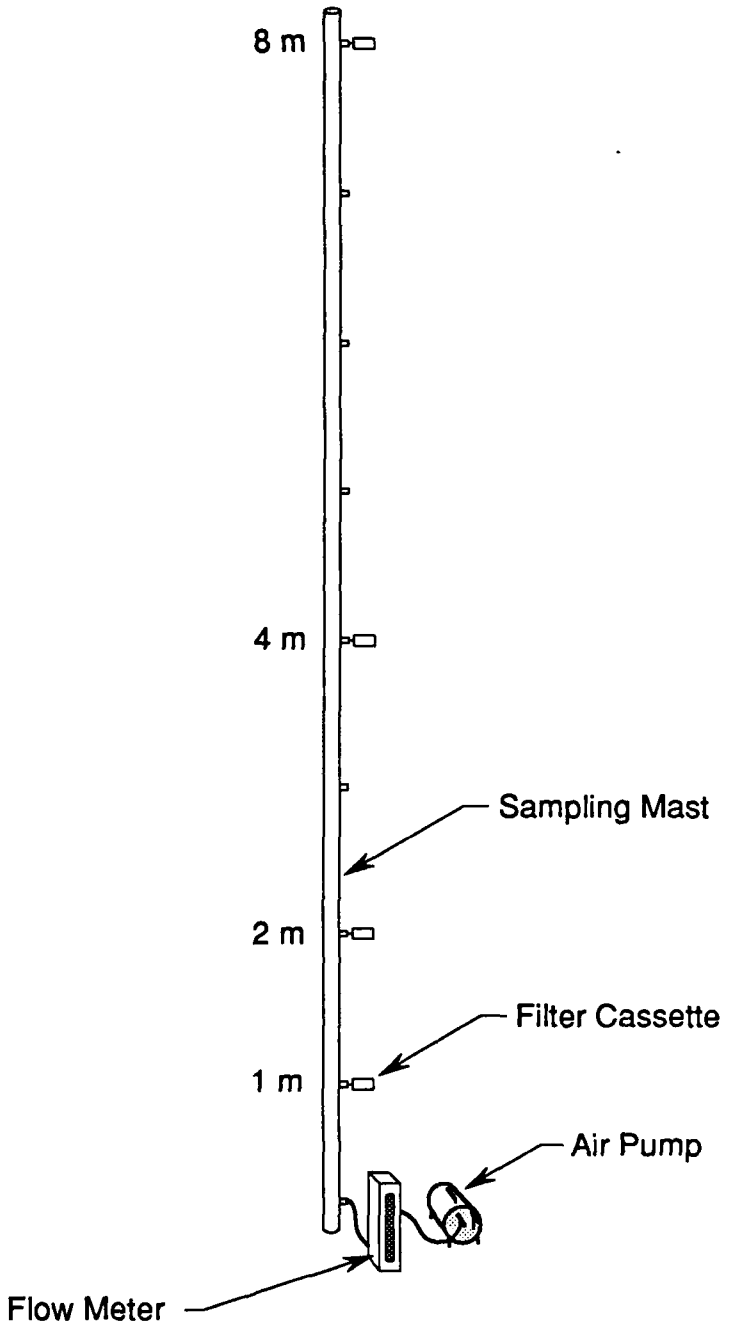

Figure 5.42 Illustration of the sampling mast/air pump assembly.

Transect 5 were aspirated at twice this rate, 47.2 Lpm (100 ft^3/hr), in order to achieve a lower detection threshold as will be explained later. DeVaull (1988) measured a pressure drop of 8.5 and 15.2 kPa across the filter cassette assembly at indicated flow rates of 23.6 and 47.2 Lpm, respectively. Since the inlet pressure to the rotameters was thus less than atmospheric pressure, the actual aspiration rate $\dot{V}_{actual}$ was greater than indicated by 4.5% and 8.5%, respectively. Assuming ideal gas behavior (Miller, 1983):

$$\dot{V}_{actual} = \dot{V}_{indicated} \sqrt{\frac{\rho_{design}}{\rho_{actual}}} = \dot{V}_{indicated} \sqrt{\frac{T_{actual}}{T_{design}} \frac{P_{design}}{P_{actual}}}. \qquad (5.42)$$

However, because the rotameters were calibrated by the manufacturer at 25 °C, the actual flow rate would have been 4.3% less than indicated for an ambient temperature of 0 °C with atmospheric pressure at the inlet. Since these errors offset each other to within the rated accuracy of the rotameters, no correction was applied to the indicated flow rates.

The mast assemblies, consisting of a sampling mast, rotameter and air pump, were organized into "modules" consisting of four or five mast assemblies and a 3.6 kW AC power generator (Generac Corp., Waukesha, WI). As illustrated in Fig. 5.43, the AC generator was positioned near the center of a module and AC power distributed to each mast by means of heavy-duty 12-gauge power cables. These cables were, unfortunately, the target of attack by small, nocturnal rodents. Generally, they only gnawed at the heavy insulation but occasionally chewed completely through the cable, necessitating repair or replacement of the cable prior to testing.

Prior to each test, the 192 filter cassettes were mounted on the masts and the connecting tubing checked. The AC generators were subsequently filled with gasoline, started and allowed to warm up. Shortly before a smoke release was commenced, the aspiration of the cassettes was initiated and the flow rate at each mast checked. Upon termination of the smoke release and after the plume had cleared the sampling network, the flow rates were again checked and any deviation from the nominal rate noted. Aspiration was subsequently discontinued and the filter cassettes collected, capped, labelled and boxed.

Upon returning to our laboratory the filters were removed from the cassettes and divided in half prior to analysis. (The filters were divided in half so that any apparent irregularities in the data subsequent to the analysis of the first half could be checked by re-examining the remaining half of the filter.) Each half filter was analyzed by gas

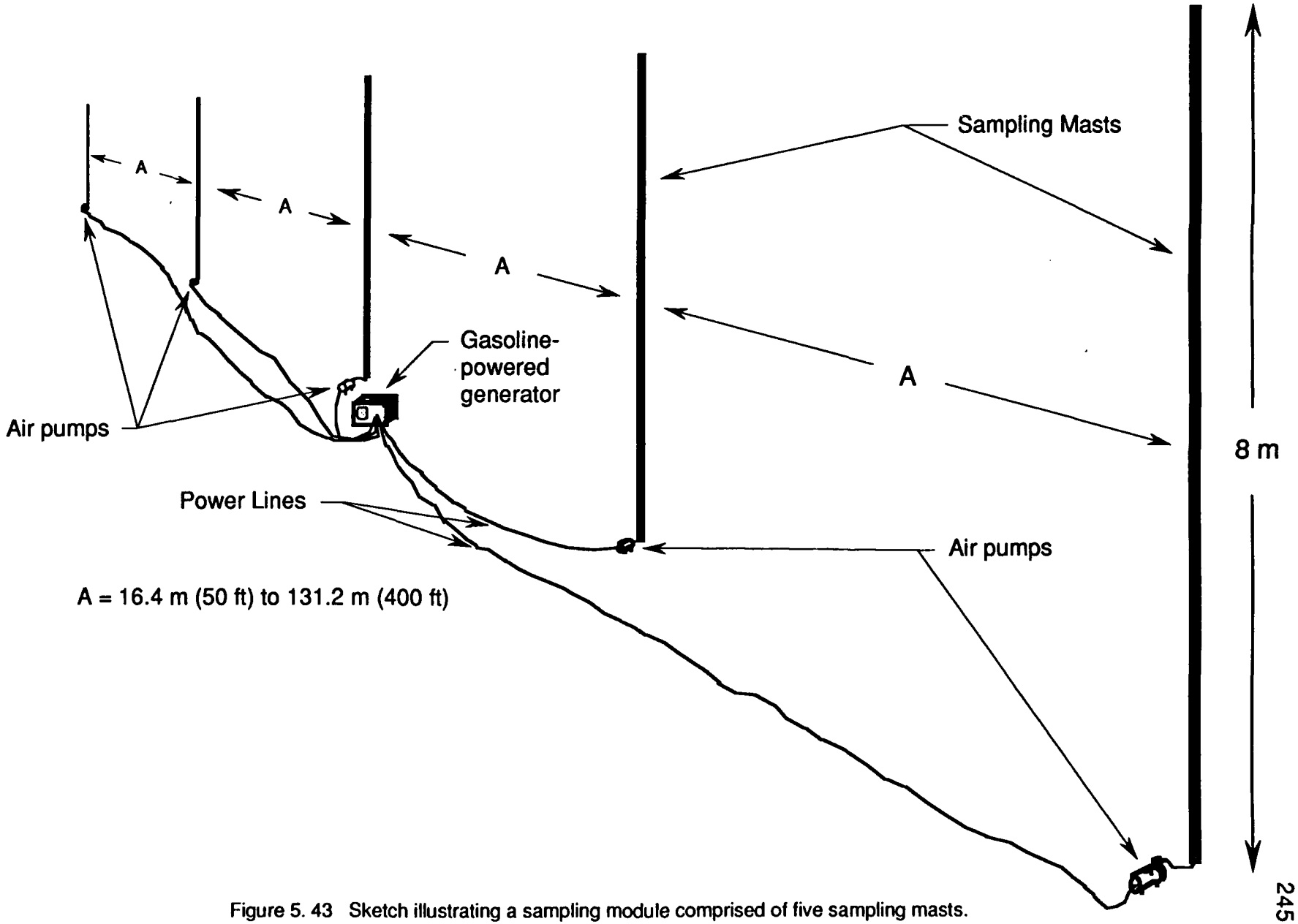

Figure 5. 43 Sketch illustrating a sampling module comprised of five sampling masts.

chromatography, which provided a precise, chemically selective method of determining the mass of fog oil collected. Calibration and background checks were performed daily; the mean background "noise" was determined to be 8.9×10^{-3} mg with a standard deviation of 7.6×10^{-3} mg. The minimum detectable mass was thus 0.021 mg (with 95% confidence) for each half filter or 0.042 mg per sample.

Although the chromatographic analysis of the samples was carried out rapidly after completion of the field work, examination of the results for controlled samples revealed that storage losses amounting to approximately 80% of the mass collected had occurred during the 2-3 week period between the field tests and the sample analysis. This was eventually determined to be due to "wicking" of the oil from the filter to the support pad. Based on the analysis of the controlled samples, a correction factor of 5 was applied to the data. A uniform correction factor proved to be adequate, based on a comparison of the results for halves of the same filters analyzed at different times, because of the rapidity with which the samples were analyzed. The standard deviation of 1.9 in the correction factor implies a ±62% uncertainty (for 90% confidence) in the reported mass. Further details of the chromatographic method and error analysis are described by DeVaull (1988).

Knowing the mass m collected on each filter, the average concentration C over the release period t_{TEST} was then calculated as

$$C = \frac{m}{\dot{\forall}\, t_{TEST}} \tag{5.43}$$

where $\dot{\forall}$ is the volumetric flow rate through the filter. The minimum detectable concentration was thus a function of the aspiration rate and test duration. For this reason the relatively large aspiration rate of 23.6 Lpm was utilized on the first four transects. Because the concentration was expected to be very small on the fifth transect, the aspiration rate was doubled to 47.2 Lpm in order to halve the detection limit.

5.6.2 Results and Discussion

The average concentrations for Tests 1103871, 1104872 and 1106871 are presented for each transect in Figs. 5.44-46. Mast number one for each transect is on the extreme right. The error bars represent the 90% confidence limits for the concentration values at the 2-m level. The concentration is given in units of mg/m^3; since 1 m^3 of air has a mass of about 1 kg ($=10^6$ mg) at 25 °C, these concentrations

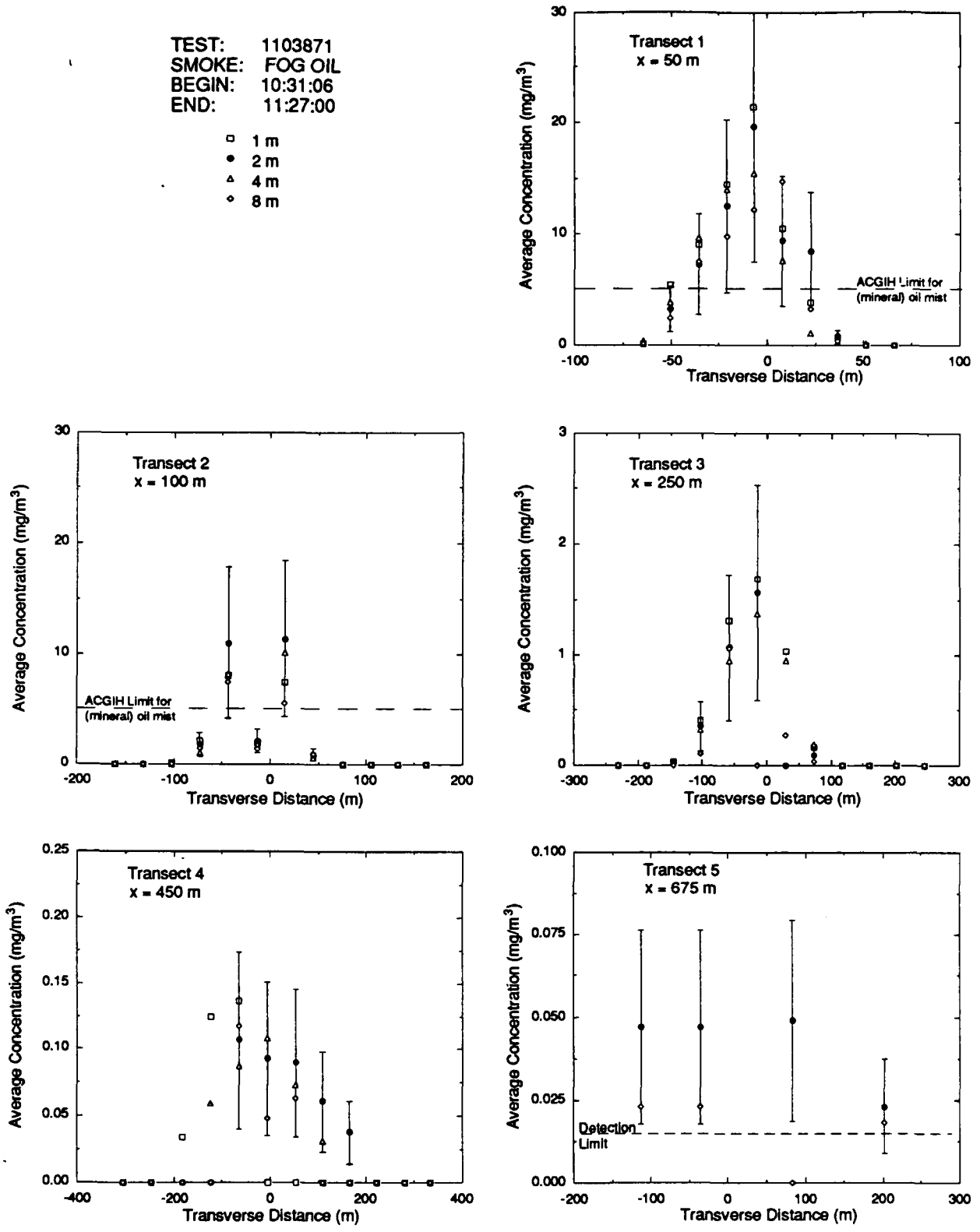

Figure 5.44 Average concentration data from test 1103871 at all levels. The error bars indicate the 90% confidence limit for the data. On transect 5, only the 2 m and 8 m levels were operated. The ACGIH limit for mineral oil mist (5 mg/m^3) is indicated; the detection limit is also shown for transect 5.

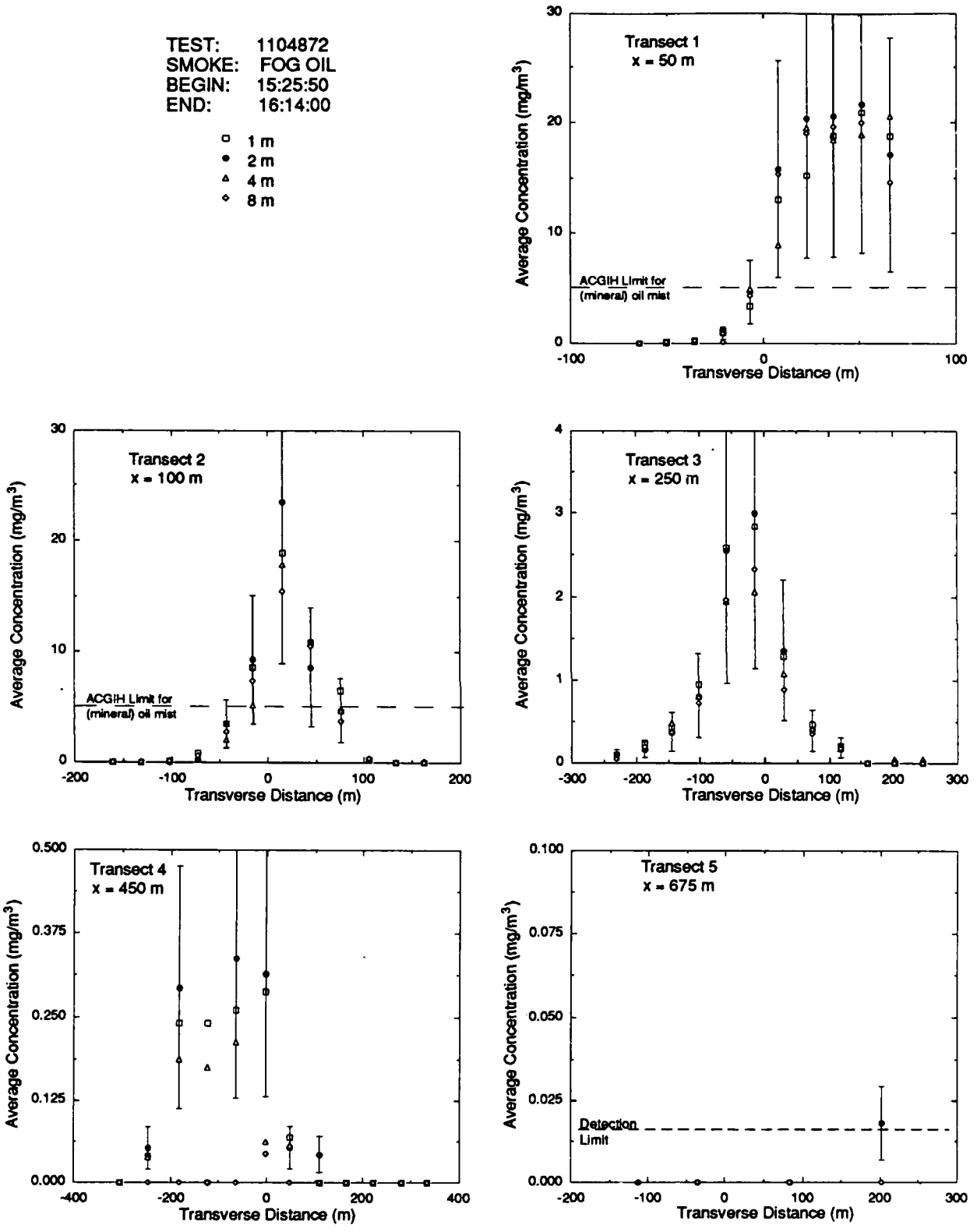

Figure 5.45 Average concentration data from test 1104872 at all levels. The error bars indicate the 90% confidence limit for the data. On transect 5, only the 2 m and 8 m levels were operated. The ACGIH limit for mineral oil mist (5 mg/m^3) is indicated; the detection limit is also shown for transect 5.

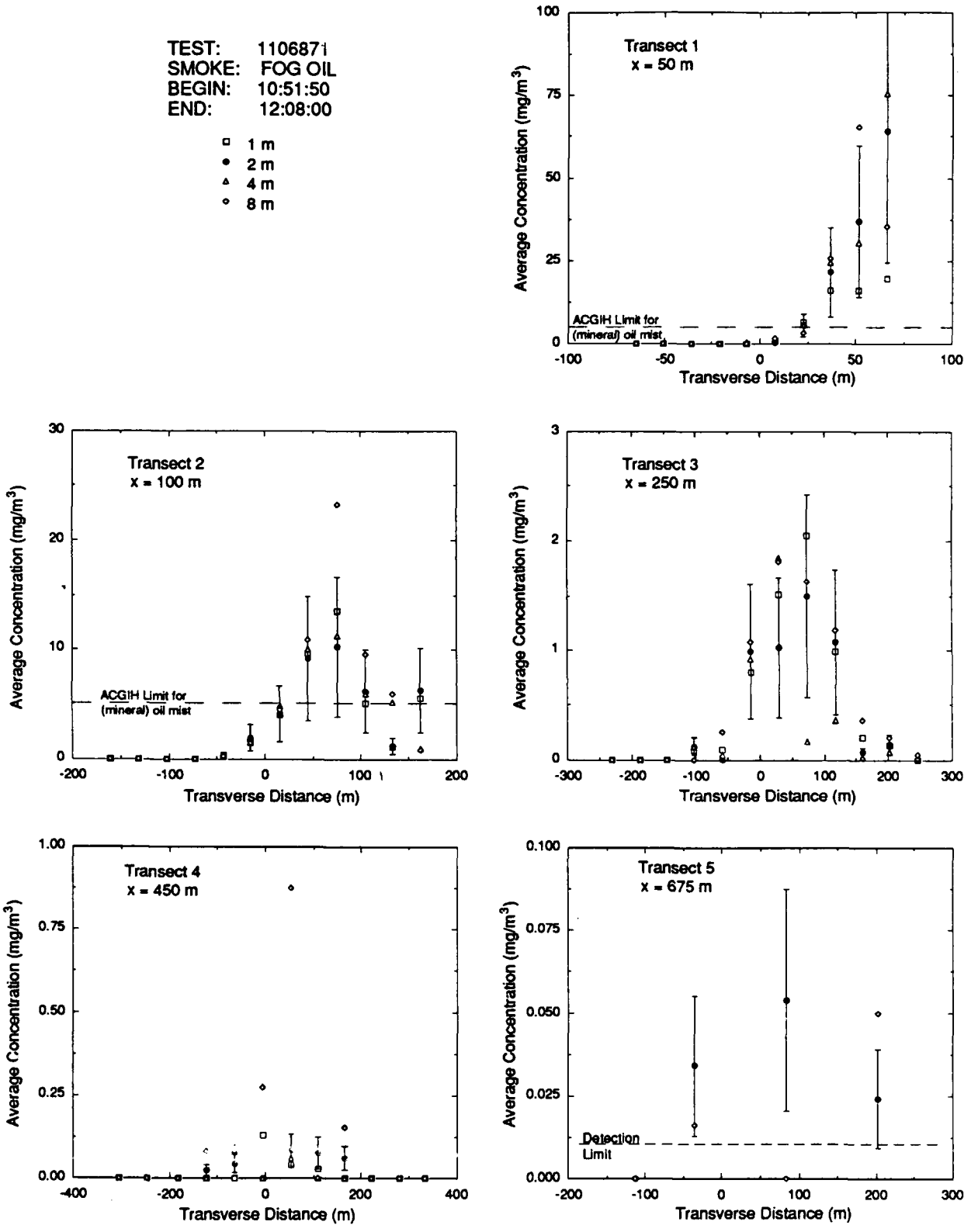

Figure 5.46 Average concentration data from test 1106871 at all levels. The error bars indicate the 90% confidence limit for the data. On transect 5, only the 2 m and 8 m levels were operated. The ACGIH limit for mineral oil mist (5 mg/m^3) is indicated; the detection limit is also shown for transect 5.

may also be read in units of parts per million (ppm), on a mass basis. For each test, the threshold limit value guideline for mineral oil mist of 5 mg/m^3 recommended by the American Conference of Governmental Industrial Hygienists (1966) is indicated. In addition, the detection limit is indicated for the fifth transect and is approximately 0.01 mg/m^3 (10 parts per *billion* by mass). This is half the limit on the first four transects because the flow rate is twice as great.

The results of Test 1103871 appear fairly typical of the dispersion from a ground-level point source. The lateral spread about the maximum concentration does not appear symmetric in these plots because the axis of the plume was at an angle of about 15° to the centerline of the sampling network for this test. The only anomalous behavior occurs on the second transect where the concentration distribution appears to be bimodal. Although the data appear suspicious, analysis of the reserved filter halves for all levels of Mast 7 confirmed the earlier measurements and no problems were noted in the field log books for this test.

The coincidence of the centerline of the smoke plume for Test 1103871 with the centerline of the sampling network demonstrates the value of the climatological analysis of the test site and supports the chosen orientation of the sampling grid. That the width of the smoke plume is completely resolved on Transects 1-4 and substantially resolved on Transect 5 validates the design of the network in terms of the length and the downwind position of the transects, as well as the number and spacing of the masts.

Test 1104872 displays a much broader peak along the first transect than 1103871 because the axis of the plume was at an angle of more than 30° to the network centerline. Note however that because the smoke generator was positioned at the extreme end of Transect 1, most of the samplers were exposed to the smoke plume. The maximum concentration marking the centerline of the plume can be readily discerned on Transects 1-4, although the plume missed the last transect because the wind direction was at a rather large angle to the network. Nevertheless, the width of the plume was substantially resolved on Transect 1 and completely resolved on Transects 2-4. This bears out our preference for transects over arcs, since a fixed source would have required additional samplers to yield an equivalent exposure. More importantly, this underscores the importance of our source locator program which allowed the source position to be determined just prior to the test based on the existing wind conditions.

Comparing the results for Tests 1103871 and 1104872 we find that the magnitude of the observed maximum concentrations are very similar. However, on

Transect 2, the concentration distribution for 1104872 has a well-defined maximum in the expected location rather than the bimodal distribution observed for 1103871. The plume widths for these tests also appear to be nearly the same for each transect. These similarities should be expected since the meteorological conditions for both tests were also quite similar.

Although nearly half of the fog-oil plume missed the first transect during Test 1106871, the plume width was well defined by the remaining four transects. Comparing the results of 1106871 with the previous two tests we see that the maximum concentration on Transect 1 for 1106871 is nearly three times the observed maximum for either 1103871 or 1104872. This may be due to a lower wind speed (1.6 m/s at 10 m) for 1106871 which was approximately one-third the wind speed for 1103871 (5.5 m/s) or 1104872 (4.7 m/s). However, the maximum values observed for Transects 2-5 were very close to those measured during the earlier tests. This may reflect the substantial difference between the wind speed observed at the release point (0.8 m/s at 2 m) and at the instrument tower (1.4 m/s at 2 m).

Whereas no significant concentration gradients were observed for Tests 1103871 and 1104872, at several locations the concentration values at the 8-m level for Test 1106871 were significantly higher than those at the lower measuring heights, especially on Transect 4. This may indicate that the plume had lifted off the ground due to the upward motion induced by thermal convection as observed in the laboratory by Deardorff and Willis (1976) and in the atmosphere during Project CONDORS.

As was discussed in Chapter 1 and demonstrated in Chapter 4, the effects of convection on the plume dispersion should become significant for values of the ratio of the boundary layer height to the Monin-Obukhov length, $h/-L \approx 10$. Values of h/-L computed from the values for L presented in Table 5.13 are given in Table 5.15.

Table 5.15. Values of the stability ratio h/-L based on Monin-Obukhov lengths given in Table 5.13.

METHOD:	Nieuwstadt/Boughton	Turner/Golder	Binkowski and Irwin
1103871	134	13	11
1104872	378	6	5
1106871	111	28	46

The values of h/-L computed using the "effective" L for simple terrain/simple meteorology from the Nieuwstadt-Boughton procedure are quite large, indicating that significant convective plume rise should be observed for all three tests. Values of the

ratio computed from the Monin-Obukhov length corresponding to the Turner stability classes are much smaller. However, substantial convective behavior would nevertheless be expected for Test 1106871, for which h/-L = 46. Some convective influence might also be anticipated for Tests 1103871 and 1104872.

In order to investigate the influence of convection on the smoke plumes, the 2-m concentration data from Tests 1103871, 1104872 and 1106871 were compared against predictions of ground level concentration produced by our stochastic model, described in Chapters 3 and 4, and by a generic Gaussian plume model given by Eq. (2.38). The Gaussian plume parameters σ_y and σ_z were determined from the measured values of U, σ_θ and σ_ϕ using Draxler's (1976) relations, Eq. (5.1-2). The only input to the stochastic model was the atmospheric stability as indicated by h/-L. Since the stochastic model assumes a simple terrain/simple meteorology situation, the values of h/-L using the effective Monin-Obukhov length from the fitting procedure were employed.

The stochastic model was started with 4000 particles. Once a particle had traveled sufficiently far downwind of the sampling locations that it no longer contributed to the concentration field, it was dropped from the simulation. This accelerated the simulation and reduced the computer time required to execute it. The simulation was complete when all particles had traveled beyond the sampling network.

Based on the analysis of the test data regarding the source and particle size distribution, both models treated the fog-oil smoke as a neutrally buoyant plume released from a continuous point source at an effective height of 2 m and at the local wind velocity. Both the stochastic and Gaussian models assumed a steady mean wind speed and direction; the stochastic model includes the variation of wind speed with elevation. Both models treated the ground as a reflective boundary, which is consistent with our findings that settling and deposition were not significant removal mechanisms.

The results of these comparisons are presented in Figs. 5.47-49 for each transect. The concentrations are presented in dimensionless form, normalized by the uniform concentration field which would result from a plane source of area h^2 extending vertically from the ground to the top of the boundary layer and laterally from -h/2 to h/2, releasing material at a rate Q with the mean wind speed U. The range of the axes in these figures was chosen to facilitate comparisons with the dimensional results presented earlier.

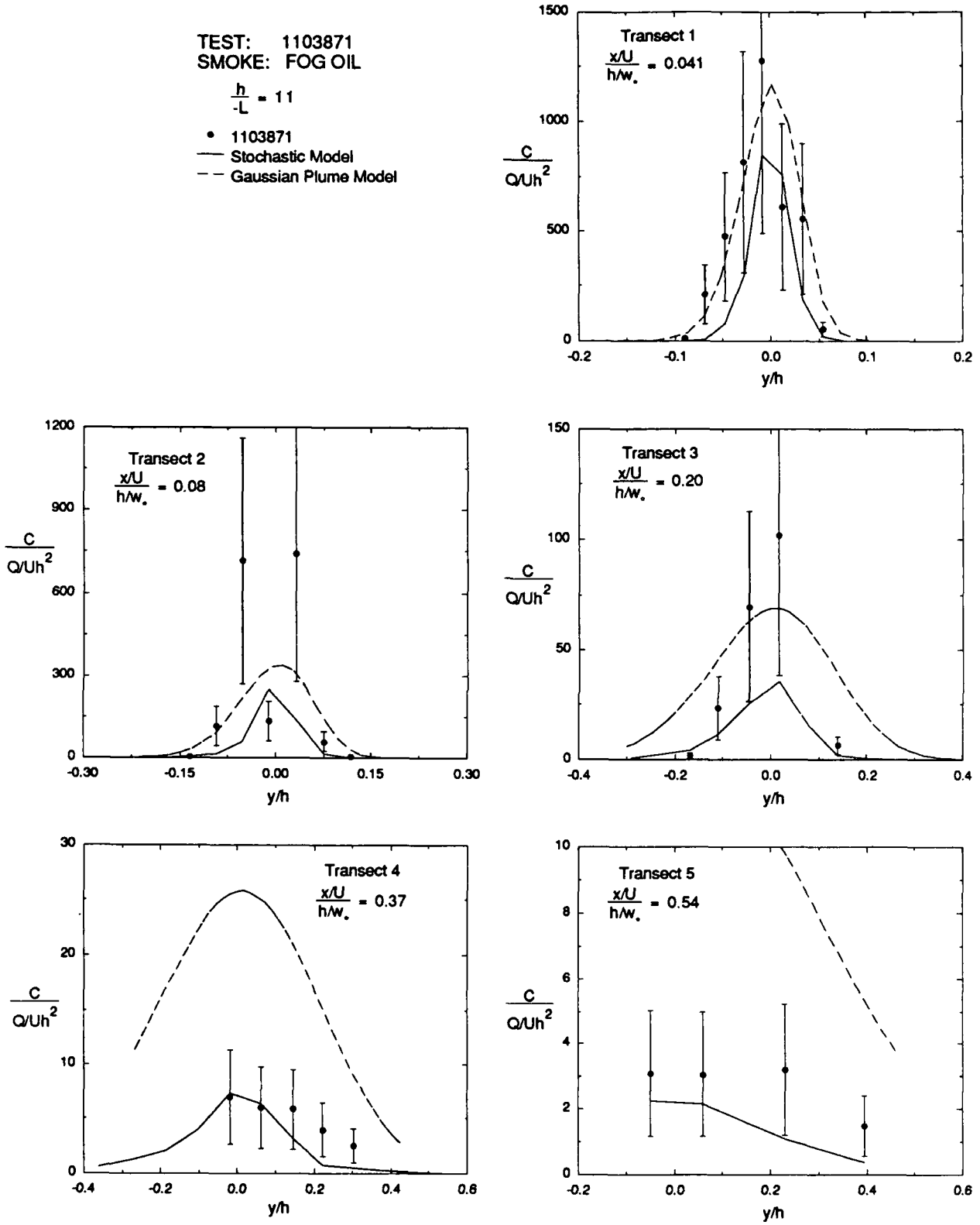

Figure 5.47 Comparison of field data from test 1103871 at the 2 m level with the predictions of the stochastic model (solid line) and the gaussian plume model (dashed line). The error bars indicate the 90% confidence limit for the data.

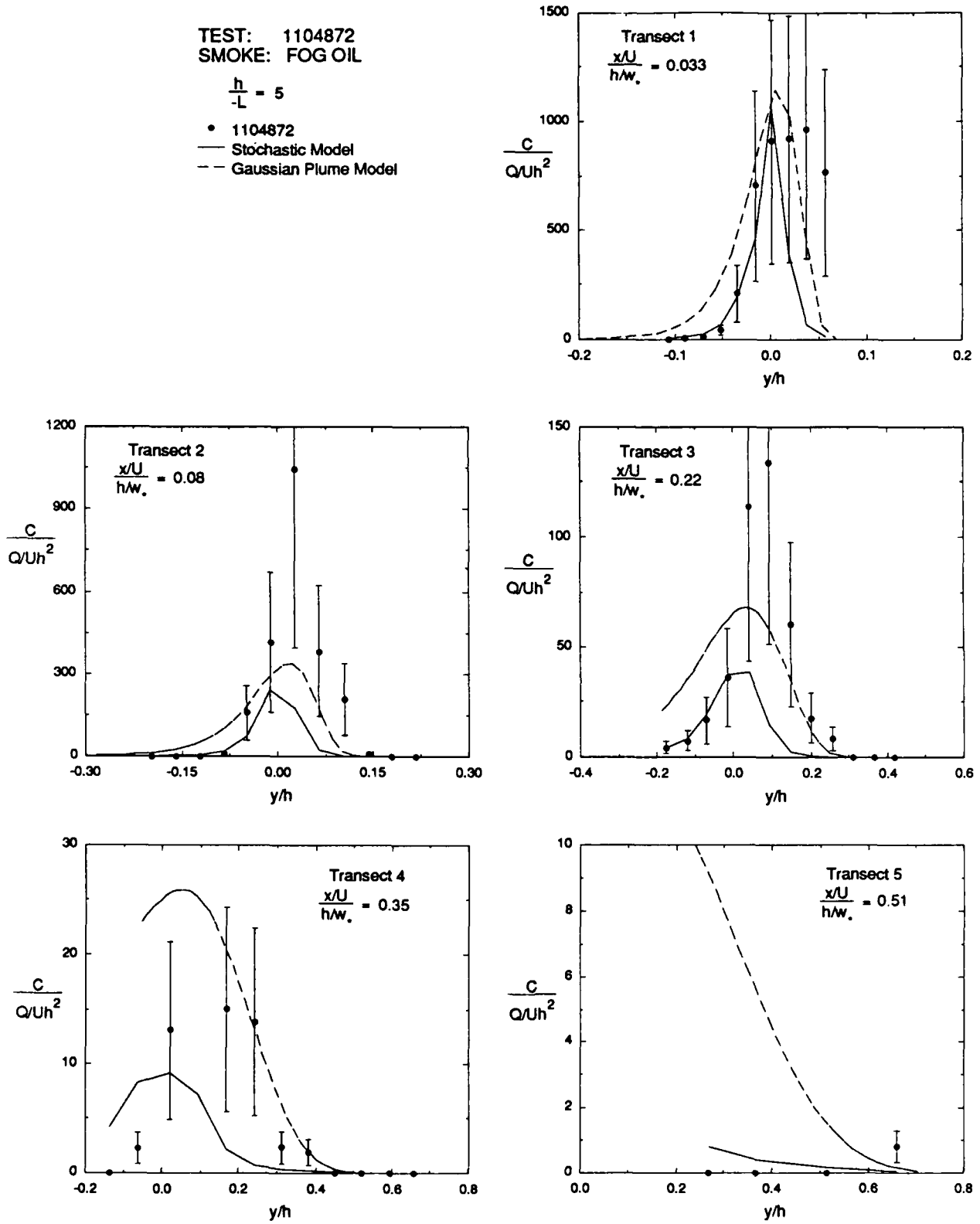

Figure 5.48 Comparison of field data from test 1104872 at the 2 m level with the predictions of the stochastic model (solid line) and the gaussian plume model (dashed line). The error bars indicate the 90% confidence limit for the data.

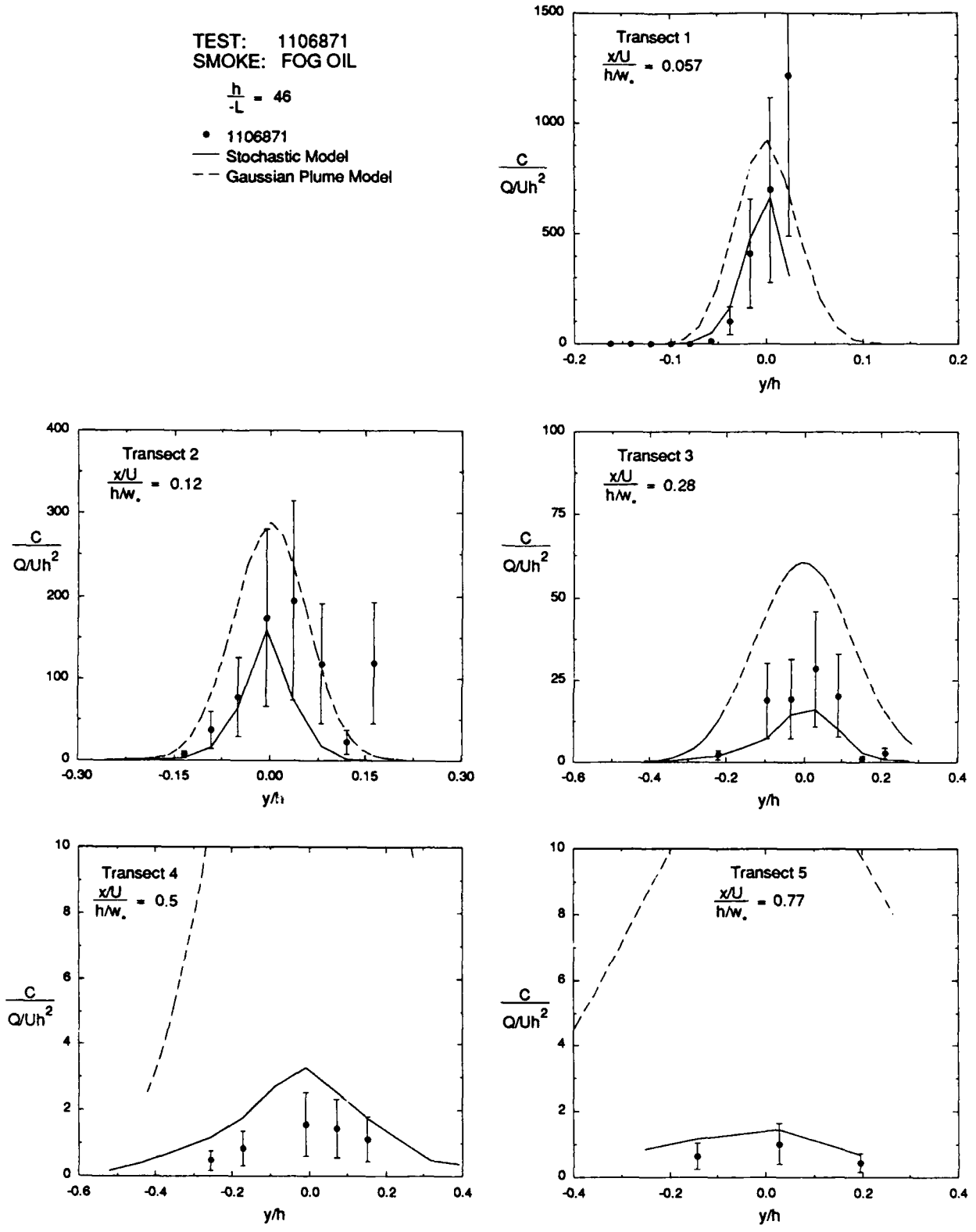

Figure 5.49 Comparison of field data from test 1106871 at the 2 m level with the predictions of the stochastic model (solid line) and the gaussian plume model (dashed line). The error bars indicate the 90% confidence limit for the data.

The comparison for Test 1103871 indicates that the maximum concentration and the lateral spreading predicted by both models are in satisfactory agreement with the data for Transect 1, given the level of uncertainty in the measurements. However, the data for Masts 6 and 8 on Transect 2 indicate a much greater maximum concentration than either model predicts, although the value for Mast 7 near the centerline is in approximate agreement with the model predictions. Both models indicate the approximately correct width for the second transect. At the third transect, both models still predict a lower maximum concentration than the data indicate but the width predicted by the stochastic model is much closer to the measured width. On the fourth and fifth transects, the reduction in ground-level concentration due to the convective lift-off of the plume are clearly evident. The stochastic model is able to correctly simulate this effect and its predicted concentration distributions are in good agreement with the data. The Gaussian plume model does not include the effects of convective rise and substantially overpredicts both the maximum concentration and the plume width.

Comparison of the model predictions with the results of Test 1104872 reveals strong similarities to Test 1103871. The maximum concentration on the first transect is predicted correctly by both models although the data indicate a greater width of spreading. On Transect 2, the data also show a slightly greater width but indicate a much greater maximum concentration as well (which is larger than the maximum concentration on Transect 1.) The third transect continues these trends: the data indicate a slightly greater width but a much greater maximum concentration than either model predicts. On Transect 4, the maximum concentration is still under-predicted by the stochastic model, but the Gaussian plume model now overpredicts substantially. The width predicted by the stochastic model is close to the spread exhibited by the data although the lateral position of the maximum concentration is slightly different. This difference may stem from local variations in the wind direction over the test site. By the time the smoke plume reached Transect 5, the effect of convection on the ground-level concentrations was significant, causing them to fall below the detection limit. The predictions of the Gaussian plume model are clearly incorrect whereas the stochastic model predicts very low values, in agreement with the test data.

One possible cause for the discrepancy between predictions and measurements near the release point may be due to the non-uniform wind field observed during these tests. All of the model predictions are based on the data gathered at the meteorological instrument tower located on Transect 4. However, the 2-m wind speed measured at the source position for Tests 1103871 and 1104872 was about half of

that measured at the 2-m level on the instrument tower; the lateral wind fluctuations, indicated by the standard deviation of the wind direction σ_θ, were approximately twice as great at the release point as at the instrument tower. (These differences may have resulted from the single row of low (8-m) trees immediately upwind of the baseline of the sampling network.) In general, a lower wind speed produces a proportionally higher maximum concentration at a given downwind distance whereas greater lateral wind fluctuations produce a greater lateral spreading. This behavior is consistent with the observed discrepancies between the models and the data at the first two transects.

At greater distances from the release point, the non-uniform upwind terrain was expected to enhance the effects of convection. The comparison of the results of Tests 1103871 and 1104872 with predictions of our stochastic model for large values of h/-L clearly supports this premise. The large discrepancy between the predictions of the Gaussian plume model and the data observed for Transects 4 and 5 indicates that the fog-oil plume had begun to rise significantly from the surface prior to reaching the fourth transect, in agreement with model predictions. Thus the effects of terrain on the dispersion have been demonstrated and effectively accounted for, albeit in an indirect manner.

During Test 1106871 much lower wind speeds were observed than for Tests 1103871 and 1104872. As a result, the complexities introduced by the non-uniform upwind terrain were reduced and the effects of convection were expected to be more pronounced than for the previous tests. A comparison of the results of the stochastic model with the data for Test 1106871 indicates strong agreement, especially regarding the convective lift-off of the plume. In addition, the values of the maximum concentration as well as the spreading of the plume predicted by the stochastic model for 1106871 also agree in general with the test results. However, the predictions of the Gaussian plume model worsen steadily with increasing downwind distance.

Because of the lower mean wind speed during Test 1106871, the dimensionless distances between the source and the transects were greater. As a result, the convective lift-off should have occurred closer to the release point. The data and the stochastic model both indicate that indeed this was the case: the qualitative and quantitative behavior of the models and data on Transects 3 and 4 for 1106871 are very similar to the trends and magnitudes observed on Transects 4 and 5 for the previous tests.

An additional perspective on the Atterbury-87 data and the stochastic model is provided by Figs. 5.50 and 5.51. These figures present comparisons of the Atterbury-87 data and the stochastic model predictions with the laboratory results of Deardorff

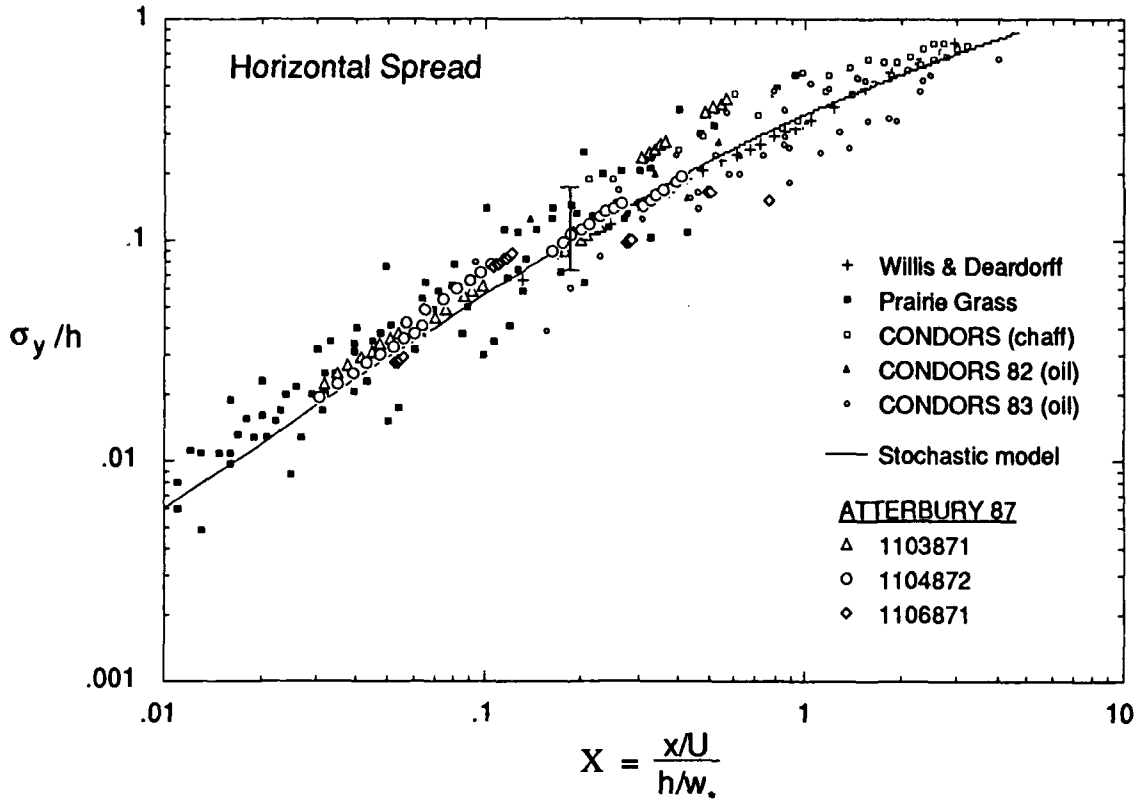

Figure 5.50 Dimensionless horizontal plume spread versus dimensionless travel time. Field data from our ATTERBURY 87 fog oil dispersion studies are compared with the results of our stochastic model as well as the water tank data of Willis & Deardorff (1975) and field data from Project Prairie Grass (Nieuwstadt, 1980) and Project CONDORS (Kaimal, et al., 1986). The error bar indicates the 90% confidence limits for the least-sqaures fit of the data to a gaussian form.

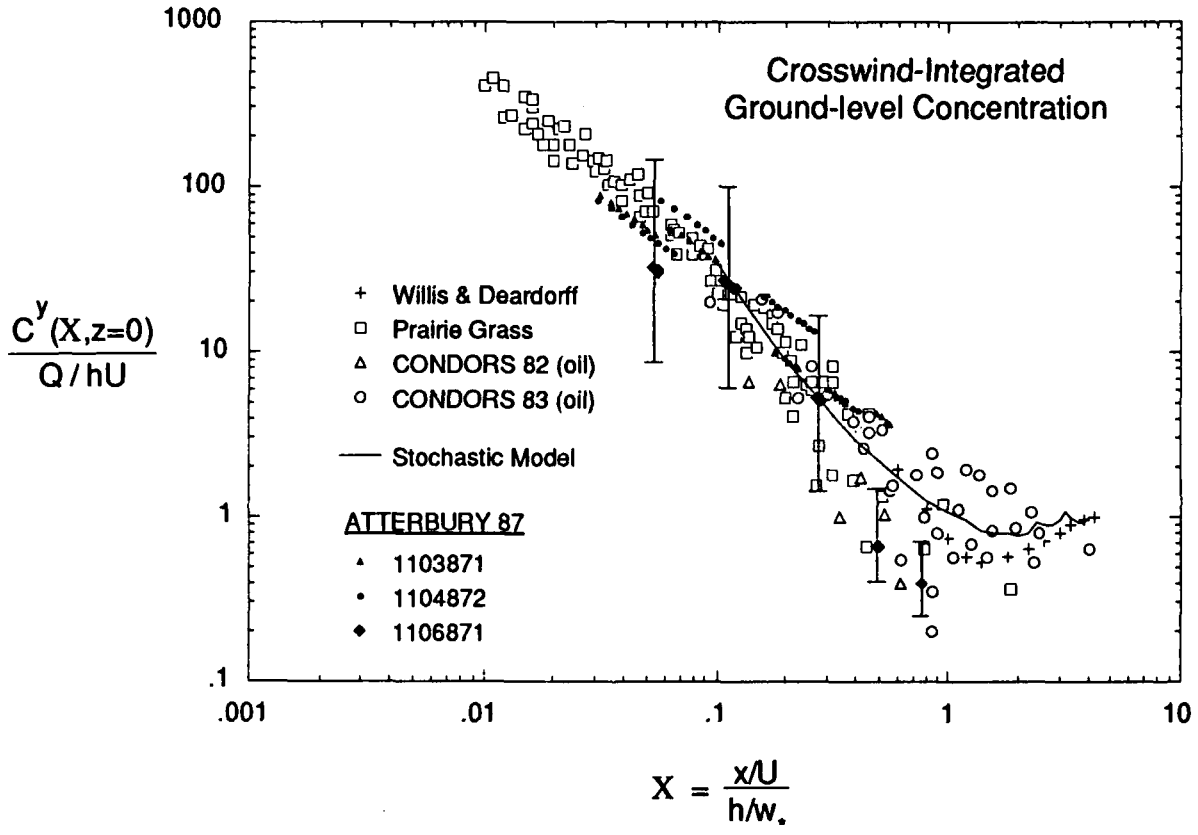

Figure 5.51 Dimensionless crosswind-integrated ground-level concentration versus dimensionless travel time. Field data from our ATTERBURY 87 fog oil dispersion studies are compared with the results of our stochastic model as well as the water tank data of Willis & Deardorff (1975) and field data from Project Prairie Grass (Nieuwstadt, 1980) and Project CONDORS (Kaimal, et al., 1986). The error bars indicate the 90% confidence limits for the least-sqaures fit of the data to a gaussian form; one error bar is shown for each transect.

and Willis (1975) and the field data collected during Project Prairie Grass (Nieuwstadt, 1980) and Project CONDORS (Kaimal et al., 1986).

Figure 5.50 shows the dimensionless lateral spread σ_y/h as a function of the dimensionless travel time X. The error bar indicates the 90% confidence interval for the least-squares fit of the Atterbury-87 data to the Gaussian profile used to compute σ_y. (The fitting procedure and error analysis is presented in Appendix E.) It is evident that the lateral spreading indicated by both the stochastic model and the Atterbury-87 data compare quite favorably with the results of other experiments.

A more severe comparison is provided in Fig. 5.51: dimensionless, crosswind-integrated ground-level concentrations predicted by the stochastic model and computed from the Atterbury-87 data are plotted along with the results of other studies. The error bars indicate the 90% confidence interval for the least-squares fit of the data to a Gaussian profile as described in Appendix E. The behavior of the stochastic model exhibits the same trends as the data, including the "dip" in the dimensionless concentration below unity at X = 1. This dip indicates the depressed surface concentration due to convective lift-off of the plume. The model does not indicate as strong a lift-off (i.e., as low a concentration) as Deardorff and Willis (1975) water tank experiments. This was also evident from other comparisons between the model and the water tank data presented in Chapter 4. However, the difference is not large, especially in comparison with the scatter in the atmospheric data. The "wiggles" which appear in the stochastic model predictions beyond X = 2 are due to the difficulty in accurately estimating ground-level concentrations when very few particles are near the surface.

The crosswind-integrated concentrations computed from the 2-m Atterbury-87 data show good agreement with the results of the other field studies. The concentrations for the fourth and fifth transect during Test 1106871 decline more quickly with distance than either the stochastic model or the water tank data indicate although they are within the scatter of the CONDORS data. This scatter reflects the difficulty in making accurate measurements of concentration at the part per billion level.

5.7 Summary

In this chapter we have presented the results of the Atterbury-87 field study of atmospheric dispersion. Four releases of fog oil smoke and five releases of HC smoke were carried out during the first two weeks in November, 1987 for atmospheric

conditions ranging from nearly neutral to moderately convective. Of the nine tests performed, eight yielded complete sets of data that will be useful for environmental assessment and model evaluation and improvement.

A thorough review of previous field studies indicated that in order to adequately describe atmospheric dispersion, data must be collected which define 1) the test site, 2) the source of the dispersing material, 3) the chemical and physical characteristics of the dispersing material, 4) the meteorological phenomena influencing the dispersion and 5) the evolution of the material plume as it moves downwind.

A discussion of the effects of terrain on local micrometeorology was followed by a description of the climatology and terrain of the test site. The Atterbury-87 test site was fairly flat, covered with 1-m tall grass, brush 1-2 m high and occasional low trees. However, the surrounding terrain rose as much as 50 m above the elevation of the site, and was densely wooded. This non-uniformity influenced the micrometeorology of the site and hence the dispersion as well. For this reason, the site was characterized as "simple terrain/complex meteorology."

The fog-oil smoke was produced by a single M3A4 smoke generator mounted in the bed of a pickup truck and released from a height of 1 m. The HC smoke was produced with 18 to 20 M5 30-lb smoke pots, generally stacked five high; the release height was thus 1.5 m. The smoke source was characterized in terms of the rate at which mass was released and the exit temperature. Measurements of the wind speed, direction, temperature and relative humidity at a height of 2 m were also carried out near the release point.

The effects of the initial jet issuing from the fog-oil smoke generator or the HC smoke pots on the plume trajectory were determined to be small, extending to a maximum height of 4 m above the release point and 25 m downwind. This conclusion is based on an analysis of the conditions at the smoke source in comparison with other experimental studies of buoyant jets in a crossflow and is confirmed by video and photographs of the plume near the source.

Measurements of the particle size distribution indicated that the fog-oil smoke is lognormally distributed. The fog-oil smoke had a mass mean diameter of 1.05 μm, a mass median (50%) diameter of 0.95 μm and a geometric standard deviation of 1.55; 98% of the fog oil smoke was between 0.3 and 3.0 μm. This is in agreement with the findings of a study by Katz et al. (1980) as well as with the results of our Dugway-85 study.

The particle size analysis for the HC smoke indicated that the particle size distribution might be bimodal, with one mode at less than 0.2 μm and the other at

about 1 μm, although the latter mode represents nearly all of the mass. The HC smoke had a mass mean diameter of 1.1 μm, a mass median diameter of 0.8 μm and a geometric standard deviation of 2.2; 98% of the HC smoke was between 0.25 and 4.0 μm. These results are in approximate agreement with the findings of Katz et al. (1980) for their only test of an actual M5 smoke pot. Our results do not agree with the mass mean diameter of 0.3 μm Katz et al. measured in a series of tests on "minipots" (12-70 g) conducted in an enclosed chamber at concentrations in the range 800 – 8000 mg/m^3. However, the conditions under which their minipot tests were performed were so different from those prevailing during our field studies involving actual M5 HC smoke pots, that differences in the results should not be surprising.

Meteorological measurements were performed at heights of 2, 4, 6 and 10 m using an instrument tower erected in the middle of the test site. Measurements included wind speed, wind azimuth, wind inclination, temperature and humidity. From these data, means, variances and power spectra were computed. Relevant length and velocity scales for the surface layer and mixed layer were determined. When appropriately scaled, the data showed good agreement with the results of extensive studies of atmospheric turbulence over flat terrain, although the complicating effects of the non-uniform terrain surrounding the Atterbury-87 test site were observed.

Time-averaged smoke concentrations were computed from the mass of smoke material collected on glass fiber filters. The measurements were carried out at 50 locations on five linear transects oriented perpendicular to the prevailing wind direction. The transects were positioned 50, 100, 250, 450 and 675 m from the release point. On the first four transects the filters were mounted at the 1, 2, 4 and 8-m levels; on the fifth transect only the 2-m and 8-m levels were used.

The maximum fog oil concentrations ranged from 30 – 75 mg/m^3 (30 – 75 ppm) on the first transect down to approximately 0.05 mg/m^3 (0.05 parts per million) on Transect 5. In general, the maximum concentration marking the centerline of the plume was observed in the data and the width of the plume was well-defined on each transect. This reflects favorably on the design and orientation of the sampling network but is also due to the use of existing meteorological data in a simple real-time dispersion model to choose the source location just prior to a test.

The results of the fog-oil tests were compared with the predictions of our stochastic model as well as a generic Gaussian plume model. The stochastic model showed good agreement with the test data, successfully predicting the dramatic reduction in ground-level concentration associated with the rising of the plume due to thermal convection. The Gaussian plume model does not predict this rise and, as a

result, substantially overpredicted the ground-level concentration at the fourth and fifth transects.

In addition, the effects of the non-uniform upwind terrain were found to be adequately described by an "effective" Monin-Obukhov length, determined by fitting the mean vertical profiles of wind speed and temperature to empirical expressions derived from data for uniformly flat terrain. The effect of the terrain was to produce large-scale, low-frequency motions similar to thermal convection and thus to influence the dispersion in the same manner as convection. Using the effective Monin-Obukhov length, the predictions of the stochastic model for uniformly flat terrain were shown to be in general agreement with the data.

Values for the lateral spread of the smoke plume and the crosswind-integrated concentration were determined from the test data and compared with the results of laboratory simulations of convective dispersion conducted by Deardorff and Willis as well as with field data from Project Prairie Grass and Project CONDORS. Within the uncertainty of the fitting procedure used to compute the spread and crosswind-integrated concentration, the Atterbury-87 fog oil data exhibited excellent agreement.

6. SUMMARY AND CONCLUSIONS

6.1 The Stochastic Model

The dispersion of airborne pollutants in the planetary boundary layer is heavily influenced by the surface heat flux. The diurnal variations in the heat flux significantly complicate the task of successfully modeling the dispersion phenomena. Previous approaches to the problem have largely ignored the affects of heat flux, treating the turbulent diffusion in a manner similar to molecular diffusion with an "eddy diffusivity" replacing the molecular diffusivity. These models predict that the centerline, defined by the maximum concentration, of a material plume will remain equal to the height at which it was released.

However, the large positive surface heat flux which occurs on clear sunny days produces strong thermal convection marked by narrow, swift updrafts ("thermals") and wide, slow downdrafts ("subsidence"). As a result, the turbulence and the turbulent diffusion in the vertical direction are highly inhomogeneous. Material plumes originating near ground-level are observed to remain near the surface due to the subsidence until, at a travel time x/U approximately equal to half the convective time scale h/w_*, the plume centerline begins to rise under the gathering influence of the rising thermals; the ground-level concentration declines accordingly. Under the influence of the subsidence, plumes originating from elevated sources rapidly travel to ground level whereupon they exhibit the same behavior as a surface release. Owing to the lack of success among existing modelling approaches to predict this behavior, we have developed a three-dimensional stochastic model in order to accurately predict the dispersion of material in the convective planetary boundary layer.

Our stochastic Monte Carlo model simulates the dispersion process by following the motions of a large number of "marked fluid particles" at discrete time intervals. The acceleration of each particle is modeled with the Langevin equation; thus, it is comprised of a deterministic component and a random component. The deterministic component accounts for the correlation of a particle's velocity with its previous value, which is characterized by the Lagrangian integral time scale. For the Langevin equation to be valid the particle acceleration must be linear in velocity, thus the simulation time step is chosen to be much smaller than the integral time scale of the velocity. By incorporating the observed variation in the local integral time scale of the

vertical velocity with elevation, our model is able to replicate the observed Lagrangian autocorrelation, becoming negative and exhibiting damped oscillations about zero.

The random component models the turbulent accelerations. At the large values of the Reynolds number which characterize atmospheric flows, the correlation time of the turbulent accelerations is much shorter than the simulation time step (on the order of the Kolmogorov time scale) and so they may be treated as a series of impulses. By integrating the acceleration over the time step, the turbulent velocity of the particle may be accurately modelled by a random process.

The probability density function for the velocity of the marked fluid particles is specified by its moments. Thomson (1984) has related these moments to the Eulerian velocity moments of the unmarked fluid by requiring that the joint, steady-state probability density function of the velocity and position of the marked fluid particles match that of the unmarked fluid. We use these relations to specify the first three moments of the each component of the particle velocity and thus accurately simulate the observed skewed distribution of the vertical velocity.

Using published expressions for the velocity moments and the Lagrangian integral scale in the convective boundary layer, we verified the predictions of our stochastic model against 1) limiting cases calculated from theory, 2) data from wind tunnel and water tank simulations of the convective boundary layer, 3) the predictions of other Monte Carlo models and 4) actual field data from Project Prairie Grass and Project CONDORS. For near-surface releases, our stochastic model predicted the convective rise of the plume centerline and the associated decrease in ground-level concentration exhibited by the test cases; the simulated elevated releases also showed the correct behavior.

The generally high level of quantitative agreement between these test cases and our model predictions is especially encouraging since the only values input to the model were $\zeta = h/-L$ (to specify the stability of the boundary layer) and the non-dimensional source height z_0/h. Here h is the height of the convective boundary layer as indicated by a temperature inversion, L is the Monin-Obukhov length and z_0 is the roughness height characterizing the surface. The efficacy of the convective scaling is evident in that the model is applicable over the range of unstable conditions encountered during the Atterbury-87 field study. Such predictions are beyond the capabilities of either the Gaussian plume or gradient-transfer models. For example, Deardorff and Willis (1975) calculated the crosswind-integrated eddy diffusion coefficient from their data for a near-surface release. They found that in much of their simulated boundary layer the eddy diffusion coefficient was negative. The success of

our stochastic model not only demonstrates its value for predicting convective dispersion but also indicates its potential for success in more complex situations.

6.2 The Atterbury-87 Dispersion Study

We designed and executed the Atterbury-87 field study of dispersion in the planetary boundary layer as part of a larger effort to acquire a database for the purposes of 1) assessing the environmental impact of military obscurant smokes deployed during training exercises, 2) evaluating existing dispersion models and 3) developing better predictive models of dispersion.

The test site was located in a grassy meadow in south-central Indiana. Because the topology and vegetation of the surrounding terrain were significantly different from that of the actual test site, the site was classified as "simple terrain/complex meteorology". Thus it was intermediate between the desert site of our Dugway-85 study ("simple terrain/simple meteorology") and the creek valley site of our Meadowbrook-87 study ("complex terrain/complex meteorology").

Four releases of fog-oil smoke and five releases of hexachloroethane (HC) smoke were conducted during which data were collected to describe 1) the smoke source, 2) the chemical and physical nature of the smoke, 3) the local micrometeorology and 4) the spatial distribution of the resulting smoke plume over the site.

Fog-oil smoke was generated using an M3A4 military smoke generator; HC smoke was produced using 30-lb M5 HC smoke pots. Neither the fog-oil nor the HC smoke plumes exhibited significant plume rise near the source despite the high temperatures at which they were released into the atmosphere.

The fog-oil smoke particles exhibited a lognormal size distribution whereas evidence suggesting a bimodal distribution of the HC smoke was observed. The mass mean and mass median diameters as well as the geometric standard deviation of the fog-oil measurements were in agreement with the findings of Katz, *et al.* (1980) as well as our own previous measurements. The bimodal nature of the HC distribution was confirmed by the measurements of Katz, *et al.* Whereas the mean and standard deviation statistics we computed for the HC smoke generally agreed with those reported by Katz, *et al.* for an actual M5 smoke pot, our results were at odds with their findings based on tests of 12-70 g "minipots." However, comparison of the minipot data with actual field results must be performed with due regard for the fact that the minipot tests were carried out in an enclosed chamber as well as at lower reaction

temperatures and at several orders of magnitude higher smoke concentrations than observed in the field.

Meteorological conditions were determined from measurements of the wind speed, wind azimuth (horizontal angle), wind inclination (vertical angle), temperature and humidity performed at four levels on a 10-m instrument tower. From these measurements, means and variances of the three components of wind velocity were computed in addition to vertical profiles of wind speed and temperature. The results were in general agreement with published results of atmospheric turbulence studies carried out for flat, uniform terrain although some deviations were noted. These were attributed to the more complex meteorological conditions expected for the Atterbury-87 test site due to the non-uniformity of the surrounding terrain.

Values of the relevant scaling parameters derived from the data as well as the Turner stability classes indicated that atmospheric conditions ranging from near-neutral to moderately convective prevailed during these tests. However, the Monin-Obukhov lengths determined by fitting the measured vertical profiles of mean wind speed and temperature to published expressions for the momentum and heat flux-profiles over flat, uniform terrain indicated a narrower range of more strongly convective conditions than did other stability indicators. These small Monin-Obukhov lengths were attributed to the relatively low-frequency motions resulting from the non-uniform upwind terrain which rose about 50 m above the mean elevation of the test site. Over uniformly flat terrain, such low-frequency motions are produced by convection alone and thus the fitting procedure indicated stronger convection than actually occurred. However, these "effective" Monin-Obukhov lengths proved useful in relating the data describing the complex meteorology of the Atterbury-87 site to empirical formulas based on data for simple meteorology and terrain.

Time-average concentrations of fog-oil smoke were measured at distances of 50, 100, 250, 450 and 675 m from the release point at levels of up to 8 m from the surface. The data clearly indicate a decrease of the maximum concentration and increase of the plume width with distance from the source. The design of the sampling network and choice of release location resulted in the complete resolution of the plume width for the second through fourth transects and a substantial resolution of the width on the first and fifth transects for each test.

Although a comparison of the data from different levels did not reveal discernable gradients in the near-surface concentrations, the level of uncertainty in the data prevents any definite conclusions being drawn in this regard.

In order to provide a "real-world" test of the stochastic model, as well as to examine the concentration data for the presence of convective plume rise, predictions of both the stochastic model and a generic Gaussian plume model were compared against the data. Good agreement was observed between the data and the stochastic model. In all cases the model-predicted decline in ground-level concentration associated with the convective rise of the plume centerline was observed in the data. The Gaussian plume model proved to be both qualitatively and quantitatively incorrect; it failed to predict the rising plume centerline and grossly over-predicted the ground level concentrations as a result. The results underscore the significant role of convection on the dispersion. Even for situations with relatively slight insolation, the interaction of the thermals and subsidence directly influence the turbulence and thus the ground-level concentrations as well.

The qualitative and quantitative agreement between the predictions of the stochastic model and the Atterbury-87 data is especially encouraging because of the complexity of the meteorology and the difficulty in determining the scaling parameters. It demonstrates the value of the stochastic approach to modelling dispersion in the convective boundary layer as well as the general validity of the Atterbury-87 results.

3.3 Recommendations for Future Work

Our work may be usefully extended in several areas. First, the model needs to be extended to include *horizontally* inhomogeneous situations, i.e., complex terrain. This would be extremely useful, since the ideal of simple terrain/simple meteorology represents one extreme of a continuous spectrum of terrain/meteorology interaction. In principle, the current stochastic model can accommodate such horizontal inhomogeneity if the horizontal variation in the velocity moments is supplied. According to Lorimer (1986) the kernal estimator can be readily extended to include the effects of variations in terrain. However, whereas most field studies provide meteorological measurements at several locations vertically, they only provide data for one horizontal location. For complex terrain, this is insufficient to adequately characterize the prevailing meteorology. During the Meadowbrook-87 study of complex terrain, measurements of the local wind speed, wind direction and temperature were carried out at a variety of locations in order to adequately describe the three-dimensional wind field.

Second, a simpler model based on the results of the stochastic simulations and capable of executing on a small, field-portable computer needs to be developed in

order to make our results available to air quality or health-effects professionals and others who require accurate predictions of dispersion. Such a model would depend on accurate estimates of the scaling parameters h, L and the convection velocity w_*, derived from local measurements of wind speed and temperature. However, the indirect estimation of the scaling lengths and velocities using present techniques designed for simple terrain/simple meteorology will prove more difficult and less accurate as the complexity of the terrain and meteorology under study are increased. The increasing uniqueness of the local conditions will render comparisons with empirical formulations derived for horizontally homogeneous terrain increasingly dubious. Improved methods for indirectly estimating these scaling lengths from local data need to be developed. In order to facilitate this development, direct estimates of the scaling parameters must be available. Therefore, fast response instrumentation (e.g., sonic anemometers) capable of providing direct measurements of the turbulent fluxes of momentum and heat should be included in future field studies, especially those for complex terrain, for the purpose of directly estimating the relevant scaling parameters. Such measurements were carried out during the Meadowbrook-87 study.

In addition to accurate estimates of the mean concentration, predictions of the peak concentration likely to occur during a specified time interval would prove extremely useful for hazard assessment purposes. Such predictions involve the phenomena of "relative diffusion" (Batchelor,1952) and require the simulation of the relative motion of pairs of particles in addition to their absolute motion. Although Durbin (1980) and Sawford (1982) have sought to extend the stochastic model to this task, verification of the model predictions is complicated by a lack of time-dependent concentration data as well as a clear theoretical framework in which to interpret the results. Recently, however, DeVaull and Dunn (1988) have made progress in both of these areas with one second-averaged concentration data collected during both the Atterbury-87 and Meadowbrook-87 field studies. Future field studies of dispersion would do well to include such continuous concentration measurements in their plans.

APPENDIX A

ERROR ANALYSIS OF PARTICLE SIZE DISTRIBUTION MEASUREMENTS

The error analysis of the particle size measurements is divided into two parts. The first part describes the errors in the statistical quantities: the mass mean diameter $\bar{d}$, the geometric mass mean diameter d_g (equal to the mass median diameter for a lognormal distribution) and the geometric standard deviation σ_g. The second part treats the errors in the cumulative distribution resulting in the error bars in Figs. 5.20-27.

Let $y_i = \ln d_i$ where d_i is the mid size of the i^{th} stage of the cascade impactor. The natural logarithm of the geometric mass mean and geometric standard deviation for the j^{th} member of the ensemble of particle size measurements performed during a test are determined as

$$\mu_j = \ln d_{g,j} = \frac{\sum_{i=1}^{S} m_{ij}\, y_i}{\sum_{i=1}^{S} m_{ij}} \tag{A.1}$$

and

$$\sigma_j^2 = (\ln \sigma_{g,j})^2 = \frac{\sum_{i=1}^{S} m_{ij}\,(y_i - \mu_j)^2}{\sum_{i=1}^{S} m_{ij}} = \frac{\sum_{i=1}^{S} m_{ij}\, y_i^2}{\sum_{i=1}^{S} m_{ij}} - \mu_i^2, \tag{A.2}$$

where, as in §5.3, m_{ij} is the mass collected on the i^{th} stage during the j^{th} measurement and S is the number of stages in the impactor. Let $m_j = \sum_{i=1}^{S} m_{ij}$ be the total mass collected during the j^{th} measurement and $M = \sum_{j=1}^{N} m_j = \sum_{j=1}^{N} \sum_{i=1}^{S} m_{ij}$ be the total mass collected during the test. Then

$$\langle \mu \rangle = \ln d_g = \frac{1}{M} \sum_{j=1}^{N} m_j \mu_j \tag{A.3}$$

and

$$\langle \sigma^2 \rangle = (\ln \sigma_g)^2 = \frac{1}{M} \sum_{j=1}^{N} m_j \sigma_j^2. \tag{A.4}$$

Clearly these are just mass-weighted ensemble averages over the N measurements. In order to determine the confidence limits on these quantities we must also know their sample variance. Thus, with the average mass collected per measurement given by $\langle m \rangle = M/N$,

$$s_\mu^2 = \frac{1}{N-1} \sum_{j=1}^{N} \frac{m_j}{\langle m \rangle} \left(\mu_j - \langle \mu \rangle\right)^2 = \frac{N}{N-1} \left[\frac{1}{M} \sum_{j=1}^{N} m_j \mu_j^2 - \langle \mu \rangle^2 \right] \tag{A.5}$$

$$s_\sigma^2 = \frac{1}{N-1} \sum_{j=1}^{N} \frac{m_j}{\langle m \rangle} \left(\sigma_j - \langle \sigma \rangle\right)^2 = \frac{N}{N-1} \left[\frac{1}{M} \sum_{j=1}^{N} m_j \sigma_j^2 - \langle \sigma \rangle^2 \right], \tag{A.6}$$

where $\sigma \equiv \sqrt{\sigma^2}$. Thus, assuming both μ_j and σ_j to be Gaussian random variables,

$$\ln d_g = \mu \pm \frac{s_\mu \, t_{n;\alpha/2}}{\sqrt{N}} \tag{A.7}$$

and

$$\ln \sigma_g = \sigma \pm \frac{s_\sigma \, t_{n;\alpha/2}}{\sqrt{N}}, \tag{A.8}$$

where $t_{n;\alpha/2}$ is the t-test value for n=N–1 degrees of freedom and α is the confidence limit. These value were obtained from Table A.4 in Bendat and Piersol, (1971), page 389. Exponentiating both sides of Eqs. (A.6-7) gives

$$d_g = \exp(\mu) \exp\left(\frac{s_\mu \, t_{n;\alpha/2}}{\sqrt{N}} \right)^{\pm 1} \tag{A.9}$$

and

$$\sigma_g = \exp(\sigma) \exp\left(\frac{s_\sigma \, t_{n;\alpha/2}}{\sqrt{N}} \right)^{\pm 1}. \tag{A.10}$$

This has been carried out for both the positive and negative exponent so that the results could be presented in the conventional form: $x = \langle x \rangle \pm \varepsilon$.

The error analysis for the mass mean diameter is similar to that given above but is somewhat simpler. The mass mean diameter is given by

$$\langle \bar{d} \rangle = \frac{1}{M} \sum_{j=1}^{N} m_j \bar{d}_j , \tag{A.11}$$

where $\bar{d}_j = \frac{1}{m_j} \sum_{i=1}^{S} m_{ij} d_i$ is the mass mean diameter computed for the j^{th} member of the ensemble of particle size measurements performed during a test. The sample variance is given by

$$s_{\bar{d}}^2 = \frac{N}{N-1} \left[\frac{1}{M} \sum_{j=1}^{N} m_j \bar{d}_j^2 - \langle \bar{d} \rangle^2 \right]. \tag{A.12}$$

Thus
$$\bar{d} = \langle \bar{d} \rangle \pm \frac{s_{\bar{d}} \, t_{n;\alpha/2}}{\sqrt{N}} \tag{A.13}$$

using the t-test values as determined above.

The error estimates for the cumulative distributions presented in Figs. 3.1-3 is based on a differential error analysis. Let the cumulative mass fraction for the j^{th} stage be denoted as F_j. Then

$$F_j = \sum_{i=1}^{j} f_i \equiv \sum_{i=1}^{j} \frac{m_i}{M} , \tag{A.14}$$

where m_i is the mass collected on the i^{th} stage, M is the total mass collected and S is the number of stages in the impactor. Clearly, $F_S = 1$. We seek the change in cumulative mass fraction for a given change in the mass collected on each stage:

$$\Delta F_j = \frac{\partial F_j}{\partial m_k} \Delta m_k , \tag{A.15}$$

where summation over repeated indices is implied. Our task is twofold; first we must determine $\frac{\partial F_j}{\partial m_k}$, and then Δm_k. Thus

$$\frac{\partial F_j}{\partial m_k} = \frac{1}{M}\frac{\partial}{\partial m_k}\sum_{i=1}^{j} m_i - \frac{1}{M^2}\sum_{i=1}^{j} m_i \cdot \frac{\partial}{\partial m_k}\sum_{i=1}^{S} m_i$$

$$= \frac{1}{M}\sum_{i=1}^{j}\frac{\partial m_i}{\partial m_k} - \frac{1}{M^2}\sum_{i=1}^{j} m_i \cdot \sum_{i=1}^{S}\frac{\partial m_i}{\partial m_k}. \qquad \text{(A.16)}$$

Since the mass collected on each stage is independent, $\partial m_i/\partial m_k = \delta_{ik}$. Substituting this into the previous equation yields

$$\frac{\partial F_j}{\partial m_k} = \frac{1}{M}\sum_{i=1}^{j}\delta_{ik} - \frac{1}{M^2}\sum_{i=1}^{j} m_i \cdot \sum_{i=1}^{S}\delta_{ik}. \qquad \text{(A.17)}$$

And so,
$$\Delta F_j = \frac{1}{M^2}\left[M\sum_{i=1}^{j}\delta_{ik}\Delta m_k - \sum_{i=1}^{j} m_i \cdot \sum_{i=1}^{S}\delta_{ik}\Delta m_k\right] \qquad \text{(A.18)}$$

or
$$\Delta F_j = \frac{1}{M^2}\left[M\sum_{i=1}^{j}\Delta m_i - \sum_{i=1}^{j} m_i \cdot \sum_{i=1}^{S}\Delta m_i\right]. \qquad \text{(A.19)}$$

The first term in the brackets accounts for the error in the cumulative mass for the j^{th} stage due to errors in the mass on stages 1 to j. The second term accounts for errors in the total mass collected due to errors in the mass on all S stages.

The error in the mass collected on each stage Δm_i has two sources: bias error due to the finite mass resolution of the instrument, $\Delta m_{instr,i}$, and random error due to a limited number of samples in the ensemble, $\sigma_{m,i}$:

$$\Delta m_i = \left((\Delta m_{instr,i})^2 + \sigma_{m,i}^2\right)^{1/2}. \qquad \text{(A.20)}$$

The sampling error is easily quantified:

$$\sigma^2_{m,i} = \frac{1}{N-1}\sum_{k=1}^{N}(m_{ik} - \langle m_i\rangle)^2 = \frac{1}{N-1}\sum_{k=1}^{N} m^2_{ik} - \frac{N}{N-1}\langle m_i\rangle^2, \qquad (A.21)$$

where

$$\langle m_i\rangle = \frac{1}{N}\sum_{k=1}^{N} m_{ik}\ , \qquad (A.22)$$

m_{ik} is the mass collected on the i^{th} stage during the k^{th} measurement and N is the number of measurements or samples in the ensemble. The mass resolution of the instrument is taken to be the amount of mass necessary to cause a 1 Hz frequency shift between the sensing and reference quartz crystals. These values are given for each stage in Table A.1.

Table A.1 Mass required to produce a 1 Hz frequency shift in PC-2 QCM cascade impactor.

STAGE	$\Delta m_{instr} \times 10^5$ (mg)
1	11.565
2	8.550
3	8.550
4	5.535
5	4.815
6	4.635
7	4.635
8	4.365
9	5.535
10	4.635

Thus assuming the random errors are normally distributed, the cumulative mass fraction can be specified with 95% confidence as

$$F_j \pm 1.96\,\Delta F_j \qquad (A.23)$$

where the value of the coefficient is determined from the normal distribution given in Table A.2 in Bendat and Piersol (1971), page 387.

Based this error analysis, an operational strategy can be devised which minimizes the total error. Since the mass resolution of the instrument is fixed, the only way to minimize the resolution error as a fraction of the mass collected on the stage is

to increase the mass collected. For a fixed volumetric flow rate (240 cm^3/min) and a given airborne concentration, this requires increasing the sampling time. However, once sufficient mass accumulates on the sensing crystal, its frequency change is no longer linearly proportional to the mass loading. At this point the instrument must be serviced before further measurements can be performed. With an upper limit on the total mass which may be collected on each stage, it is desirable to minimize the sampling time for each measurement in order to maximize the number of independent samples of the size distribution and thereby minimize the random error. Therefore the sampling time for each measurement should be chosen so as to collect the minimum amount of mass which will render a valid estimate of the size distribution (the manufacturer recommends a sampling time which will cause a 30 Hz frequency shift on the stage with the greatest loading) and a large number of measurements should be performed until the instrument response becomes non-linear. This was the strategy employed in measuring the size distribution of the oil fog.

APPENDIX B

THE DYNAMIC RESPONSE OF METEOROLOGICAL INSTRUMENTATION

The recommendations of the American Meteorological Society (Randerson, 1984) regarding instrumentation for boundary layer measurements is presented in Table B.1.

Table B.1 Recommended instrument capabilities for boundary layer measurements (Randerson, 1984).

Quantity	Height	Accuracy	Sampling Interval	Response
u, v, w	10 m	0.2 m/s	1-5 s	Distance Constant ≤ 5 m
θ, ϕ	10 m	5°A, 1°R	1-5 s	Distance Constant ≤ 5 m Damping Ratio ≥ 0.4
T	2, 10 m	1°A, 0.1°R	30 s	1 minute
z_i	–	50 m	–	–

These recommendations may be compared against the values for the instrumentation employed during the Atterbury-87 tests, presented in Table B.2.

Table B.2 Capabilities of instrumentation employed during Atterbury-87.

Quantity	Height	Accuracy	Sampling Interval	Response
u	2,4,6,10 m	0.2 m/s	1 s	Distance Constant = 2.7 m
θ	2,4,6,10 m	5°A, 0.1°R	1 s	Distance Constant = 0.70 m Damping Ratio = 0.51
ϕ	4,6,10 m	5°A, 0.1°R	1 s	Distance Constant = 0.69 m Damping Ratio = 0.53
T	2, 10 m	0.1°A, 0.1°R	1 s	10 s
z_i	–	–	–	–

In these tables, A denotes absolute accuracy and R denotes relative accuracy. The comparatively poor absolute accuracy of the azimuth and inclination measured with the bivanes and microvane is due to the difficulty in aligning the instrument, both horizontally (with a compass heading) and vertically (with a bullseye level).

The dynamic response of the instrumentation was calculated following the analysis of Mason and Moses (1984). The cup anemometer is modeled as a first order

system. Its dynamic response is completely specified by the distance constant L. The gain factor G is given by

$$G = \left[1 + (\omega\tau)^2\right]^{-1/2} = \left[1 + (2\pi L/\lambda)^2\right]^{-1/2}, \qquad \text{(B.1)}$$

where $\omega = 2\pi n$, the angular frequency;
$\tau = L/U$, the time constant;
L = the distance constant;
U = the mean wind speed;
$\lambda = U/n$, the wavelength.

The bivanes and the microvane are second order systems and require two parameters to describe their behavior: the (undamped) natural wavelength λ_n and the damping coefficient ζ. The gain factor is given by

$$G = \left\{4\zeta^2(\omega/\omega_n)^2 + \left[1-(\omega/\omega_n)^2\right]^2\right\}^{-1/2}$$

or

$$= \left\{4\zeta^2(\lambda_n/\lambda)^2 + \left[1-(\lambda_n/\lambda)^2\right]^2\right\}^{-1/2}, \qquad \text{(B.2)}$$

where $\omega = 2\pi n$, the angular frequency;
ω_n = undamped natural frequency;
ζ = the damping ratio;
$\lambda = 2\pi U/\omega$, the wavelength.

Although the distance constant is appropriate for first order systems such as the cup anemometers, it is not sufficient to describe the vanes. Nevertheless it is commonly used to compare these different types of sensors. To determine the distance constant for a vane, we use the following expression derived by Mason and Moses (1984) for the temporal response of the vane to an initial angular displacement θ_o. Note that time has been replaced by $t = x/U$.

$$\frac{\theta}{\theta_o} = \left(1-\zeta^2\right)^{-1/2} \exp\left[-\frac{2\pi\zeta x}{\lambda_n}\right] \cos\left[\frac{2\pi}{\lambda_n}\left(1-\zeta^2\right)^{1/2} x - \beta\right],$$

where

$$\beta = \tan^{-1}\left(\frac{\zeta}{\left(1-\zeta^2\right)^{1/2}}\right). \qquad \text{(B.3)}$$

The distance constant is determined iteratively from Eq. (B.3), which still contains both the natural wavelength and the damping ratio, by finding the distance x (≡L) such that $\frac{\theta}{\theta_o} = 1 - e^{-1}$.

The values of the threshold, distance constant, natural wavelength and damping ratio for the instrumentation used during Atterbury-87 are given in Table B.3.

Table B.3 Response specifications of Atterbury-87 wind instrumentation.

Instrument	Threshold (m/s)	Distance Constant (m)	Natural Wavelength (m)	Damping Ratio
Cup Anemometer	0.3	2.7	–	–
Microvane	0.4	0.7	4.2	0.51
Bivane	0.2	0.69	4.1	0.53
Wind Monitor-AQ:				
Propeller	0.3	1.2	–	–
Tail Vane	0.5	0.65	4.0	0.41

Based on Eqs. (B.1-2) and Table B.3, the dynamic response of the instrumentation to a sinusoidal input has been calculated and plotted for wind speeds of 2, 4 and 8 m/s. The response of the Wind Monitor-AQ used to to measure wind speed and direction at the source is presented in Fig. B.1. The response of the Cup Anemometer, Microvane and Bivane are presented in Fig. B.2.

In order to assess the impact of the instrument response on the data, one must consider the frequency range represented by the data. The upper bound must be the Nyquist or "folding" frequency, defined as $n_N = 1/(2\Delta t)$ where Δt is the sampling interval in seconds. Our data were collected at one second intervals so $n_N = 0.5$ Hz. The lower bound is determined by the length of the sampling record, which was about one hour. Thus the lowest resolvable frequency was about 3×10^{-4} Hz.

As Fig. B.1 indicates, the low speed response of the Wind Monitor propeller rolls off beginning at 0.1 Hz to approximately at 50% attenuation at 0.5 Hz upper limit. Because the peak of the horizontal variance spectra occurs at about 0.005 Hz, this response would not have a significant impact on the measured variances. At low speeds, the response of the Wind Monitor tail vane exhibits amplification beginning at 0.1 Hz and reaching a maximum of 30% at 0.5 Hz when the natural frequency is

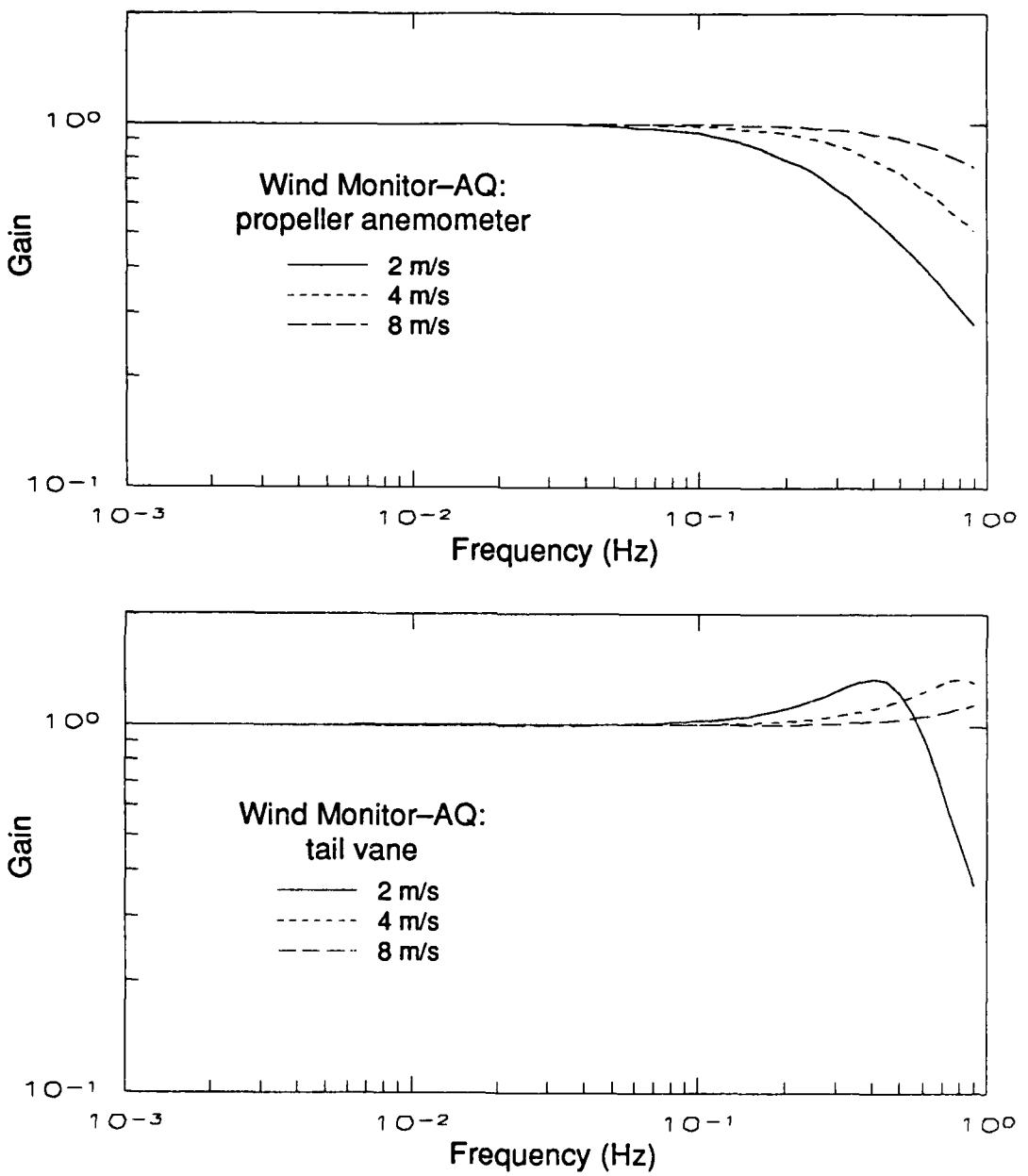

Figure B.1 Dynamic response of the Wind Monitor-AQ propeller and tail vane to a sinusoidal forcing.

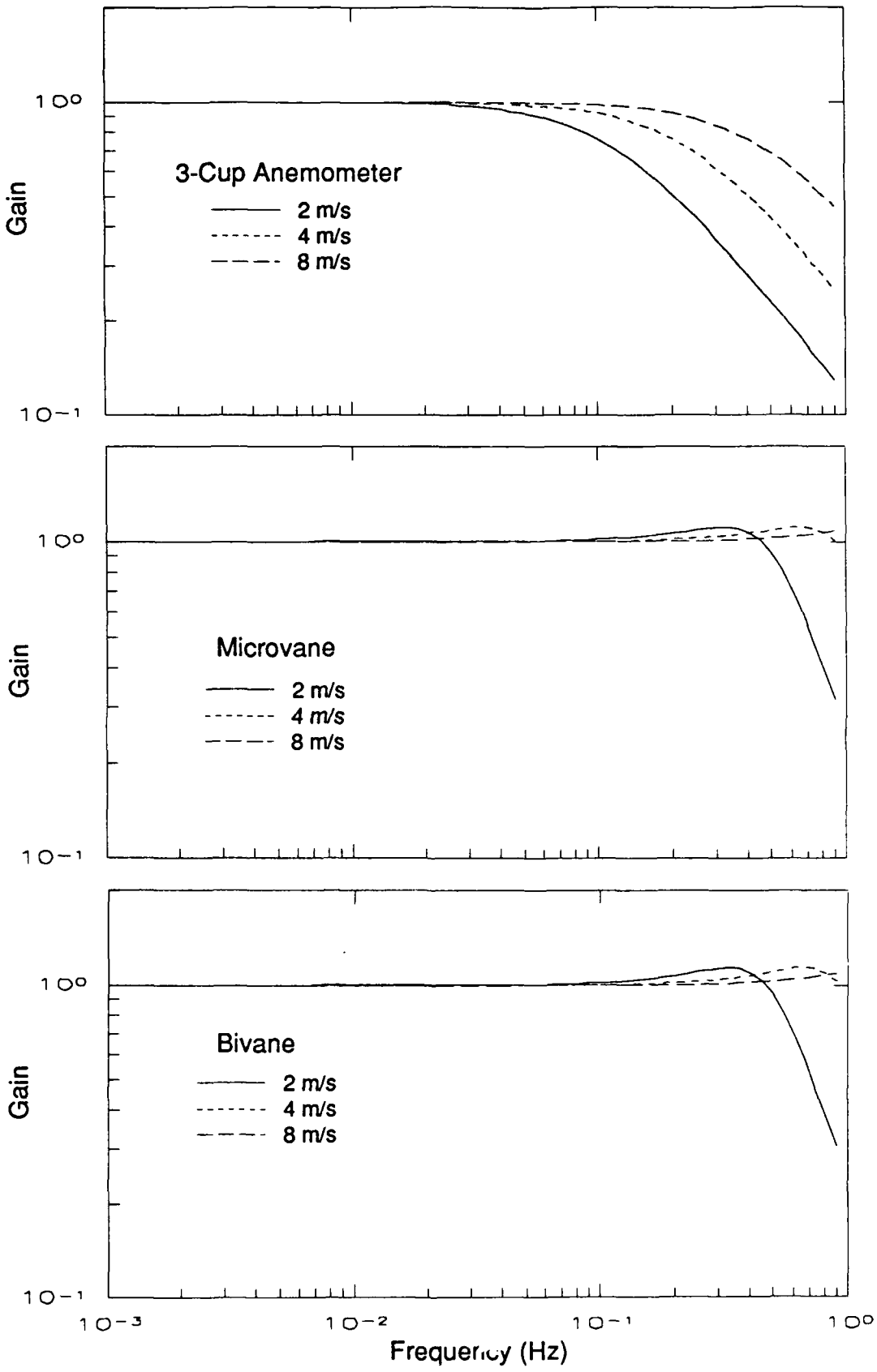

Figure B.2 Dynamic response of the 3-Cup Anemometer, Microvane and Bivane to a sinusoidal forcing.

reached. This is also has little effect on the measure values since the amplified frequencies contribute little to the variance.

The gain function for the Cup Anemometer, shown in Fig. B.2, begins to roll off at a lower frequency than the Wind Monitor propeller due to the greater mass of the cup wheel. Although the mean wind speed did not fall to 2 m/s for any of the Atterbury-87 tests, the effect of the attenuated response at frequencies above 0.1 Hz is apparent in the plots of the axial spectral data (Figs. 5.33-40).

The response of the Microvane and Bivane are very similar and quite flat over the range of interest. Therefore any effects on the data must be due entirely to the Cup response. Because the peak of the horizontal velocity spectra is much lower than the region of attenuated cup response, no corrections to the horizontal variances were necessary.

APPENDIX C

SUMMARY OF METEOROLOGICAL DATA

TEST: 1103871

QUANTITY	2 m	4 m	6 m	10 m
U (m/s)	4.56	5.07	5.36	5.75
$\bar{u}$ (m/s)	3.52	4.87	5.16	5.54
$\bar{\theta}$ (°)	†	233	238	239
$\bar{T}$ (°C)	23.14	22.34	22.20	22.73
$\overline{RH}$ (%)	43	–	–	–
σ_s (m/s)	1.26	1.36	1.41	1.48
σ_θ (°)	†	16.99	16.54	16.24
σ_ϕ (°)	–	8.17	8.48	8.80
σ_u (m/s)	2.19	1.39	1.45	1.52
σ_v (m/s)	2.29	1.38	1.42	1.49
σ_w (m/s)	–	0.69	0.92	0.94

SCALING PARAMETERS:

u_* (m/s)	0.61
L (m)	-63
w_* (m/s)	1.83
z_i (m)	668
z_o (cm)	20
power law exponent – U	0.143
power law exponent – $\bar{u}$	0.250

NOTES:
† Sensor malfunction.

TEST: 1104872

QUANTITY	2 m	4 m	6 m	10 m
U (m/s)	3.69	4.23	4.53	4.91
$\overline{u}$ (m/s)	3.46	3.99	4.30	4.66
$\overline{\theta}$ (°)	254	254	259	261
$\overline{T}$ (°C)	24.65	23.96	24.46	26.54
$\overline{RH}$ (%)	47	–	–	–
σ_s (m/s)	1.06	1.16	1.20	1.25
σ_θ (°)	20.53	19.43	18.51	18.59
σ_ϕ (°)	–	7.82	7.77	8.24
σ_u (m/s)	1.05	1.16	1.20	1.26
σ_v (m/s)	1.29	1.39	1.43	1.54
σ_w (m/s)	–	0.56	0.75	0.78

SCALING PARAMETERS:

u_* (m/s)	0.44
L (m)	-243
w_* (m/s)	1.00
z_i (m)	1135
z_o (cm)	20
power law exponent – U	0.176
power law exponent – $\overline{u}$	0.183

NOTES:

TEST: 1106871

QUANTITY	2 m	4 m	6 m	10 m
U (m/s)	1.63	1.75	1.80	1.88
$\bar{u}$ (m/s)	1.36	1.47	1.54	1.60
$\bar{\theta}$ (°)	228	232	237	240
$\bar{T}$ (°C)	8.01	7.17	7.48	7.12
$\overline{RH}$ (%)	40	–	–	–
σ_s (m/s)	0.56	0.58	0.57	0.57
σ_θ (°)	40.92	39.13	36.47	35.40
σ_ϕ (°)	–	11.68	12.89	14.92
σ_u (m/s)	0.70	0.70	0.68	0.70
σ_v (m/s)	0.81	0.86	0.87	0.90
σ_w (m/s)	–	0.33	0.44	0.49

SCALING PARAMETERS:

u_* (m/s)	0.26
L (m)	-12
w_* (m/s)	1.30
z_i (m)	557
z_o (cm)	20
power law exponent – U	0.087
power law exponent – $\bar{u}$	0.103

NOTES:

TEST: 1109871

QUANTITY	2 m	4 m	6 m	10 m
U (m/s)	3.59	3.99	4.18	4.43
$\overline{u}$ (m/s)	3.52	3.93	4.11	4.36
$\overline{\theta}$ (°)	30	26	27	25
$\overline{T}$ (°C)	6.02	5.28	5.23	5.34
$\overline{RH}$ (%)	76	–	–	–
σ_s (m/s)	0.93	1.00	1.00	1.01
σ_θ (°)	11.16	11.08	10.56	10.99
σ_ϕ (°)	–	6.36	6.92	7.97
σ_u (m/s)	0.93	1.00	1.00	1.03
σ_v (m/s)	0.70	0.72	0.75	0.80
σ_w (m/s)	–	0.47	0.65	0.75

SCALING PARAMETERS:

u_* (m/s)	0.51
L (m)	-46
w_* (m/s)	1.68
z_i (m)	649
z_o (cm)	20
power law exponent – U	0.129
power law exponent – $\overline{u}$	0.130

NOTES:

TEST: 1110871

QUANTITY	2 m	4 m	6 m	10 m
U (m/s)	5.89	6.55	6.83	7.26
$\bar{u}$ (m/s)	5.70	6.38	6.65	7.07
$\bar{\theta}$ (°)	32	34	34	34
$\bar{T}$ (°C)	3.41	2.54	2.62	2.46
$\overline{RH}$ (%)	65	–	–	–
σ_s (m/s)	1.56	1.62	1.65	1.74
σ_θ (°)	14.82	13.50	13.15	13.18
σ_ϕ (°)	–	7.50	8.38	9.29
σ_u (m/s)	1.54	1.61	1.63	1.74
σ_v (m/s)	1.51	1.53	1.56	1.63
σ_w (m/s)	–	0.89	1.22	1.41

SCALING PARAMETERS:

u_* (m/s)	0.72
L (m)	-110
w_* (m/s)	1.57
z_i (m)	448
z_o (cm)	20
power law exponent – U	0.127
power law exponent – $\bar{u}$	0.132

NOTES:

TEST: 1110872

QUANTITY	2 m	4 m	6 m	10 m
U (m/s)	4.30	4.75	4.99	5.33
$\overline{u}$ (m/s)	4.18	4.62	4.85	5.17
$\overline{\theta}$ (°)	11	25	26	24
$\overline{T}$ (°C)	3.39	2.65	2.68	2.69
$\overline{RH}$ (%)	49	–	–	–
σ_s (m/s)	1.08	1.12	1.15	1.23
σ_θ (°)	13.87	13.70	13.66	14.38
σ_ϕ (°)	–	6.92	7.52	8.33
σ_u (m/s)	1.06	1.12	1.16	1.28
σ_v (m/s)	1.05	1.11	1.14	1.22
σ_w (m/s)	–	0.61	0.82	0.93

SCALING PARAMETERS:

u_* (m/s)	0.57
L (m)	-68
w_* (m/s)	1.42
z_i (m)	434
z_o (cm)	20
power law exponent – U	0.132
power law exponent – $\overline{u}$	0.132

NOTES:

TEST: 1112871

QUANTITY	2 m	4 m	6 m	10 m
U (m/s)	4.22	4.60	4.81	5.08
$\bar{u}$ (m/s)	4.03	4.43	4.64	4.91
$\bar{\theta}$ (°)	206	220	225	226
$\bar{T}$ (°C)	13.24	12.29	12.52	12.48
$\overline{RH}$ (%)	38	–	–	–
σ_s (m/s)	1.18	1.27	1.31	1.33
σ_θ (°)	17.76	16.17	15.88	15.34
σ_ϕ (°)	–	8.29	8.82	9.78
σ_u (m/s)	1.18	1.26	1.30	1.32
σ_v (m/s)	1.25	1.27	1.30	1 34
σ_w (m/s)	–	0.64	0.89	0.94

SCALING PARAMETERS:

u_* (m/s)	0.54
L (m)	-63
w_* (m/s)	1.73
z_i (m)	816
z_o (cm)	20
power law exponent – U	0.115
power law exponent – $\bar{u}$	0.121

NOTES:

TEST: 1113871

QUANTITY	2 m	4 m	6 m	10 m
U (m/s)	3.59	4.00	4.20	4.46
$\bar{u}$ (m/s)	3.44	3.85	4.05	4.30
$\bar{\theta}$ (°)	220	234	239	241
$\bar{T}$ (°C)	12.45	11.54	11.78	11.71
$\overline{RH}$ (%)	48	–	–	–
σ_s (m/s)	0.96	1.04	1.05	1.07
σ_θ (°)	17.14	16.19	15.77	15.51
σ_ϕ (°)	–	8.34	8.77	9.87
σ_u (m/s)	0.96	1.04	1.06	1.08
σ_v (m/s)	1.04	1.09	1.11	1.15
σ_w (m/s)	–	0.57	0.77	0.83

SCALING PARAMETERS:

u_* (m/s)	0.49
L (m)	-53
w_* (m/s)	1.41
z_i (m)	500
z_o (cm)	20
power law exponent – U	0.132
power law exponent – $\bar{u}$	0.137

NOTES:

APPENDIX D

SUMMARY OF AVERAGE CONCENTRATION DATA FOR FOG OIL TESTS

In this appendix, the average fog oil concentration from tests 1103871, 1104871, 1104872 and 1106871 are tabulated. The first column, marked "T" indicates the transect number. The second column, marked "M" indicates the mast number on that transect, as given in Fig. 5.6. The third and fourth columns give the north and east coordinates of the mast position in meters with respect to the origin of the sampling network, indicated in Figs. 5.6 and 5.7. The elevation of each sampling location in meters above mean sea level is given in column five. Columns 6 - 9 give the average concentration in mg/m^3 obtained at each location for the four sampling heights. All samples which were below the detection threshold have been replaced by a value of zero.

TEST: 1103871

T	M	North (m)	East (m)	Elev. (m)	Average Concentration (mg/m^3) 1m	2m	4m	8m
1	1	-11.74	80.91	217.90	0.000e+00	0.000e+00	0.000e+00	0.000e+00
1	2	-1.72	70.60	217.80	0.522e-01	0.000e+00	0.710e-01	0.409e-01
1	3	8.56	60.21	218.00	0.592e+00	0.810e+00	0.256e+00	0.380e+00
1	4	18.79	50.09	218.20	0.391e+01	0.848e+01	0.110e+01	0.322e+01
1	5	28.84	39.81	218.00	0.105e+02	0.935e+01	0.757e+01	0.146e+02
1	6	39.40	29.12	217.50	0.215e+02	0.196e+02	0.154e+02	0.122e+02
1	7	49.40	19.26	217.30	0.145e+02	0.125e+02	0.140e+02	0.975e+01
1	8	59.25	9.23	217.00	0.906e+01	0.726e+01	0.961e+01	0.745e+01
1	9	69.73	-1.41	217.30	0.540e+01	0.326e+01	0.390e+01	0.237e+01
1	10	79.86	-11.48	217.70	0.161e+00	0.173e+00	0.309e+00	0.145e+00
2	1	-41.51	188.66	218.80	0.000e+00	0.000e+00	0.000e+00	0.000e+00
2	2	-21.26	166.70	218.30	0.000e+00	0.000e+00	0.000e+00	0.000e+00
2	3	-2.33	146.13	218.10	0.000e+00	0.000e+00	0.000e+00	0.000e+00
2	4	18.00	124.27	217.80	0.417e-01	0.480e-01	0.476e-01	0.363e-01
2	5	38.66	102.09	217.80	0.794e+00	0.900e+00	0.657e+00	0.916e+00
2	6	59.08	80.00	217.40	0.746e+01	0.114e+02	0.101e+02	0.552e+01
2	7	79.04	58.26	217.00	0.192e+01	0.207e+01	0.185e+01	0.125e+01
2	8	98.76	36.81	216.90	0.811e+01	0.110e+02	0.815e+01	0.751e+01
2	9	118.23	15.59	216.70	0.216e+01	0.178e+01	0.109e+01	0.143e+01
2	10	138.04	-5.82	216.50	0.698e-01	0.437e-01	0.000e+00	0.505e-01
2	11	157.94	-27.24	216.00	0.000e+00	0.000e+00	0.000e+00	0.000e+00
2	12	178.00	-48.97	215.90	0.000e+00	0.000e+00	0.000e+00	0.000e+00
3	1	0.34	348.20	222.50	0.000e+00	0.000e+00	0.000e+00	0.000e+00
3	2	31.28	317.25	221.20	0.000e+00	0.000e+00	0.000e+00	0.000e+00
3	3	61.53	287.01	220.20	0.000e+00	0.000e+00	0.000e+00	0.000e+00
3	4	91.82	256.71	221.10	0.000e+00	0.000e+00	0.000e+00	0.000e+00
3	5	122.60	225.94	221.70	0.167e+00	0.972e-01	0.195e+00	0.410e-01
3	6	153.63	194.91	221.20	0.103e+01	0.000e+00	0.950e+00	0.277e+00
3	7	183.99	164.54	220.80	0.169e+01	0.156e+01	0.138e+01	0.000e+00
3	8	215.13	133.40	220.60	0.131e+01	0.107e+01	0.956e+00	0.106e+01
3	9	246.44	102.10	219.30	0.412e+00	0.360e+00	0.330e+00	0.106e+00
3	10	276.73	71.80	218.20	0.404e-01	0.313e-01	0.345e-01	0.000e+00
3	11	306.66	41.87	215.70	0.000e+00	0.000e+00	0.000e+00	0.000e+00
3	12	337.14	11.39	215.00	0.000e+00	0.000e+00	0.000e+00	0.000e+00
4	1	74.65	543.58	227.30	0.000e+00	0.000e+00	0.000e+00	0.000e+00
4	2	113.90	507.57	225.10	0.000e+00	0.000e+00	0.000e+00	0.000e+00
4	3	154.51	466.39	221.50	0.000e+00	0.000e+00	0.000e+00	0.000e+00
4	4	194.30	427.28	219.50	0.000e+00	0.383e-01	0.000e+00	0.000e+00
4	5	235.05	388.29	219.20	0.000e+00	0.611e-01	0.305e-01	0.000e+00
4	6	275.46	349.29	219.70	0.000e+00	0.899e-01	0.725e-01	0.629e-01
4	7	316.45	308.66	221.10	0.000e+00	0.929e-01	0.108e+00	0.476e-01
4	8	357.69	267.32	219.90	0.137e+00	0.107e+00	0.873e-01	0.117e+00
4	9	398.79	225.88	218.30	0.125e+00	0.000e+00	0.592e-01	0.000e+00
4	10	439.98	184.07	216.30	0.340e-01	0.000e+00	0.000e+00	0.000e+00
4	11	485.52	137.42	215.40	0.000e+00	0.000e+00	0.000e+00	0.000e+00
4	12	526.27	95.19	216.20	0.000e+00	0.000e+00	0.000e+00	0.000e+00
5	1	335.56	620.69	216.00		0.228e-01		0.176e-01
5	2	419.59	537.61	217.30		0.494e-01		0.000e+00
5	3	503.65	453.75	215.60		0.471e-01		0.227e-01
5	4	558.50	398.49	215.30		0.474e-01		0.231e-01

TEST: 1104871

T	M	North (m)	East (m)	Elev. (m)	Average Concentration (mg/m^3) 1m	2m	4m	8m
1	1	-11.74	80.91	217.90	0.000e+00	0.000e+00	0.000e+00	0.000e+00
1	2	-1.72	70.60	217.80	0.000e+00	0.000e+00	0.000e+00	0.000e+00
1	3	8.56	60.21	218.00	0.000e+00	0.000e+00	0.000e+00	0.000e+00
1	4	18.79	50.09	218.20	0.118e+00	0.000e+00	0.791e-01	0.000e+00
1	5	28.84	39.81	218.00	0.464e+01	0.113e+02	0.117e+02	0.444e+01
1	6	39.40	29.12	217.50	0.210e+02	0.200e+02	0.170e+02	0.191e+02
1	7	49.40	19.26	217.30	0.211e+02	0.533e+02	0.198e+02	0.289e+02
1	8	59.25	9.23	217.00	0.209e+02	0.312e+02	0.159e+02	0.130e+02
1	9	69.73	-1.41	217.30	0.819e+01	0.723e+01	0.373e+01	0.311e+01
1	10	79.86	-11.48	217.70	0.531e+00	0.000e+00	0.000e+00	0.000e+00
2	1	-41.51	188.66	218.80	0.000e+00	0.000e+00	0.000e+00	0.000e+00
2	2	-21.26	166.70	218.30	0.000e+00	0.000e+00	0.000e+00	0.000e+00
2	3	-2.33	146.13	218.10	0.000e+00	0.000e+00	0.000e+00	0.000e+00
2	4	18.00	124.27	217.80	0.000e+00	0.000e+00	0.000e+00	0.000e+00
2	5	38.66	102.09	217.80	0.000e+00	0.000e+00	0.000e+00	0.000e+00
2	6	59.08	80.00	217.40	0.160e+01	0.343e+00	0.160e+01	0.191e+01
2	7	79.04	58.26	217.00	0.106e+02	0.000e+00	0.350e+01	0.875e+01
2	8	98.76	36.81	216.90	0.297e+01	0.000e+00	0.000e+00	0.000e+00
2	9	118.23	15.59	216.70	0.000e+00	0.000e+00	0.000e+00	0.134e+01
2	10	138.04	-5.82	216.50	0.508e+00	0.342e+00	0.261e+00	0.339e+00
2	11	157.94	-27.24	216.00	0.000e+00	0.000e+00	0.000e+00	0.000e+00
2	12	178.00	-48.97	215.90	0.000e+00	0.000e+00	0.000e+00	0.000e+00
3	1	0.34	348.20	222.50	0.000e+00	0.000e+00	0.000e+00	0.000e+00
3	2	31.28	317.25	221.20	0.000e+00	0.000e+00	0.000e+00	0.000e+00
3	3	61.53	287.01	220.20	0.000e+00	0.000e+00	0.000e+00	0.000e+00
3	4	91.82	256.71	221.10	0.000e+00	0.000e+00	0.000e+00	0.000e+00
3	5	122.60	225.94	221.70	0.000e+00	0.000e+00	0.000e+00	0.000e+00
3	6	153.63	194.91	221.20	0.595e-01	0.000e+00	0.864e-01	0.000e+00
3	7	183.99	164.54	220.80	0.931e-01	0.853e+00	0.860e+00	0.680e+00
3	8	215.13	133.40	220.60	0.241e+00	0.639e+00	0.367e+00	0.926e+00
3	9	246.44	102.10	219.30	0.000e+00	0.343e+00	0.397e+00	0.345e+00
3	10	276.73	71.80	218.20	0.000e+00	0.000e+00	0.000e+00	0.248e+00
3	11	306.66	41.87	215.70	0.000e+00	0.000e+00	0.000e+00	0.000e+00
3	12	337.14	11.39	215.00	0.000e+00	0.000e+00	0.000e+00	0.000e+00
4	1	74.65	543.58	227.30	0.000e+00	0.000e+00	0.000e+00	0.000e+00
4	2	113.90	507.57	225.10	0.000e+00	0.000e+00	0.000e+00	0.000e+00
4	3	154.51	466.39	221.50	0.000e+00	0.000e+00	0.000e+00	0.000e+00
4	4	194.30	427.28	219.50	0.000e+00	0.000e+00	0.000e+00	0.000e+00
4	5	235.05	388.29	219.20	0.000e+00	0.000e+00	0.000e+00	0.000e+00
4	6	275.46	349.29	219.70	0.000e+00	0.000e+00	0.000e+00	0.000e+00
4	7	316.45	308.66	221.10	0.183e+00	0.000e+00	0.712e-01	0.000e+00
4	8	357.69	267.32	219.90	0.000e+00	0.000e+00	0.000e+00	0.000e+00
4	9	398.79	225.88	218.30	0.253e+00	0.210e+00	0.126e+00	0.687e-01
4	10	439.98	184.07	216.30	0.191e+00	0.000e+00	0.000e+00	0.000e+00
4	11	485.52	137.42	215.40	0.000e+00	0.000e+00	0.000e+00	0.000e+00
4	12	526.27	95.19	216.20	0.000e+00	0.000e+00	0.000e+00	0.000e+00
5	1	335.56	620.69	216.00		0.612e-01		0.104e+00
5	2	419.59	537.61	217.30		0.000e+00		0.000e+00
5	3	503.65	453.75	215.60		0.000e+00		0.000e+00
5	4	558.50	398.49	215.30		0.783e-01		0.133e+00

TEST: 1104872

T	M	North (m)	East (m)	Elev. (m)	Average Concentration (mg/m^3) 1m	2m	4m	8m
1	1	-11.74	80.91	217.90	0.188e+02	0.172e+02	0.206e+02	0.145e+02
1	2	-1.72	70.60	217.80	0.209e+02	0.217e+02	0.189e+02	0.200e+02
1	3	8.56	60.21	218.00	0.188e+02	0.206e+02	0.185e+02	0.197e+02
1	4	18.79	50.09	218.20	0.152e+02	0.204e+02	0.195e+02	0.190e+02
1	5	28.84	39.81	218.00	0.130e+02	0.158e+02	0.891e+01	0.153e+02
1	6	39.40	29.12	217.50	0.343e+01	0.469e+01	0.489e+01	0.430e+01
1	7	49.40	19.26	217.30	0.111e+01	0.909e+00	0.911e+00	0.145e+00
1	8	59.25	9.23	217.00	0.259e+00	0.217e+00	0.155e+00	0.215e+00
1	9	69.73	-1.41	217.30	0.970e-01	0.920e-01	0.460e-01	0.830e-01
1	10	79.86	-11.48	217.70	0.530e-01	0.000e+00	0.000e+00	0.000e+00
2	1	-41.51	188.66	218.80	0.000e+00	0.000e+00	0.158e+00	0.000e+00
2	2	-21.26	166.70	218.30	0.000e+00	0.000e+00	0.000e+00	0.000e+00
2	3	-2.33	146.13	218.10	0.230e+00	0.182e+00	0.380e+00	0.373e+00
2	4	18.00	124.27	217.80	0.657e+01	0.467e+01	0.472e+01	0.379e+01
2	5	38.66	102.09	217.80	0.109e+02	0.859e+01	0.108e+02	0.105e+02
2	6	59.08	80.00	217.40	0.189e+02	0.235e+02	0.179e+02	0.154e+02
2	7	79.04	58.26	217.00	0.855e+01	0.926e+01	0.521e+01	0.731e+01
2	8	98.76	36.81	216.90	0.348e+01	0.353e+01	0.206e+01	0.278e+01
2	9	118.23	15.59	216.70	0.826e+00	0.189e+00	0.500e+00	0.546e+00
2	10	138.04	-5.82	216.50	0.170e+00	0.000e+00	0.830e-01	0.114e+00
2	11	157.94	-27.24	216.00	0.550e-01	0.000e+00	0.370e-01	0.000e+00
2	12	178.00	-48.97	215.90	0.000e+00	0.000e+00	0.000e+00	0.000e+00
3	1	0.34	348.20	222.50	0.000e+00	0.000e+00	0.410e-01	0.000e+00
3	2	31.28	317.25	221.20	0.000e+00	0.000e+00	0.410e-01	0.000e+00
3	3	61.53	287.01	220.20	0.000e+00	0.000e+00	0.000e+00	0.000e+00
3	4	91.82	256.71	221.10	0.202e+00	0.189e+00	0.182e+00	0.184e+00
3	5	122.60	225.94	221.70	0.459e+00	0.397e+00	0.424e+00	0.357e+00
3	6	153.63	194.91	221.20	0.129e+01	0.136e+01	0.107e+01	0.880e+00
3	7	183.99	164.54	220.80	0.284e+01	0.301e+01	0.206e+01	0.232e+01
3	8	215.13	133.40	220.60	0.259e+01	0.256e+01	0.194e+01	0.197e+01
3	9	246.44	102.10	219.30	0.949e+00	0.811e+00	0.811e+00	0.722e+00
3	10	276.73	71.80	218.20	0.427e+00	0.373e+00	0.474e+00	0.362e+00
3	11	306.66	41.87	215.70	0.225e+00	0.164e+00	0.174e+00	0.198e+00
3	12	337.14	11.39	215.00	0.890e-01	0.970e-01	0.720e-01	0.410e-01
4	1	74.65	543.58	227.30	0.000e+00	0.000e+00	0.000e+00	0.000e+00
4	2	113.90	507.57	225.10	0.000e+00	0.000e+00	0.000e+00	0.000e+00
4	3	154.51	466.39	221.50	0.000e+00	0.000e+00	0.000e+00	0.000e+00
4	4	194.30	427.28	219.50	0.000e+00	0.000e+00	0.000e+00	0.000e+00
4	5	235.05	388.29	219.20	0.000e+00	0.430e-01	0.000e+00	0.000e+00
4	6	275.46	349.29	219.70	0.710e-01	0.530e-01	0.540e-01	0.000e+00
4	7	316.45	308.66	221.10	0.281e+00	0.311e+00	0.590e-01	0.470e-01
4	8	357.69	267.32	219.90	0.262e+00	0.338e+00	0.213e+00	0.000e+00
4	9	398.79	225.88	218.30	0.240e+00	0.000e+00*	0.175e+00	0.000e+00
4	10	439.98	184.07	216.30	0.241e+00	0.294e+00	0.186e+00	0.000e+00
4	11	485.52	137.42	215.40	0.400e-01	0.520e-01	0.380e-01	0.000e+00
4	12	526.27	95.19	216.20	0.000e+00	0.000e+00	0.000e+00	0.000e+00
5	1	335.56	620.69	216.00		0.180e-01		0.000e+00
5	2	419.59	537.61	217.30		0.000e+00		0.000e+00
5	3	503.65	453.75	215.60		0.000e+00		0.000e+00
5	4	558.50	398.49	215.30		0.000e+00		0.740e-01

*Chromatography system crashed; data lost.

TEST: 1106871

T	M	North (m)	East (m)	Elev. (m)	Average Concentration (mg/m^3) 1m	2m	4m	8m
1	1	-11.74	80.91	217.90	0.199e+02	0.643e+02	0.755e+02	0.355e+02
1	2	-1.72	70.60	217.80	0.159e+02	0.369e+02	0.305e+02	0.653e+02
1	3	8.56	60.21	218.00	0.162e+02	0.216e+02	0.245e+02	0.258e+02
1	4	18.79	50.09	218.20	0.632e+01	0.550e+01	0.552e+01	0.307e+01
1	5	28.84	39.81	218.00	0.772e+00	0.577e+00	0.101e+01	0.159e+01
1	6	39.40	29.12	217.50	0.175e+00	0.141e+00	0.215e+00	0.131e+00
1	7	49.40	19.26	217.30	0.569e-01	0.120e+00	0.745e-01	0.239e-01
1	8	59.25	9.23	217.00	0.000e+00	0.000e+00	0.000e+00	0.000e+00
1	9	69.73	-1.41	217.30	0.452e-01	0.000e+00	0.000e+00	0.000e+00
1	10	79.86	-11.48	217.70	0.000e+00	0.000e+00	0.000e+00	0.000e+00
2	1	-41.51	188.66	218.80	0.558e+01	0.626e+01	0.970e+00	0.849e+00
2	2	-21.26	166.70	218.30	0.105e+01	0.122e+01	0.513e+01	0.586e+01
2	3	-2.33	146.13	218.10	0.502e+01	0.620e+01	0.587e+01	0.947e+01
2	4	18.00	124.27	217.80	0.136e+02	0.103e+02	0.112e+02	0.233e+02
2	5	38.66	102.09	217.80	0.964e+01	0.914e+01	0.995e+01	0.109e+02
2	6	59.08	80.00	217.40	0.402e+01	0.410e+01	0.477e+01	0.440e+01
2	7	79.04	58.26	217.00	0.153e+01	0.194e+01	0.151e+01	0.144e+01
2	8	98.76	36.81	216.90	0.274e+00	0.386e+00	0.212e+00	0.216e+00
2	9	118.23	15.59	216.70	0.000e+00	0.000e+00	0.000e+00	0.000e+00
2	10	138.04	-5.82	216.50	0.000e+00	0.000e+00	0.000e+00	0.000e+00
2	11	157.94	-27.24	216.00	0.000e+00	0.000e+00	0.000e+00	0.000e+00
2	12	178.00	-48.97	215.90	0.000e+00	0.000e+00	0.000e+00	0.000e+00
3	1	0.34	348.20	222.50	0.000e+00	0.000e+00	0.295e-01	0.473e-01
3	2	31.28	317.25	221.20	0.136e+00	0.140e+00	0.734e-01	0.204e+00
3	3	61.53	287.01	220.20	0.204e+00	0.678e-01	0.299e-01	0.363e+00
3	4	91.82	256.71	221.10	0.990e+00	0.107e+01	0.364e+00	0.118e+01
3	5	122.60	225.94	221.70	0.204e+01	0.150e+01	0.170e+00	0.163e+01
3	6	153.63	194.91	221.20	0.151e+01	0.103e+01	0.184e+01	0.180e+01
3	7	183.99	164.54	220.80	0.794e+00	0.987e+00	0.912e+00	0.107e+01
3	8	215.13	133.40	220.60	0.101e+00	0.000e+00	0.439e-01	0.249e+00
3	9	246.44	102.10	219.30	0.871e-01	0.123e+00	0.119e+00	0.000e+00
3	10	276.73	71.80	218.20	0.000e+00	0.000e+00	0.000e+00	0.000e+00
3	11	306.66	41.87	215.70	0.000e+00	0.000e+00	0.000e+00	0.000e+00
3	12	337.14	11.39	215.00	0.000e+00	0.000e+00	0.000e+00	0.000e+00
4	1	74.65	543.58	227.30	0.000e+00	0.000e+00	0.000e+00	0.000e+00
4	2	113.90	507.57	225.10	0.000e+00	0.000e+00	0.000e+00	0.000e+00
4	3	154.51	466.39	221.50	0.000e+00	0.000e+00	0.000e+00	0.000e+00
4	4	194.30	427.28	219.50	0.000e+00	0.592e-01	0.000e+00	0.154e+00
4	5	235.05	388.29	219.20	0.284e-01	0.759e-01	0.000e+00	0.000e+00
4	6	275.46	349.29	219.70	0.385e-01	0.825e-01	0.602e-01	0.875e+00
4	7	316.45	308.66	221.10	0.129e+00	0.000e+00	0.000e+00	0.273e+00
4	8	357.69	267.32	219.90	0.000e+00	0.440e-01	0.835e-01	0.905e-01
4	9	398.79	225.88	218.30	0.000e+00	0.248e-01	0.000e+00	0.791e-01
4	10	439.98	184.07	216.30	0.000e+00	0.000e+00	0.000e+00	0.000e+00
4	11	485.52	137.42	215.40	0.000e+00	0.000e+00	0.000e+00	0.000e+00
4	12	526.27	95.19	216.20	0.000e+00	0.000e+00	0.000e+00	0.000e+00
5	1	335.56	620.69	216.00		0.238e-01		0.496e-01
5	2	419.59	537.61	217.30		0.538e-01		0.000e+00
5	3	503.65	453.75	215.60		0.343e-01		0.156e-01
5	4	558.50	398.49	215.30		0.000e+00		0.000e+00

APPENDIX E

FITTING A GAUSSIAN PROFILE TO DATA BY THE METHOD OF LEAST-SQUARES

We seek to fit the concentration data to a Gaussian function representing the ground-level concentration due to a continuous point source:

$$C(x,y) = \frac{Q}{\pi U \sigma_y \sigma_z} \exp\left[-\frac{y^2}{2\sigma_y^2}\right]. \tag{E.1}$$

We are close enough to the source that the growth of the plume is proportional to the downwind distance x; thus, let $\sigma_y = ax$ and $\sigma_z = bx$ and substitute back into Eq. (E.1):

$$C(x,y) = \frac{A}{x^2} \exp\left[-\frac{y^2}{Bx^2}\right], \tag{E.2}$$

where $A = \frac{Q}{\pi U a b}$ and $B = 2a^2$. Take the natural logarithm of both sides of Eq. (E.2):

$$\ln C = \ln A - \ln x^2 - \frac{1}{B}\frac{y^2}{x^2}. \tag{E.3}$$

Let $\eta = \ln C + \ln x^2$, $\alpha = \ln A$, $\beta = -\frac{1}{B}$ and $\xi = (y/x)^2$, then Eq. (E.3) becomes the simple linear expression

$$\eta = \alpha + \beta\xi. \tag{E.4}$$

Because the uncertainty in the concentration ΔC is not a constant, but rather is a constant *fraction* of the concentration (i.e., $\Delta C/C$ = constant), no weighting needs to be applied to the linearized equation in order to achieve the best fit in the least-squares sense. To see this, note that the uncertainty in the logarithm of the concentration is $\Delta \ln C = \Delta C/C$ = constant. Thus all transformed data have equal uncertainties and no weighting is needed. A simple linear least-squares method may therefore be used to compute α and β.

Once the coefficients α and β have been determined, we can solve for A and a:

$$A = \exp(\alpha) \tag{E.5}$$

and

$$a = \left(\frac{-1}{2\beta}\right)^{1/2}; \tag{E.6}$$

thus the centerline concentration $C(x,0) = \frac{A}{x^2}$ and the spread $\sigma_y = ax$. The crosswind-integrated concentration $C^y(x)$ is determined from these according to the expression

$$C^y(x) = \int_{-\infty}^{\infty} C(x,y)\, dy = \int_{-\infty}^{\infty} C(x,0)\, \exp\left[-\frac{y^2}{2\sigma_y^2}\right] dy = \sqrt{2\pi}\,\sigma_y\, C(x,0) = \sqrt{2\pi}\,\frac{aA}{x}. \tag{E.7}$$

In order to estimate the uncertainty in C^y and σ_y, we must first estimate the uncertainty in the fitting coefficients α and β, denoted as $\Delta\alpha$ and $\Delta\beta$, respectively. These may be computed from the results of the least-squares fitting procedure using Eqs. (4.69-72) from Bendat and Piersol (1971, page 131). The uncertainty in the centerline concentration is equal to the uncertainty in A:

$$A = \exp(\alpha \pm \Delta\alpha) = \exp(\alpha)\, \exp(\pm \Delta\alpha). \tag{E.8}$$

Thus the uncertainty in C(x,0) is given by the factor $\exp(\pm \Delta\alpha)$. The expression for the uncertainty in a (and therefore in σ_y) is more complex:

$$a = \sqrt{B/2} = \left(-\frac{1}{2}\,\frac{1}{\beta \pm \Delta\beta}\right)^{1/2} = \left(-\frac{1}{2}\,\frac{1/\beta}{1 \pm \Delta\beta/\beta}\right)^{1/2} = \left(\frac{-1}{2\beta}\right)^{1/2}\left(\frac{1}{1 \pm \Delta\beta/\beta}\right)^{1/2}. \tag{E.9}$$

The uncertainty in σ_y is given by the factor $\left(\frac{1}{1 \pm \Delta\beta/\beta}\right)^{1/2}$. The uncertainty in C^y is thus the product of the uncertainties in a and A (i.e., the uncertainties in C(x,0) and σ_y):

$$\exp(\pm \Delta\alpha)\left(\frac{1}{1 \pm \Delta\beta/\beta}\right)^{1/2}. \tag{E.10}$$

REFERENCES

Adrian, R. J., R. T. D. S. Ferreira and T. Boberg, 1986: "Turbulent Thermal Convection in Wide Horizontal Fluid Layers," Experiments in Fluids, 4, 121-141.

American Conference of Governmental Industrial Hygienists, 1966: "Industrial Ventilation – A Manual of Recommended Practice," Committee on Industrial Ventilation, Lansing, MI.

American Petroleum Institute, 1958: "Selected Values of Properties of Hydrocarbons and Related Compounds," Project 44, Chemical and Petroleum Research Laboratory, Carnegie Institute of Technology, Pittsburgh, PA.

Angell, J. K., 1964: "Measurements of Lagrangian and Eulerian Properties of Turbulence at a Height of 2,500 ft.," Quart. J. Roy. Met. Soc., 90, 57-51.

Angell, J. K., D. H. Pack, W. H. Hoecker and N. Delver, 1970: "Lagrangian-Eulerian Time-Scale Ratios Estimated from Constant Volume Balloon Flights Past a Tall Tower," Quart. J. Roy. Met. Soc., 97, 87-92.

Baerentsen, J. H. and R. Berkowicz, 1984: "Monte Carlo Simulation of Plume Dispersion in the Convective Boundary Layer," Atmos. Envir., 18, 701-712.

Barad, M. L., 1956: "Project Prairie Grass: A Field Program in Diffusion," Volumes 1 and 2, Geophs. Res. Papers No. 59, Air Force Cambridge Research Center, AD-152572 and AD-152573.

Barr, S. and W. E. Clements, 1984: "Diffusion Modelling: Principles of Application," Atmospheric Science and Power Production, Randerson, D. (ed.), U S Dept. of Commerce, DOE/TIC-27601 (DE84005177), 584-619.

Batchelor, G. K., 1950: "The Application of the Similarity Theory of Turbulence to Atmospheric Diffusion," Quart. J. Roy. Met. Soc., 76, 133-146.

Batchelor, G. K., 1952: "Diffusion in a Field of Homogeneous Turbulence II: The Relative Motion of Particles," Proc. Phil. Soc., Cambridge, 48, 345-362.

Belyaev, S. P. and L. M. Levin, 1974: "Techniques for Collection of Representative Aerosol Samples," J. Aerosol Sci., 5, 325-338.

Bendat, J. S. and A. G. Piersol, 1971: Random Data: Analysis and Measurement Procedures, John Wiley and Sons, New York.

Benkley, C. W. and L. L. Schulman, 1979: "Estimating Hourly Mixing Depths from Historical Data," J. Appl. Met., 18, 772-780.

Berkowicz, R. and L. P. Prahm, 1979a: "Generalization of K-Theory for Turbulent Diffusion, Part I: Spectral Turbulent Diffusivity Concept," J. Appl. Meteorol., 18, 266-272.

Berkowicz, R. and L. P. Prahm, 1980: "On the Spectral Turbulent Diffusivity Theory for Homogeneous Turbulence," J. Fluid Mech., 100, 433-448.

Boughton, B. A., 1983: "Turbulent Atmospheric Transport and Deposition of Particles with Settling and Evaporation", Ph.D. Thesis, University of Illinois, Urbana, IL.

Boughton, B. A., J. M. DeLaurentis and W. E. Dunn, 1987: "A Stochastic Model of Particle Dispersion in the Atmosphere," Bound. Layer Met., 40, 147-163.

Briggs, G. A., W. L. Eberhard, J. E. Gaynor, W. R. Moninger and T. Uttal, 1983: "Convective Diffusion Field Measurements Compared with Laboratory and Numerical Experiments," 7th American Meteorological Society Symposium on Turbulence and Diffusion, November, 1985, Boulder, CO.

Brigham, E. O., 1974: The Fast Fourier Transform, Prentice-Hall, Engelwood Cliffs.

Brusasca, G., G. Tinarelli, D. Anfossi and P. Zanetti, 1987: "Particle Modeling Simulation of Atmospheric Dispersion using the MC-LAGPAR Package," Environmental Software, 2, 151-158.

Businger, J. A., J. C. Wyngaard, Y. Izumi and E. F. Bradley, 1971: "Flux-Profile Relationships in the Atmospheric Surface Layer," J. Atmos. Sci., 28, 181-189.

Cauhey, S. J. and S. G. Palmer, 1979: "Some Aspects of Turbulence Structure Through the Depth of the Convective Boundary Layer," Quart. J. Roy. Met. Soc., 105, 811-827.

Cauhey, S. J., M. Kitchen and J. R. Leighton, 1983: "Turbulence Structure in Convective Boundary Layers and Implications for Diffusion," Bound. Layer Met., 36, 345-352.

Cederwall, R. T., W. D. Ohmstede and R. E. Meyers, 1985: "Planetary Boundary Layer Structure Derived from Large Eddy Simulation for Benchmark Stability Categories," Preprint for November 1985 American Meteorological Society Conference on Atmospheric Diffusion, Colorado.

Chandrasekhar, S., 1943: "Stochastic Problems in Physics and Astronomy," Rev. Mod. Phys., 15, 1-89, reprinted in: Selected Papers on Noise and Stochastic Processes, 1954, Wax, N. (ed.), Dover, New York.

Chatwin, P. C., and C. M. Allen, 1985: "A Note on Time Averages in Turbulence with Reference to Geophysical Applications," Tellus, 37B, 46-49.

Clarke, J. F., J. K. S. Ching and J. M. Godowitch, 1983: "Lagrangian and Eulerian Time Scale Relationships and Plume Dispersion fromt the Tennessee Plume Study," 6th American Meteorological Society Symposium on Turbulence and Diffusion, March, 1983, Boston, MA.

Clough, W. S., 1973: "Transport of Particles to Surfaces," J. Aerosol Sci., 4, 227-234.

Corrsin, S., 1959: "Progress Report on Some Turbulent Diffusion Research," Adv. in Geophys., 6, 161-164.

Corrsin, S., 1963: "Estimates of the Relations Between Eulerian and Lagrangian Scales in Large Reynolds Number Turbulence," J. Atmos. Sci., 20, 115-119.

Csanady, G. T., 1973: Turbulent Diffusion in the Environment, D. Reidel, Boston.

Deardorff, J., 1970: "A Three-Dimensional Numerical Investigation of the Idealized Planetary Boundary Layer," Geophs. Fluid Dyn., 1, 377-410.

Deardorff, J. W., 1972: "Numerical Investigation of Neutral and Unstable Planetary Boundary Layers," J. Atmos. Sci., 29, 91-115.

Deardorff, J. W., 1973: "Three-Dimensional Numerical Modeling of the Planetary Boundary Layer," in: Workshop on Micrometeorology, Haugen, D. A. (ed.), Amer. Meteor. Soc., Boston.

Deardorff, J. W., 1974: "Three-Dimensional Study of the Height and Mean Structure of a Heated Planetary Boundary Layer," Bound. Layer Met., 7, 81-106.

Deardorff, J. W. and G. E. Willis, 1975: "A Parameterization of Diffusion into the Mixed Layer," J. Appl. Meteor., 14, 1451-1458.

Deardorff, J. W., 1985: "Laboratory Experiments on Diffusion: the Use of Convective Mixed-Layer Scaling," J. Clim. Appl. Meteorl., 24, 1143-1151.

De Baas, A. F., H. Van Dop and F. T. M. Nieuwstadt, 1986: "An Application of the Langevin Equation for Inhomogeneous Conditions to Dispersion in a Convective Boundary Layer," Quart. J. Roy. Met. Soc., 112, 165-180.

DeLaurentis, J. M. and B. A. Boughton, "A Comparison of Generators for Psuedo-Random Normal Deviates," SAND88-0952•UC-32, Sandia National Laboratories, NM.

DeVaull, G. E. and W. E. Dunn, 1988: "A Model-Data Comparison for Mean and Instantaneous Smoke Cencentrations Downwind from a Fog-Oil Smoke Generator," 9th Annual EOSAEL/TWI Conference, 29 November-1 December, 1988, White Sands Missile Range, NM.

DeVaull, G. E., W. E. Dunn, J. C. Liljegren and A. J. Policastro, 1988: "Development and Evaluation of a Sampling and Analysis Method for Fog-Oil Smoke," AD _____, University of Illinois, Urbana, IL 84PP4822.

Doran, J. C., T. W. Horst and P. W. Nickola, 1978a: "Variations in Measured Values of Lateral Diffusion Parameters," J. Appl. Meteor., 17, 825-831.

Doran, J. C., T. W. Horst and P. W. Nickola, 1978b: "Experimental Observations of the Dependence of Lateral and Vertical Dispersion Characteristics on Source Height," Atmos. Envir., 12, 2259-2263.

Draxler, R. R., 1976: "Determination of Atmospheric Diffusion Parameters," Atmos. Envir., 10, 99-105.

Dunn, W. E., J. A. Leylek and R. M. Chittenden, 1982: "A Laboratory Study of Buoyant Jets in Crossflow," International Association of Hydraulic Research Cooling Tower Workshop, 12-15 October 1982, Budapest, Hungary.

Durbin, P. A., 1980: "A Stochastic Model of Two-Particle Dispersion and Concentration Fluctuations in Homogeneous Turbulence," J. Fluid Mech., 100, 279-302.

Durbin, P. A., 1983: Stochastic Differential Equations and Turbulent Dispersion, NASA Ref. Pub. 1103.

Durham, M. D. and D. A. Lundgren, 1980: "Evaluation of Aerosol Aspiration Efficiency as a Function of Stokes Number, Velocity Ratio and Nozzle Angle," J. Aerosol Sci., 11, 179-188.

Dyer, A. J. and B. B. Hicks, 1970: "Flux-Gradient Relationships in the Constant Flux Layer," Quart. J. Roy. Met. Soc., 96, 715-721.

Dyer, A. J., 1974: "A Review of Flux-Profile Relationships," Bound. Layer Met., 7, 363-372.

Dyer, A. J. and E. F. Bradley, 1982: "An Alternative Analysis of Flux-Gradient Relationships at the 1976 ITCE," Bound. Layer Met., 22, 3-19.

Ermak, D. L., 1977: "An Analytical Model for Air Pollutant Transport and Deposition from a Point Source," Atmos. Envir., 11, 231-237.

Fan, L.-T., 1967: "Turbulent Buoyant Jets into Stratified or Flowing Ambient Fluids," Ph. D. Thesis, California Institute of Technology, Pasadena, CA.

Ferreira, R. T. D. S., 1978: "Unsteady Turbulent Thermal Convection," Ph. D. Thesis, University of Illinois, Urbana, IL.

Fiedler, B. H., 1984: "An Integral Model for the Vertical Turbulent Flux of a Scalar in a Mixed Layer," J. Atmos. Sci., 41, 674-680.

Fiedler, B. H. and C.-H. Moeng, 1985: "A Practical Integral Closure Model for Mean Vertical Transport of a Scalar in a Convective Boundary Layer," J. Atmos. Sci., 42.

Garland, J. A., 1982: "Dry Deposition of Small Particles to Grass in Field Conditions," Precipitation Scavenging, Dry Deposition, and Resuspension, Vol. 2, H. R. Pruppacher, R. G. Semonin and W. G. N. Slinn, (eds.), Elsevier, New York, 849-857.

Gifford, F. A., 1955: "A Simultaneous Lagrangian-Eulerian Turbulence Experiment," Monthly Weather Rev., 83, 293-301.

Gifford, F. A., 1961: "Use of Routine Meteorological Observations for Estimating Atmospheric Dispersion," Nucl. Safety, 2, 47-51.

Gifford, F. A., 1980: "Smoke as a Quantitative Atmospheric Diffusion Tracer," Atmos. Envir., 14, 1119-1121.

Gryning, S.-E., A. P. Van Ulden and S. E. Larsen, 1983: "Dispersion from a Continuous Ground-Level Source Investigated by a K Model," Quart. J. Roy. Met. Soc., 109, 355-364.

Hanna, S. R., 1979: "Some Statistics of Lagrangian and Eulerian Wind Fluctuations," J. Appl. Meteor., 18, 518-525.

Hanna, S. R., 1981: "Lagrangian and Eulerian Time-Scale Relations in the Daytime Boundary Layer," J. Appl. Meteor., 20, 242-249.

Hanna, S. R., 1984: "Applications in Air Pollution Modeling," in: Atmospheric Turbulence and Air Pollution Modeling, Nieuwstadt, F. T. M. and H. van Dop (eds.), D. Reidel, Boston, 275-310.

Hansen, F. V., 1980: "Flux-Profile Relationships for Development of Standards of Comparison," ASL Internal Report, US Army Atmospheric Sciences Laboratory, White Sands Missile Range, NM.

Hansen, F. V., 1989: Procedures for the Manual Application of PSMOKE: A Line Source Model for the M5 Smoke Pot, U S Army Atmospheric Sciences Laboratory, Las Cruces, NM.

Haugen, D. A., 1959: "Project Prairie Grass: A Field Program in Diffusion," Volume 3, Geophs. Res. Papers No. 59, Air Force Cambridge Research Center, AD-217076.

Haugen, D. A., 1966: "Some Lagrangian Properties of Turbulence Deduced from Atmospheric Diffusion Experiments," J. Appl. Meteor., 5, 646-652.

Hay, J. S. and F. Pasquill, 1957: "Diffusion from a Fixed Source at a Height of a Few Hundred Feet in the Atmosphere," J. Fluid Mech., 2, 299-310.

Hay, J. S. and F. Pasquill, 1959: "Diffusion from a Continuous Source in Relation to the Spectrum and Scale of Turbulence," Adv. in Geophys., 6, 345-365.

Herring, J. R., 1977: "Subgrid Scale Modeling - An Introduction and Overview," in: Turbulent Shear Flows I, Springer-Verlag, New York, 347-352.

Hinds, W. C., 1982: Aerosol Technology – Properties, Behavior and Measurement of Airborne Particles, John Wiley and Sons, New York.

Højstrup, Jørgen, 1982: "Velocity Spectra in the Unstable Planetary Boundary Layer," J. Atmos. Sci., 39, 2239-2248.

Horst, T. W., 1979: "Lagrangian Similarity Modeling of Vertical Diffusion from a Ground-Level Source," J. Appl. Met., 18, 733-740.

Hunt, J. C. R., J. C. Kaimal and J. E. Gaynor, 1985: "Some Observations of Turbulence Structure in Stable Layers," Quart. J. Roy. Met. Soc, 111, 793-815.

Hunt, J. C. R., 1984a: "Turbulence Structure in Convective and Shear-Free Boundary Layers," J. Fluid Mech., 138, 161-184.

Hunt, J. C. R., 1984b: "Diffusion in the Stable Boundary Layer," in: Atmospheric Turbulence and Air Pollution Modeling, Nieuwstadt, F. T. M. and H. van Dop (eds.), D. Reidel, Boston, 231-274.

Hunt, J. C. R. and A. H. Weber, 1979: "A Lagrangian Statistical Analysis of Diffusion from a Ground-Level Source in a Turbulent Boundary Layer," Quart. J. Roy. Met. Soc., 105, 423-443.

Irwin, J. S., 1983: "Estimating Plume Dispersion - A Comparison of Several Sigma Schemes," J. Clim. Appl. Meteorol., 22, 92-114.

Irwin, J. S. and F. S. Binkowski, 1980: "Estimation of the Monin-Obukhov Scaling Length Using On-Site Instrumentation," Atmos. Envir., 15, 1091-1094.

Jenkins, R. A., T. M. Gayle, J. S. Wike and D. L. Manning, 1982: "Sampling and Chemical Characterization of Concentrated Smokes," Toxic Materials in the Atmosphere, ASTM STP 786, American Society for Testing and Materials, 153-166.

Kaimal, J. C., J. C. Wyngaard, Y. Izumi and O. R. Cote, 1972: "Spectral Characteristics of Surface Layer Turbulence," Quart. J. Roy. Meteor. Soc., 98, 653-689.

Kaimal, J. C., D. A. Haugen, O. R. Cote, Y. Izumi, S. J. Caughey and C. J. Readings, 1976: "Turbulence Structure in the Convective Boundary Layer," J. Atmos. Sci., 33, 2152-2169.

Kaimal, J. C., 1978: "Horizontal Velocity Spectra in an Unstable Surface Layer," J. Atmos. Sci., 35, 18-23.

Kaimal, J. C., W. L. Eberhard, W. R. Moninger, J. E. Gaynor, S. W. Troxel, T. Uttal, G. A. Briggs and G. E. Start, 1986: "Project CONDORS – Convective Diffusion Observed by Remote Sensors," Report No. 7, Boulder Atmospheric Observatory, Boulder, CO.

Katz, S., A. Snelson, R. Farlow, R. Welker and S. Mainer, 1980: Physical and Chemical Characterization of Military Smokes –Part I: Final Report on Hexachloroethane Smoke," AD _____, IIT Research Institute, Chicago, IL, DAMD17-78-C-8085.

Katz, S., A. Snelson, R. Butler, R. Farlow, R. Welker, S. Mainer and N. Rajendran, 1980: Physical and Chemical Characterization of Military Smokes –Part II: Final Report on Fog Oils and Oil Fogs," AD _____, IIT Research Institute, Chicago, IL, DAMD17-78-C-8085.

Kumar, R., 1983: "Studies in Unsteady Penetrative Thermal Convection," Ph. D. Thesis, University of Illinois, Urbana, IL.

Kumar, R. and R. J. Adrian, 1986: "Higher Order Moments in the Entrainment Zone of Turbulent Thermal Convection," J. Heat Transfer, 108, 323-329.

Laktionov, A. G., 1969: "Aspiration of an Aerosol Into a Vertical Tube from a Flow Transverse to it," AD 760947, National Technical Information Service (NTIS).

Lamb, R. G., 1978: "A Numerical Simulation of Dispersion from an Elevated Point Source in the Convective Planetary Boundary Layer," Atmos. Envir., 12, 1297-1304.

Lamb, R. G., H. Hogo and L. E. Reid, 1979: "A Lagrangian Approach to Modeling Air Pollutant Dispersion," EPA-600/4-79-023, U.S. Environmental Protection Agency.

Lamb, R. G., 1980: "Mathematical Principles of Turbulent Diffusion Modeling," in: Atmospheric Planetary Boundary Layer Physics, A. Longhetto (ed.), Elsevier, New York, 173-210.

Lamb, R. G., 1981: "A Scheme for Simulating Particle-Pair Motions in a Turbulent Fluid," J. Comp. Phys., 39, 329-346.

Lamb, R. G., 1984: "Diffusion in the Convective Boundary Layer," in: Atmospheric Turbulence and Air Pollution Modeling, Nieuwstadt, F. T. M. and H. van Dop (eds.), D. Reidel, Boston, 159-229.

Launder, B. E., 1978: "Heat and Mass Transport," in: Turbulence, second edition, P. Bradshaw (ed.), Springer-Verlag, New York, 231-287.

Lee, J. T. and G. L. Stone, 1983: "Eulerian-Lagrangian Relationships in Monte Carlo Simulations of Turbulent Diffusion," Atmos. Envir., 17, 2483-2487.

Legg, B. J., 1983: "Turbulent Dispersion from an Elevated Line Source: Markov Chain Simulations of Concentration and Flux Profiles," Quart. J. Roy. Met. Soc., 109, 645-660.

Legg, B. J. and M. R. Raupach, 1982: "Markov-Chain Simulation of Particle Dispersion in Inhomogeneous Flows: The Mean Drift Velocity Induced by a Gradient in Eulerian Velocity Variance," Bound. Layer Met., 24, 3-13.

Lenschow, D. H., 1970: "Airplane Measurements of Planetary Boundary Layer Structure," J. Appl. Met., 9, 874-884.

Lenschow, D. H. and P. L. Stephens, 1980: "The Role of Thermal in the Convective Boundary Layer," Bound. Layer Met., 19, 509-532.

Lenschow, D. H., J. C. Wyngaard and W. T. Pennell, 1980: "Mean-Field and Second-Moment Budgets in a Baroclinic, Convective Boundary Layer," J. Atmos. Sci., 37, 1313-1326.

Leonard, A., 1974: "Energy Cascade in Large Eddy Simulations of Turbulent Fluid Flows," Advances in Geophysics, Vol. 18, Academic Press, 237-248.

Lewellen, W. S., 1977: "Use of Invariant Modeling," in: Handbook of Turbulence, Vol. 1, Frost, W. and T. H. Moulder (eds.), Plenum, 237-280.

Ley, A. J., 1982: "A Random Walk Simulation of Two-Dimensional Turbulent Diffusion in the Neutral Surface Layer," Atmos. Envir., 16, 2799-2808.

Ley, A. J. and D. J. Thomson, 1983: "A Random Walk Model of Dispersion in the Diabatic Surface Layer," Quart. J. Roy. Met. Soc., 109, 847-880.

Leylek, J. A., 1984: "An Experimental Study of Single and Multiple Turbulent Buoyant Jets in Crossflow," Ph. D. Thesis, University of Illinois, Urbana, IL.

Liljegren, J. C., W. E. Dunn, G. E. DeVaull and A. J. Policastro, 1988: "Field Study of Fog Oil Smoke," AD _____, University of Illinois, Urbana, IL 84PP4822.

Lorimer, G. S., 1986: "The Kernal Method for Air Quality Modelling – I. Mathematical Foundation," Atmos. Envir., 20, 1447-1452.

Love, M. D. and D. C. Leslie, 1977: "Studies of Subgrid Modeling with Classical Closures and Burgers Equation," in: Turbulent Shear Flows I, Springer-Verlag, New York, 353-369.

Mansour, N. N., P. Moin, W. C. Reynolds and J. H. Ferziger, 1977: "Improved Methods for Large Eddy Simulation of Turbulence," in: Turbulent Shear Flows I, Springer-Verlag, New York, 386-401.

Mason, C. J. and H. Moses, 1984: "Meteorological Instrumentation," Atmospheric Science and Power Production, Randerson, D. (ed.), U S Dept. of Commerce, DOE/TIC-27601 (DE84005177), 85-103.

Meyers, R. M., W. D. Ohmstede and R. T. Cederwall, 1985: "A Model of Finite Velocity Diffusion Dynamics from Large Eddy Simulation, Exhibiting Both Space and Time Memory," Preprint for November 1985 American Meteorological Society Conference on Atmospheric Diffusion, Colorado.

Mikkelsen, T., 1982: "A Statistical Theory on the Turbulent Diffusion of Gaussian Puffs," Risø-R-475, RISØ National Laboratory, Denmark.

Mikkelsen, T., 1983: "The Borris Field Experiment: Observations of Smoke Diffusion in the Surface Layer over Homogeneous Terrain," Risø-R-479, RISØ National Laboratory, Denmark.

Miller, R. W., 1983: Flow Measurement Engineering Handbook, McGraw-Hill, New York.

Moeng, C.-H., 1984: "A Large Eddy Simulation Model for the Study of Planetary Boundary Layer Turbulence," J. Atmos. Sci., 41, 2052-2062.

Moeng, C.-H. and J. C. Wyngaard, 1984: "Statistics of Conservative Scalars in the Convective Boundary Layer," J. Atmos. Sci., 41, 3161-3169.

Monin, A. S. and A. M. Obukhov, 1954: "Basic Laws of Turbulent Mixing in the Ground Layer of the Atmosphere," translated from Trudy Geofiz. Inst. Akad. Nauk SSSR, 151(24), 163-187, reprinted in Aerophysics of Air Pollution, AIAA Selected Reprint Series Vol. 9, Fay, J. A. and D. P. Hoult (eds.), AIAA Press, New York.

Monin, A. S., 1959: "Smoke Propagation in the Atmospheric Surface Layer," Adv. in Geophs., 6, 331-343.

Monin, A. S. and A. M. Yaglom, 1971: Statistical Fluid Mechanics: Mechanics of Turbulence, Vol. 1 (Engl. trnsl.), MIT Press, Cambridge.

Neumann, J., 1978: "Some Observations on the Simple Exponential Function as a Lagrangian Velocity Correlation Function in Turbulent Diffusion," Atmos. Envir., 12, 1965-1968.

Nickola, P. W., 1977: "The Hanford 67-Series: A Volume of Atmospheric Field Dispersion Measurements," PNL-2433, Pacific Northwest Laboratory, EY-76-C-06-1830.

Nickola, P. W., J. V. Ramsdell, C. S. Glantz and R. E. Kerns, 1983: "Hanford Atmospheric Dispersion Data: 1960 Though June 1967," PNL-4814, Pacific Northwest Laboratory.

Nieuwstadt, F., 1977: "The Computation of the Friction Velocity and Temperature Scale from Temperature and Wind Profiles by Least-Squares Methods," Bound. Layer Met., 14, 235-246.

Nieuwstadt, F. T. M., 1980: "Application of Mixed-Layer Similarity to the Observed Dispersion from a Ground-level Source," J. Appl. Meteorol., 19, 157-162.

Olesen, H. R., S. E. Larsen, and J. Højstrup, 1984: "Modeling Velocity Spectra in the Lower Part of the Planetary Boundary Layer," Bound. Layer Met., 29, 285-312.

Orszag, S. A., 1970: "Analytical Theories of Turbulence," J. Fluid Mech., 41, 363-386.

Panofsky, H. A., H. Tennekes, D. H. Lenschow and J. C. Wyngaard, 1977: "The Characteristics of Turbulent Velocity Components in the Surface Layer under Convective Conditions," Bound. Layer Met., 11, 355-361.

Panofsky, H. A. and J. A. Dutton, 1984: Atmospheric Turbulence, John Wiley and Sons, New York.

Papoulis, A., 1984: Probability, Random Variables and Stochastic Processes, (2nd ed.), McGraw-Hill, New York.

Pasquill, F., 1974: Atmospheric Diffusion, (2nd ed.), John Wiley and Sons, New York.

Pasquill, F. and F. B. Smith, 1983: Atmospheric Diffusion, (3rd ed.), Ellis Horwood, New York.

Paulson, C. A., 1970: " The Mathematical Representation of Wind Speed and Temperature Profiles in the Unstable Atmospheric Surface Layer," J. Appl. Meteor., 9, 857-861.

Petersen, R. L., 1978: "Plume Rise and Dispersion for Varying Ambient Turbulence, Thermal Stratification and Stack Exit Conditions," Ph. D. Thesis, Colorado State University, Fort Collins, CO.

Philip, J. R. , 1967: "Relations Between Eulerian and Lagrangian Statistics," Phys. Fluids Supplement, 10, S69-S71.

Policastro, A. J. and W. E. Dunn, 1985: "Survey and Evaluation of Field Data Suitable for Smoke Hazard Evaluation," AD A161 880, University of Illinois, Urbana, IL 84PP4822.

Poreh, M. and J. E. Cermak, 1984: "Wind Tunnel Simulation of Diffusion in a Convective Boundary Layer," Bound. Layer Met., 30, 431-455.

Poreh, M. and J. E. Cermak, 1985: "Study of Neutrally Buoyant Plumes in a Convective Boundary Layer with Mean Velocity and Shear," 7th American Meteorological Society Symposium on Turbulence and Diffusion, November, 1985, Boulder, CO.

Pope, S. B., 1987: "Consistency Conditions for Random-Walk Models of Turbulent Dispersion," Phys. Fluids, 30, 2374-2379.

Prahm, L. P., R. Berkowicz and O. Christensen, 1979: "Generalization of K Theory for Turbulent Diffusion, Part II: Spectral Diffusivity Model for Plume Dispersion," J. Appl. Meteorol., 18, 273-282.

Rabiner, L. R., 1979: "Power Spectrum Analysis and Correlation," in: Programs for Digital Signal Processing, IEEE Press, New York.

Rajagopal, A. K. and E. C. G. Sudarshan, 1974: "Some Generalizations of the Marcinkiewicz Theorem and its Implications to Certain Approximation Schemes in Many-Particle Physics," Phys. Rev. A, 10, 1852-1857.

Randerson, D., 1984: "Power Production and the Atmosphere," Atmospheric Science and Power Production, Randerson, D. (ed.), U S Dept. of Commerce, DOE/TIC-27601 (DE84005177), 1-31.

Raupach, M. R. and A. S. Thom, 1981: "Turbulence in and Above Plant Canopies," Ann. Rev. Fluid Mech., 13, 97-129.

Reid, J. D., 1979: "Markov Chain Simulations of Vertical Dispersion in the Neutral Surface Layer for Surface and Elevated Releases," Bound. Layer Met., 16, 3-22.

Reynolds, W. C. and T. Cebeci, 1978: "Calculation of Turbulent Flows," in: Turbulence, second edition, P. Bradshaw (ed.), Springer-Verlag, New York, 193-229.

Roberts, O. F. T., 1923: "The Theoretical Scattering of Smoke in a Turbulent Atmosphere," Proc. Roy. Soc., A, 104, 640-654.

Rote, D. M., 1980: "Gaussian Plume Models," in: Atmospheric Planetary Boundary Layer Physics, A. Longhetto (ed.), Elsevier, New York, 211-228.

Rounds, W., 1955: "Solutions of the Two-Dimensional Diffusion Equation," Trans. Amer. Geophys. Union, 36, 395-405.

Saffman, P. G., 1963: "An Approximate Calculation of Lagrangian Autocorrelation for Stationary Homogeneous Turbulence," J. Appl. Sci. Res., 11, 245-255.

Sawford, B. L., 1982: "Lagrangian Monte Carlo Simulation of the Turbulent Motion of a Pair of Particles," Quart. J. Roy. Met. Soc., 108, 207-213.

Sawford, B. L., 1986: "Generalized Random Forcing in Random-Walk Turbulent Dispersion Models," Phys. Fluids, 29, 3582-3585.

Sehmel, G. A., 1967: "Estimation of Airstream Concentrations of Particulates from Subisokinetically Obtained Filter Samples," Am. Ind. Hyg. Assoc. J., 28, 243-253.

Sehmel, G. A., 1973: "Particle Eddy Diffusivities and Deposition Velocities for Isothermal Flow and Smooth Surfaces," J. Aerosol Sci., 4, 125-138.

Smith, F. B. and R. M. Blackall, 1979: "The Application of Field Experimental Data to the Parameterization of Disperison Plumes from Ground-Level and Elevated Sources," Mathematical Modelling of Turbulent Diffusion in the Environment, Harris, C. J. (ed.), Academic Press, as cited by Pasquill and Smith, 1983.

Sutton, O. G., 1932: "A Theory of Eddy Diffusion in the Atmosphere," Proc. Royal Soc., A, 135, 143-165, reprinted in Aerophysics of Air Pollution, AIAA Selected Reprint Series Vol. 9, Fay, J. A. and D. P. Hoult (eds.), AIAA Press, New York.

Sutton, O. G., 1934: "Wind Structure and Evaporation in a Turbulent Atmosphere," Proc. Roy. Soc., A, 146, 701-722.

Sutton, O. G., 1947a: "The Problem of Diffusion in the Lower Atmosphere," Quart. J. Roy. Met. Soc., 73, 257-281.

Sutton, O. G., 1947b: "The Theoretical Distribution of Airborne Pollution From Factory Chimneys," Quart. J. Roy. Met. Soc., 73, 426-436.

Sutton, O. G.,1953: Micrometeorology, McGraw-Hill, New York.

Taylor, G. I., 1921: "Diffusion by Continuous Movements," Proc. London Math. Soc.," 20, 196-212, reprinted in Aerophysics of Air Pollution, AIAA Selected Reprint Series Vol. 9, Fay, J. A. and D. P. Hoult (eds.), AIAA Press, New York.

Taylor, G. I., 1959: "The Present Position in the Theory of Turbulent Diffusion," Adv. in Geophs., 6, 101-112.

Telford, J. W. and J. Warner, 1964: "Fluxes of Heat and Vapor in the Lower Atmosphere Derived from Aircraft Observations," J. Atmos. Sci., 21, 539-548.

Tennekes, H. and J. L. Lumley, 1972: A First Course in Turbulence, MIT Press, Cambridge.

Tennekes, H., 1979: "The Exponential Lagrangian Correlation Function and Turbulent Diffusion in the Inertial Subrange," Atmos. Envir., 13, 1565-1567.

Tennekes, H., 1984: "Similarity Relations, Scaling Laws and Spectral Dynamics," in: Atmospheric Turbulence and Air Pollution Modeling, Nieuwstadt, F. T. M. and H. van Dop (eds.), D. Reidel Boston, 37-68.

Thomson, D. J., 1984: "Random Walk Modeling of Diffusion in Inhomogeneous Turbulence," Quart. J. Roy. Met. Soc., 110, 1107-1120.

Thomson. D. L., 1987: "Criteria for the Selection of Stochastic Models of Particle Trajectories in Turbulent Flows," J. Fluid Mech., 180, 529-556.

Uhlenbeck, G. E. and L. S. Ornstein, 1930: "On the Theory of Brownian Motion," Phys. Rev., 36, 823-841, reprinted in: Selected Papers on Noise and Stochastic Processes, 1954, Wax, N. (ed.), Dover, New York.

US Army, 1964: Technical Bulletin: M1 10-lb HC Smoke Pot and M5 30-lb Smoke Pot, TB-CML-100.

US Army, 1985: Operator's Manual, M3A4 Smoke Generator (1040-01-143-9506), TM 3-1040-276-10.

US Army, 1987: Smoke Operations, FC-3-50-1.

Van Dop, H., F. T. M. Nieuwstadt and J. C. R. Hunt, 1985: "Random Walk Models for Particle Displacements in Inhomogeneous Unsteady Flows," Phys. Fluids, 28, 1639-1653.

Van Stijn, Th. L. and F. T. M. Nieuwstadt, 1986: "On the Relation Between a Lagrangian and a Eulerian Model of Diffusion in Homogeneous, Stationary and Non-Gaussian Turbulence," Atmos. Envir., 6, 1111-1120.

Van Ulden, A. P., 1978: "Simple Estimates for Vertical Diffusion from Sources Near the Ground," Atmos. Envir., 12, 2125-2129.

Waldron, A. W., 1977: "Turbulent Measurements on a Forty-Eight Meter Tower in Desert Terrain," DPG Document No. M615A, US Army Dugway Proving Ground, Dugway, UT.

Wang, C. W. and Uhlenbeck, 1945: On the Theory of Brownian Motion II," Rev. Mod. Phys., 17, 323-342, reprinted in: Selected Papers on Noise and Stochastic Processes, 1954, Wax, N. (ed.), Dover, New York.

Warner, J. and J. W. Telford, 1963: "Some Patterns of Convection in the Lower Atmosphere," J. Atmos. Sci., 20, 313-318.

Warner, J. and J. W. Telford, 1967: "Convection Below Cloud Base," J. Atmos. Sci., 24, 374-382.

Willis, G. E. and J. W. Deardorff, 1974: "A Laboratory Model of the Unstable Planetary Boundary Layer," J. Atmos. Sci., 31, 1297-1307.

Willis, G. E. and J. W. Deardorff, 1976a: "A Laboratory Model of Diffusion into the Convective Planetary Boundary Layer," Quart. J. Roy. Met. Soc., 102, 427-445.

Willis, G. E. and J. W. Deardorff, 1976b: "On the Use of Taylor's Translation Hypothesis for Diffusion in the Mixed Layer," Quart. J. Roy. Met. Soc., 102, 817-822.

Willis, G. E. and J. W. Deardorff, 1978: "A Laboratory Study of Dispersion from an Elevated Source Within a Modeled Convective Boundary Layer," Atmos. Envir., 12, 1305-1311.

Willis, G. E. and J. W. Deardorff, 1981: "A Laboratory Study of Dispersion from a Source in the Middle of the Convectively Mixed Layer," Atmos. Envir., 15, 109-117.

Willis, G. E. and J. W. Deardorff, 1983: "On Plume Rise Within a Convective Boundary Layer," Atmos. Envir., 17, 2435-2447.

Wilson, J. D., G. W. Thurtell and G. E. Kidd, 1981a: "Numerical Simulation of Particle Trajectories in Inhomogeneous Turbulence I: Systems with Constant Turbulent Velocity Scale," Bound. Layer Met., 21, 295-313.

Wilson, J. D., G. W. Thurtell and G. E. Kidd, 1981b: "Numerical Simulation of Particle Trajectories in Inhomogeneous Turbulence II: Systems with Variable Turbulent Velocity Scale," Bound. Layer Met., 21, 423-441.

Wilson, J. D., G. W. Thurtell and G. E. Kidd, 1981c: "Numerical Simulation of Particle Trajectories in Inhomogeneous Turbulence III: Comparison of Predictions with Experimental Data for the Atmospheric Surface Layer," Bound. Layer Met., 21, 443-463.

Wyngaard, J. C., O. R. Coté and Y. Izumi, 1971: "Local Free Convection, Similarity, and the Budgets of Shear Stress and Heat Flux," J. Atmos. Sci., 28, 1171-1182, as cited by Willis and Deardorff (1976b).

Wyngaard, J. C., 1984: "Boundary Layer Modeling," in: Atmospheric Turbulence and Air Pollution Modeling, Nieuwstadt, F. T. M. and H. van Dop (eds.), D. Reidel, Boston, 69-106.

Wyngaard, J. C., 1985: "Structure of the Planetary Boundary Layer and Implications for its Modeling," J. Clim. and Appl. Met., 24, 1131-1142.

Young, H. D., 1976: Fundamentals of Waves, Optics, and Modern Physics, 2nd edition, McGraw-Hill.

DOCUMENT DISTRIBUTION LIST

No. of Copies	
15	Commander U.S. Army Biomedical Research and Development Laboratory ATTN: SGRD-UBZ-RA Fort Detrick, Frederick, MD 21701-5010
2	Commander U.S. Army Medical Research and Development Command ATTN: SGRD-RMI-S Fort Detrick, Frederick, MD 21701-5012
1	Commander U.S. Army Laboratory Command Army Research Office ATTN: SLCRO-GS/Dr. Walter Bach, Jr. Research Triangle Park, NC 27709-2211
1	Battelle-Pacific Northwest Laboratory ATTN: Dr. Peter van Voris P.O. Box 999 Richland, WA 99352
1	Commander U.S. Army Environmental Hygiene Agency ATTN: HSHB-ME-AA/Mr. Jeff Kirkpatrick Aberdeen Proving Ground, MD 21010-5423
1	Commander Chemical Research, Development and Engineering Center ATTN: SMCCR-ST/Mr. Ron O. Pennsyle Aberdeen Proving Ground, MD 21020